Generalized Quantum Defect Methods in Quantum Chemistry

by

Serhan Altunata

Submitted to the Department of Chemistry
in partial fulfillment of the requirements for the degree of

Doctor of Philosophy in Physical Chemistry

at the

MASSACHUSETTS INSTITUTE OF TECHNOLOGY

May 2006

Author . . . .
Department of Chemistry
May 23, 2006

Certified by . . . .
Robert W. Field
Haslam and Dewey Professor of Chemistry
Thesis Supervisor

Accepted by . . . .
Robert W. Field
Chairman, Department Committee on Graduate Students

This doctoral thesis has been examined by a Committee of the Department of Chemistry that included

Professor Sylvia T. Ceyer____
(Chairman)
Professor Jianshu Cao____

Professor Robert W. Field____
(Thesis Supervisor)

Generalized Quantum Defect Methods in Quantum Chemistry

by

Serhan Altunata

Submitted to the Department of Chemistry
on May 23, 2006, in partial fulfillment of the
requirements for the degree of
Doctor of Philosophy in Physical Chemistry

Abstract

The reaction matrix of multichannel quantum defect theory, **K**, gives a complete picture of the electronic structure and the electron ↔ nuclear dynamics for a molecule. The reaction matrix can be used to examine both bound states and free electron scattering properties of molecular systems, which are characterized by a Rydberg/scattering electron incident on an ionic-core. An *ab initio* computation of the reaction matrix for fixed molecular geometries is a substantive but important theoretical effort. In this thesis, a generalized quantum defect method is presented for determining the reaction matrix in a form which minimizes its energy dependence. This reaction matrix method is applied to the Rydberg electronic structure of Calcium monofluoride. The spectroscopic quantum defects for the $^2\Sigma^+$,$^2\Pi$, $^2\Delta$, and $^2\Phi$ states of CaF are computed using an effective one-electron calculation. Good agreement with the experimental values is obtained. The Σ-symmetry eigenquantum defects obtained from the CaF reaction matrix are found to have an energy dependence characteristic of a resonance. The analysis shows that the main features of the energy-dependent structure in the eigenphases are a consequence of a broad shape resonance in the $^2\Sigma^+$ Rydberg series. This short-lived resonance is spread over the entire $^2\Sigma^+$ Rydberg series and extends well into the ionization continuum. The effect of the shape resonance is manifested as a *global* "scarring" of the Rydberg spectrum, which is distinct from the more familiar *local* level-perturbations. This effect has been unnoticed in previous analyses.

The quantum chemical foundation of the quantum defect method is established by a many-electron generalization of the reaction matrix calculation. Test results that validate the many-electron theory are presented for the quantum defects of the $1s\sigma_g np\sigma_u$ $^1\Sigma_u^+$ Rydberg series of the hydrogen molecule. It is possible that the reaction matrix calculations on CaF and H_2 can pave the way for a novel type of quantum chemistry that aims to calculate the electronic structure over the entire bound-state region, as opposed to the current methods that focus on state by state calculations.

Thesis Supervisor: Robert W. Field
Title: Haslam and Dewey Professor of Chemistry

Acknowledgments

At the end of this long journey, it is my pleasure to extend my warm gratitude to the many wonderful people I have met over the years. One among these people takes a special precedence. My advisor, Prof. Robert W. Field, has given me the complete freedom to pursue my curiosity since the first day I arrived at MIT. He provided constant guidance, encouraging, smiling, and somehow, always knowing where to go next. He never told me I was wrong, even when he knew I was dead wrong, but always chose to wait and allow me to discover the truth on my own. As I look back upon what I have achieved, I realize that he has been the greatest teacher and mentor in my life. Thank you, Bob, for making this an extraordinary experience. None of this would have been possible without you.

I would like to thank my parents for their love, support and raising me the way I am. I devote this thesis to them in our native language Turkish:

Sevgili Annem ve Babam, Iste sonunda bu tezide bitirdim! Goztepe'nin kenar mahallesinde futbol oynayan kopuk cocugun buralara gelecegini bir tek siz gordunuz. Gozunuzu kirpmadan, varinizla, yokunuzla beni desteklediniz. Sizin sevginiz olmadan bunlarin hicbiri mumkun olmazdi. Tessekur kelimesi size az kalir. Hazirlanin, daha nice basarilara birlikte yuruyecegiz. Bu arada en buyuk cim bom!

I would like to warmly thank Prof. Jianshu Cao for his valuable collaboration and guidance. I have truly enjoyed working with him on my semiclassical Rydberg wavepacket project, which bore my first, and probably the most memorable, paper in Physical Review A. Prof. Sylvia T. Ceyer is also greatly acknowledged for the valuable comments she has provided as my thesis committee chair.

I would like to thank the members of the Robert W. Field group for helping me merge my theoretical studies with experimental work. I have learnt much from them and benefited greatly from fruitful discussions on spectroscopy. Specifically, I feel privileged to have worked with Vladimir Petrovic and Bryan Wong on various challenging and interesting theoretical projects. I would also like to thank Ryan Thom, who has patiently answered my endless questions on a wide range of topics in spectroscopy. My special thanks goes to our past member Jason O. Clevenger for welcoming me to the Rydberg project when I first joined the Robert W. Field group.

I would like to express my gratitude to the members of the MIT theoretical group. It has been a great pleasure to share a work space with them. They have made many precious contributions to my scientific knowledge through discussions and our competitive problem solving sessions. I would like to thank Steve Presse, Jim Witkoskie, Xiang Xia, Shilong Yeng, Jianlan Wu, Chiao-Lun Cheng, and Ophir Flomenbo for making the zoo an enjoyable and welcoming environment.

I would like to thank my sister, Selen, for being the wise guide in my life. She has shown me the right choices and helped me to navigate many of the challenges of graduate school. She is a great buddy to have.

I would like to thank Cindy for her continuous support and caring. She has been my source of inspiration during both the pleasant times and the hardships that I have experienced during my stay at MIT. I would like to thank her for being part of my life.

Contents

List of Figures

List of Tables

Chapter 1

Introduction

Multichannel quantum defect theory (MQDT) [112] is a powerful tool used in the analysis of Rydberg spectra of atoms and molecules. Stated most simply, MQDT is an extension of continuum scattering theory to the energy region below an ionization threshold. In atoms, the theory is capable of describing how an infinity of Rydberg states is perturbed by one or more interloping states that originate from different electronic configurations [87]. In molecules, MQDT provides a quantitative characterization of the electron/ro-vibrational interactions that lead to non-adiabatic flow of energy between the electronic and nuclear degrees of freedom [47]. Contrary to the widely used effective Hamiltonian methods, MQDT represents the entire molecular Rydberg spectrum in terms a quantum defect matrix, which depends on the point-group symmetry, nuclear geometry, and electronic energy. It is this property of MQDT that allows for an analysis of perturbations of global extent. Such a representation would be intractable in an effective Hamiltonian treatment. The main objective of this project is to develop efficient and reliable methods for the first principles calculation of the elements of the quantum defect matrix. In particular, we are interested in using the *ab initio* quantum defect matrix to understand the causes and the consequences of rich resonance behavior encountered commonly in Rydberg spectra. Such resonance behavior can arise from the accidental matching of classical frequencies associated with electronic and nuclear motions in the molecule or it may arise within the electronic structure in the form of a *shape resonance* [16].

The theory developed here is not specialized to a particular molecule; all molecule-specific approximations are avoided and it is constructed to be universally applicable to all types of Rydberg states. However, the calcium monofluoride (CaF) molecule has been extensively studied by this group and a vast amount of experimental data exists on its Rydberg structure [37, 65, 40]. For this reason, the CaF molecule is used as a model system to validate the derived theories. In the process, we uncover an aspect of the electronic structure of this well-studied molecule using the tools of MQDT, which had been unnoticed . This discovery of a broad shape resonance in the Rydberg states of CaF and the consequent breakdown of *Mulliken's rule* [1] is described in **Chapter 5**.

1.1 Historical Account of MQDT

Early use of MQDT had been restricted to empirical analyses of atomic Rydberg spectra. MQDT was in part invented as a theory capable of describing the strong perturbation of a Rydberg series by an interloping state, i.e. a state, which belongs to a different configuration of the ionic core. An illustrative example of this situation is found in the $(5s\ nd)^1D_2$ Rydberg series of cadmium. This Rydberg series is strongly perturbed by a doubly excited configuration of the type $(5p^2)^1D_2$, which is located energetically above the $Cd^+(5s)$ ionization threshold, as shown in Fig. 1-1. All members of the Rydberg series are shifted to lower energy as a consequence of the perturbation. An analysis by MQDT accurately accounts for the level shifts in terms of a quantum defect that varies slowly with energy along the Rydberg series [87].

More generally, MQDT provides a convenient means to disentangle one multiply and strongly perturbed series from another Rydberg series that converges to a different ionization threshold. This is accomplished by a device called the Lu-Fano plot [79], which is illustrated for several observed Rydberg series of Xe in Fig. 1-2.

---

[1] Mulliken's rule describes a generic property of Rydberg states. It states that every wavefunction member of a Rydberg series is built on an innermost lobe, which remains invariant in shape and nodal position as a function of excitation energy [90]. Mulliken's rule is the underlying basis for many of the Rydberg scaling laws [74] that are used in analysis of Rydberg spectra.

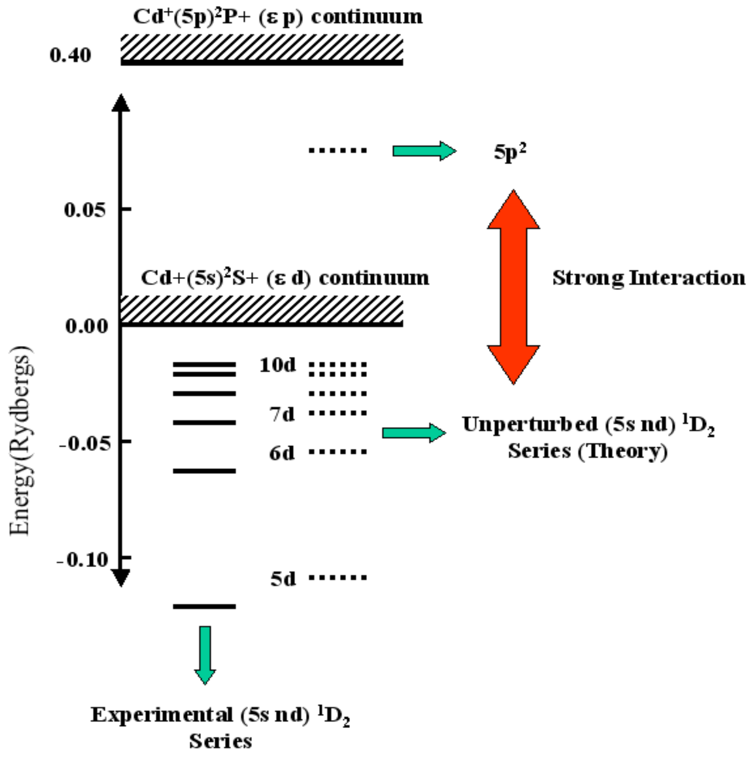

Figure 1-1: Schematic representation of the $(5s\ nd)^1D_2$ Rydberg series of Cd. The dashed lines represent the unperturbed $(5s\ nd)^1D_2$ series calculated by MQDT without taking into account the configuration interaction with the $(5p^2)^1D_2$ doubly excited state, which lies above the $Cd^+(5s)$ ionization threshold. When this interaction is turned on, all of the Rydberg levels are shifted down in energy. The effects of the interaction are distributed throughout the Rydberg series and cannot easily be captured in a state-by-state calculation. This sketch has been constructed using energy data reported in reference [87].

Photoabsorption by the Xe atom, initially in its ${}^1S_0$ ground state, leads to J=1, odd parity states that belong to five different Rydberg series in the *jj* coupling scheme [2]. Three of these series, $5p^5({}^2P_{3/2})ns_{1/2}$, $5p^5({}^2P_{3/2})nd_{3/2}$ and $5p^5({}^2P_{3/2})nd_{5/2}$, converge to the $5p^5({}^2P_{3/2})$ ionization threshold. The remaining two, $5p^5({}^2P_{1/2})ns_{1/2}$ and $5p^5({}^2P_{1/2})nd_{3/2}$, converge to the $5p^5({}^2P_{1/2})$ threshold. The Lu-Fano plot in Fig. 1-2 displays the variation of the quantum defects in each of the measured levels with respect to binding energy measured below the second $5p^5({}^2P_{1/2})$ threshold. For this analysis, two different effective principal quantum numbers are defined for each level as,

$$T_m = T_{1\infty} - R/n_{1m}^{*2} \tag{1.1}$$

$$T_m = T_{2\infty} - R/n_{2m}^{*2}, \tag{1.2}$$

where T_m is the term value for the measured level, $R = 109736.31cm^{-1}$ is the Rydberg constant, n_1^*, n_2^* are the effective principal quantum numbers in the two ionization channels and $T_{1\infty}, T_{2\infty}$ are the ionization limits. From Eq. 1.1, the quantum defect modulo one can be defined as,

$$\mu_m = mod(-n_{1m}^*, 1), \tag{1.3}$$

The MQDT quantization condition [112, 79] implies that μ_m is an implicit function of n_{2m}^* and a plot of this function with respect to $mod(n_{2m}^*, 1)$ is the Lu-Fano plot.

The Lu-Fano plot constructed in this fashion, gives information about which of the Rydberg series are perturbed and allows for a visual estimation of the strengths of these perturbations. Some of the qualitative aspects of the Lu-Fano plot can be discussed in this chapter, postponing the in-depth theoretical study to **Chapter 2**. If the perturbations are weak, most of the quantum defects lie on flat portions of the curves (i.e. they are energy independent) with very sharp rises seen close to the below ionization Feshbach-type resonances (these resonances are the members of the

---

[2] For an introduction to atomic term symbols and coupling schemes, the reader can study reference [58] by Gerhard Herzberg.

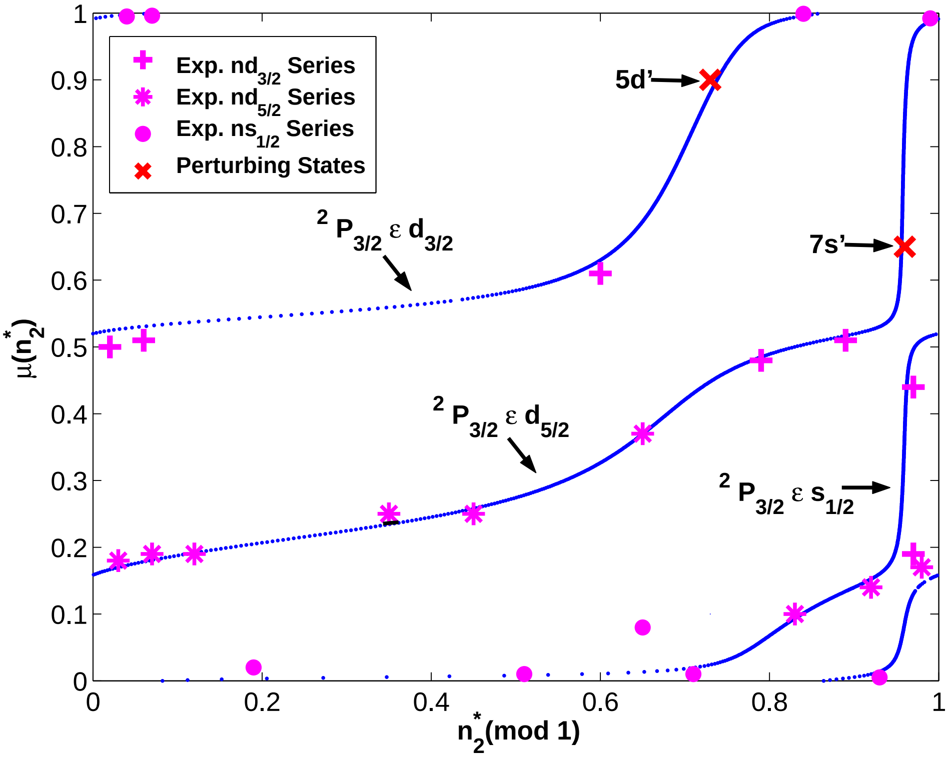

Figure 1-2: The Lu-Fano plot for the J=1 odd parity $5p^5(^2P_{3/2})ns_{1/2}$, $5p^5(^2P_{3/2})nd_{3/2}$ and $5p^5(^2P_{3/2})nd_{5/2}$ series of Xe, which converge to the $5p^5(^2P_{3/2})$ ionization threshold. Each of these series is characterized by a quantum defect $\mu(n_2^*)$ that is a smooth function of the principal quantum number n_2^*, as measured from the $5p^5(^2P_{1/2})$ ionization threshold. The notation ϵ is used to denote a continuous generalization of the discrete quantum number n^*. The circles, star and plus signs mark the positions of the experimentally measured and assigned Rydberg states from [77]. The smooth quantum defect curves are obtained from an MQDT fit to the experimental results. The states labeled 5d and 7s are Feshbach type below-ionization resonances that are members of the $5p^5(^2P_{1/2})ns_{1/2}$ and $5p^5(^2P_{1/2})nd_{3/2}$ series. The resonances cause rapid increases in the quantum defects as the resonance energy is approached from below. The energy width across which the quantum defect increases measures the strength of the interaction between the Rydberg series and the perturbing configurations (see **Chapter 2** section 2.5 for an explanation of how the energy width is a quantitative indicator of interaction strength). The 5d and 7s perturbing configurations interact primarily with the $ns_{1/2}$ and $nd_{3/2}$ series, respectively. However, the overall perturbation of the Rydberg series is much weaker for the 7s case than the 5d case. The gaps at the avoided crossings give a visual estimate of the strength of the Rydberg/Rydberg interactions between Rydberg series that converge to the same ionization threshold, $5p^5(^2P_{3/2})$. The principal quantum number, n_2^*, on the horizontal axis is plotted modulo 1. In **Chapter 2** an explanation is given that this range of the principal quantum number is sufficient to characterize the global spectrum, because the Lu-Fano plot is periodic on the unit square in the n_2^*, μ plane. The Lu-Fano plot was regenerated from energy data published in references [79, 88, 77].

$^2P_{1/2}$ns and nd series). As the interactions become stronger, the quantum defect increases are spread over a larger energy interval indicating a broader resonance. In Fig. 1-2, notice that the sum of the quantum defects [3] associated with the three Rydberg series converging to the $^2P_{3/2}$ threshold increases by one unit in the vicinity of a Feshbach resonance. This is a consequence of resonance scattering theory, which is presented in **Chapter 2**. It can be seen that the $^2P_{1/2}$5d resonance interacts most strongly with the $^2P_{3/2}$ns series, because the increase of the $^2P_{3/2}$ns quantum defect occurs over a broader energy interval. Similarly, the Lu-Fano plot shows that the $^2P_{1/2}$7s resonance interacts mostly with the $^2P_{3/2}$nd$_{3/2}$ series, although the overall perturbation of the Rydberg series by this state is weaker than that of the $^2P_{1/2}$5d state. The gaps between the avoided crossings of the non-intersecting quantum defect curves are proportional to the strength of the Rydberg/Rydberg interactions between Rydberg series that converge to the same ionization threshold [59, 41]. The sizes of these gaps are measured as the differences in abscissa of the lower inflection point and the point of closest approach between the two branches [41]. Extension of the Lu-Fano plot above the first ionization threshold can be used to determine the position and width of autoionizing resonances and shape resonances [45, 27].

The mixing of two channels that converge to spin-orbit split doublet states of the ion-core (J^+=3/2 and 1/2) is an example of a frame transformation [112]. In order to clarify this, let us imagine the Rydberg electron as an incoming scattering particle. At short electronic radial distance, the Rydberg electron is indistinguishable from the remaining electrons in the ion-core; in this range, the electron recombines with the ion to form a neutral atom with well defined total spin and orbital angular momentum (LS coupling). At larger electronic radial distance, the system approaches the fragmentation limit in which the ion-core and the departing electron may be treated as two distinguishable particles with their own well-defined orbital and spin angular momenta (jj coupling). The only way the fragmentation channels can mix is through the recoupling of the electron with the ion-core at short-range. Therefore, the

---

[3] The analytical continuation of this sum above the $^2P_{3/2}$ threshold multiplied by π is the well-known *eigenphase* sum in multichannel scattering theory.

interaction is a consequence of short-range physics and the transformation from the short-range channel wavefunctions to the long-range channel wavefunctions is called a frame transformation [112].

In order to see how the Lu-Fano plot transparently gives information about the frame transformation, it is best to study the simple case of two weakly interacting channels. Consider the ns type, J=1, odd parity Rydberg series of Ne. As shown by the corresponding Lu-Fano plot in Fig. 1-3, the jj coupled J = 1 fragmentation channels, $^2\mathrm{P}_{3/2}\mathrm{ns}_{1/2}$ and $^2\mathrm{P}_{1/2}\mathrm{ns}_{1/2}$, interact very weakly. The quantum defects of the states that lie along the horizontal and vertical branches of the curves show no variation with energy, indicating that these states are strictly jj coupled. The only departure from jj coupling occurs for those states that lie close to the curved sections along the main diagonal (shown as a dashed line). These states are not pure jj coupled states; they show a tendency toward LS recoupling. There are two states, 3s and 3s', that lie *exactly* on the main diagonal described by $\delta = -n^*_{3/2} = -n^*_{1/2}$. This implies that the quantum defects for these states are identical to the *eigenquantum* defects for the short-range channels [34], which are LS coupled. Therefore, these states are strictly LS coupled and they correspond to the singlet and triplet states of the atom.

The analogous frame transformation in molecular Rydberg spectra expresses the physical effect known as l-uncoupling [47]. In the case of a diatomic molecule, the frame transformation is from a state in which the orbital angular momentum of the Rydberg electron precesses about the internuclear axis (Hund's case b coupling) to a state in which the orbital angular momentum of the Rydberg electron precesses about the nuclear rotation axis (limiting Hund's case d coupling) [74] [4]. A good example of l-uncoupling is found in the Rydberg spectrum of the hydrogen molecule.

Photoabsorption by the H_2 $^1\Sigma_g^+$ (v=0, J=0) ground state leads to the J=1, $1s\sigma_g\mathrm{np}\sigma_u$ $^1\Sigma_u^+$ and $1s\sigma_g\mathrm{np}\pi_u$ $^1\Pi_u^+$ Rydberg series in Hund's case (b). Since the molecule is para-hydrogen, the rotational states of the ion are restricted to even

---

[4] There are a total of fifteen Hund's cases that describe rotational-electronic coupling in molecules. They result from combinations of the three coupling cases for the ion-core and five coupling cases for the Rydberg electron [63]. It is a straightforward exercise in angular momentum algebra to transform from one Hund's case to another. Further discussion is provided in reference [74] by Lefebvre-Brion and Field.

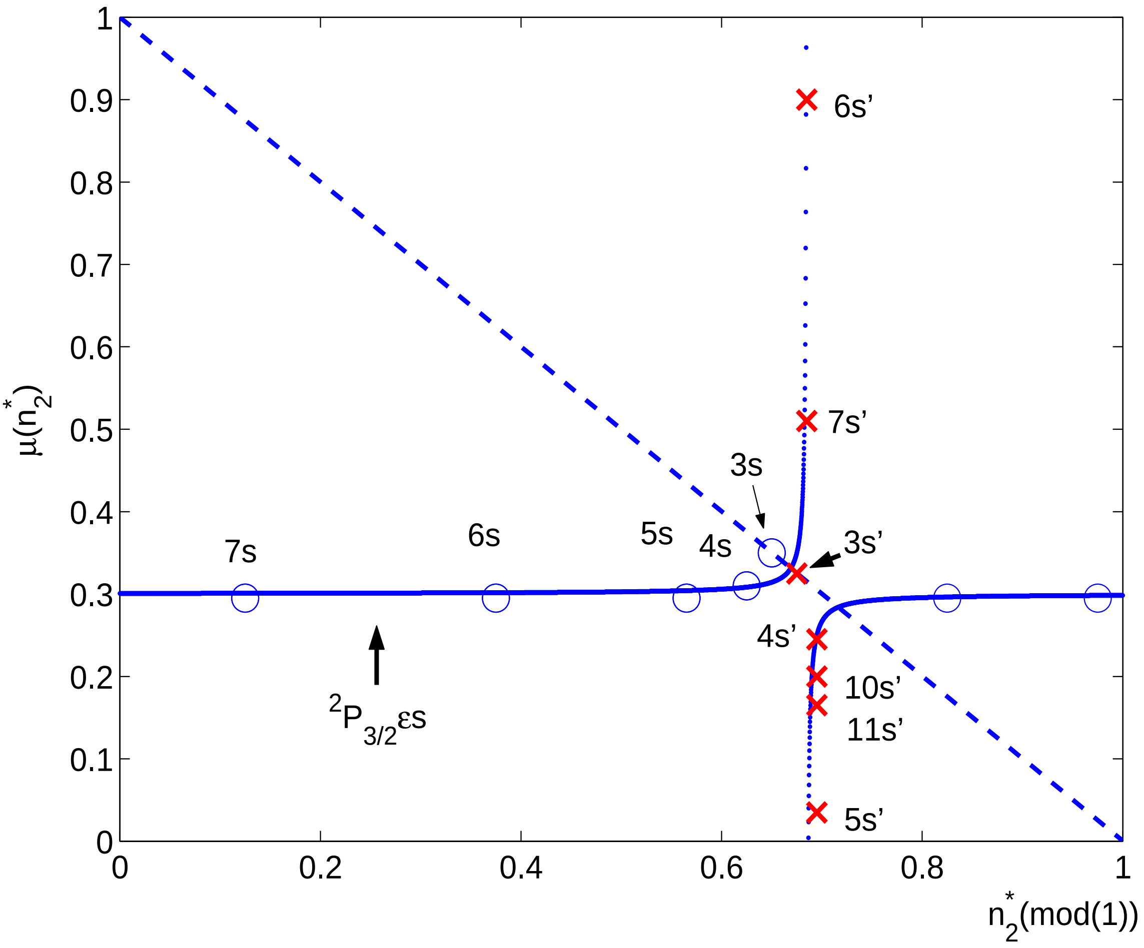

Figure 1-3: The Lu-Fano plot for the ${}^2P_{3/2}ns_{1/2}$ Rydberg series of Ne. The experimentally measured $ns_{1/2}$ levels are marked by circles. The s' notation describes the $ns_{1/2}$ type configurations, which converge to the ${}^2P_{1/2}$ threshold. The Rydberg spectrum of Ne is much less perturbed than that of Xe shown in Fig. 1-2. The quantum defects are found to be almost independent of energy. The two states, 3s and 3s', that lie along the diagonal are exactly in the LS coupling limit. Other states are strictly in the jj coupling limit because they either lie on a horizontal branch (constant quantum defect in the ${}^2P_{3/2}$ channel) or a vertical branch (constant quantum defect in the ${}^2P_{1/2}$ channel). The Lu-Fano plot was generated from a fit to data reported in reference [123].

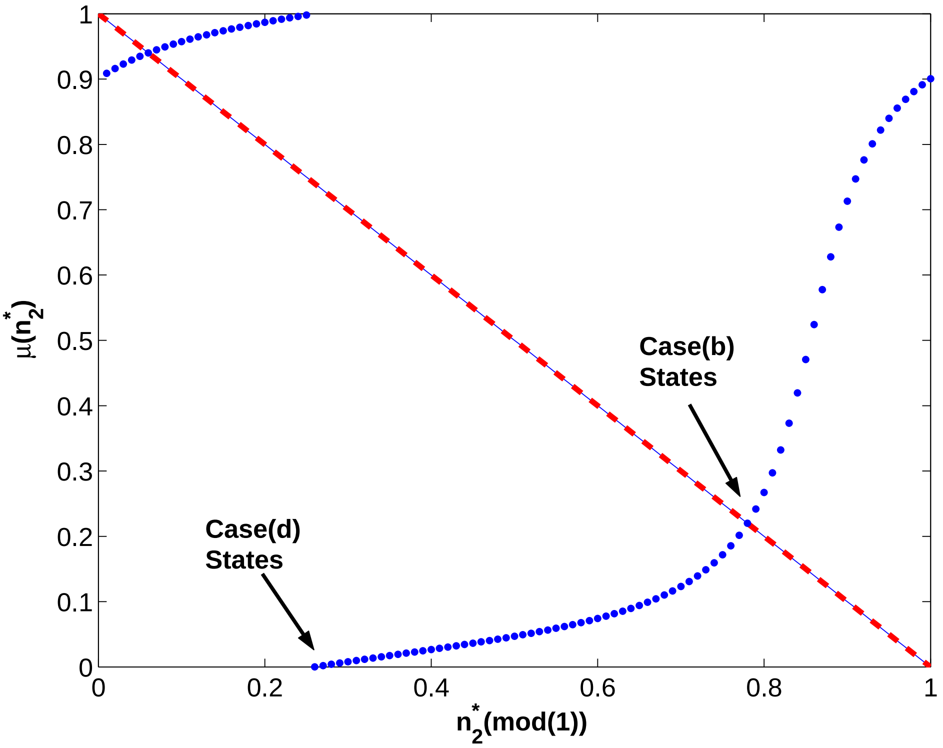

Figure 1-4: The Lu-Fano plot for the $N^+ = 0, ns$ Rydberg series of H_2. The Lu-Fano plot was generated from a fit to data provided in references [57, 112, 129]. The states that are well described by case (b) coupling lie along the curved portions of the plot, close to the main diagonal. The states that are well described by case (d) coupling lie on the horizontal or vertical branches, as indicated by the arrows.

values of the ion-core rotational quantum number, N^+, and the lowest two rotational levels have rotational quantum numbers $N^+ = 0$ and $N^+ = 2$. The two short-range channels in Hund's case (b) correlate to the two ionization channels in Hund's case (d) that converge to the $N^+ = 0$ and $N^+ = 2$ thresholds with increasing principal quantum number. This correlation is a consequence of the mixing of the two short-range channels due to l-uncoupling as the series limit is approached. In this sense, the rotationally split levels of the hydrogen ion-core are analogous to the doublet split levels of Ne$^+$, while the Hund's case (b) coupled short-range channels of the hydrogen molecule are analogous to the LS coupled short-range channels of the Ne atom.

Proceeding as in the Ne example, we can extract the information that the Lu-Fano plot shown in Fig. 1-4 provides about the l-uncoupling as the series limit is approached below the first ionization threshold. Based on our previous study of Ne, we know that the states that are dominantly in case (b) lie close to the main diagonal, the states that are intermediate between cases(b) and (d) lie along the curved portions, and the states that are strictly in case (d) are found on the flat (horizontal or vertical) branches of the curves. In contrast to the Ne example, more states are intermediate between Hund's cases (b) and (d) as indicated by the wider regions of curvature evident on the Lu-Fano plot.

The hydrogen molecule example shows that the main utility of MQDT for molecular structure and dynamics is the determination of the strength of rovibronic channel interactions that describe the flow of energy between the electronic degrees of freedom and the rotations and vibrations of the nuclei. When conditions for a resonance are met, these interactions lead to non-adiabatic processes, such as rotational autoionization, dissociative recombination, and associative ionization in molecular excited states. These processes, which are central to interstellar chemistry [70], are summarized in Table 1.1. Rotational autoionization occurs when a diatomic molecule, AB, resonantly absorbs radiation with energy $\hbar\omega$, where $\hbar$ is the Planck constant divided by 2π and ω is the angular frequency of radiation in radians/seconds. Photoabsorption produces an excited diatomic molecule in an electronic state with principal quantum number, n^*, and an ion-core rotational quantum number, $N^+ = Y$. Subsequently, this intermediate state of the molecule decays into the electronic continuum above the $N^+ = X < Y$ state of the ion, yielding the products shown in Table I. Dissociative recombination results when an electron resonantly impacts a molecular ion to form a neutral species [5]. As a result, an intermediate state forms in which the diatomic molecule is in an excited electronic state that converges to some vibrational level of the ion-core $v^+ = Y$. In the final step, the Rydberg state couples to a repulsive valence electronic state (usually through a charge transfer process) causing the molecule to dissociate into two neutral atoms in electronic states with principal quantum numbers n_1^* and n_2^*. The diabatic electronic character of the repulsive valence state determines the final electronic states of the neutral atoms in the disso-

---

[5] This process is commonly known as resonant electron capture.

Table 1.1: Processes that Result from Non-Adiabatic Chemical Dynamics

Process	Reactants	Intermediate	Products
Rotational Autoionization	$AB + \hbar\omega$	$AB(n^*, N^+ = Y)$	$AB^+(N^+ = X < Y)$ $+ e^- (\hbar k)$
Dissociative Recombination	$AB^+ + e^- (\hbar k)$	$AB(n^*, v^+ = Y)$	$A(n_1^*) + B(n_2^*)$
Associative Ionization	$A + B$	$AB(n^*, v^+ = Y > 0)$	$AB^+(v^+ = 0) + e^-$

ciation channel. Associative ionization occurs when an electronically excited neutral atom collides with another neutral atom to form a diatomic molecule in an excited electronic state that belongs to a series converging to a vibrational state of the ion core, $v^+ = Y > 0$. In analogy to rotational autoionization, this state decays into the electronic continuum above the $v^+ = 0$ level of the ion, yielding the products shown in Table I.

Empirical analyses have been the more common application of MQDT in electronic spectroscopy. The Lu-Fano plots can be constructed from experimental data alone, and then fit to a functional form provided by the MQDT quantization condition [47]. In the fit, a set of parameters is determined that describe the short-range eigenchannel wavefunctions. This set of parameters yields the main construct of quantum defect theory, which is the quantum defect matrix μ or the equivalent reaction matrix $\mathbf{K}$ [6][112]. **Chapter 2** presents the theory of the quantum defect matrix. The key point is that knowledge of the short-range quantum defect matrix amounts to a complete description of the global electronic spectrum of an atom or a molecule. In the analysis of molecular Rydberg spectra, the apparatus of the Lu-Fano plot is seldom used because of the typically much larger number (than 2) of interacting channels. Instead, the global spectrum is fit directly to the short range quantum defect matrix to uncover the most important interactions between the observed Rydberg series [65]. The increased number of interacting channels in molecular systems requires a higher dimension quantum defect matrix and a larger number of fit parameters. In order for

---

[6] In **Chapter 2**, it is shown that $\mu = \frac{1}{\pi} arctan(\mathbf{K})$ in the (0, π) branch of the inverse tangent function.

such a fit to converge, good initial guesses for the reaction matrix elements are needed to be input to the non-linear fit program. A good initial guess would be provided by a short-range reaction matrix determined from a first principles electronic structure calculation. Thus, there is a need for theory to complement experimental analyses in both the implementation and interpretation phases. This need underscores the importance of developing methods for the *ab initio* determination of reaction matrices.

1.2 Current Progress

Ab initio calculation of reaction matrices is a challenging task. Since the short-range reaction matrix describes a physical situation in which the electron is strongly coupled to the molecular body-frame, the Born-Oppenheimer approximation can be used. However, the calculation requires theoretical methods from scattering theory that are not part of traditional quantum chemistry. The scattering approach uses the analytical properties of the scattering matrix on an energy mesh to locate a quasi-continuum of states close to ionization thresholds [16]. On the other hand, the configuration interaction approach of quantum chemistry relies on expansions over discrete basis set functions to determine the electronic eigenstates [128]. Such expansions over a discrete set of functions often suffers from extremely slow convergence to the quasi-continuum of levels observed in the experiment [33].

The theorist is then faced with a practical choice. The first choice is to build a complete quantum scattering calculation for the system under study. The cost of ”re-inventing” the wheel is that the calculation would not be able to take advantage of the known quantum chemistry methods that have been tested many times for accuracy and efficiency. The second choice is to build the reaction matrix calculation on the same principles that are used in quantum chemistry so that the two methods can merge seamlessly. The latter choice is adopted in this thesis and novel quantum defect methods are developed that can be embedded directly into standard quantum chemistry. This choice has a clear advantage over the first approach. If the quantum defect method can be embedded in quantum chemistry, then the reaction matrix calculation would have transferability to the extent that the methods of quantum chemistry are universally applicable to all molecular systems.

A complete quantum scattering calculation begins from the close-coupling equations of scattering theory, which are derived in references [13, 28]. In the close-coupling approximation, the infinite number of coupled integro-differential equations satisfied by the electron radial functions are truncated to a finite set, so that they can be solved using numerical techniques. However, these numerical techniques typically employ computationally expensive iteration methods and the overall calculation becomes time-consuming when a large number of coupled integro-differential equations are retained in the truncated set [14]. For this reason, the close-coupling approximation is suited for the few-channel problem, which is adequate for calculations of collision cross sections at low electron energy [115, 121].

At higher collision energies, where a large number collision channels interact, the close-coupling approximation is computationally infeasible. The majority of work that is now published on the first principles calculation of reaction matrices relies on the use of **R**-matrix theory, which was invented by Eugene Wigner in the 1940's [135]. Unlike the close-coupling approximation, **R**-matrix theory is capable of handling the interacting many-channel problem. In the spirit of MQDT, **R**-matrix theory introduces a separation of coordinate space into short- and long-range regions. The complicated short-range forms of the electronic radial wavefunctions are not computed explicitly but they are instead represented by a matrix of radial logarithmic derivatives (the **R** matrix) [7] calculated at an imaginary boundary that separates the short- and long-range regions (the **R** matrix box). The theory was originally utilized to calculate nuclear reaction rates [72], but was adapted later to atomic physics by Burke and co-workers [14, 12, 10]. Later, **R**-matrix calculations for diatomic molecules were carried out by Schneider [105, 106], Burke [11], Shimamura [113], Noble [133], and Tennyson [131]. Only very recently, **R**-matrix calculations on polyatomic molecules were reported by Morgan et al. [89].

The accuracy of the results obtained from the standard **R**-matrix calculations

---

[7] The **R** matrix differs from the **K** matrix, which refers the reaction matrix here.

are far from satisfactory, especially for the polyatomic molecule case. The problem can be traced back to the use of an expansion of the collision wavefunction in terms of a basis, which is complete inside the **R**-matrix box. This expansion yields the **R** matrix in terms of a Lorentz series, with poles located at the molecular Hamiltonian's eigenvalues, that depend on the boundary conditions imposed at the imaginary surface surrounding the **R**-matrix box [12]. However, the Lorentz series suffers from very slow convergence because of the effects of remote levels that make a non-zero contribution to the electron wavefunction's phase shift. The effects of the remote levels can be partially accounted for by the Buttle correction [15]. However, a different approach is needed to achieve the near-spectroscopic accuracy customary in quantum chemical calculations.

Walter Kohn's variational version of **R**-matrix theory [69] yields directly the eigenvalues and eigenvectors of the **R** matrix. Since it bypasses the expansion of the **R** matrix in terms of a Lorentz series, this approach does not present a convergence problem. Calculations by Fano [33], Greene [44], Aymar [6], and Jungen [130] have shown that the variational **R**-matrix method is accurate and reliable. On the other hand, the applications of the variational **R**-matrix method have been limited to only few-electron atoms and molecules. This is because the method requires the use of non-conventional basis functions whose logarithmic derivatives are not fixed but span a range of values on the **R**-matrix boundary. Therefore, all matrix elements must be calculated numerically, since no analytical expressions exist as in the Gaussian-based quantum chemistry program.

Chapter 3 presents a new variational **R**-matrix method optimized for molecular problems. This method combines features from the close-coupling approximation with a basis set calculation, while imposing a stationary constraint as per the variational approach. The new method is capable of being embedded in a standard quantum chemistry calculation.

Chapter 4 applies the new method to calculate the Rydberg spectrum of the molecule CaF. The eigenquantum defects as a function of energy, the scattering, differential, and integral photoionization cross sections are presented. The computed results are shown to be in excellent agreement with the experiment.

Chapter 5 discusses an MQDT analysis that finds a broad shape resonance spread over the entire Rydberg spectrum of CaF. The effects of this broad shape resonance are manifest as subtle yet significant violations of Mulliken's rule for Rydberg states [90](see footnote 1 on page 36 for a statement of Mulliken's rule). This implies that CaF has a fundamentally different spectrum that cannot be analyzed using the familiar Rydberg scaling laws, although no dramatic level interactions and perturbations are evident.

Chapter 6 develops the many-electron generalization of the **R**-matrix theory introduced in **Chapter 3** and presents preliminary results of a two electron calculation on H_2.

Chapter 7 summarizes the current achievements and concludes with future directions.

1.2.1 Connection between the Effective Hamiltonian and MQDT

At the end of this introduction, it is important to address the question of whether a simpler effective Hamiltonian method can be used to treat Rydberg spectra instead of the complicated machinery of MQDT. An effective Hamiltonian approach is faced with the same kind of problems as encountered by configuration interaction treatments. These are the effects of remote levels that perturb a given n^* complex from neighboring principal quantum numbers. Although these perturbations may be weak, they may result in observable shifts in the energy levels, since there is an infinite number of perturbers. However, if the effects of these remote perturbers are taken into account *a-priori* in terms of an eigenquantum defect, then an effective Hamiltonian calculation indeed becomes feasible. In a first step, an MQDT calculation can determine the eigenquantum defects to be input to the effective Hamiltonian model. Then the effective Hamiltonian can be used to calculate total term values of the ro-vibrational states accessible in the experiment. Here, an effective Hamiltonian is built upon the results of the *ab initio* MQDT calculation from **Chapter 4** and it is used to calculate the $n^* = 13$ f complex of CaF to spectroscopic accuracy.

Let H denote the electronic Hamiltonian operator of an isolated system that can be partitioned as,

$$H = H_o + \lambda H_1, \tag{1.4}$$

where H_o is a zero order Hamiltonian with the known spectrum,

$$H_o|n\alpha) = T_{n\alpha}|n\alpha) \qquad T_{n\alpha} = -\frac{R}{(n-\mu_\alpha)^2},\ n = 1, \ldots, \infty, \tag{1.5}$$

where $T_{n\alpha}$ is the energy eigenvalue in Rydbergs, μ_α is the eigenquantum defect, and n is the principal quantum number. Thus, we can construct an effective Hamiltonian, H_n^{eff} in the k-fold quasi-degenerate subspace of the Hilbert space spanned by the eigenstates of H_o as,

$$H_n^{eff} = \sum_{\alpha} |n\alpha)T_{n\alpha}(\alpha n| + \sum_{\alpha,\alpha'} |n\alpha)T_{n\alpha,\alpha'}(\alpha' n|. \tag{1.6}$$

Here, $T_{n\alpha,\alpha'}$ are the off-diagonal matrix elements due to λH_1,

$$T_{n\alpha,\alpha'} = \lambda(n\alpha|H_1|n\alpha'). \tag{1.7}$$

For concreteness, we can specialize to a diatomic molecule in Hund's case (b) electronic rotational coupling and associate with the quantum number α the combinations of electronic orbital angular momentum, l, and its projection along the internuclear axis, λ,

$$|\alpha) \equiv |l\lambda) = \sum_{m_l} |lm_l)D^l_{m_l\lambda}(0, \beta, \gamma). \tag{1.8}$$

In Eq. 1.8, $D^l_{m_l\lambda}(0, \beta, \gamma)$ are the Euler rotation matrix elements [139] that depend on the two Euler angles β and γ and m_l is the projection of l on a space-fixed axis. The first Euler angle α is set to zero, since only two Euler rotations are required to specify the body frame for a diatomic molecule (see Fig. 1-5). The perturbation matrix elements originate from (i) l-mixing due to anisotropy in the core potential function and (ii) l-uncoupling due to the rotating molecular body-frame,

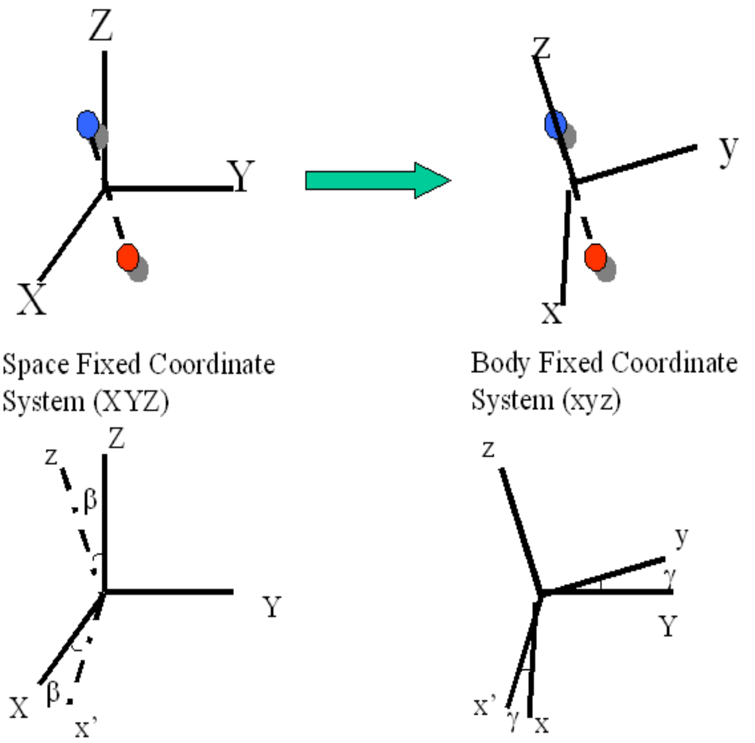

Figure 1-5: Euler rotations from the space-fixed coordinate system to the body-fixed coordinate system. The body-frame is obtained from the space-fixed coordinate system by (i) an Euler rotation through an angle β about the space-fixed Y-axis and (ii) an Euler rotation through an angle γ about the body-fixed z axis, as shown in the lower two panels. Capital letters (XYZ) are used to denote the space-fixed coordinate system whereas small letters (xyz) are used to denote the body-fixed coordinate system.

$$H_1 = X_{core} + \sum_{N^+\Lambda^+lN} |N^+\Lambda^+lNM_N) \left(B^+N^+(N^++1) - \Lambda^{+2}\right) (N^+\Lambda^+lNM_N|, \quad (1.9)$$

where λ^+ is the projection of the total core angular momentum N^+ on the internuclear axis, M_N is the projection of the total angular momentum N on the space fixed axis and B^+ is the rotational constant for the ion. In the absence of electric and magnetic fields, different values of M_N are energetically degenerate and this quantum number can be taken to be zero. The matrix elements of the l-mixing operator, X_{core}, can be determined from the potential function that is used to model the electrostatic interactions between the electron and the ion-core. These interactions are often described in terms of a multipole expansion [134] [8]. The matrix elements of the remaining rotational part, H_{rot}, can be derived by expanding [9],

$$|N^+\Lambda^+lNM_N) = \textstyle\sum_{M_{N^+}m_l} |N^+; M_{N^+}\Lambda^+)|lm_l)(N^+M_{N^+}lm_l|N, M_N) \quad (1.10)$$

$$= \textstyle\sum_{M_{N^+}m_l\lambda} |N^+; M_{N^+}\Lambda^+)D^{l*}_{m_l\lambda}(0,\beta,\gamma)|l\lambda)(N^+M_{N^+}l, m_l|N, M_N) \quad (1.11)$$

where Eq.1.11 used the inverse of Eq. 1.8. Next we have,

$$\textstyle\int d\Omega \sum_{M_{N^+}m_l} |\beta,\gamma)(\beta,\gamma|N^+; M_{N^+}\Lambda^+)D^{l*}_{m_l\lambda}(N^+M_{N^+}lm_l|NM_N) \quad (1.12)$$

$$= \tfrac{\sqrt{2N^++1}}{(\int d\Omega)^{1/2}} \textstyle\int d\Omega \sum_{M_{N^+}m_l} |\beta,\gamma)D^{N^+*}_{M_N^+\Lambda^+}D^{l*}_{m_l\lambda}(N^+M_{N^+}lm_l|N, M_N) \quad (1.13)$$

$$= \tfrac{\sqrt{2N^++1}}{(\int d\Omega)^{1/2}} \textstyle\int d\Omega \sum_{\Lambda} |\beta,\gamma)D^{N*}_{M_N\Lambda}(N^+\Lambda^+l\lambda|N, \Lambda) \quad (1.14)$$

$$= \tfrac{\sqrt{2N^++1}}{\sqrt{2N+1}} \textstyle\sum_{\Lambda} |N; M_N\Lambda)(N^+\Lambda^+l\lambda|N, \Lambda) \quad (1.15)$$

Using Eq. 1.15 in Eq 1.11, we obtain

$$|N^+\Lambda^+lNM_N) = \frac{\sqrt{2N^++1}}{\sqrt{2N+1}} \sum_{\Lambda\lambda} |N; M_N\Lambda)|l\lambda)(N^+\Lambda^+l\lambda|N, \Lambda). \quad (1.16)$$

---

[8] A multipole expansion is useful for the analysis of non-penetrating states, which are characterized by large values of orbital angular momentum ($l \geq 3$). Other parameterizations of X_{core} should be used for penetrating states to account for the short-range distortions of the charge on the ion as well as electron exchange effects. These parameterizations are possible in terms of pseudopotentials that are optimized on the results of multiconfiguration Hartree-Fock calculations [95].

Equations 1.16 and 1.9 allow for the computation of the matrix elements of H_{rot} in the unsymmetrized case (b) basis as,

$$(N\Lambda M_N l\lambda|H_{rot}|N\Lambda' M_N l\lambda') = \tag{1.17}$$
$$\tfrac{1}{2N+1}\textstyle\sum_{N^+\Lambda^+}(2N^+ + 1)(N^+\Lambda^+ l\lambda|N\Lambda)(B^+ N^+(N^+ + 1) - \Lambda^{+2})(N^+\Lambda^+ l\lambda'|N\Lambda').$$

The derivation has so far neglected to account for the symmetries of the exact Hamiltonian. The exact Hamiltonian is invariant under inversion of all electronic and nuclear coordinates about the origin of the space fixed axial system and its eigenstates are simultaneous eigenstates of the corresponding parity operator, I. The effective Hamiltonian must reflect this symmetry in order to account for the unbroken parity with increased rotational quantum number, N. This can be accomplished by restricting the representation of the effective Hamiltonian to subspaces spanned by symmetrized Hund's case (b) bases that are eigenstates of the parity operation. The parity operation in the space-fixed coordinate system is equivalent to a reflection of the electronic coordinates through a plane containing the nuclei in the body frame (the σ_v operation) and a replacement in the Euler angles $\beta, \gamma \rightarrow \pi - \beta, \gamma + \pi$. Choosing the xz plane shown in Fig. 1-5 as the plane of reflection for the σ_v operation and the body-fixed z-axis as the quantization axis, we can determine that

$$\sigma_v|l\lambda) = (-1)^{\lambda}|l - \lambda) \tag{1.18}$$
$$\sigma_v|\Lambda^+) = (-1)^{\Lambda^+}| - \Lambda^+) \tag{1.19}$$
$$D^N_{\Lambda M_N}(0, \pi - \beta, \gamma + \pi) = (-1)^{N+\Lambda} D^N_{-\Lambda M_N}(0, \beta, \gamma). \tag{1.20}$$

Therefore, the properly symmetrized case (b) functions for the parity operation are,

$$|l\lambda N\Lambda M_N\eta) = \tfrac{\sqrt{2N+1}}{\sqrt{8\pi^2(1+\delta_{\Lambda,0}\delta_{\lambda,0})}}\{|N\Lambda M_N)|l\lambda) + \eta|N - \Lambda M_N)|l - \lambda)\} \tag{1.21}$$
$$= \tfrac{\sqrt{2N+1}}{\sqrt{8\pi^2(1+\delta_{\Lambda,0}\delta_{\lambda,0})}}\left\{|\lambda^+)|l\lambda)D^N_{\Lambda,M} + \eta| - \lambda^+)|l - \lambda)D^N_{-\Lambda,M}\right\}, \tag{1.22}$$

where $\eta^2 = 1$ and the normalization constant $8\pi^2 = \int d\Omega$. In the symmetrized version, it is understood that $\lambda, \Lambda \geq 0$ whereas in the unsymmetrized version signed values are used for both λ and Λ. The application of the parity operator on the symmetrized case (b) basis ket in Eq. 1.22 produces,

$$I|l\lambda N\Lambda M_N\eta) = (-1)^N\eta|l\lambda N\Lambda M_N\eta) \tag{1.23}$$

The matrix elements of the rotational Hamiltonian can be recalculated in the symmetrized Hund's case (b) basis. Alternatively, we can use the result in the unsymmetrized basis with signed quantum numbers and account for symmetry based on group theoretical arguments. The Hamiltonian in the unsymmetrized representation is reducible and can be decomposed into two irreducible representations for $\eta = 1$ and $\eta = -1$ by a similarity transform. The eigenvectors of each irreducible sub-block of the Hamiltonian form a basis which transforms to case (d) according to the $\eta = 1$ and $\eta = -1$ representations, respectively.

The CaF molecule has a $^1\Sigma^+$ ion-core, which implies $\Lambda^+ = 0$ and forces $\lambda = \Lambda$. In addition, Eq. 1.21 gives the restriction $\lambda \leq N$. For the $n^* = 13, l = 3$ complex of CaF, there will be seven sets of levels corresponding to the seven dimensional state space, also spanned by signed $\lambda = -3\ldots 3$. Four of these levels will transform according to the $\eta = 1$ representation, whereas the remaining three will transform according to $\eta = -1$. This follows from the observation that the number of $\eta = 1$ levels should exceed by one the number $\eta = -1$ levels at a given value of rotational quantum number, because the symmetrized hund's case (b) basis vanishes for $\lambda = 0$ and $\eta = -1$. The η-representation to which each state belongs can be determined from an eigenvector analysis at each N.

The term values for the CaF $n^* = 13$ f complex were calculated from the effective Hamiltonian in Eq. 1.6 that used the eigenquantum defects determined *ab initio* in **Chapter 4**. In these calculations, the operator X_{core} was set to zero as appropriate for a non-penetrating type state. It should be noted that this assumption implies that l is a good quantum number for the 13f complex. This would be a poor zero-order picture for penetrating states of CaF, which has a highly dipolar ion-core.

The resultant reduced term value plots for the $\eta = 1$ and $\eta = -1$ symmetries are

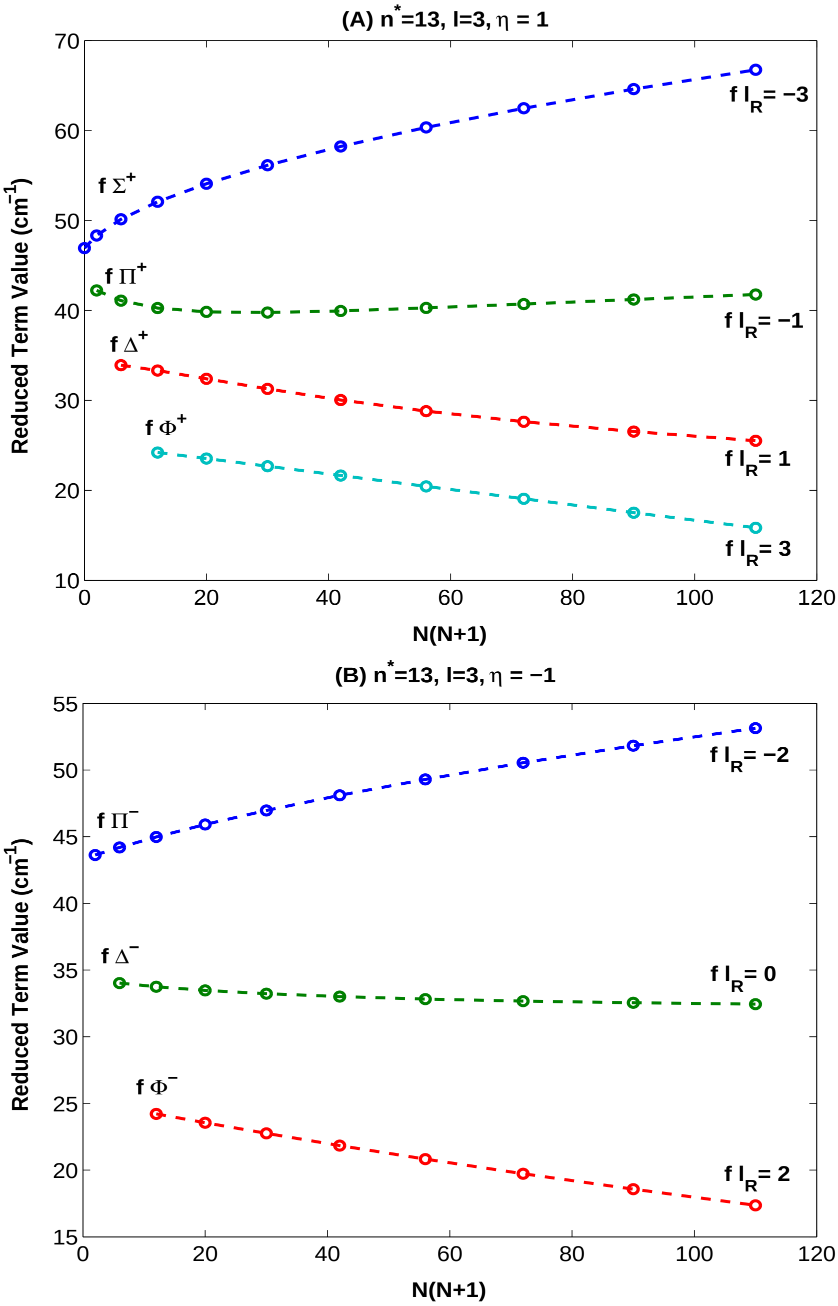

Figure 1-6: Reduced term value plots obtained from the effective Hamiltonian calculation of CaF for $l = 3$ non-penetrating states. The term values are calculated using the formula $T_{Ni} = IP + T_i - BN(N+1) - 47000$, where the index i refers the i'th eigenvalue of the effective Hamiltonian. (A) Reduced term values for $\eta = 1$ symmetry. At low N, the eigenstates are assigned as $f\Sigma^+$,$f\Pi^+$, $f\Delta^+$ and $f\Phi^+$ based on their dominant λ character. At high N, the eigenstates recouple to case(d) and they are assigned as $fl_R = -3, -1, 0, 1, 3$ based on their dominant N^+ character. $l_R = N - N^+$ is the projection of l on the molecular rotation axis; see text for more details about l_R. (B) Reduced term values for $\eta = -1$ symmetry. In this case the case (b) states $f\Pi^-$, $f\Delta^-$ and $f\Phi^-$ correlate with the remaining projections $l_R = -2, 0, 2$ at high N.

shown in Fig. 1-6. These plots display the variation of the quantity

$$T_{Ni} = IP + T_i - B^+ N(N+1) - 47000 cm^{-1} \tag{1.24}$$

with N. In this equation, T_i refers to the i'th eigenvalue of the effective Hamiltonian, $IP = 47685.87 cm^{-1}$ is the energy needed to ionize CaF from its $X^2\Sigma^+$, $N = 0, v = 0$ ground state, producing an ion in its $X^1\Sigma^+$, $N^+ = 0, v^+ = 1$ state and $B^+ = 0.35 cm^{-1}$ is the rotational constant. Based on the well known Hund's case (b) level structure formula [65], the reduced term values computed in this fashion must remain constant as a function of N, if the molecule is in Hund's case (b) for all values of the rotational quantum number. The curved nature of the reduced term value plots in Fig. 1-6 is a consequence of the change in the pattern-forming quantum number from N at low values of N to N^+ at higher values of N.

The basis for this change in the pattern-forming quantum number can be understood by the following device. The off-diagonal elements of the effective Hamiltonian expressed in the case (b) basis increase in magnitude with increasing N. This follows from the restricted summation over N^+ that starts from a large minimum value of $|N - l|$ at high values of N. These off-diagonal elements cause the eigenstates of the effective Hamiltonian to become mixtures of the case (b) states in the form,

$$|iNl\eta) = \sum_{\lambda} |l\lambda N M_N \eta) c_{\lambda i}, \tag{1.25}$$

where $c_{\lambda i}$ are called the mixing coefficients. The squared values of the computed mixing coefficients, $c^2_{\lambda i}$, are plotted in Fig. 1-7 as a function of N. The case (b) basis set is shown for $\lambda = 0, 1, 2, 3$, which correspond respectively to the irreducible representations $\Sigma, \Pi, \Delta, \Phi$ of the molecular point group $C_{\infty v}$. The figures suggest that the fractionation of the eigenstates into the case (b) basis increases with increasing N due to the increasing magnitude of the off-diagonal matrix elements.

At sufficiently high values of N, the magnitude of the off-diagonal matrix elements become larger than the differences between the eigenvalues of H_o. In such a limit, the perturbing term H_1 becomes the zero-order Hamiltonian, switching places with

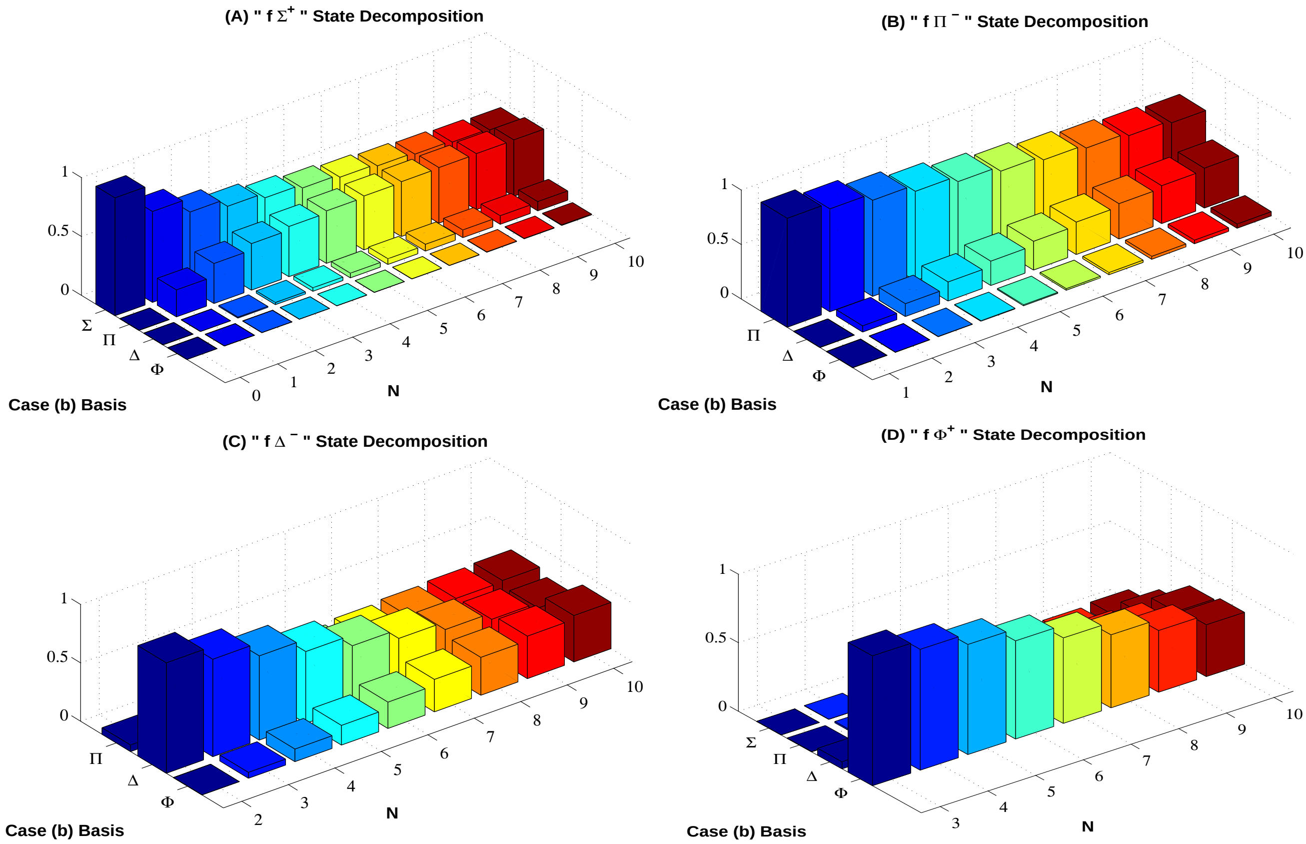

Figure 1-7: The evolution of case(b) character as a function of rotational quantum number. The heights of the bar graphs are the squares of the mixing coefficients, $c_{\lambda i}$, of Eq. 1.25. The partial characters are shown for $\lambda = 0, 1, 2, 3$, which correspond respectively to the irreducible representations $\Sigma, \Pi, \Delta, \Phi$ of $C_{\infty v}$. Σ and Φ states are displayed for $\eta = 1$ and Π and Δ states are displayed for $\eta = -1$. At low N, the molecular eigenstates are nearly pure Hund's case (b) states and assignments in terms of the case (b) labeling are valid. As N increases, the Hund's case(b) states begin to mix. The mixing occurs in steps of one in λ with the selection rule $\Delta\lambda = \pm 1$. At N $\geq$ 10, the states are strongly mixed and the case (b) labeling is no longer appropriate. The strong case (b) mixing is a consequence of eigenstate recoupling to case (d).

H_o. Therefore, a recoupling of the eigenstates to case (d) occurs in which the portion H_1 of the effective Hamiltonian is diagonal by construction. This is demonstrated by Fig. 1-9, which shows the amplitude squared mixing coefficients $|c_{N^+i}|^2$ of the various eigenstates in the 13f complex at N =10. These mixing coefficients are obtained from a case (d) expansion of the eigenstates as,

$$|iNl\eta) = \sum_{N^+} |lN^+NM_N\eta)c_{N^+i}. \tag{1.26}$$

The eigenstates shown in Fig. 1-9 are dominantly single-N^+ states with perturbative mixtures of other N^+ states.

A useful bookkeeping device can be introduced for describing the conserved parity of eigenstates that recouple to case (d). This bookkeeping device is the l_R quantum number, which is defined as

$$l_R = N - N^+. \tag{1.27}$$

Since $\mathbf{l} = \mathbf{N} - \mathbf{N}^+$, the values of l_R range from $-l \cdots l$ for large values of N and N^+. Thus, l_R has the properties of a projection; in the large N and N^+ limit, it is the projection of l on the vector that points in the direction of $\mathbf{N}^+$ i.e the rotation axis for a ${}^1\Sigma^+$ core. This is easily demonstrated by figure 1-8.

Complete recoupling to case(d) is achieved only in the limit $N \rightarrow \infty$. l_R is conserved in this asymptotic limit and as a good quantum number, it characterizes the *limiting* Hund's case (d) rotation-electronic coupling. For finite but large N, l_R is approximately conserved and can nevertheless be used to label an eigenstate, as in Figs 1-7 and 1-9. In this labeling, the use of l_R is rigorous only pertaining to parity of a pure case (d) eigenstate.

The space-fixed projection of a case (d) state for a ${}^1\Sigma^+$ core is,

$$(\theta, \phi, \Theta, \Phi|lN^+NM_N) = \sum_{m_l, M_{N^+}} Y_{lm_l}(\theta, \phi)Y_{N^+M_{N^+}}(\Theta, \Phi)(lm_lN^+M_{N^+}|NM_N), \tag{1.28}$$

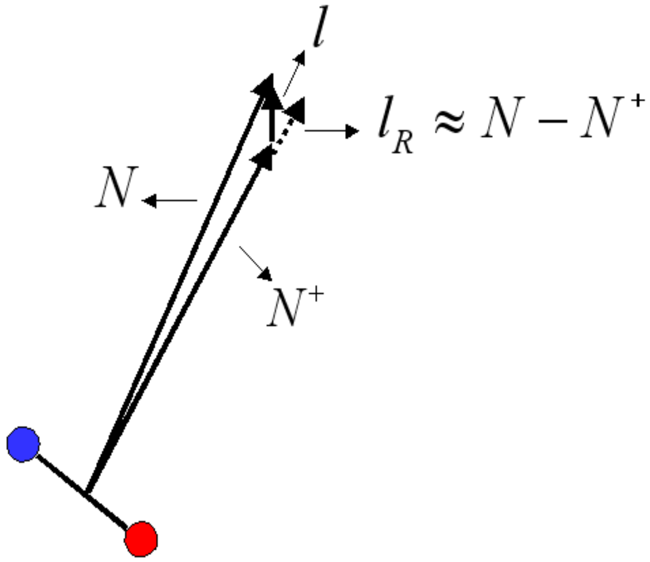

Figure 1-8: The definition of l_R as a projection on the rotation axis. The total angular momentum N is obtained from the angular momentum addition $\mathbf{N} = \mathbf{l} + \mathbf{N}^+$. Therefore, when the quantum numbers N and N^+ are much larger than l, the vectors $\mathbf{N}$ and $\mathbf{N}^+$ are approximately parallel. The projection of $\mathbf{l}$ on $\mathbf{N}^+$ is shown as the dashed vector. In the asymptotic N and N^+ limit, the magnitude of this projection is equal to N- N^+. The quantum number N^+ is obtained from the angular momentum addition $\mathbf{N}^+ = \mathbf{R} + \mathbf{L}^+$, where $\mathbf{R}$ is the angular momentum of the rotation of the nuclei and $\mathbf{L}^+$ is the orbital angular momentum of the core. In the typical case of a ${}^1\Sigma^+$ core, the vectors $\mathbf{L}^+$ and $\mathbf{R}$ are parallel and thus the rotational axis of the ion-core lies along the $\mathbf{N}^+$ vector. This justifies the meaning of l_R as a projection on the molecular rotation axis.

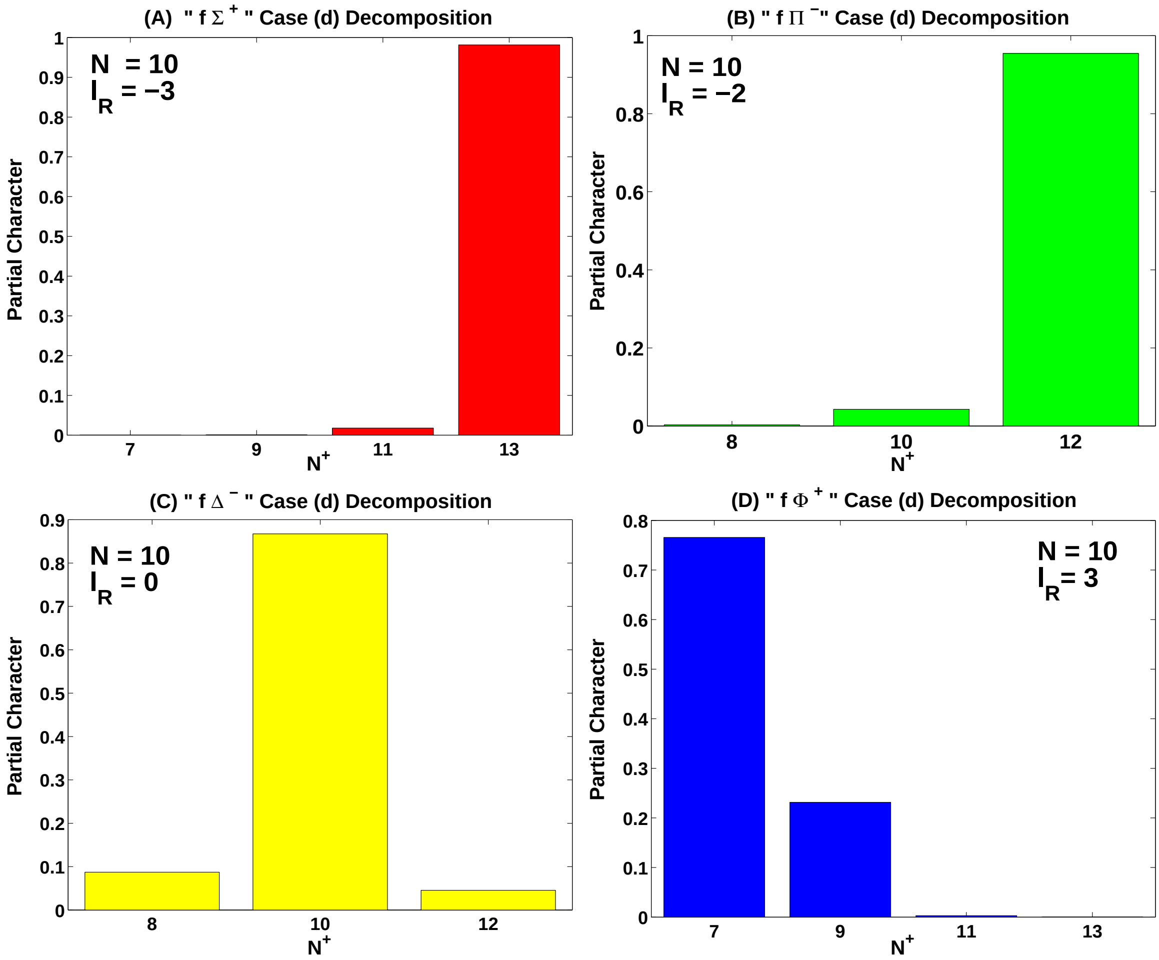

Figure 1-9: The partial case (d) characters of molecular eigenstates at N=10. The heights of the bar graphs are equal to the $c^2_{N^+i}$ of Eq. 1.26. (A) The partial character of the N=10, f Σ^+ state. This state has dominant $N^+ = 13$, $l_R = -3$ character. (B) The partial character of the N=10, f Π^- state. This state has dominant $N^+ = 12$, $l_R = -2$ character. (C) The partial character of the N=10, f Δ^- state. This state has dominant $N^+ = 10$, $l_R = 0$ character. (D) The partial character of the N=10, f Φ^+ state. This state has dominant $N^+ = 7$, $l_R = 3$ character.

where θ and ϕ are the angular coordinates that describe the orientation of the electron's position vector $\mathbf{r}$ in the space fixed axis and Θ and Φ are the angular coordinates that describe the orientation of the vector $\mathbf{R}$ that connects the nuclei of Ca and F. The functions $Y_{lm_l}(\theta,\phi)$ and $Y_{N^+M_{N^+}}(\Theta,\Phi)$ are spherical harmonics. The quantum numbers m_l and M_{N^+} refer to projections of $\mathbf{l}$ and $\mathbf{N}^+$ on the space fixed coordinate axis, Z. The application of the inversion operator on this state is,

$$I(\theta,\phi,\Theta,\Phi)(\theta,\phi,\Theta,\Phi|lN^+NM_N) \tag{1.29}$$

$$= \textstyle\sum_{m_l,M_{N^+}} Y_{lm_l}(\pi-\theta,\phi+\pi)Y_{N^+M_{N^+}}(\pi-\Theta,\Phi+\pi)(lm_lN^+M_{N^+}|NM_N) \tag{1.30}$$

$$= \textstyle\sum_{m_l,M_{N^+}} (-1)^l Y_{lm_l}(\theta,\phi)(-1)^{N^+}Y_{N^+M_{N^+}}(\Theta,\Phi)(lm_lN^+M_{N^+}|NM_N) \tag{1.31}$$

$$= (-1)^{l+N^+}\textstyle\sum_{m_l,M_{N^+}} Y_{lm_l}(\theta,\phi)Y_{N^+M_{N^+}}(\Theta,\Phi)(lm_lN^+M_{N^+}|NM_N). \tag{1.32}$$

Thus, $|lN^+NM_N)$ is automatically an eigenstate of I with an eigenvalue $(-1)^{l+N^+}$. [9]. Then, an eigenstate of the effective Hamiltonian whose parity is determined as $\eta(-1)^N$ according to Eq. 1.23 can be mixtures of case (d) states whose l and N^+ values are restricted to satisfy $\eta(-1)^N = (-1)^{l+N^+}$. Substituting l_R for N^+, we can re-write this restriction as,

$$\eta(-1)^N = (-1)^{l-l_R}(-1)^N, \tag{1.33}$$

which implies $\eta = l - l_R$. Therefore, for $l = 3$ and $\eta = 1$, the values of l_R are restricted to $l_R = -3,-1,1,3$, whereas they are restricted to $l_R = -2,0,2$ for $\eta = -1$. This justifies the use of η for the definition of a case (d) basis state in Eq. 1.26. Equation 1.33 is also the basis for the various labeling schemes in terms of l_R that are used in Figs. 1-6 and 1-9. Figure 1-9 clearly displays the recoupling to case (d) at N=10 and the use of l_R as an approximately good quantum number.

According to the effective Hamiltonian results displayed in Fig. 1-6A, the electronic state of CaF that is assigned as $f\Sigma^+$ at low N, correlates approximately with

---

[9] This expression is specific to a $^1\Sigma^+$ core.

Table 1.2: Comparison of observed total term values from Gittins et al. [40] and calculated values using the present effective Hamiltonian for $\eta = 1$

N	13 f(-3) Obs.	13 f(-3) Calc.	13 f(-1) Obs.	13 f(-1) Calc.	13 f(1) Obs.	13 f(1) Calc.
0		47046.9				
1		47049.1		47043.0		
2	47057.3	47052.4		47043.3		47036.1
3	47059.2	47056.5		47044.7		47037.8
4	47064.3	47061.5	47047.5	47047.2		47039.8
5	47069.6	47067.3	47051.2	47050.9	47042.3	47042.4
6	47075.5	47073.8	47055.5	47055.5	47045.6	47045.6
7	47082.2	47081.1	47060.9	47061.0	47049.7	47049.5
8	47089.8	47089.1	47067.2	47067.4	47054.5	47054.3
9	47098.1	47097.9	47074.3	47074.5	47060.1	47059.8
10	47107.3	47107.5	47082.1	47082.5	47066.5	47066.2

Table 1.3: Comparison of observed total term values from Gittins et al. [40] and calculated values using the present effective Hamiltonian for $\eta = -1$

N	13 f(-2) Obs.	13 f(-2) Calc.	13 f(0) Obs.	13 f(0) Calc.	13 f(2) Obs.	13 f(2) Calc.
1		47044.4				
2		47046.4		47036.2		
3		47049.4		47038.2		47028.7
4	47053.0	47053.3	47040.6	47040.9		47031.0
5	47057.5	47058.1	47044.0	47044.3		47033.9
6	47063.5	47063.6	47048.2	47048.5	47039.1	47037.4
7	47070.0	47070.0	47053.2	47053.5	47042.9	47041.5
8	47077.1	47077.2	47058.9	47059.3	47047.4	47046.4
9	47085.0	47085.1	47065.5	47065.8	47052.6	47051.9
10	47093.6	47093.8	47072.8	47073.1	47058.2	47058.1

a single $fl_R = -3$ state at high N. The states that are assigned as $f\Pi^+$,$f\Delta^+$ and $f\Phi^+$ correlate with $l_R = -1, 1, 3$ states respectively, in the case (d) limit. Fig. 1-6B shows the analogous results for the $\eta = -1$ symmetry. In this case, the correlation is between the sets Π^-, Δ^-, Φ^- and $l_R = -2, 0, 2$. These results indicate that the states with negative projection along the rotation axis are destabilized (i.e. pushed up in energy), whereas the states with positive projection along the rotation axis are stabilized (i.e. pushed down in energy) with increasing N.

Tables 1.2 and 1.3 show comparisons of the observed total term values from Gittins et al. [40] and the calculated total term values using the present effective Hamiltonian for $\eta = 1$ and $\eta = -1$ symmetries. In most cases, there is very close agreement between the experimental and theoretical results. The largest differences between experiment and theory are on the order of 5 cm^{-1} and they occur at low N for the 13f $l_R = -3$ states. Gittins et al. [40] find that these states are perturbed by the 13.19 Σ^+, v=1 state and this perturbation cannot be captured by the current effective Hamiltonian. In addition, smaller discrepancies on the order of $2cm^{-1}$ arise for the 13f $l_R = 2$ states, whose assignments are not secure according to Gittins et al. [40]. For all other states the differences between experiment and theory are less than 1 cm^{-1}.

In common spectroscopic applications of the effective Hamiltonian theory, the parameters describing the effective Hamiltonian are fit to the experimental results to obtain agreement between the observed and calculated total term values. However, no attempt has been made to fit the parameters of the present effective Hamiltonian to the observed term values; this effective Hamiltonian is *ab initio* in the sense that the only input it requires are the calculated eigenquantum defects from **Chapter 4**. The powerful combination of the effective Hamiltonian theory and MQDT makes it possible to compute an electronic spectrum without the need for a prior experiment. With the advent of such a combination of methods and perfection of the first-principles MQDT calculations, simulations of more complicated electronic spectra will be possible.

Chapter 2

Formalism of Multichannel Quantum Defect Theory

2.1 Introduction

Multichannel quantum defect theory is the study of electron scattering in the field of a positive ion. For this reason, it is founded upon the theory of Coulomb scattering and the analytical properties of the Coulomb wavefunctions as a function of collision energy. This chapter begins with a description of the Coulomb scattering problem and presents a derivation of the radial Coulomb functions f and g that are used in MQDT. The precise concept of a collision channel is subsequently introduced and the single-channel theory is discussed with applications to alkali atoms. The multichannel theory is derived as a generalization of the single-channel case and the mathematical foundation of the Lu-Fano plot is presented. This is followed by the derivation of the frame-transformation equations, specializing to molecular applications of MQDT. The chapter concludes with a discussion of shape and Feshbach type scattering resonances and resonance scattering theory. The presentation in this chapter is technical and serves to complement the more qualitative aspects of MQDT that are discussed in **Chapter 1**.

2.2 Coulomb Scattering

The theory of Coulomb scattering is presented in many graduate level quantum mechanics books such as the texts by Messiah [85], Sakurai [104] and Newton [96]. The text book treatment typically starts from the separation of variables in parabolic coordinates of the Coulomb radial equation and aims to derive the Rutherford formula for the Coulomb scattering cross section. This is accomplished by passing directly to the asymptotic limit using Laplace transforms and complex variable methods. MQDT requires knowledge of the properties of the Coulomb functions at short-range in addition to the asymptotic limit. This results in a need to pursue the analysis beyond the degree that is given in standard texts.

The treatment that is developed here relies heavily on the theory of the confluent hypergeometric function [73]. The confluent hypergeometric function is a precursor to a variety of important special functions in quantum mechanics, such as the Laguerre polynomials, Bessel functions, and Airy functions. The analysis follows the original derivations presented by Seaton in references [107, 108, 109, 110, 111]. A more physical approach, that starts from the WKB solutions of the Coulomb radial equation, is presented by Rau and Fano [34], Greene, Fano and Strinati [46], and Greene, Rau and Fano [50]. Efficient numerical methods for determining the Coulomb functions are discussed by Texier and Jungen [66].

In atomic units, the time independent Schrödinger equation for an electron scattering in the field of a bare nucleus of total positive charge +Z is,

$$-\frac{1}{2}\nabla^2\psi(\mathbf{r}) - \frac{Z}{r}\psi(\mathbf{r}) = E\psi(\mathbf{r}). \tag{2.1}$$

Upon substituting $\psi(\mathbf{r}) = \frac{u_l(r)}{r}Y_{lm}(\theta,\phi)$ in spherical polar coordinates and using the identity,

$$\nabla^2\left(\frac{u_l(r)}{r}Y_{lm}(\theta,\phi)\right) = \left(\frac{d^2}{dr^2} + \frac{l(l+1)}{2r^2}\right)\frac{u_l(r)}{r}Y_{lm}(\theta,\phi), \tag{2.2}$$

equation 2.1 reduces to the radial Coulomb Schr$\ddot{o}$dinger equation,

$$\left(\frac{d^2}{dr^2} - \frac{l(l+1)}{r^2} + \frac{2Z}{r} + E_{rydberg}\right) u_l(r) = 0, \tag{2.3}$$

where $E_{rydberg} = 2E\,(au)$ is the collision energy in Rydbergs and $Y_{lm}(\theta, \phi)$ is a spherical harmonic. The differential equation in Eq. 2.3 can be solved exactly by reducing it to the *confluent hypergeometric equation* discussed in [2, 73]. This is accomplished by substituting,

$$\rho = Zr \quad and \quad \epsilon = E_{rydberg}/Z^2, \tag{2.4}$$

in Eq. 2.3 to yield,

$$\left(\frac{d^2}{d\rho^2} - \frac{l(l+1)}{\rho^2} + \frac{2}{\rho} + \epsilon\right) u_l(\rho) = 0. \tag{2.5}$$

Letting $l = \lambda + \frac{1}{2}$ and $\epsilon = -\frac{1}{\kappa^2}$ in Eq. 2.5 gives,

$$\left(\frac{d^2}{d\rho^2} - \frac{\lambda^2 - \frac{1}{4}}{\rho^2} + \frac{2}{\rho} - \frac{1}{\kappa^2}\right) u_\lambda(\rho) = 0. \tag{2.6}$$

A final substitution of $z = \frac{2\rho}{\kappa}$ in Eq. 2.6 results in,

$$\left(\frac{d^2}{dz^2} - \frac{\lambda^2 - \frac{1}{4}}{z^2} + \frac{\kappa}{z} - \frac{1}{4}\right) u_\lambda(z) = 0. \tag{2.7}$$

Equation 2.7 is the Whittaker equation, the solutions of which are known. We first consider the more general case for which λ is not restricted to a half integer, as in Eq.2.5. For arbitrary λ, a solution of the Whittaker equation that is regular at the origin is,

$$M_{\kappa,\lambda}(z) = e^{-\frac{1}{2}z} z^{\frac{1}{2}+\lambda} {}_1F_1(\frac{1}{2} + \lambda - \kappa, 1 + 2\lambda, z), \tag{2.8}$$

where ${}_1F_1$ denotes the confluent hypergeometric function. In the definition of Eq. 2.8, the confluent hypergeometric function is singular when $1 + 2\lambda$ equals zero or a negative integer [83]. A physically acceptable solution to the radial Coulomb equation is the regularized Whittaker function defined as,

$$y_1(\kappa, \lambda, z) = \frac{\kappa^{\lambda+\frac{1}{2}}}{\Gamma(1+2\lambda)} M_{\kappa,\lambda}(z), \tag{2.9}$$

where the term Γ refers to the Euler gamma function, which removes the singularity in the confluent hypergeometric function. The significance of $\kappa^{\lambda+\frac{1}{2}}$ as a normalization constant will be apparent later in the derivation. The term λ enters through λ^2 in Eq. 2.7, so a second linearly independent solution to the Coulomb radial equation can be obtained as,

$$y_2(\kappa, \lambda, z) = y_1(\kappa, -\lambda, z). \tag{2.10}$$

However, it can be shown that the two solutions y_1 and y_2 are not linearly independent when $\lambda = l + \frac{1}{2}$. From the properties of the confluent hypergeometric function, the solution in Eq. 2.9 has the series expansion,

$$y_1(\kappa, \lambda, z) = \frac{\kappa z^{\lambda+\frac{1}{2}} exp(-z/2)}{\Gamma(\lambda + \frac{1}{2} - \kappa)} \sum_{n=0}^{\infty} \frac{\Gamma(\lambda + \frac{1}{2} - \kappa + n)}{\Gamma(2\lambda + 1 + n)} \frac{z^n}{n!}. \tag{2.11}$$

If we let $\lambda = l + \frac{1}{2}$ where l is an integer as in Eq. 2.5, we get from Eqs. 2.11 and 2.10,

$$y_2(\kappa, l + \frac{1}{2}, z) = \frac{(\kappa z)^{-l} exp(-z/2)}{\Gamma(-l - \kappa)} \sum_{n=0}^{\infty} \frac{\Gamma(-l - \kappa + n)}{\Gamma(-2l + n)} \frac{z^n}{n!}. \tag{2.12}$$

Since,

$$\frac{1}{\Gamma(-n)} = 0, \qquad for \quad n = 0, 1, 2, \cdots, \tag{2.13}$$

Eq. 2.12 becomes,

$$y_2(\kappa, l+\frac{1}{2}, z) = \frac{(\kappa z)^{-l} exp(-z/2)}{\Gamma(-l-\kappa)} \sum_{n=2l+1}^{\infty} \frac{\Gamma(-l-\kappa+n)}{\Gamma(-2l+n)} \frac{z^n}{n!} \tag{2.14}$$

$$y_2(\kappa, l+\frac{1}{2}, z) = \frac{\kappa^- l(z)^{l+1} exp(-z/2)}{\Gamma(-l-\kappa)} \sum_{n=0}^{\infty} \frac{\Gamma(l-\kappa+1+n)}{\Gamma(n+1)} \frac{z^n}{n!} \frac{1}{(n+1)_{2l+1}} \tag{2.15}$$

$$y_2(\kappa, l+\frac{1}{2}, z) = \frac{\kappa^- l(z)^{l+1} exp(-z/2)}{\Gamma(-l-\kappa)} \sum_{n=0}^{\infty} \frac{\Gamma(l-\kappa+1+n)}{\Gamma(n+1)} \frac{z^n}{n!} \frac{\Gamma(n+1)}{\Gamma(n+2l+2)} \tag{2.16}$$

$$y_2(\kappa, l+\frac{1}{2}, z) = \frac{\kappa^- l(z)^{l+1} exp(-z/2)}{\Gamma(-l-\kappa)} \sum_{n=0}^{\infty} \frac{\Gamma(l-\kappa+1+n)}{\Gamma(n+2l+2)} \frac{z^n}{n!}, \tag{2.17}$$

where the Pochhammer symbol $(z)_n$, is used in Eq. 2.15,

$$(z)_n = z(z+1)(z+2)\cdots(z+n-1) = \frac{\Gamma(z+n)}{\Gamma(z)}. \tag{2.18}$$

Now we define,

$$A(\kappa, \lambda) = \frac{\Gamma(\kappa+\lambda+\frac{1}{2})}{\kappa^{2\lambda}\Gamma(\kappa-\lambda+\frac{1}{2})} \tag{2.19}$$

and multiply Eq. 2.17 on the left with $-A(\kappa, l+\frac{1}{2})^{-1}$ to obtain,

$$y_2(z)A^{-1} = -(z\kappa)^{l+1} exp(-z/2) \tfrac{\Gamma(\kappa-l)}{\Gamma(-l-\kappa)\Gamma(\kappa+l+1)} \textstyle\sum_{n=0}^{\infty} \tfrac{\Gamma(l-\kappa+1+n)}{\Gamma(n+2l+2)} \tfrac{z^n}{n!} \tag{2.20}$$

$$= \tfrac{(z\kappa)^{l+1} exp(-z/2)}{\Gamma(l+1-\kappa} \textstyle\sum_{n=0}^{\infty} \tfrac{\Gamma(l-\kappa+1+n)}{\Gamma(n+2l+2)} \tfrac{z^n}{n!}. \tag{2.21}$$

Equation 2.21 is obtained from Eq. 2.20 using the relation,

$$\Gamma(n-1+z) = (n-2+z)(n-3+z)\cdots z\Gamma(z). \tag{2.22}$$

Equation 2.21 implies, through Eq.2.11 that,

$$y_2(\kappa, l+\frac{1}{2}, z) = -A(\kappa, l+\frac{1}{2}) y_1(\kappa, l+\frac{1}{2}, z). \tag{2.23}$$

Thus, the two solutions are not linearly independent for the physical case $\lambda = l + \frac{1}{2}$.

A third solution that is linearly independent from y_1 for $\lambda = l + \frac{1}{2}$ can be defined as,

$$y_3(\kappa, \lambda, z) = \frac{A(\kappa, \lambda) cos(2\pi\lambda) y_1(\kappa, \lambda, z) - y_2(\kappa, \lambda, z)}{sin(2\pi\lambda)}. \tag{2.24}$$

The solution y_3 remains finite in the limit $\lambda \to l + \frac{1}{2}$.

We can now define the two energy-normalized linearly independent solutions to the Coulomb radial equation as,

$$f_l(\epsilon, r) = \tfrac{1}{\sqrt{2}} A^{\frac{1}{2}} y_1(\kappa, l + \tfrac{1}{2}, z) \tag{2.25}$$

$$g_l(\epsilon, r) = \tfrac{1}{\sqrt{2}} A^{-\frac{1}{2}} y_3(\kappa, l + \tfrac{1}{2}, z) \tag{2.26}$$

2.2.1 Asymptotic Limit

For $|z|$ large, the asymptotic form of the regularized confluent hypergeometric function is given in [2] as,

$$\frac{{}_1F_1(a, b, z)}{\Gamma(b)} = \frac{e^{-i\pi a}}{\Gamma(b-a)} + \frac{e^z z^{a-b}}{\Gamma(a)} \tag{2.27}$$

Using Eq. 2.27 in Eq. 2.9, we obtain,

$$\begin{aligned} y_1(\kappa, \lambda, z) &\to_{|z|\to\infty} \kappa^{\lambda+\frac{1}{2}} e^{-z/2} z^{\frac{1}{2}+\lambda} \left\{ \tfrac{e^{-i\pi(\frac{1}{2}+\lambda-\kappa)} z^{\kappa-\lambda-\frac{1}{2}}}{\Gamma(\lambda+\kappa+\frac{1}{2})} + \tfrac{e^z z^{-(\frac{1}{2}+\lambda+\kappa)}}{\Gamma(\lambda+\frac{1}{2}-\kappa)} \right\} &(2.28)\\ &\to_{|z|\to\infty} \kappa^{\lambda+\frac{1}{2}} \left\{ e^{-z/2} \tfrac{e^{-i\pi(\frac{1}{2}+\lambda-\kappa)} z^{\kappa}}{\Gamma(\lambda+\kappa+\frac{1}{2})} + e^{z/2} \tfrac{z^{-\kappa}}{\Gamma(\lambda+\frac{1}{2}-\kappa)} \right\} &(2.29) \end{aligned}$$

Continuum Solutions

For continuum solutions, we have $\epsilon > 0$. We let $\kappa = i\gamma$ with $\gamma = \sqrt{1/\epsilon} = \frac{1}{k}$ and k is the magnitude of the wavevector. For real λ and $Z = 1$, we can derive the following set of relations:

$$\kappa^{\lambda+\frac{1}{2}} = (i\gamma)^{\lambda+\frac{1}{2}} = e^{i\frac{\pi}{2}(\lambda+\frac{1}{2})}\gamma^{\lambda+\frac{1}{2}}$$

$$e^{-z/2} = e^{ir/\gamma} \quad e^{z/2} = e^{-ir/\gamma}$$

$$z^{\kappa} = (-\tfrac{2ir}{\gamma})^{i\gamma} = \left(e^{-i\frac{\pi}{2}}e^{log(2r/\gamma)}\right)^{i\gamma} = e^{\frac{\pi}{2}\gamma}e^{i\gamma log(2r/\gamma)}$$

$$z^{-\kappa} = e^{-\frac{\pi}{2}\gamma}e^{-i\gamma log(2r/\gamma)}$$

$$\tfrac{1}{\Gamma(\lambda+\kappa+\frac{1}{2})} = \tfrac{1}{|\Gamma(\lambda+i\gamma+\frac{1}{2})|}e^{-iarg(\Gamma(\lambda+i\gamma+\frac{1}{2}))}$$

$$\tfrac{1}{\Gamma(\lambda-\kappa+\frac{1}{2})} = \tfrac{1}{|\Gamma(\lambda+i\gamma+\frac{1}{2})|}e^{iarg(\Gamma(\lambda+i\gamma+\frac{1}{2}))}$$

Using these relations in Eq. 2.29, we obtain

$$y_1(\kappa,\lambda,z) \rightarrow_{\infty} \tilde{C}\left\{e^{i\left(r/\gamma-\frac{\pi}{2}(\frac{1}{2}+\lambda)+\gamma log(2r/\gamma)-arg(\Gamma(\lambda+i\gamma+\frac{1}{2}))\right)} + c.c\right\} \tag{2.30}$$

$$y_1(\kappa,\lambda,z) \rightarrow_{\infty} Ccos\left(r/\gamma-\tfrac{\pi}{2}(\tfrac{1}{2}+\lambda)+\gamma log(2r/\gamma)-arg(\Gamma(\lambda+i\gamma+\tfrac{1}{2}))\right) \tag{2.31}$$

$$y_1(\kappa,\lambda,z) \rightarrow_{\infty} Csin\left(r/\gamma-\tfrac{\pi}{2}\lambda+\tfrac{\pi}{4}+\gamma log(2r/\gamma)-arg(\Gamma(\lambda+i\gamma+\tfrac{1}{2}))\right) \tag{2.32}$$

$$C = \tfrac{2\gamma^{\lambda+\frac{1}{2}}e^{-\frac{\pi}{2}\gamma}}{|\Gamma(\lambda+i\gamma+\frac{1}{2})|}, \quad \tilde{C} = \tfrac{C}{2}. \tag{2.33}$$

Putting $\lambda = l + \frac{1}{2}$ in Eq, 2.32 we arrive at,

$$y_1(\kappa,\lambda,r\rightarrow\infty) = Csin\phi_l(r,k), \tag{2.34}$$

where $\phi_l(r,k)$ is the Coulomb phase defined as in Eq. 2.32,

$$\phi_l(r,k) = kr - \frac{l\pi}{2} + \frac{1}{k}log(2kr) - arg(\Gamma(l+1+i/k) \tag{2.35}$$

For low energy scattering, $k \sim 0$ and $\gamma >> 0$. In this limit, we can approximate $A(\gamma, l+\frac{1}{2})$ of Eq. 2.19 as,

$$A(\gamma, l+\frac{1}{2}) = \frac{\Gamma(i\gamma+l+1)}{(i\gamma)^{2l+1}\Gamma(i\gamma-l)} \sim 1. \tag{2.36}$$

This approximation follows from Eq. 2.18. Furthermore, we can use the asymptotic expansion ($|z| \to \infty$) of the gamma function [2],

$$\Gamma(az+b) \sim \sqrt{2\pi}e^{-az}(az)^{az+b-\frac{1}{2}} \qquad arg(z) < \pi, a > 0 \tag{2.37}$$

in combination with Eq. 2.36 to show that

$$C * A(\gamma, l+\tfrac{1}{2})^{1/2} = \tfrac{2\gamma^{l+1}e^{-\frac{\pi}{2}\gamma}}{|\Gamma(l+1+i\gamma)|}\left(\tfrac{\Gamma(i\gamma+l+1)}{(i\gamma)^{2l+1}\Gamma(i\gamma-l)}\right)^{1/2} \tag{2.38}$$

$$\sim \sqrt{\tfrac{2\gamma}{\pi}}. \tag{2.39}$$

Equations 2.39 and 2.25 together demonstrate that,

$$f_l(\epsilon = k^2, r \to \infty) = \sqrt{\frac{1}{\pi k}} sin\phi_l(r,k). \tag{2.40}$$

Using Eq. 2.40 in Eq. 2.24 and applying l'Hospital's rule in the limit $\lambda \to l + \frac{1}{2}$, it is easily shown that,

$$g_l(\epsilon = k^2, r \to \infty) = -\sqrt{\frac{1}{\pi k}} cos\phi_l(r,k). \tag{2.41}$$

Equations 2.40 and 2.41 imply that the functions f_l and g_l are $\pi/2$ out of phase for large r.

The Wronskian

It is known from the theory of ordinary differential equations [61] that any two linearly independent solutions to a second order differential equation must satisfy the Wronskian relation given by,

$$W(f_l(\epsilon,r), g_l(\epsilon,r)) = f_l(\epsilon,r)\frac{dg_l(\epsilon,r)}{dr} - \frac{df_l(\epsilon,r)}{dr}g_l(\epsilon,r) = constant, \tag{2.42}$$

for all values of r. From Eqs. 2.40 and 2.41, we compute the Wronskian constant to be,

$$W(f_l(\epsilon,r), g_l(\epsilon,r)) = \frac{1}{\pi}. \tag{2.43}$$

We will make extensive use of the Wronskian relation in Eq. 2.43 later in this thesis.

2.2.2 Behavior of the Coulomb functions at $r = 0$

Equation 2.11 shows that,

$$f_l(\epsilon, r \to 0) \sim r^{l+1}. \tag{2.44}$$

Since f_l goes smoothly to zero as $r \to 0$, it is called the regular Coulomb function. Equations 2.12 and 2.24 imply that,

$$g_l(\epsilon, r \to 0) \sim r^{-l}. \tag{2.45}$$

Thus g_l has an inverse singularity at $r = 0$. For this reason, it is called the irregular Coulomb function.

2.2.3 Continuum Normalization

We define the differential operator,

$$O = \left(\frac{d^2}{dr^2} - \frac{l(l+1)}{r^2} + \frac{2Z}{r} \right), \tag{2.46}$$

and the functions,

$$f_1 = f_l(\epsilon, r) \qquad f_2 = f_l(\epsilon', r). \tag{2.47}$$

Since f_1 and f_2 are both solutions to the Coulomb radial equation, we have,

$$(O + \epsilon) f_1 = 0 \qquad (O + \epsilon') f_2 = 0. \tag{2.48}$$

Next we consider the expression,

$$\int_0^r dr' \left(f_1(r')(O + \epsilon') f_2(r') - f_2(r')(O + \epsilon) f_1(r') \right) = 0. \tag{2.49}$$

Integrating by parts and using Eq. 2.44, Eq. 2.49 can be simplified to,

$$f_1(r)\frac{df_2(r)}{dr} - f_2(r)\frac{df_1(r)}{dr} = (\epsilon - \epsilon')\int_0^r dr' f_1(r')f_2(r') \tag{2.50}$$

$$\int_0^r dr' f_1(r')f_2(r') = \frac{W(f_1(r), f_2(r))}{\epsilon - \epsilon'} \tag{2.51}$$

In the limit $r \rightarrow \infty$ we can compute the Wronskian using Eqs. 2.44 and 2.45 as,

$$W(f_1(r), f_2(r)) = \frac{1}{\pi} sin(\phi_l(r, \epsilon) - \phi_l(r, \epsilon')). \tag{2.52}$$

Since $\epsilon = k^2$, in the limit as $\epsilon' \rightarrow \epsilon$ we have

$$(\epsilon - \epsilon') = 2k(k - k'). \tag{2.53}$$

Thus,

$$\frac{W(f_1(r), f_2(r))}{\epsilon - \epsilon'} = \frac{sin(\phi_l(r, \epsilon) - \phi_l(r, \epsilon'))}{2k\pi(k - k')} \tag{2.54}$$

From Eqs. 2.54, 2.35 and the following definition of the Dirac-delta function,

$$\delta(x) = \lim_{a \rightarrow 0} \frac{1}{\pi x} sin(\frac{x}{a}), \tag{2.55}$$

we deduce that,

$$\frac{W(f_1(r), f_2(r))}{\epsilon - \epsilon'} = \frac{1}{2k}\delta(k - k') = \delta(\epsilon - \epsilon'). \tag{2.56}$$

It follows from Eq. 2.51 that

$$\int_0^\infty dr' f_1(r')f_2(r') = \delta(\epsilon - \epsilon'). \tag{2.57}$$

Hence the function $f_l(\epsilon, r)$ is normalized to a Delta function per unit energy in Rydbergs.

2.2.4 Solutions at Negative Energy

The solutions at negative energy are obtained from the analytical continuation of the Coulomb functions defined in Eqs. 2.25 and 2.26 to $\epsilon < 0$. At small r, the negative energy solutions differ from the continuum solutions by slight shifts in the radial nodal positions. However, the asymptotic forms change appreciably, becoming a superposition of decaying and growing exponentials as a function of r as opposed to the oscillatory functions obtained at $\epsilon > 0$. These asymptotic forms can be derived from Eq. 2.29 with the substitution $\kappa = \nu$, where ν is a real, positive valued variable. This yields,

$$f_l(\epsilon = -\frac{1}{\nu^2}, r \rightarrow \infty) \sim \frac{1}{\sqrt{2\pi}} \left(\nu\Gamma(l+1+\nu)\Gamma(\nu-l)\right)^{\frac{1}{2}} e^{r/\nu} \left(\frac{2r}{\nu}\right)^{-\nu} sin\pi(\nu-l) + ae^{-r/\nu}, \tag{2.58}$$

where the parameter a is independent of r. In obtaining Eq. 2.58 from Eq. 2.29 we use the identity,

$$\frac{1}{\Gamma(z)\Gamma(1-z)} = \frac{sin\pi z}{\pi}. \tag{2.59}$$

Substitution of Eq. 2.58 in Eq. 2.24 and the application of l'Hosptial's rule in the limit as $\lambda \rightarrow l + \frac{1}{2}$ gives,

$$g_l(\epsilon = -\frac{1}{\nu^2}, r \rightarrow \infty) \sim -\frac{1}{\sqrt{2\pi}} \left(\nu\Gamma(l+1+\nu)\Gamma(\nu-l)\right)^{\frac{1}{2}} e^{r/\nu} \left(\frac{2r}{\nu}\right)^{-\nu} cos\pi(\nu-l) + be^{-r/\nu}, \tag{2.60}$$

where the parameter b is independent of r. Equations 2.58 and 2.60 show that both f and g are exponentially divergent in the asymptotic limit, for $\epsilon < 0$.

2.2.5 Bound States of the Coulomb potential

Bound states are obtained from the constraint that any physical wavefunction representing a bound state should be normalizable to unity over all space. Since the function g_l has an inverse singularity at $r = 0$ for arbitrary l, the normalization constraint precludes the irregular function as a candidate for a bound state solution. The bound state radial wavefunctions are given by f_l evaluated at energies for which the coefficient of the exponentially growing factor in Eq. 2.58 vanishes. This leads to the energy constraint,

$$sin\pi(\nu - l) = 0. \tag{2.61}$$

Equation 2.61 implies,

$$\nu - l = m, \qquad m = 1, 2, \cdots \tag{2.62}$$

$$\sqrt{-\tfrac{1}{\epsilon}} = \nu = n + l \tag{2.63}$$

$$\epsilon = -\tfrac{1}{n^2}, \qquad n = m + l \tag{2.64}$$

Equation 2.64 is the familiar formula for the hydrogenic energy levels in Rydberg energy units. In Eq. 2.62, m cannot start from zero or be negative, because the Γ function has poles at zero and negative integers, giving rise to divergent terms in Eqs. 2.58 and 2.60 when $m = 0$ or negative.

2.2.6 Phase-Amplitude Form of the Coulomb Functions

The asymptotic limits for the positive and negative scattering energies of the regular and the irregular Coulomb functions, given in Eqs. 2.40, 2.41 and in Eqs. 2.58, 2.60, motivate the introduction of the phase-amplitude form of the Coulomb functions. We define,

$$f_l(\epsilon, r) = \tfrac{1}{\sqrt{\pi}}\alpha_l(\epsilon, r) sin\phi_l(\epsilon, r) \tag{2.65}$$

$$g_l(\epsilon, r) = -\tfrac{1}{\sqrt{\pi}}\alpha_l(\epsilon, r) cos\phi_l(\epsilon, r). \tag{2.66}$$

From the previously derived asymptotic limits,

$$\alpha(\epsilon = k^2, r \to \infty) = \tfrac{1}{k} \tag{2.67}$$

$$\phi_l(\epsilon = k^2, r \to \infty) = kr - \tfrac{l\pi}{2} + +\tfrac{1}{k}log(2kr) - arg(\Gamma(l + 1 + i/k), \quad \epsilon > 0 \tag{2.68}$$

and

$$\alpha(\epsilon=-\tfrac{1}{\nu^2}, r\to\infty) = \tfrac{1}{\sqrt{2\pi}}\left(\nu\Gamma(l+1+\nu)\Gamma(\nu-l)\right)^{\frac{1}{2}} e^{r/\nu}\left(\tfrac{2r}{\nu}\right)^{-\nu} \tag{2.69}$$

$$\phi_l(\epsilon=-\tfrac{1}{\nu^2}, r\to\infty) = \pi(\nu-l), \qquad \epsilon<0. \tag{2.70}$$

Equations 2.67 and 2.68 show that the amplitude factor, α_l, tends to a constant and the phase factor, ϕ_l tends to an r-dependent divergent function as r goes to infinity, for $\epsilon > 0$. In contrast, Eqs. 2.69 and 2.70 show that the amplitude factor tends to an r-dependent divergent function and the phase factor, ϕ_l tends to a constant as r goes to infinity, for $\epsilon < 0$. The term $\phi_l(\epsilon, r\to\infty)$ is called the accumulated Coulomb phase and takes on the value $\pi(\nu-l)$ for $\epsilon<0$. At short range, the amplitude and the phase factors are defined respectively as,

$$\phi_l(\epsilon,r) = -arctan\left(\tfrac{f_l(\epsilon,r)}{g_l(\epsilon,r)}\right) \tag{2.71}$$

$$\alpha_l(\epsilon,r) = \sqrt{\pi} f_l(\epsilon,r) cosec\phi_l(\epsilon,r) \tag{2.72}$$

The phase-amplitude form unifies the description of the negative and positive energy Coulomb wavefunctions, making explicit the $\pi/2$ phase-lag relationship between the two solutions. Furthermore, the Coulomb functions are presented in the same form as the solutions obtained using the much simpler WKB theory and this enables more facile connections to the results obtained from the WKB analysis [50].

2.2.7 Plots of the Coulomb Functions

Figures 2-1, 2-2, and 2-3 display the regular and the irregular Coulomb waves as functions of the radial coordinate, r, for angular momenta $l = 0, 1, 2$ and energies, E= -0.05, 0, and 0.1 au, respectively. Some important properties of the Coulomb functions are clearly visible in these plots. Comparison of Fig.2-2A and B shows that the maxima in the plot of the regular Coulomb function coincide with the radial nodes of the irregular Coulomb function. This is a consequence of the $\pi/2$ phase-lag relationship that is explicit in the phase-amplitude form of Eq. 2.66. The Coulomb functions oscillate with shorter wavelengths at higher energy, resulting in an inward shift in the radial nodes as the energy increases above the threshold. However, the innermost lobes remain invariant with increasing energy. This invariance follows from the energy normalization imposed on the Coulomb functions and it forms the basis for the Rydberg scaling laws that are commonly used in the analysis of Rydberg spectra [74].

Figure 2-1B shows that the irregular Coulomb functions are not infinite at the origin for $l = 0$, s-waves. However, the r-reduced radial functions $R_{l=0}(r) = g_{l=0}(r)/r$ are still infinite at the origin [53] and the s-wave irregular functions can no longer describe the hydrogenic radial wavefunctions.

Figures 2-2A and 2-2B display the corresponding regular and irregular Coulomb functions for $l = 1$, p-waves. At this increased value of the angular momentum, the innermost lobes of the regular functions are pushed out to larger r with respect to the innermost lobes of the regular s-waves. Physically, this is due to the presence of a centrifugal barrier in the effective radial potential, which reduces the amplitudes in the electron wavefunctions at small values of r. The deep singularities in the irregular functions at $r = 0$ are visible in Fig. 2-1B. The regular $l = 2$, d-waves shown in Figs. 2-2A have very small amplitudes close to the origin due to the stronger centrifugal barrier experienced by the d-waves. Similarly, the divergences in the irregular $l = 2$, d-waves begin at larger values of r relative to the divergences in the p-waves. **Chapter 3** shows that this high-angular momentum behavior has important implications for the choice of value for the **R**-matrix radius used in *ab initio* calculations.

At values of the parameter $\nu = n$, where $n = 1, 2, \cdots$, the coefficient of the exponentially divergent term in the regular Coulomb functions vanishes for all l. For these cases, the regular Coulomb functions reduce, up to a normalization constant, to the hydrogenic radial functions. The $l = 0$ and $l = 1$ hydrogenic solutions are shown for $n = 10$, $E = -1/2n^2\, au = -0.03125\, au$ in Fig. 2-4. In order to describe physical bound states, these wavefunctions must be normalized to unity over the

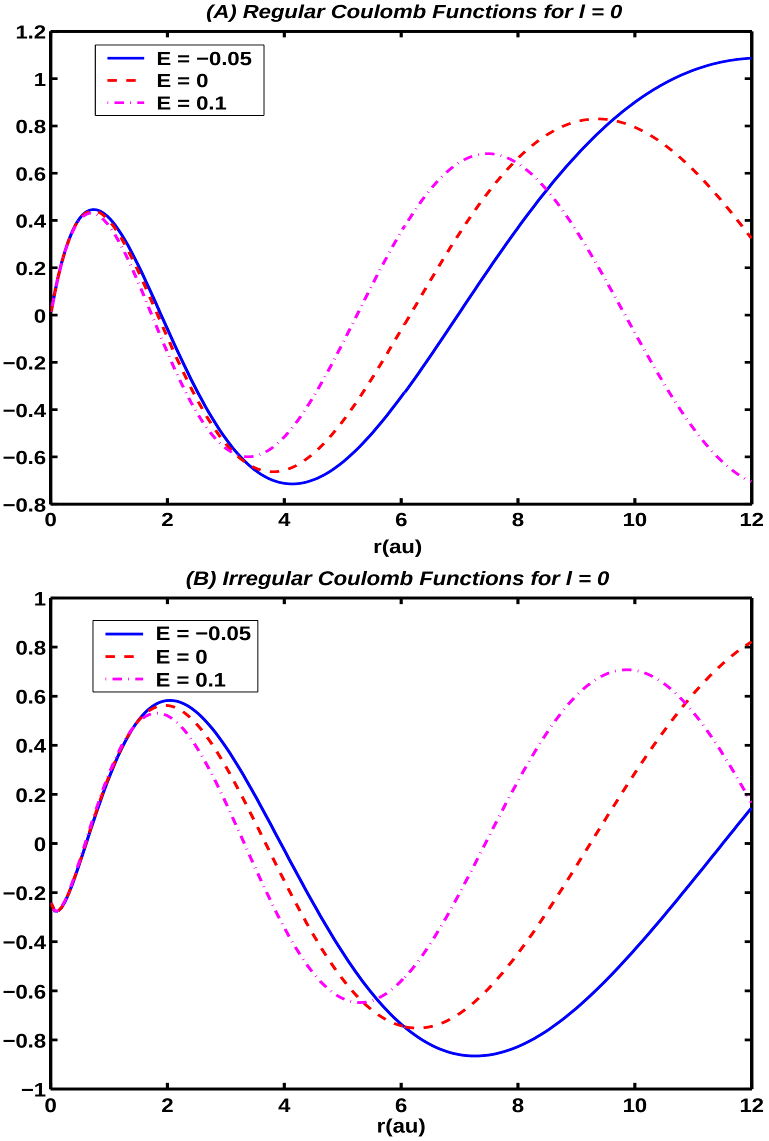

Figure 2-1: (A) The plots of the regular Coulomb waves, $f_{l=0}(\epsilon, r)$, as functions of the radial coordinate, r. The regular functions are shown for three different energies, E = -0.05, 0, and 0.1 au, respectively. At higher energy, the Coulomb functions oscillate with shorter wavelength, causing an inward shift in the radial nodes. However, the innermost lobes remain invariant with increasing energy. This is a consequence of energy normalization imposed on the Coulomb functions. (B) The plot of the irregular Coulomb function, $g_{l=0}(\epsilon, r)$, as a function of the radial coordinate, r. The irregular Coulomb functions are shown for the same set of energies as in Fig. 2-1A. The irregular Coulomb function is $\pi/2$ out of phase with the regular Coulomb function and its radial nodes coincide with the maxima in $f_{l=0}(\epsilon, r)$.

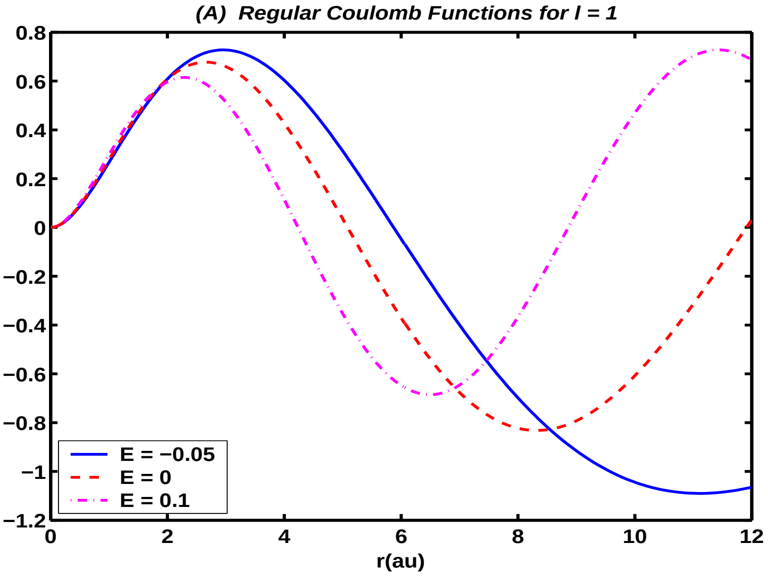
(A) Regular Coulomb Functions for l = 1

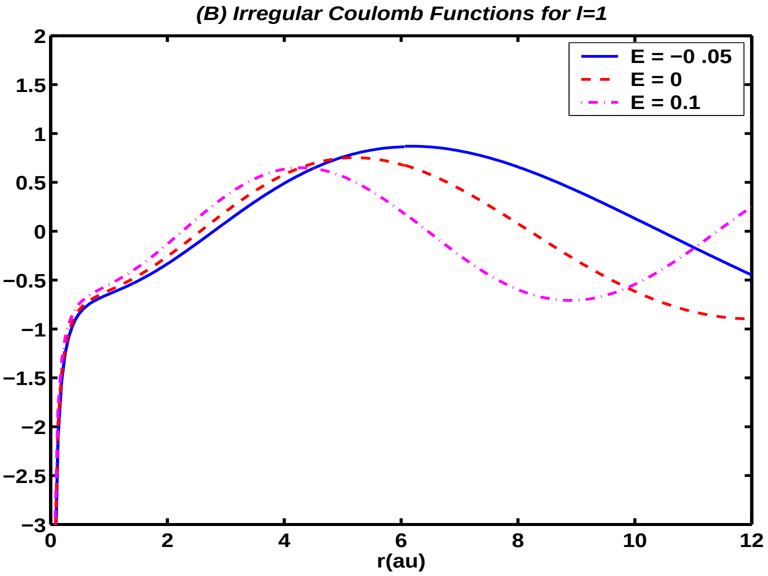
(B) Irregular Coulomb Functions for l=1

Figure 2-2: (A) The plots of the regular Coulomb waves, $f_{l=1}(\epsilon, r)$, as functions of the radial coordinate, r. The regular functions are shown for three different energies, E = -0.05, 0, and 0.1 au, respectively. The positions of the innermost lobes of the p-waves are shifted to larger r with respect to the positions of the innermost lobes of the s-waves plotted in Fig. 2-1A. This is a consequence of the presence of a centrifugal barrier in the effective radial potential, which prevents the electron from approaching $r = 0$. (B) The plots of the irregular Coulomb waves, $g_{l=1}(\epsilon, r)$, as functions of the radial coordinate, r. The irregular Coulomb functions are shown for the same set of energies as in Fig. 2-2A. The r^{-l} type deep singularities are visible near the origin.

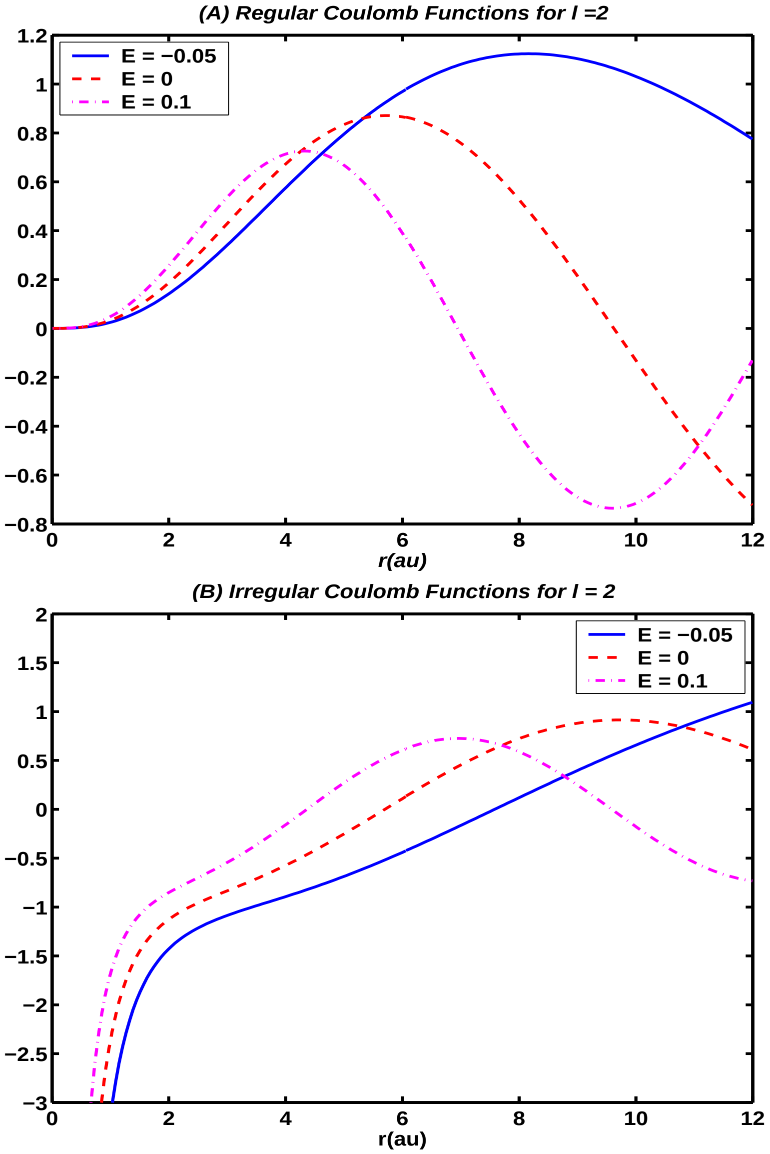

Figure 2-3: (A) The plots of the regular Coulomb waves, $f_{l=2}(\epsilon, r)$, as functions of the radial coordinate, r. The regular functions are shown for three different energies, E = -0.05, 0, and 0.1 au, respectively. The l = 2, d-waves experience a stronger centrifugal barrier and they have relatively smaller amplitudes close to the origin than the amplitudes of the lower-l angular momentum waves. (B) The plots of the irregular Coulomb waves, $g_{l=2}(\epsilon, r)$, as functions of the radial coordinate, r. The irregular Coulomb functions are shown for the same set of energies as in Fig. 2-3A. The divergences in the d-waves begin at larger values of r with respect to the radial positions of divergences in the p-waves. This high angular momentum behavior restricts the choice of value for the **R**-matrix radius used in the calculations presented in **Chapter 3**.

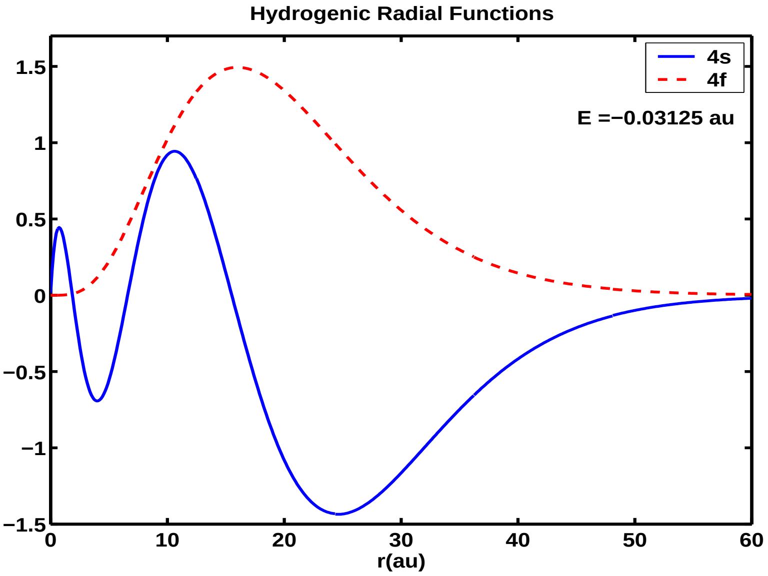

Figure 2-4: The unnormalized hydrogenic radial wavefunctions for the principal quantum number n = 4 and orbital angular momenta $l = 0, 1$. The hydrogenic functions are obtained from $f_l(E, r)$ evaluated at $E = -1/2n^2$. In analogy to the regular Coulomb functions, the normalized hydrogenic wavefunctions have innermost lobes that remain approximately invariant in shape and nodal position with increasing n. However, the amplitudes in these innermost lobes scale as $n^{-3/2}$, because of space normalization. The $n^{-3/2}$ scaling law is attributed to Mulliken, who discussed it in reference [90].

interval $r \in [0 \cdots \infty]$. The bound state solutions are given as,

$$u_{nl}(r) = \frac{1}{\sqrt{N}} f_l(-\frac{1}{2n^2}, r), \tag{2.73}$$

where

$$N = \int_0^\infty dr f_l^2(-\frac{1}{2n^2}, r). \tag{2.74}$$

The space normalization in Eq. 2.73 slightly alters the innermost lobe invariance property of the Coulomb functions discussed previously. While the innermost lobes remain invariant as a function of the principal quantum number, n, in nodal positions and shape, the amplitudes in the innermost lobes change, scaling as $n^{-3/2}$. This scaling relationship results in (i) the $n^{-3/2}$ scaling law for the ground state to

Rydberg transition dipole matrix elements, (ii) the $n^{-3/2}$ scaling of the perturbation matrix elements for the valence/Rydberg interactions, and (iii) the n^{-3} scaling of the Rydberg/Rydberg interaction matrix elements [74]. The innermost lobe invariance property was discussed by Mulliken in reference [90] and it is sometimes referred to as 'Mulliken's law' [1].

2.2.8 Coulomb Scattering Matrix

In order to obtain the Coulomb scattering matrix, we define the incoming and outgoing Coulomb partial waves as,

$$\psi_l^+(\epsilon, r) = -\left(g_l(\epsilon, r) - i f_l(\epsilon, r)\right) \tag{2.75}$$

$$\psi_l^-(\epsilon, r) = -\left(g_l(\epsilon, r) + i f_l(\epsilon, r)\right). \tag{2.76}$$

The asymptotic limits of the incoming and outgoing partial waves are obtained from Eqs. 2.40 and 2.41 as,

$$\psi_l^+(\epsilon, r \to \infty) = \tfrac{1}{\sqrt{\pi k}} e^{i\eta_l(r,k)} e^{i\sigma_l} \tag{2.77}$$

$$\psi_l^-(\epsilon, r \to \infty) = \tfrac{1}{\sqrt{\pi k}} e^{-i\eta_l(r,k)} e^{-i\sigma_l}, \tag{2.78}$$

where we define the quantities,

$$\eta_l(r, k) = kr - \tfrac{l\pi}{2} + \tfrac{1}{k} log(2kr) \tag{2.79}$$

$$\sigma_l = arg(\Gamma(l + 1 - i/k)). \tag{2.80}$$

The partial waves for the stationary states of the collision are defined as,

$$F_l(\epsilon, r) = \sqrt{\pi} e^{i\sigma_l} \left(\psi^- - \psi^+\right) \tag{2.81}$$

$$= \sqrt{\tfrac{1}{k}} \left(e^{-i\eta_l(r,k)} - e^{2i\sigma_l} e^{i\eta_l(r,k)}\right). \tag{2.82}$$

---

[1] Prof. Bob Field has brought to my attention that it was Slater who first discussed this invariance property.

The factor $\sqrt{\pi}e^{i\sigma_l}$ in Eq. 2.81 is a normalization constant and $F_l(\epsilon, r)$ is normalized to unit radial flux. This is easily seen by computing the current density for the incoming and outgoing portions of $F_l(\epsilon, r)$ as,

$$j^{\pm} = Im\left(F_l^*(\epsilon, r)^{\pm}\frac{dF_l(\epsilon, r)^{\pm}}{dr}\right), \tag{2.83}$$

where,

$$F_l(\epsilon, r)^- = e^{-i\eta_l(r,k)} \tag{2.84}$$

$$F_l(\epsilon, r)^+ = e^{2i\sigma_l}e^{i\eta_l(r,k)}. \tag{2.85}$$

Equation Eq. 2.83 yields $j^+ = -j^- = 1$. The pure phase factor, $e^{2i\sigma_l}$, in Eq. 2.82 is called the Coulomb scattering matrix in the orbital angular momentum representation and the parameter, σ_l, defines the Coulomb phase shift. The Coulomb scattering matrix can be written in the alternate form,

$$e^{2i\sigma_l} = \frac{\Gamma(l+1-i/k)}{\Gamma(l+1+i/k)}. \tag{2.86}$$

It is shown in Messiah [85] that the function $\psi_c(\mathbf{r})$, defined as a Legendre series expansion over the partial waves $F_l(\epsilon, r)$ as,

$$\psi_c(\mathbf{r}) = \frac{1}{2\sqrt{k}r}\sum_{l=0}^{\infty}(2l+1)i^{l+1}F_l(\epsilon, r)P_l(cos\theta), \tag{2.87}$$

has the closed form asymptotic limit,

$$\psi_c(\mathbf{r}) = exp(ikz - i/k\,logk(r-z)) + f(\theta)exp(ikr + i/k\,log2kr), \tag{2.88}$$

where,

$$f(\theta) = \frac{1}{2ik}\sum_{l=0}^{\infty}(2l+1)\frac{\Gamma(l+1-i/k)}{\Gamma(l+1+i/k)}P_l(cos\theta) \tag{2.89}$$

and $P_l(x)$ are the Legendre polynomials. The quantity $f(\theta)$ is called the scattering amplitude. The wavefunction $\psi_c(\mathbf{r})$ describes the stationary state of the collision for the typical experimental situation in which an electron is incident from $z = -\infty$ toward a target proton positioned at the coordinate system origin and scattered in the direction θ, subsequently hitting a detector positioned at a distance r from the target. No additional coordinates need to be specified, since the collision is planar. The series expansion for $f(\theta)$ can be summed to closed form. The result is,

$$f(\theta) = \frac{1}{2k^2} cosec^2(\theta/2)\, exp\left(i/k\, log\, 1/2\, (1 - cos\theta) + i\pi + arg(\frac{(1-i/k)}{(1+i/k)})\right). \quad (2.90)$$

Equation 2.90 yields the Coulomb differential cross section for scattering in terms of the Rutherford formula,

$$\frac{d\sigma}{d\Omega} = |f(\theta)|^2 = \frac{1}{4k^4 sin^4 \frac{1}{2}\theta}. \quad (2.91)$$

2.2.9 Bound States as Poles of the Coulomb Scattering Matrix

The analytical continuation of the Coulomb scattering matrix to $E < 0$ is obtained from Eq. 2.86 as,

$$S_c(\nu) = \frac{\Gamma(l+1-\nu)}{\Gamma(l+1+\nu)}, \quad (2.92)$$

where $E = -1/2\nu^2$. Thus, the poles of the scattering matrix correspond to the poles of the Gamma function, which are located at zero and negative integers. This implies that the scattering matrix has poles at the values of ν such that,

$$l + 1 - \nu = -m \qquad m = 0, 1, \cdots - \infty \quad (2.93)$$

$$\nu = m + l + 1. \quad (2.94)$$

Equation 2.94 yields again the familiar formula for the bound states of the hydrogen atom.

This result indicates that an entirely independent theory of bound states can be developed based on the analytical properties of the scattering matrix defined as a function of complex valued energy. Quite generally, the bound state energies of a quantum mechanical system are located at energies for which the scattering matrix is infinite. Thus, at the energies of the bound states, the scattered partial waves represent only outgoing waves at infinity. For the Coulomb problem, the infinite number of bound state energies lie on the negative real axis in the interval [-1/2,0]. Thus, the outgoing waves become decaying exponentials due to the replacement $k \rightarrow i/\nu$. This view of bound states becomes very useful in the theory of quasi-bound levels, which are located at the poles of the scattering matrix on the fourth quadrant of the complex E-plane [71].

The Coulomb scattering phase shift derived in Eq. 2.80 has a branch-cut discontinuity across the positive real axis on the complex $z = l + 1 - i/k$ plane and it is only physically meaningful when defined modulo π. However, a phase shift as a continuous function of energy can be obtained by allowing function evaluation on neighboring Riemann sheets and keeping track of the passings by adding unity to a winding number every time the parameter z crosses the branch-cut discontinuity [2]. The continuous Coulomb phase shift calculated in this fashion is plotted as a function of energy in Fig. 2-5. As the energy approaches zero from above, the winding number for the scattering phase shift increases without bound and the phase shift diverges to negative infinity. The threshold (E=0) value of the scattering phase shift equals the number of bound states supported by the potential [104, 96]. Thus, the divergence of the Coulomb phase shift at the E=0 threshold is a consequence of the infinite number of bound levels in the presence of a Coulomb potential.

Typically, long-range potentials such as the Coulomb or point-dipole potentials support an infinity of bound levels, which results in an undesired (divergent) energy dependence in the scattering matrix close to thresholds. This leads to difficulties in the application of MQDT to polar molecules, the effective potentials of which have both Coulomb and strong dipole contributions.

---

[2] This procedure is required since arg(z) is otherwise a multi-valued function.

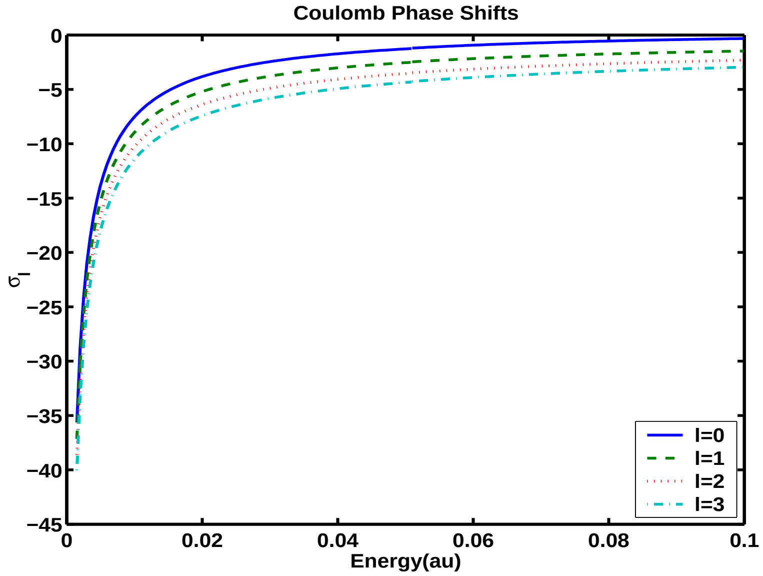

Figure 2-5: The Coulomb phase shifts as functions of collision energy. The calculated phase shifts are shown for angular momenta l=0, 1, 2 and 3. The phase shifts diverge to negative infinity at the ionization threshold, $E = 0$. The divergences are consequences of the existence of an infinity of Rydberg states that are densely located slightly below the ionization threshold. At higher energy, the phase shifts for each of the angular momenta monotonically increase to zero. Therefore, the scattering matrix approaches unity in the high energy limit. This limiting value of the scattering matrix implies an incoming partial wave that is exactly in phase with the outgoing partial-wave, i.e. the electron experiences no time-delay when scattering in the Coulomb potential. This last statement is justified by the time-dependent version of scattering theory [34].

2.3 Single Channel Theory

The single channel theory considers the collision of an electron with an ion-core that has internal structure. In this case, the physical situation is dictated by the quantum state of the ion-core, unlike the case of Coulomb scattering for which the ion-core is a structureless proton. The stationary states of the collision are expressed as functions of coordinates τ that correspond to the internal degrees of freedom and the coordinate r that measures the radial distance between the two collision partners. The internal state of the ion-core + electron system, $\Phi_0(\tau)$, is a vector coupled product of the electronic and ion-core quantum numbers and it has definite total angular momentum and parity. In the case of an atom, we can use the LS coupling scheme to express,

$$\Phi_0(\tau) =$$

$$\sum_{M_{S_0} m_{s_0} M_{L_0} m_{l_0}} \psi_{E_0 S_0 L_0 M_{S_0} M_{L_0}}(\mathbf{r}_i, \sigma_i) Y_{l_0 m_{l_0}}(\theta, \phi) \omega_{m_{s_0}}(\sigma) (\tfrac{1}{2} S_0 m_{s_0} M_{S_0} | S M_S)(l_0 L_0 m_{l_0} M_{L_0} | L M_L),$$

where $\mathbf{r}_i, \sigma_i$ are the position and spin coordinates of the electrons on the ion core, θ, ϕ, σ are the angular and spin coordinates of the scattered electron, Y_{lm} denotes a spherical harmonic and ω is the spin function. In quantum chemistry notation [128], the spin function is characterized as,

$$\omega_{\frac{1}{2}}(\sigma) = \alpha(\sigma) \tag{2.95}$$

$$\omega_{-\frac{1}{2}}(\sigma) = \beta(\sigma) \tag{2.96}$$

$$\textstyle\int d\sigma \alpha^*(\sigma)\alpha(\sigma) = \int d\sigma \beta^*(\sigma)\beta(\sigma) = 1 \tag{2.97}$$

$$\textstyle\int d\sigma \alpha^*(\sigma)\beta(\sigma) = \int d\sigma \beta^*(\sigma)\alpha(\sigma) = 0. \tag{2.98}$$

The quantum numbers L_0 and S_0 are the total orbital and spin angular momentum quantum numbers of the ion-core. Similarly l_0 and $s_0 = \frac{1}{2}$ are the orbital and spin angular momentum quantum numbers for the electron. These quantum numbers are vector coupled to form a total orbital angular momentum L and total spin angular momentum S for the whole system. The letter m is used to refer to space-fixed projections of the aforementioned angular momenta. $\psi_{E_0 S_0 L_0 M_{S_0} M_{L_0}}$ is an electronic eigenstate of the ion-core with energy eigenvalue E_0. The internal state $\Phi_0(\tau)$ is said to define a *collision channel* . In molecular applications, the collision channel is a vector coupled product in the Hund's case that is appropriate for the molecule under study.

The single channel stationary state of the collision is expressed as,

$$\Psi = \Phi_0(\tau)\frac{1}{r}F_0(r), \tag{2.99}$$

where $F_0(r)$ is a radial function for the scattered electron. The effects of electron exchange are neglected in Eq. 2.99. This is a good approximation if the ion-core is in a closed-shell electronic state [112]. The exchange effects will be taken into account in **Chapter 6**. The radial differential equation for $F_0(r)$ is derived from the matrix element,

$$(\Phi_0|H - E|\Psi) = 0, \tag{2.100}$$

where H and E are the Hamiltonian and the total energy of the system. We use the definition of Φ_0 and Eq. 2.99 in Eq.2.100 to obtain,

$$\left(\frac{d^2}{dr^2} - \frac{l_0(l_0+1)}{r^2} + 2(E - E_0) - 2V_0(r)\right) F_0(r) = 0, \tag{2.101}$$

where

$$V_0(r) = (\Phi_0|\sum_{n=1}^{N} \frac{1}{|\mathbf{r} - \mathbf{r_n}|} - \frac{N+1}{r}|\Phi_0). \tag{2.102}$$

In Eq. 2.102, N is the total number of electrons on the ion-core and N+1 is the positive charge on the nucleus. The interelectronic repulsion terms can be expanded in a Legendre series as,

$$\frac{1}{|\mathbf{r} - \mathbf{r_n}|} = \sum_{l=0}^{\infty} P_l(\hat{\mathbf{r}}.\hat{\mathbf{r}}_\mathbf{n})\frac{r_<^l}{r_>^{l+1}}, \tag{2.103}$$

where $r_< = r_n$, $r_> = r$ if $r > r_n$ and $r_> = r_n$, $r_< = r$ if $r < r_n$.

From Eq. 2.103 and by neglecting all potential terms that decrease faster than $\frac{1}{r}$, we can obtain the asymptotic limit of Eq. 2.102 as,

$$V_0(r \to \infty) = -\frac{1}{r}. \tag{2.104}$$

Therefore, the conditions for Coulomb scattering apply. At this point we invoke the central assumption of quantum defect theory, which states that,

$$V_0(r > r_0) = -\frac{1}{r}, \tag{2.105}$$

for some finite r_0.

The radial solution, $F_0(r)$, is required to be bounded at the origin. Since the centrifugal potential dominates at small r, $F_0(r)$ satisfies,

$$F_0(r \to 0) = cr^{l_0+1}, \tag{2.106}$$

where c is some constant. Based on the central assumption of MQDT in Eq. 2.104, the potential function is purely Coulombic for values of r larger than r_0. Then the general solution $F_0(r)$ must be given by some arbitrary linear combination of the regular and irregular Coulomb functions beyond r_0, i.e.,

$$F_0(r > r_0) = I_0 f_{l_0}(\epsilon_0, r) - J_0 g_{l_0}(\epsilon_0, r), \tag{2.107}$$

where $\epsilon_0 = E - E_0$. The values of the parameters I_0 and J_0 are determined from the asymptotic boundary conditions imposed on $F_0(r)$. Physically relevant solutions are the radial functions that satisfy: (i) vanishing boundary conditions for bound states, (ii) standing waves for collision eigenstates, and (iii) incoming/outgoing boundary conditions for scattering waves. Each of the three physically relevant solutions can be obtained elegantly from the reaction matrix normalized solution.

The reaction matrix normalized solution is defined as,

$$F_0^K(r > r_0) = I_0^{-1} F_0(r > r_0) = f_{l_0}(\epsilon_0, r) - J_0 I_0^{-1} g_{l_0}(\epsilon_0, r) \tag{2.108}$$

$$= f_{l_0}(\epsilon_0, r) - K_{l_0}(\epsilon_0) g_{l_0}(\epsilon_0, r), \tag{2.109}$$

where $K_{l_0}(\epsilon_0) = J_0 I_0^{-1}$ is the single channel reaction matrix. The quantum defect, $\mu_{l_0}(\epsilon_0)$, is obtained from the reaction matrix as,

$$tan\pi\mu_{l_0}(\epsilon_0) = K_{l_0}(\epsilon_0). \tag{2.110}$$

2.3.1 Bound States

For $\epsilon_0 < 0$, the asymptotic limit of $F_0^K(r)$ can be obtained from Eqs. 2.58 and 2.60 as,

$$F_0^K(r \to \infty) = \frac{1}{\sqrt{2\pi}} \left(\nu\Gamma(l_0+1+\nu)\Gamma(\nu-l_0)\right)^{1/2} e^{r/\nu} \left(\frac{2r}{\nu}\right)^{-\nu} \{sin\pi(\nu-l_0) + tan\pi\mu_{l_0}(\nu)cos\pi(\nu-l_0)\} \tag{2.111}$$

where $\nu = \sqrt{-\frac{1}{\epsilon_0}}$. The coefficient of $e^{r/\nu}$ must vanish for bound states. This leads to the condition,

$$sin\pi(\nu-l_0) + tan\pi\mu_{l_0}(\nu)cos\pi(\nu-l_0) = 0 \tag{2.112}$$

$$cos\pi\mu_0(\nu)sin\pi(\nu-l_0) + sin\pi\mu_{l_0}(\nu)cos\pi(\nu-l_0) = 0 \tag{2.113}$$

$$sin\pi(\nu-l_0+\mu_{l_0}) = 0. \tag{2.114}$$

Equation 2.114 implies that bound states occur at values of ν such that,

$$\nu = m + l_0 - \mu_{l_0}(\nu) \qquad m = 1, 2 \cdots \infty. \tag{2.115}$$

The integer m cannot be zero or negative for the reasons provided in Section 2.2.5. Equation 2.115 yields the Rydberg formula,

$$E = E_0 - \frac{1}{2(n-\mu_{l_0}(E))^2} \qquad n = m + l_0,\ m = 1, 2 \cdots \infty. \tag{2.116}$$

The quantum defect as a function of energy can be determined by fitting the Rydberg formula to the observed energy levels.

2.3.2 Collision Eigenstates

For $\epsilon_0 > 0$ the asymptotic limit of the Coulomb functions given in Eqs.2.40 and 2.41 can be used to determine the asymptotic limit of the reaction matrix normalized solution as,

$$F_0^K(r \to \infty) = \frac{1}{\sqrt{\pi k}} \left(sin\phi_{l_0}(r,k) + tan\pi\mu_{l_0} cos\phi_{l_0}(r,k) \right), \tag{2.117}$$

where $k = \sqrt{\epsilon_0}$. We rescale Eq. 2.117 to obtain the collision eigenstate as,

$$F_0^c(r \to \infty) = cos\pi\mu_{l_0} F_0^K(r) \tag{2.118}$$

$$= \frac{1}{\sqrt{\pi k}} \left(cos\pi\mu_{l_0} sin\phi_{l_0}(r,k) + sin\pi\mu_{l_0} cos\phi_{l_0}(r,k) \right) \tag{2.119}$$

$$= \frac{1}{\sqrt{\pi k}} \left(sin(\phi_{l_0}(r,k) + \pi\mu_{l_0}) \right). \tag{2.120}$$

Equation 2.120 shows that the collision eigenstate is related to the regular Coulomb function, but with an additional phase shift $\pi\mu_{l_0}$. Thus, π *times the quantum defect is the scattering phase shift.*

2.3.3 Scattering Wave

The collision eigenstate in Eq. 2.119 can be rewritten in terms of the outgoing/incoming waves of Eqs. 2.75 and 2.76 as,

$$F_0^c(r) = cos\pi\mu_{l_0} \left(\frac{\psi_{l_0}^+ - \psi_{l_0}^-}{2i} \right) + sin\pi\mu_{l_0} \left(\frac{\psi_{l_0}^+ + \psi_{l_0}^-}{2} \right). \tag{2.121}$$

The scattering wave is obtained from the collision eigenstate by rescaling as,

$$F_0^S(r) = -2ie^{i\pi\mu_l} F_0^c(r) = \psi_{l_0}^- - e^{2i\pi\mu_l}\psi_{l_0}^+. \tag{2.122}$$

Equation 2.122 defines the scattering matrix as,

$$S_{l_0}(\epsilon_0) = e^{2i\pi\mu_l} = \frac{1 + iK_{l_0}(\epsilon_0)}{1 - iK_{l_0}(\epsilon_0)}. \tag{2.123}$$

Collision observables such as the differential and integral cross sections can now be calculated from $S_{l_0}(\epsilon_0)$ as in Section 2.2.8. The results presented in Sections 2.3.1, 2.3.2, and 2.3.3 imply the important conclusion that all of the bound and continuum properties of the ion-core + electron system can be determined from a single energy dependent parameter, the quantum defect.

2.3.4 Applications of the Single Channel Theory: Alkali Atoms

Single channel theory finds its most useful applications in the study of Rydberg states of alkali atoms. The alkali atoms have simple closed shell cores and the ion-core potentials can be approximated accurately by Hartree-Slater type pseudopotentials. These pseudopotentials have the form [20],

$$V_0(r) = -\frac{1}{r} - \frac{(Z-1)}{r} e^{-a_{l_0} r}, \tag{2.124}$$

where Z is the nuclear charge and the parameter a_{l_0} is chosen to give the best agreement with the experimental energy levels. More realistic pseudopotentials that take into account core polarization and electron exchange effects can be developed [120]. However, it has been shown that the Hartree-Slater potential in Eq. 2.124 is sufficiently accurate for the alkali atoms [20]. Here, we present a sample calculation of the quantum defect for the s and p Rydberg series of the lithium atom. The calculation serves to illustrate some important analytical properties of the quantum defect in the absence of resonance behavior. These properties are expected to remain valid regardless of the complexity of the problem.

For the lithium atom, the potential parameters a_s and a_p have been determined to be both equal to 2.13. We choose the K-matrix radius, r_0, to be equal to ten [3] and normalize our radial solution such that,

$$F_0(r \to 0) = r^{l_0+1}. \tag{2.125}$$

Equation 2.125 determines the value and the derivative $F_0(r)$ in the vicinity of the origin. Therefore, the radial Schrödinger equation can be numerically solved by propagating $F_0(r)$ outward from $r \sim 0$ to $r = r_0$ by the method of finite differences [99]. The calculated radial channel wavefunctions, $F_0(r)$, for s and p waves are shown in Fig. 2-6 at an energy $\epsilon_0 = 0.1au$. The procedure yields the value and the derivative of $F_0(r)$ at $r = r_0$. From the

---

[3] Quantitatively, r_0 can be chosen such that the difference between the ion-core potential and the Coulomb potential is less than one part in a thousand at $r = r_0$.

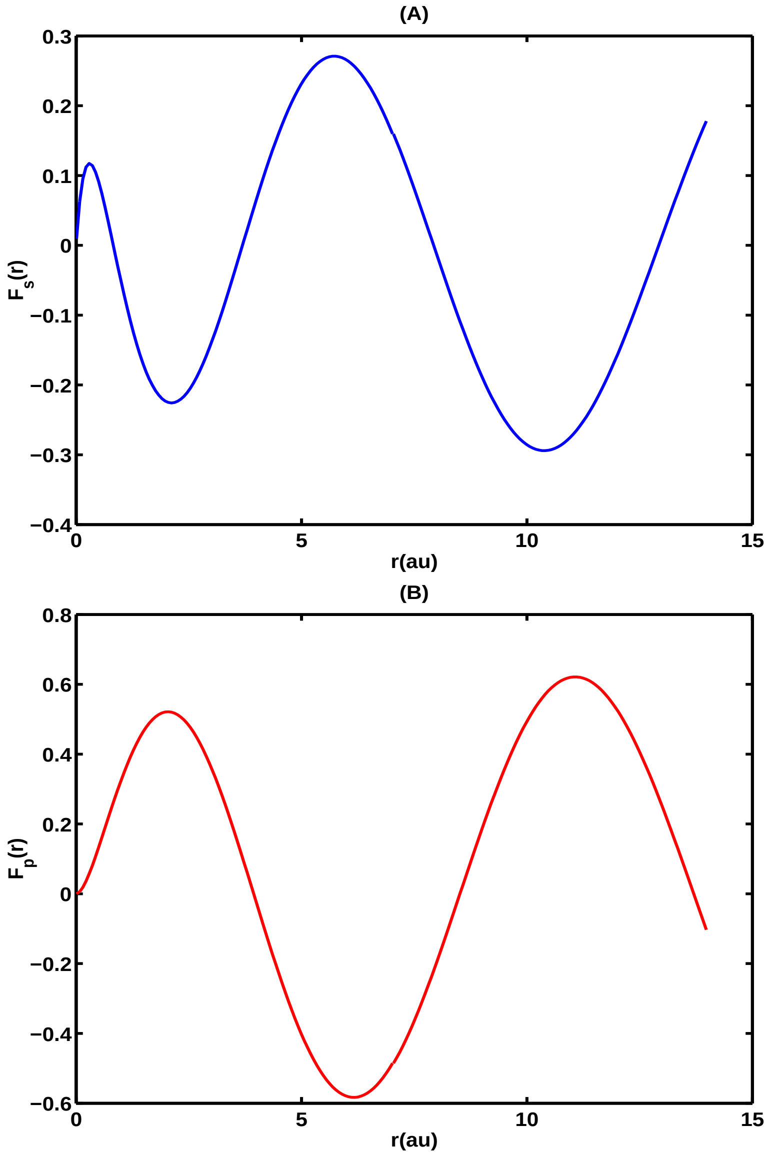

Figure 2-6: (A) The numerically determined radial channel wavefunction, $F_0(r)$, for the $l_0 = 0$, s-wave channel. The positions of the first few radial nodes are shifted inward relative to the positions of the inner radial nodes of the regular s-wave Coulomb function shown in Fig. 2-1A. This is because the electron sees an effective nuclear charge, Z(r), that increases toward Z as r approaches zero. The deep potential well at small r results in larger kinetic energy and faster oscillations in the wavefunction. (B) The numerically determined radial channel wavefunction, $F_0(r)$, for the $l_0 = 1$, p-wave channel. Similarly, the positions of the first few radial nodes are shifted inward relative to the positions of the inner radial nodes of the regular p-wave Coulomb function shown in Fig. 2-2A.

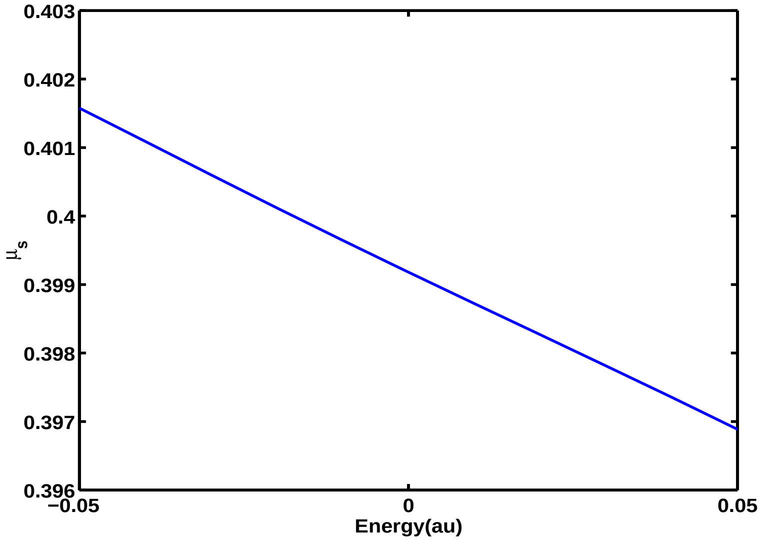

Figure 2-7: The calculated quantum defect for the s Rydberg series of the lithium atom. Above the $E = 0$ ionization threshold, π times the quantum defect becomes the s-wave scattering phase shift for the $e + Li^+$ collision. The quantum defect varies slowly as a function of energy in contrast with the strong energy dependence of the long-range Coulomb phase shift. The quantum defect curve has a negative slope for all energies. As explained in **Chapter 5**, the negative slope of the quantum defect vs E indicates that the s-waves of the lithium atom are of penetrating-type.

Wronskian condition in Eq. 2.43, the constants I_0 and J_0 in Eq. 2.108 can be computed as,

$$I_0 = \pi \left(F_0(r_0) g'_{l_0}(\epsilon_0, r_0) - F'_0(r_0) g_{l_0}(\epsilon_0, r_0) \right) \tag{2.126}$$

$$J_0 = \pi \left(F_0(r_0) g'_{l_0}(\epsilon_0, r_0) - F'_0(r_0) g_{l_0}(\epsilon_0, r_0) \right) . \tag{2.127}$$

The quantum defect modulo unity can now be determined from Eq. 2.110. The calculated quantum defects for the s and p Rydberg series of lithium are shown as a function of channel collision energy ($E - E_0 = 2\epsilon_0$) in Figs. 2-7 and 2-8.

The quantum defects for both s and p partial waves have weak and linear energy dependences. They change by approximately five parts in a thousand over an energy interval of 0.1 au. The reason for the near energy independence of the quantum defect is due to the calculation of the reaction matrix at short-range ($r = r_0$). At small values of r, the electron falls in toward the core and picks up a very large kinetic energy. This kinetic energy is fractionally much less dependent on the channel collision energy than the kinetic energy at

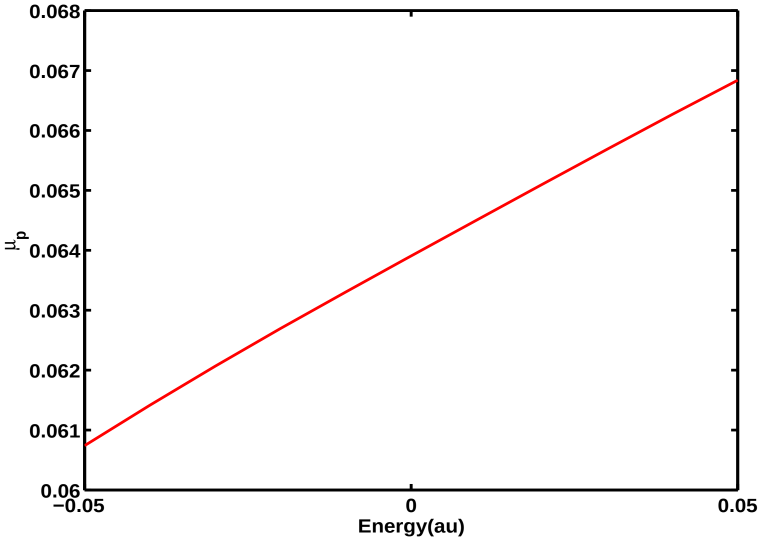

Figure 2-8: The calculated quantum defect for the p Rydberg series of the lithium atom. Above the $E = 0$ ionization threshold, π times the quantum defect becomes the p-wave scattering phase shift for the $e + Li^+$ collision. The quantum defect varies slowly and linearly with energy and has a positive slope. As explained in **Chapter 5**, the positive slope of the quantum defect vs E indicates that the p-waves of the lithium atom are of nonpenetrating-type.

long-range; it dominantly depends on the potential function or the charge on the nucleus. For this reason, the collision wavefunction at small r and hence the short-range reaction matrix is largely insensitive to the choice of collision energy. The computed values of the quantum defects compare favorably with the experimentally determined quantum defects, which are reported in reference [20] as $\mu_s = 0.4$ and $\mu_p = 0.05$. The near energy independence of the quantum defect contrasts with the strong energy dependences of the Coulomb phase shifts shown in Fig. 2-5. This implies that the calculated K-matrix in the case of the lithium atom is free of all long-range (Coulomb) field influences.

The quantum defect method is efficient and reliable for the numerical solution of the one dimensional radial Schrödinger equation. The bound state wavefunctions are constructed piecewise by numerical integration in the interval $[0, r_0]$ and by forming the appropriate linear combination of the Coulomb functions for $r > r_0$ in order to enforce continuity of the wavefunction at $r = r_0$. This method is much less time-consuming to implement than the standard Numerov-Cooley method [19], because it shifts the boundary condition at $r \to \infty$

to $r = r_0$ [4].

2.4 Multichannel Theory

We obtain the multichannel theory by an immediate matrix generalization of the single channel theory. The multichannel stationary state of the collision is expressed as,

$$\Psi = \sum_{i=1}^{N_c} \phi_i(\tau) \frac{1}{r} F_i(r), \tag{2.128}$$

in an expansion over N_c number of channels. The superposition of the internal states, $\phi_i(\tau)$, for each channel indexed by i in Eq. 2.128 makes it possible to include the possibility of electron impact excitation of the ion-core. In some references, the channels used in the expansion of Eq. 2.128 are called ionization or fragmentation channels. The radial channel wavefunctions satisfy the close-coupling equations,

$$\left(\frac{d^2}{dr^2} - \frac{l_0(l_0+1)}{r^2} + 2(E - E_i) \right) F_i(r) - 2 \sum_{i'} V_{ii'}(r) F_{i'}(r) = 0, \tag{2.129}$$

in analogy to Eq. 2.101. In Eq. 2.129, E_i is the energy eigenvalue for the $i'th$ state of the ion-core and the potential energy matrix is defined as,

$$V_{i'i}(r) = (\Phi_{i'} | \sum_{n=1}^{N} \frac{1}{|\mathbf{r} - \mathbf{r_n}|} - \frac{N+1}{r} | \Phi_i) \tag{2.130}$$

and can be approximated as,

$$V_{i'i}(r > r_0) \sim -\frac{1}{r}, \tag{2.131}$$

based on the reasons delineated in Section 2.3 . We solve Eqs. 2.129 subject to the boundary condition,

$$F_i(r \sim 0) = c_i r^{l_i+1}. \tag{2.132}$$

We postpone application of the asymptotic boundary conditions, which are to be determined by the physical situation we wish to investigate. It is known from the general theory of

---

[4] The Numerov-Cooley method is surprisingly tricky to implement for the Coulomb potential. An algorithm that appears to be stable is provided in the following website: http://theochem.uwaterloo.ca/ leroy/

coupled differential equations [61, 21] that a set consisting of N_c coupled, second-order linear equations with N_c specified boundary conditions has N_c linearly independent solutions. We label these linearly independent solutions by the index j and rewrite Eq. 2.128 for each linearly independent solution as,

$$\Psi_j = \sum_{i=1}^{N_c} \phi_i(\tau) \frac{1}{r} F_{ij}(r). \tag{2.133}$$

It is convenient to introduce a matrix notation, which simplifies further manipulations. We represent the stationary states of the collision as a matrix $\mathbf{F}$, the matrix elements of which contain only the radial portion of the channel wavefunctions:

$$\mathbf{F}_{ij} = F_{ij}(r). \tag{2.134}$$

There is a one-to-one correspondence between the j'th column of $\mathbf{F}$ and the linearly independent solutions, Ψ_j. For example, we can linearly transform $\mathbf{F}$ to obtain an alternative set of solutions, $\tilde{\mathbf{F}}$, as,

$$\tilde{\mathbf{F}} = \mathbf{F}\mathbf{T}, \tag{2.135}$$

where the columns of the transformation $\mathbf{T}$ are linearly independent [5]. The matrix $\tilde{\mathbf{F}}$ corresponds to an alternative set of linearly independent solutions, $\{\tilde{\Psi}_j\}$, such that,

$$\tilde{\Psi}_j = \textstyle\sum_i^{N_c} \phi_i(\tau) \frac{1}{r} \tilde{F}_{ij}(r) \tag{2.136}$$

$$\tilde{\Psi}_j = \textstyle\sum_{i,j'=1}^{N_c} \phi_i(\tau) \frac{1}{r} F_{ij'}(r) T_{j'j}. \tag{2.137}$$

We define the diagonal matrices $\mathbf{f}$ and $\mathbf{g}$ such that,

$$\mathbf{f}_{ij} = f_{l_i}(\epsilon_i, r)\delta_{ij} \tag{2.138}$$

$$\mathbf{g}_{ij} = g_{l_i}(\epsilon_i, r)\delta_{ij}, \tag{2.139}$$

$$\tag{2.140}$$

where $\epsilon_i = 2(E - E_i)$. By Eq. 2.131, the solution $\mathbf{F}$ can be expressed for $r > r_0$, as a linear

---

[5] In other words, $\mathbf{T}$ is of rank N_c.

combination of **f** and **g**,

$$\mathbf{F}(r > r_0) = \mathbf{fI} - \mathbf{gJ}, \tag{2.141}$$

where

$$\mathbf{I}_{ij} = \pi \left(F_{ij}(r_0) g'_{l_i}(\epsilon_i, r_0) - F'_{ij}(r_0) g_i(\epsilon_i, r_0) \right) \tag{2.142}$$

$$\mathbf{J}_{ij} = \pi \left(F_{ij}(r_0) g'_{l_i}(\epsilon_i, r_0) - F'_{ij}(r_0) g_{l_i}(\epsilon_i, r_0) \right), \tag{2.143}$$

in analogy to Eqs. 2.126 and 2.127. The reaction matrix normalized solutions can be obtained by transforming **F** as,

$$\mathbf{F^K} = \mathbf{FI}^{-1} \tag{2.144}$$

$$= \mathbf{f} - \mathbf{gK}, \tag{2.145}$$

where Eq. 2.145 defines the multichannel reaction matrix as,

$$\mathbf{K} = \mathbf{JI}^{-1}. \tag{2.146}$$

The multichannel quantum defect matrix is obtained from the reaction matrix as,

$$\mu = \frac{1}{\pi} arctan \mathbf{K} \tag{2.147}$$

These two matrices, μ and **K**, are the central constructs of MQDT.

2.4.1 The Case where All Channels are Closed: Bound States

A channel is said to be closed if the channel collision energy, $\epsilon_i < 0$. The physical situation in a closed channel corresponds to scattering at negative energy. We let $\epsilon_i = -\frac{1}{\nu_i^2}$. For all channels closed, the asymptotic limit of the reaction matrix normalized solutions follows from Eqs.2.58 and 2.60 as,

$$\mathbf{F^K}(r \to \infty) = (\mathbf{Si} + \mathbf{CoK}), \tag{2.148}$$

where

$$\mathbf{Si}_{ij} = \frac{1}{\sqrt{2}\pi} e^{r/\nu_i} \left(\frac{2r}{\nu_i}\right)^{-\nu_i} \left(\nu_i \Gamma(\nu_i + l_i + 1)\Gamma(\nu - l_i)\right)^{1/2} sin\pi(\nu_i - l_i)\delta_{ij} \tag{2.149}$$

$$\mathbf{Co}_{ij} = \frac{1}{\sqrt{2}\pi} e^{r/\nu_i} \left(\frac{2r}{\nu_i}\right)^{-\nu_i} \left(\nu_i \Gamma(\nu_i + l_i + 1)\Gamma(\nu - l_i)\right)^{1/2} cos\pi(\nu_i - l_i)\delta_{ij}. \tag{2.150}$$

Let $\mathbf{b}$ denote the column vector for a bound state. The bound state, just as any other state, is given by some linear combination of the general solutions $\mathbf{F}$. We write this linear combination as,

$$\mathbf{b} = \mathbf{F}\mathbf{B}, \tag{2.151}$$

where $\mathbf{B}$ is a column vector. The bound state asymptotic boundary condition requires that the coefficients of the increasing exponentials in Eq. 2.148 must vanish in each channel. This condition leads to the set of equations,

$$\sum_j \left[sin\pi(\nu_i - l)\delta_{ij} + cos\pi(\nu_i - l)\mathbf{K}_{ij}\right]\mathbf{B}_j = 0 \tag{2.152}$$

$$\sum_j \left(tan\pi\nu_i\delta_{ij} + \mathbf{K}_{ij}\right)\mathbf{B}_j = 0. \tag{2.153}$$

Non-trivial solutions to Eq. 2.153 are found at values of ν_i such that,

$$det|tan\pi\nu_i\delta_{ij} + \mathbf{K}_{ij}| = 0. \tag{2.154}$$

Equation 2.154 is the MQDT quantization condition. If we are interested in values of energy that are very far below all ionization thresholds, we can make the approximation

$$\epsilon_i = 2(E - E_i) \approx 2(E - E_0) \approx \epsilon_0, \tag{2.155}$$

for all i, where E_0 denotes the lowest ionization threshold. In this approximation Eq. 2.154 becomes an eigenvalue equation, the solution of which is,

$$tan\pi\nu_0 = -tan\pi\mu_\alpha(\nu_0), \tag{2.156}$$

where $tan\pi\mu_\alpha(\nu_0)$ denotes an eigenvalue of the reaction matrix. The quantities $\mu_\alpha(\nu_0)$ are called the eigenquantum defects. Equation 2.156 implies that,

$$\nu_0 = n - \mu_\alpha(\nu_0) \qquad n = 1, 2 \cdots \infty \tag{2.157}$$

$$E_n = E_0 - \frac{1}{2(n - \mu_\alpha(\nu_0))^2}. \tag{2.158}$$

Equation 2.158 is the generalized Rydberg formula of MQDT and it remains valid far from ionization thresholds. Each different value of α labels a different Rydberg series.

The Lu-Fano Plot

The Lu-Fano plot is an useful device for visualizing channel interactions for the two-channel problem. The Lu-Fano plot can be generalized for more than two channels [6]. However, the reaction matrix is usually used directly to analyze the many-channel problem, because the parametric equations of the Lu-Fano plot become cumbersome and impractical for a fit to experimental data. The Lu-Fano plot finds its full qualitative power in the case of two channels.

The Lu-Fano plot is derived from the MQDT quantization condition in Eq. 2.154. In a first step, the MQDT quantization condition is re-written in a representation in which the reaction matrix is diagonal (the eigenchannel representation). In order to derive this representation, we write Eq. 2.148 as,

$$\mathbf{F^K} = \mathbf{Si} - \mathbf{CoU}tan\pi\mu_\alpha\mathbf{U}^T, \tag{2.159}$$

where the columns of $\mathbf{U}$ are the eigenvectors of the reaction matrix. The eigenchannel representation is obtained by transforming $\mathbf{F^K}$ as,

$$\mathbf{F}^\alpha = \mathbf{F^K}\mathbf{U}cos\pi\mu_\alpha \tag{2.160}$$

$$= \mathbf{SiU}cos\pi\mu_\alpha + \mathbf{CoU}sin\pi\mu_\alpha. \tag{2.161}$$

---

[6] An example is provided in **Chapter 1**, where the Lu-Fano plot is constructed for five of the Rydberg channels of the Xe atom.

In component form, the eigenchannels can be written as,

$$\mathbf{F}_{ij}^{\alpha} = \frac{1}{\sqrt{2\pi}} e^{r/\nu_i} \left(\frac{2r}{\nu_i}\right)^{-\nu_i} \left(\nu_i \Gamma(\nu_i + l_i + 1)\Gamma(\nu - l_i)\right)^{1/2} \mathbf{U}_{i\alpha} sin\pi(\nu_i - l_i + \pi\mu_\alpha). \quad (2.162)$$

The vanishing boundary condition imposed at $r = \infty$ yields the form of the MQDT quantization condition that is used to generate the Lu-Fano plot [7],

$$det|\mathbf{U}_{i\alpha} sin\pi(\nu_i + \pi\mu_\alpha)| = 0. \quad (2.163)$$

For the two-channel problem, the orthogonal eigenvectors of the reaction matrix can be written as

$$\mathbf{U}_1 = \begin{pmatrix} cos\theta \\ sin\theta \end{pmatrix} \quad (2.164)$$

$$\mathbf{U}_2 = \begin{pmatrix} -sin\theta \\ cos\theta \end{pmatrix}, \quad (2.165)$$

where θ is interpreted as a rotation angle in channel space. From Eqs. 2.164 and 2.165, we can write the quantization condition explicitly as,

$$F(\nu_2, \nu_1) = cos^2\theta sin\pi(\nu_1 + \mu_{\alpha_1}) sin\pi(\nu_2 + \mu_{\alpha_2}) + sin^2\theta sin\pi(\nu_1 + \mu_{\alpha_2}) sin\pi(\nu_2 + \mu_{\alpha_1}) = 0. \quad (2.166)$$

For each given bound state with energy E_n, we can define two effective principal quantum numbers as,

$$n_1 = \sqrt{\frac{1}{2(E_1 - E_n)}} \quad (2.167)$$

$$n_2 = \sqrt{\frac{1}{2(E_2 - E_n)}}, \quad (2.168)$$

where E_1 and E_2 are the ionization thresholds for channels 1 and 2. In the (ν_1, ν_2) plane, the point (n_1, n_2) must lie on the curve defined by the set of points (ν_1, ν_2) that satisfy the quantization condition in Eq. 2.166. Equation 2.166 implies that the plot of $F(\nu_1, \nu_2)$ is periodic in squares of unit side length in the (ν_1, ν_2) plane. That is, the value of $F(\nu_1, \nu_2)$ is

---

[7] We do not need to include l_i in Eq. 2.163, because l_i is an integer

the same at the point (ν_1', ν_2') such that $\nu_1' = \nu_1 + 1$ and $\nu_2' = \nu_2 + 1$. Then, it is sufficient to plot $F(\nu_2, \nu_1)$ within the first quadrant unit square [8] to describe the entire spectrum. This requires that the principal quantum numbers determined from the spectrum are evaluated modulo one:

$$n_1 = mod(\sqrt{\frac{1}{2(E_1 - E_n)}}, 1) \tag{2.169}$$

$$n_2 = mod(\sqrt{\frac{1}{2(E_2 - E_n)}}, 1). \tag{2.170}$$

When the two principal quantum numbers are defined modulo one, the negative of the principal quantum number, $-\nu_1$, is the quantum defect, μ_1, in the first channel. The Lu-Fano plot is typically constructed from the set of points (ν_2, μ_1) that satisfy $F(\nu_2, \mu_1 = -\nu_1) = 0$ in the first quadrant. Lu-Fano plots for four different values of the rotation angle, θ, and fixed eigenquantum defect values $\mu_{\alpha_1} = 0.4$ and $\mu_{\alpha_2} = 0.6$ are shown in Fig. 2-9. When $\theta = 0$, the Lu-Fano plot consists of a vertical and a horizontal branch that cross through each other. This implies a constant quantum defect for the two ionization channels in the absence of channel interaction and mixing. When $\theta \neq 0$, the quantum defect varies in both the vertical and horizontal branches resulting in the appearance of an avoided crossing between the two branches. The non-constant values of the quantum defects imply that the two ionization channels are strongly mixed on the curved portions of the plot.

Figures 2-9B and C demonstrate that the gap between the two branches increases as θ increases toward $\pi/4$. A value of $\theta = \pi/4$ implies that the two channels are completely mixed, as can be inferred from Eqs. 2.164 and 2.165. The eigenchannel decomposition begins to return to the uncoupled channel limit as θ increases above $\pi/4$ toward a value of $\pi/2$. This is the reason for the appearance of a smaller gap in Fig 2-9C for $\theta = 3\pi/8$. The Lu-Fano plot reduces to the two vertical branches shown in Fig. 2-9A at $\theta = \pi/2$. Clearly, the gap between the two branches in the Lu-Fano plot provides a visual estimate of the channel interaction strength.

The quantum defect parameters can be obtained from the Lu-Fano plot by the following device. At the points such that $\nu_1 = \nu_2 = -\mu_1$, Eq. 2.166 is satisfied when $\mu_1 = \mu_{\alpha_1}$ or

---

[8] The first quadrant unit square is chosen by convention. Sometimes it is more instructive to use the interval [-1/2, 1/2] rather than [0, 1], especially when nonpenetrating states lie close to integer principal quantum numbers.

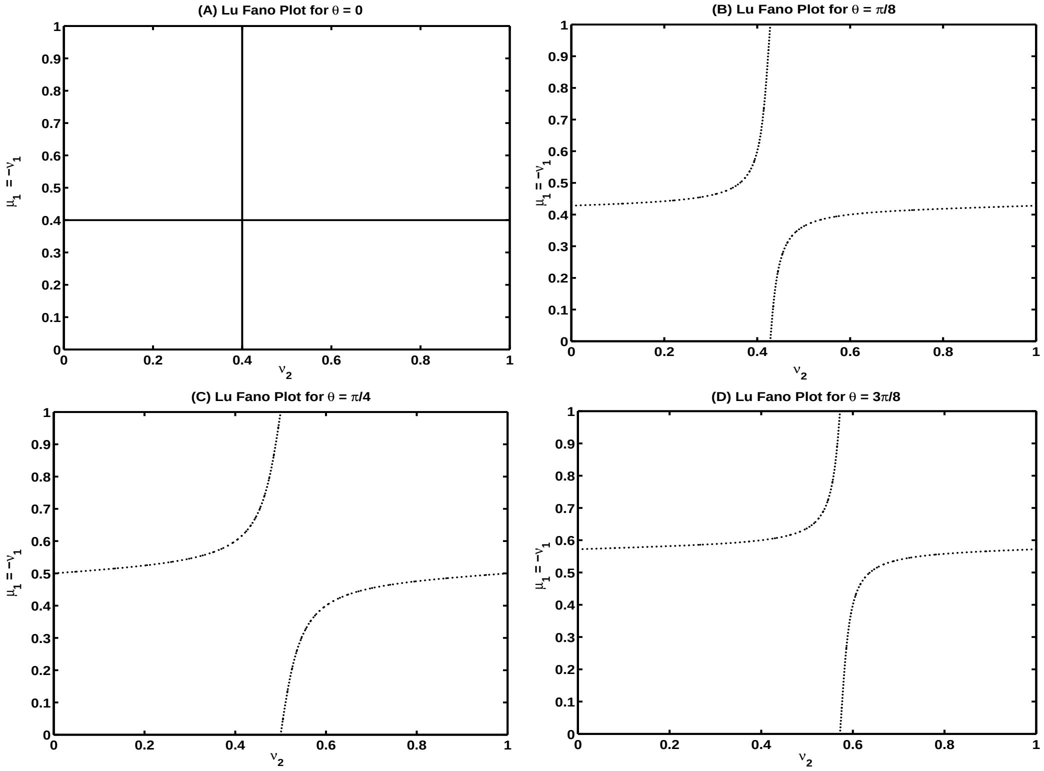

Figure 2-9: Lu-Fano Plots calculated for eigenquantum defects $\mu_{\alpha_1} = 0.6$ and $\mu_{\alpha_2} = 0.4$. (A) The Lu-Fano plot for $\theta = 0$. In this case of a vanishing rotation angle, the channels do not interact and the Lu-Fano plot consists of a horizontal and a vertical branch that depict constant quantum defects in the two ionization channels. (B) The Lu-Fano plot for $\theta = \pi/8$. A non-zero value of the rotation angle results in a Lu-Fano plot with curvature in both branches. The curvature and the non-zero slope in the branches depict energy dependences of the quantum defects in the two ionization channels. These energy dependences are a consequence of channel interactions and mixings. The slope at each point on the Lu-Fano plot is equal to the amplitude squared ratio of the ionization channels in the collision stationary state. Maximal channel mixing occurs at the inflection points on the graph. The magnitude of the repulsion between the two branches at the avoided crossing is proportional to the off-diagonal matrix element of the reaction matrix. (C) The Lu-Fano plot for $\theta = \pi/4$. The magnitude of the gap at the avoided crossing is larger than the magnitude of the gap at the avoided crossing visible in (B). This implies a stronger channel coupling at this value of θ. (D) The Lu-Fano plot for $\theta = 3\pi/8$. The channel interaction is weaker for this case than the interaction in (C), as evidenced by the smaller gap at the avoided crossing. The channel interactions get weaker as θ approaches the uncoupled channel limit, $\theta = \pi/2$.

$\mu_1 = \mu_{\alpha_2}$. Thus the eigenquantum defects can be determined from the ordinates of the intersection of the curve $F(\nu_2, \mu_1) = 0$ with the main diagonal $\mu_1 = -\nu_2$. The derivative of the quantum defect with respect to ν_2 is obtained from Eq. 2.166 as,

$$\frac{\partial \mu_1}{\partial \nu_2} = \frac{cos^2\theta sin\pi(\nu_1 + \mu_{\alpha_1})cos\pi(\nu_2 + \mu_{\alpha_2}) + sin^2\theta sin\pi(\nu_1 + \mu_{\alpha_2})cos\pi(\nu_2 + \mu_{\alpha_1})}{cos^2\theta cos\pi(\nu_1 + \mu_{\alpha_1})sin\pi(\nu_2 + \mu_{\alpha_2}) + sin^2\theta sin\pi(\nu_2 + \mu_{\alpha_1})cos\pi(\nu_1 + \mu_{\alpha_1})}. \quad (2.171)$$

It follows from Eq. 2.171 that the slope of the quantum defect with respect to ν_2 is equal to $tan^2\theta$ and $\cot^2\theta$ at the two intersections of the Lu-Fano plot with the main diagonal. Therefore,

$$\theta = arctan\left(\frac{\partial \mu_1}{\partial \nu_2}\right)^{1/2}|_{\nu_1=\nu_2=-\mu_{\alpha_1}} \qquad or \quad (2.172)$$

$$\theta = arccot\left(\frac{\partial \mu_1}{\partial \nu_2}\right)^{1/2}|_{\nu_1=\nu_2=-\mu_{\alpha_2}}. \quad (2.173)$$

Using Eqs. 2.172 and 2.173, the reaction matrix can be determined from a graphical analysis of the Lu-Fano plot. Fano [112] shows that the slope of Eq. 2.171 at any point (ν_2, μ_1) on the $F(\nu_2, \mu_1) = 0$ curve may be interpreted as the ratio of the amplitudes (or the fractional characters) of the two fragmentation channels in the collision eigenchannel. This ratio, sometimes called the branching ratio, is given as,

$$\frac{\partial \mu_1}{\partial \nu_2} = \left(\frac{Z_2}{Z_1}\right)^2. \quad (2.174)$$

Thus, when a branch is horizontal all of the amplitude is in the first channel whereas when a branch is vertical all the amplitude is in the second channel. In the general case when the Lu-Fano plot has curvature, the magnitudes of the slopes at various points yield the branching ratios into the two fragmentation channels. The inflection points mark the states for which the channels are maximally mixed. This mathematical result forms the basis for much of the qualitative discussion in **Chapter 1**.

The magnitudes of the gaps at the avoided crossings (the repulsion between the two branches) shown in Figs.2-9B-D are proportional to the off-diagonal matrix element of the reaction matrix [41]. The gap is quantitatively measured as the difference between the abscissa at the inflection point to the abscissa at the point of closest approach of the two branches [41]. The tangent of π times this distance yields the off-diagonal element of the reaction matrix in a phase-renormalized representation [41]. The graphical analysis for determining the quantum defect parameters from the Lu-Fano plot is outlined on the expanded view of Fig. 2-9 shown in Fig. 2-10.

2.4.2 The Case for All Channels Open: Continuum

A collision channel is said to be open if the collision energy $\epsilon_i > 0$. We let $k_i^2 = \epsilon_i$. For all channels open, the reaction matrix normalized solutions in Eq. 2.141 can be expressed as,

$$\begin{aligned}
\mathbf{F}^K(r > r_0) &= \mathbf{f} - \mathbf{g}\mathbf{K} && (2.175)\\
&= -\tfrac{1}{2i}\left((-\mathbf{g} - i\mathbf{f})(\mathbf{I} - i\mathbf{K}) - (-\mathbf{g} + i\mathbf{f})(\mathbf{I} + i\mathbf{K})\right) && (2.176)\\
&= -\tfrac{1}{2i}\left(\underline{\psi}^-(\mathbf{I} - i\mathbf{K}) - \underline{\psi}^+(\mathbf{I} + i\mathbf{K})\right), && (2.177)
\end{aligned}$$

where $\mathbf{I}$ is an N_c dimensional identity matrix and $\underline{\psi}^\pm$ denote diagonal matrices of functions, the diagonal elements of which correspond to $\psi_{l_i}^\pm(\epsilon_i, r)$. The scattering solutions are obtained by transforming $\mathbf{F}^\mathbf{K}$ as,

$$\begin{aligned}
\mathbf{F}^\mathbf{S} &= -2i\mathbf{F}^K(\mathbf{I} - i\mathbf{K})^{-1} && (2.178)\\
&= \underline{\psi}^- - \underline{\psi}^+(\mathbf{I} + i\mathbf{K})(\mathbf{I} - i\mathbf{K})^{-1} && (2.179)\\
&= \underline{\psi}^- - \underline{\psi}^+\mathbf{S}. && (2.180)
\end{aligned}$$

Equation 2.180 defines the multichannel scattering matrix as,

$$\mathbf{S} = (\mathbf{I} + i\mathbf{K})(\mathbf{I} - i\mathbf{K})^{-1}, \qquad (2.181)$$

which is the multichannel generalization of Eq. 2.123. By definition we can express the reaction matrix as,

$$\mathbf{K} = \mathbf{U} tan\pi\mu_\alpha \mathbf{U}^T, \qquad (2.182)$$

where $\mathbf{U}$ is the orthogonal matrix of eigenvectors and $tan\pi\mu_\alpha$ is the diagonal matrix of eigenvalues of the reaction matrix. The eigenquantum defect, μ_α, was defined in Section 2.4.1. From the factorization of the reaction matrix in Eq. 2.182, we can rewrite,

$$\begin{aligned}
(\mathbf{I} + i\mathbf{K}) &= \mathbf{U} e^{i\pi\mu_\alpha} cos\pi\mu_\alpha \mathbf{U}^T && (2.183)\\
(\mathbf{I} - i\mathbf{K})^{-1} &= \mathbf{U}^T cos\pi\mu_\alpha^{-1} e^{i\pi\mu_\alpha} \mathbf{U}. && (2.184)
\end{aligned}$$

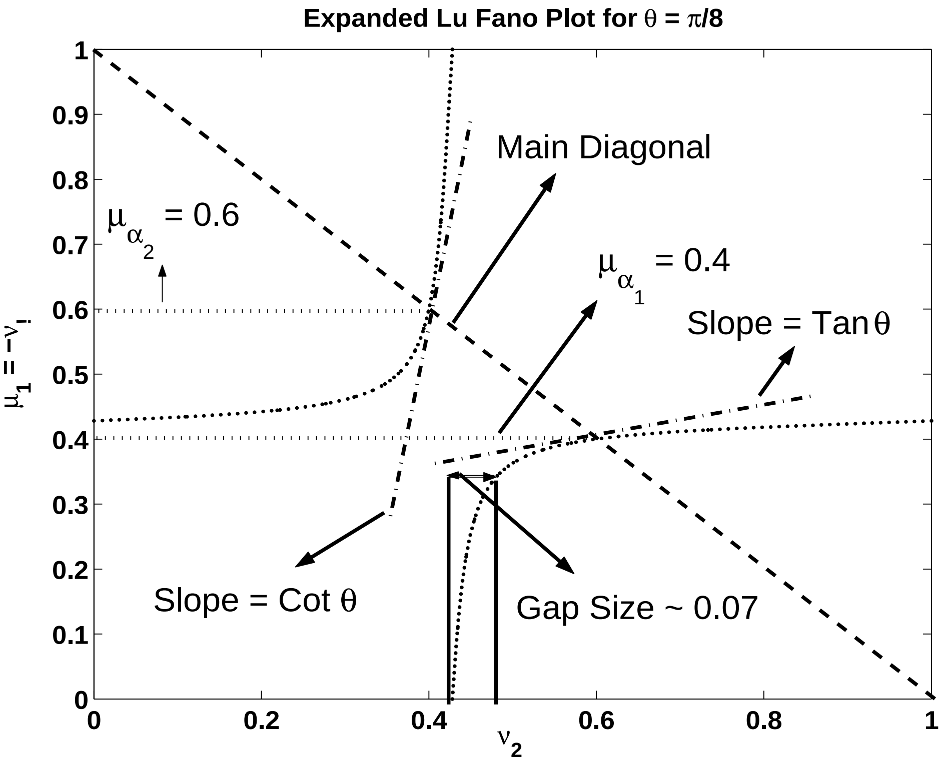

Figure 2-10: The graphical analysis for determining the quantum defect parameters from the Lu-Fano plot. The eigenquantum defects are equal to the ordinates of the intersections of the main diagonal with the two branches of the Lu-Fano plot. The slopes of the tangent lines to the Lu-Fano plot at the two intersection points are $cot\theta$ for $\nu_2 = -\nu_1 = \mu_{\alpha_2}$ and $tan\theta$ for $\nu_2 = -\nu_1 = \mu_{\alpha_1}$. Therefore, the rotation angle can be determined from the slope of the tangent line at either of the intersection points. As marked in the plot, the gap is measured as the difference between the abscissa at the inflection point of the lower branch to the abscissa at the point of closest approach of the two branches. The tangent of π times this value gives the off-diagonal element of the reaction matrix in a special phase-renormalized form. This form of the reaction matrix is derived in reference [41].

From Eqs. 2.183 and 2.184, an alternate definition of the symmetric scattering matrix is obtained as,

$$\mathbf{S} = \mathbf{U} e^{2i\pi\mu_\alpha} \mathbf{U}^T, \tag{2.185}$$

which is also the multichannel generalization of Eq. 2.123 in terms of the scattering phase shifts. The amplitude-squared elements of the scattering matrix, $|\mathbf{S}|^2_{ij}$, are interpreted as the probability amplitude for a transition from an incoming channel j of the system to an outgoing channel i, after the collision of the electron with the ion-core [9]. The scattering observables such as the differential and integral cross sections can be computed from the scattering matrix, following the procedure outlined in Section 2.2.8.

2.4.3 The Case of a Mixture of Closed and Open Channels: Autoionizing Resonances

In the case of a mixture of closed and open channels, vanishing asymptotic boundary conditions must be imposed in the closed channels whereas incoming/outgoing wave asymptotic boundary conditions must be imposed in the open channels. The use of bound state boundary conditions in the closed channels results in occurrences of poles of the scattering matrix that lie on the fourth quadrant in the complex-E plane. These types of poles of the scattering matrix are known as Feshbach resonances and they correspond to quasi-bound levels that exist for finite amounts of time before decaying into an adjacent continuum [10]. This process, which is illustrated in Fig. 2-11, is called autoionization in MQDT. A related process is predissociation, which arises in molecular applications of MQDT. Predissociation is the fragmentation of the molecule into two separated atoms and it is a consequence of the interaction of Rydberg states with a repulsive valence electronic state. The mathematical

---

[9] In other words, $|\mathbf{S}|^2_{ij}$ is the probability amplitude for electron impact excitation from j to i.

[10] In reality, all states accessible by the experiment are quasi-bound states in the sense of the true Hamiltonian of the system. The true Hamiltonian of the system differs from the Hamiltonian for the isolated system that we use in the quantum mechanical calculations. The true Hamiltonian involves infinitely many degrees of freedom due to external perturbations such as collision of the molecule with other molecules in the container or with the walls of the container. These types of perturbations can be rigorously accounted for by a statistical treatment. Nevertheless, we can include the external perturbations in the isolated model if we accept that all states are quasi-bound states with a finite natural life-time. A rigorous analysis of the natural life-time is not attempted in this thesis, but there are many treatments available elsewhere. However, we note that the natural life-times are typically much longer than the life-times of the autoionizing resonances described here. Exceptions might arise under extreme experimental conditions of temperature and pressure.

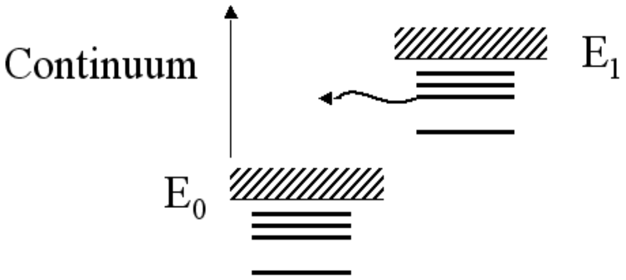

Figure 2-11: A schematic representation of autoionizing resonances. The Rydberg states converging to an ionization threshold with energy E_1 (an excited state of the ion-core) interact with the continuum above a lower ionization threshold with energy E_0. The coupling to the continuum causes the Rydberg levels to become quasi-bound states that exist for finite amounts of time. They autoionize by decaying into the adjacent continuum. Autoionizing resonances appear as broadened lines in Rydberg spectra.

analysis of both types of Feshbach resonances are identical. We return to this topic after introducing resonance scattering theory in Section 2.5.

2.4.4 The Frame Transformation

In this section, we specialize to the molecular applications of MQDT. The molecular applications require the full machinery of the multichannel theory, because even for elastic scattering, the problem is of a multichannel nature due to the nonspherical nature of the molecular ion-core and orbital angular momentum mixing [11] . The inelastic processes arise from the rovibrational channel interactions that result in exchange of energy between the Rydberg electron and the ro-vibrational degrees of freedom. The stationary state of the collision is given by Eq. 2.133, while each channel is associated with a set of quantum

---

[11] In some molecular applications, the orbital angular momentum quantum number of the Rydberg electron is assumed to be approximately conserved. This is the case in the H_2 example presented in **Chapter 1**. Such an assumption is a poor approximation for polar or non-planar molecules.

numbers that describe the internal state of the core and the orbital angular momentum for the departing electron. For a diatomic molecule with a case (b) ion-core, these quantum numbers can be written as,

$$i \equiv \left\{v^+, N^+, n^+, \Lambda^+, l_i, \eta^+\right\}, \tag{2.186}$$

where the superscript + denotes quantum numbers that describe the quantum state of the ion-core. These quantum numbers include, the vibrational quantum number (v^+), the rotational quantum number(N^+), the quantum number for the electronic state of the ion-core (n^+), and the projection of the ion-core orbital angular momentum on the internuclear axis (Λ^+). On the other hand, l_i is the value of the orbital angular momentum quantum number of the Rydberg electron in the specified channel, i. The quantum number $\eta = \pm 1$ is a symmetry index that yields the parity eigenvalue for the overall state of the ion-core as,

$$I|v^+, N^+, n^+, \eta^+) = \eta^+(-1)^{N^+}|v^+, N^+, n^+, \eta^+). \tag{2.187}$$

A detailed explanation of the symmetry index, η, is provided in **Chapter 1**, Eqs. 1.19-1.23. The internal state for the $i'th$ channel can be written as,

$$\begin{aligned}\phi_i \equiv \sum_m Y_{l_i m}(\theta,\phi)\left(|\Lambda^+)D^{N^+}_{\Lambda^+,M-m} + \eta^+|-\Lambda^+)D^{N^+}_{-\Lambda^+,M-m}\right)\frac{1}{R}X^{n^+,\Lambda^+,N^+}_{v^+}(R)\\ \times(l_i M N^+ M-m|NM)\left(\frac{2N^+ + 1}{8\pi^2 + \delta_{\Lambda^+0}}\right)^{\frac{1}{2}},\end{aligned}$$

where R is the internuclear distance and $\frac{1}{R}X^{n^+,\Lambda^+,N^+}_{v^+}(R)$ is a vibrational wavefunction that depends on the electronic-rotation state of the ion-core. For low energy scattering, electronic excitation of the ion-core by electron impact can be neglected and Λ^+, n^+ can be taken as conserved quantities. Typically, these quantum numbers would denote the ground electronic state of the ion-core. The definition, ϕ_i of the channel internal state yields a long-range reaction matrix for each value of the conserved quantities, $\eta^+, N, \Lambda^+, n^+$ as,

$$\mathbf{K}_{ij} = \mathbf{K}^{N,\eta^+,\Lambda^+,n^+}_{l_i N^+ v^+, l_j N^{+\prime} v^{+\prime}}. \tag{2.188}$$

Theoretically, the long-range reaction matrix can be computed using Eqs. 2.141 and 2.146. However, this turns out to be exceedingly difficult in practice. The difficulty arises from the evaluation of the potential energy matrix elements in Eq. 2.130 that requires an integration over functions, which are expressed in a mixture of body fixed and space-fixed coordinates. These integrations would simplify if the stationary state of the collision could somehow be expressed purely in body-fixed coordinates. In other words, we seek a Born-Oppenheimer factorization of the collision stationary state, so that the powerful integration methods of quantum chemistry can be employed in the reaction matrix calculation. The Born-Oppenheimer factorization of the collision stationary state is made possible by the principle of frame transformation [30, 64]. For this reason, the frame transformation forms the essential link between quantum defect theory and ordinary quantum chemistry. The frame transformation is based on the observation that there exists a region of space, characterized by electronic distances $r_0 < r < r_2$, such that all interactions are Coulombic and the electron is sufficiently close to the ion-core as to permit the Born-Oppenheimer approximation to be valid. The various electronic distances that depict the range of validity of the Born-Oppenheimer approximation and the fragmentation limit in which Eq. 2.186 applies, are diagrammatically shown in Fig. 2-12. In the Born-Oppenheimer region, we define short-range channels of the form,

$$s \equiv \left\{l_s, \lambda, \Lambda^+, n^+, \eta\right\}, \tag{2.189}$$

where λ is the projection of l_i on the internuclear axis and η is an alternate symmetry index used in the definition of the short-range internal states. The short-range internal states are defined as,

$$\phi_s \equiv \left(Y_{l\lambda}(\theta', \phi')|\Lambda^+)D^N_{\lambda+\Lambda^+M} + \eta Y_{l-\lambda}(\theta', \phi')| - \Lambda^+)D^N_{-\lambda-\Lambda^+M}\right) \frac{X^{n^+,\Lambda^+,N^+}_{v^+}(R)}{R} \left(\frac{2N+1}{8\pi^2 + \delta_{\Lambda^+0}\delta_{\lambda 0}}\right)^{\frac{1}{2}}, \tag{2.190}$$

and the channel energy is given by $\epsilon_s = 2(E_s - E)$. Next, we assume that the spacings between the ro-vibrational levels of the ion-core are small in comparison to the electronic binding energy. Therefore, we drop the s subscript on ϵ and approximate,

$$\epsilon_s \approx \epsilon_0 \approx \epsilon, \tag{2.191}$$

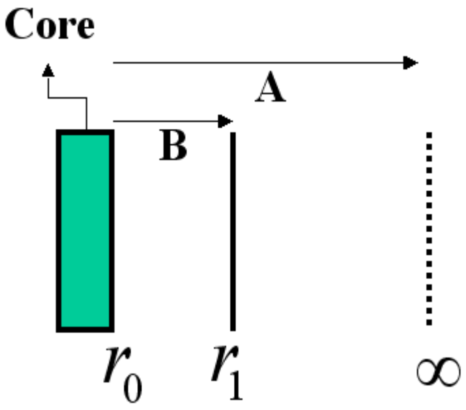

Figure 2-12: Electronic radial distances characterizing the frame transformation. The core is in the range $0 < r < r_0$. In this region, complicated many-body interactions prevail and there is no simple description of the Rydberg electron's motion. When $r > r_0$ all interactions between the ion-core and the electron are Coulombic. The region labeled B is characterized by electronic radial distances such that $r_0 < r < r_1$. In this region, the electron is sufficiently close to the ion-core as to permit the Born-Oppenheimer approximation to be valid. Therefore the channel wavefunction can be expressed using body-fixed coordinates in terms of a Born-Oppenheimer factorization (short-range channel wavefunction). The analytic form of this wavefunction is known since all interactions are Coulombic. Beyond r_1, the electronic kinetic energy becomes smaller than the rovibrational energy spacings of the core, rendering the Born-Oppenheimer assumption invalid. The region labeled A is characterized by radial distances such that $r > r_0$. In this range, the long-range representation in terms of the fragmentation channels in Eq. 2.186 is valid. The long-range representation does not assume a Born-Oppenheimer factorization. Regions A and B overlap in the interval $r_0 < r < r_1$. In this overlap region, the short-range channel wavefunction can be transformed to the form of the long-range wavefunction. The equations of this transformation that connect the two representations are called frame transformation equations, since they involve coordinate transformations from body-fixed to space-fixed coordinates.

for all s. In Eq. 2.191, $\epsilon_0 = E_0 - E$, where E_0 is the energy of the ion-core ground state. The short-range channel internal state yields the definition of the short-range reaction matrix as,

$$\mathbf{K}_{st}(R) = \mathbf{K}_{l_s\lambda_s l_t\lambda_t}(R)\delta_{\lambda_s\lambda_t}. \tag{2.192}$$

The short-range reaction matrix depends parametrically on the internuclear distance and it is an appropriate subject for an electronic structure calculation. In order to make the connection to the long-range representation, we expand the collision stationary state in the Born-Oppenheimer region as,

$$\begin{aligned}
\Psi_t(\tau) &= \textstyle\sum_s \phi_s F_{st}(r_0 < r < r_1) && (2.193)\\
&= \textstyle\sum_s \phi_s \left(f_{l_s}(\epsilon, r)\delta_{st} - g_{l_s}(\epsilon, r)\mathbf{K}_{st}(R)\right) && (2.194)\\
&= \textstyle\sum_i \phi_i f_{l_t}(\epsilon, r)(\phi_i|\phi_t) - \sum_i \phi_i \sum_s g_{l_s}(\epsilon, r)(\phi_i|\mathbf{K}_{st}(R)|\phi_s). && (2.195)
\end{aligned}$$

Next, we transform Eq. 2.195 as,

$$\begin{aligned}
\Psi_j(\tau) &= \textstyle\sum_t \Psi_t(\tau)(\phi_t|\phi_j) && (2.196)\\
&= \textstyle\sum_{it} \phi_i f_{l_t}(\epsilon, r)(\phi_i|\phi_t)(\phi_t|\phi_j) - \sum_i \phi_i \sum_{ts} g_{l_s}(\epsilon, r)(\phi_i|\mathbf{K}_{st}(R)|\phi_s)(\phi_t|\phi_j) && (2.197)\\
&= \textstyle\sum_i \phi_i \left(f_{l_i}(\epsilon_i, r)\delta_{ij} - g_{l_i}(\epsilon_i, r)\sum_{ts}(\phi_i|\mathbf{K}_{st}(R)|\phi_s)(\phi_t|\phi_j)\right). && (2.198)
\end{aligned}$$

Equation 2.198 follows from Eq. 2.197 because of Eq. 2.191 and the result that $(\phi_i|\mathbf{K}_{st}(R)|\phi_s) = 0$ unless $l_i = l_s$. Equation 2.198 defines the long-range reaction matrix in terms of the short-range matrix as,

$$\mathbf{K}_{ij} = \sum_{ts}(\phi_i|\mathbf{K}_{st}(R)|\phi_s)(\phi_t|\phi_j). \tag{2.199}$$

An explicit form for the long-range reaction matrix is derived using the definitions of ϕ_i and ϕ_s to yield,

$$\mathbf{K}^{N,\eta^+,\lambda^+,n^+}_{l_iN^+v^+,l_jN^{+'}v^{+'}} = \sum_\lambda (N^+|\lambda)^{l_iN^+\eta+\Lambda^+\eta\lambda N}(v^+|K_{l_i,l_j,\lambda}(R)|v^{+'})(\lambda|N^{+'})^{l_jN^{+'}\eta+\Lambda^+\eta\lambda N} \tag{2.200}$$

where,

$$(v^+|K_{l_i,l_j,\lambda}(R)|v^{+'}) = \int dR X^{n^+,\Lambda^+,N^+}_{v^+}(R)K_{l_i,l_j,\lambda}(R)X^{n^+,\Lambda^+,N^{+'}}_{v^{+'}}(R) \tag{2.201}$$

and,

$$(\lambda|N^+)^{lN^{+'}\eta+\Lambda^+\eta\lambda N} = (l\lambda, N^+\Lambda^+|lN^+N\Lambda)\frac{(2N^++1)^{1/2}}{(2N+1)^{1/2}}\frac{1+\eta\eta^+(-1)^{N-l-N^+}}{2}. \quad (2.202)$$

Equation 2.200 constitutes the ro-vibrational frame transformation. The frame transformation relation implies that *all* ro-vibrational channel interactions embodied by the long-range reaction matrix can be determined from knowledge of the short-range reaction matrix. Therefore, *ab initio* reaction matrix calculations aim to compute the short-range reaction matrix and they make use of the clamped-nuclei (Born-Oppenheimer) approximation.

Several useful approximations of the frame transformation can be obtained. First, if the inter-nuclear motion is neglected, Eq. 2.200 simplifies to,

$$\mathbf{K}^{N,\eta^+,\lambda^+,n^+}_{l_iN^+,l_jN^{+'}} = \sum_{\lambda}(N^+|\lambda)^{l_iN^+\eta+\Lambda^+\eta\lambda N}K_{l_i,l_j,\lambda}(R_{eq})(\lambda|N^{+'})^{l_jN^{+'}\eta+\Lambda^+\eta\lambda N}, \quad (2.203)$$

where R_{eq} is the equilibrium internuclear distance of the ion-core in its specified electronic state. The reduced frame transformation in Eq.2.203 is often sufficient to study electron-rotation interactions (i.e. l-uncoupling). Building from this result, we can include small oscillations of the nuclei about the equilibrium geometry by expanding to first order in R,

$$\begin{aligned}
\mathbf{K}^{N,\eta^+,\lambda^+,n^+}_{l_iN^+v^+,l_jN^{+'}v^{+'}} &= \textstyle\sum_{\lambda}(N^+|\lambda)^{l_iN^+\eta+\Lambda^+\eta\lambda N}K_{l_i,l_j,\lambda}(R_{eq})(\lambda|N^{+'})^{l_jN^{+'}\eta+\Lambda^+\eta\lambda N}\delta_{v^+v^{+'}} \\
&+\textstyle\sum_{\lambda}(N^+|\lambda)^{l_iN^+\eta+\Lambda^+\eta\lambda N}\frac{\partial K_{l_i,l_j,\lambda}(R_{eq})}{\partial R}(\lambda|N^{+'})^{l_jN^{+'}\eta+\Lambda^+\eta\lambda N}(v^{+'}|(R-R_{eq})|v^+) \\
&= \textstyle\sum_{\lambda}(N^+|\lambda)^{l_iN^+\eta+\Lambda^+\eta\lambda N}K_{l_i,l_j,\lambda}(R_{eq})(\lambda|N^{+'})^{l_jN^{+'}\eta+\Lambda^+\eta\lambda N}\delta_{v^+v^{+'}} \\
&+\textstyle\sum_{\lambda}(N^+|\lambda)^{l_iN^+\eta+\Lambda^+\eta\lambda N}\frac{\partial K_{l_i,l_j,\lambda}(R_{eq})}{\partial R}(\lambda|N^{+'})^{l_jN^{+'}\eta+\Lambda^+\eta\lambda N} \\
&\times\frac{1}{\sqrt{2\mu_{nuc}\omega_e^+}}\left(\sqrt{v^++1}\,\delta_{(v^++1)v^{+'}}+\sqrt{v^+}\,\delta_{(v^+-1)v^{+'}}\right),
\end{aligned}$$

where μ_{nuc} is the reduced nuclear mass and ω_e^+ is the ion-core vibrational frequency. This expression of the frame transformation can employed in a fit of the quantum defect parameters (the reaction matrix) to experimental data, which samples electron-vibration channel interactions but is insensitive to the energy dependence of the short-range reaction matrix. In the absence of resonances, we can also write an explicit energy dependence of the short-range reaction matrix by expanding about the binding energy $\epsilon = 0$ to first order in ϵ. This yields,

$$\begin{gathered}
\mathbf{K}^{N,\eta^+,\lambda^+,n^+}_{l_iN^+v^+,l_jN^{+\prime}v^{+\prime}} = \\
\textstyle\sum_\lambda (N^+|\lambda)^{l_iN^+\eta+\Lambda^+\eta\lambda N} \left(K_{l_i,l_j,\lambda}(R_{eq}) + \frac{\partial K_{l_i,l_j,\lambda}(R_{eq})}{\partial \epsilon}\epsilon \right) (\lambda|N^{+\prime})^{l_jN^{+\prime}\eta+\Lambda^+\eta\lambda N} \delta_{v^+v^{+\prime}} \\
+ \textstyle\sum_\lambda (N^+|\lambda)^{l_iN^+\eta+\Lambda^+\eta\lambda N} \frac{\partial K_{l_i,l_j,\lambda}(R_{eq})}{\partial R} (\lambda|N^{+\prime})^{l_jN^{+\prime}\eta+\Lambda^+\eta\lambda N} \\
\times \frac{1}{\sqrt{2\mu_{nuc}\omega_e^+}} \left(\sqrt{v^+ + 1}\,\delta_{(v^+ +1)v^{+\prime}} + \sqrt{v^+}\,\delta_{(v^+ -1)v^{+\prime}} \right),
\end{gathered}$$

This expression can be employed in the fit if there is sufficient data to sample energy dependences. However, the formula becomes inadequate for a fit in the presence of shape and Feshbach resonances. In such cases, resonance formulas that describe the explicit energy dependences of elements of the reaction matrix must be used. These resonance formulas are derived in Section 2.5.

The Molecular Eigenquantum Defects

The asymptotic limits of the Born-Oppenheimer factorized collision stationary states are,

$$\mathbf{F} = \mathbf{f}(\epsilon, r) - \mathbf{g}(\epsilon, r)\mathbf{K}(R), \tag{2.204}$$

where $\mathbf{K}(R)$ is the short-range reaction matrix. Application of the asymptotic boundary conditions for bound states to Eq. 2.204 yields, from Eqs.2.157 and 2.158, the Rydberg formula,

$$E_n(R) = E_0(R) - \frac{1}{2(n - \mu_\alpha(n, R))^2}, \tag{2.205}$$

where $E_0(R)$ is the energy of the ion-core ground electronic state and $\mu_\alpha(n, R)$ is the molecular eigenquantum defect. The R-dependence of the eigenquantum defect follows from the R-dependence of the short-range reaction matrix. In Eq. 2.205, the values of $E_0(R)$ as a function of R form the potential energy curve for the ground electronic state of the ion, whereas $E_n(R)$ is the potential energy curve for the $n'th$ excited electronic state within a given Rydberg series (labeled by α) of the neutral molecule. The eigenquantum defects can be obtained by inverting Eq. 2.205, if the potential curves $E_n(R)$ and $E_0(R)$ are known. These curves can be determined from a standard electronic structure calculation. There are several difficulties associated with this kind of approach that must be mentioned.

First, the potential energy curves, $E_n(R)$, obtained from the output of a high-level electronic structure code, such as *Gausian 03*, become increasingly more inaccurate for higher electronic states. The inaccuracy arises from the divergent nature of the density of electronic states near ionization thresholds, which cannot be reproduced by an expansion of the electronic wavefunction over a finite basis, as is the case in a variational calculation. One can assume that the eigenquantum defects have a very weak and linear energy dependence, as for the eigenquantum defects of the Li atom calculated in Section 2.3.4. Then, the eigenquantum defects as a function of energy can be calculated from the lowest few excited electronic states of the molecule, which are accurately determined by the quantum chemistry code. However, the weak energy dependence assumption is again violated in the presence of resonances.

An additional difficulty is that the inversion of the molecular potential curves yields only the eigenquantum defects of the reaction matrix, but not its eigenvectors. The full short-range reaction matrix must be known for the purposes of the frame transformation and the analysis of the ro-vibrational channel interactions. The energy eigenvalues $E_n(R)$ may potentially be used in a fit that employs the MQDT quantization condition to determine the multidimensional reaction matrix. However, such a fit is likely to suffer from convergence problems in high dimensional problems, without a good initial guess for the reaction matrix. In light of these difficulties, it is desirable to develop an electronic structure calculation that produces directly the short-range reaction matrix. This is the topic of **Chapter 3**.

2.5 Resonance Scattering Theory

The theory of resonances can be rigorously derived using a wavepacket description and the time-dependent version of scattering theory [34, 18]. In the time-independent picture, a resonance theory that is consistent with observations can be developed from a formal ansatz. This ansatz, which is motivated in Section 2.2.9, states that quasi-bound levels occur at the poles of the scattering matrix on the fourth quadrant of the complex E plane. For the single channel case, the scattering matrix with such a pole can be expressed as,

$$S_l = \frac{E - E_{res} - i\frac{\Gamma}{2}}{E - E_{res} + i\frac{\Gamma}{2}} e^{2i\mu_l^0}, \tag{2.206}$$

where μ_l^0 is a resonance free background phase shift. The quasi-bound level described by the pole of the scattering matrix has an energy $E_{res} - i\frac{\Gamma}{2}$ and a time evolution factor,

$$e^{-iEt} = e^{-i(E_{res}-i\frac{\Gamma}{2})t} = e^{-iE_{res}t}e^{-\frac{\Gamma}{2}t}. \tag{2.207}$$

Thus, the square amplitude probability of finding the system in a quasi-bound level decreases exponentially with time as $e^{-\Gamma t}$. We identify $\frac{1}{\Gamma}$ as the lifetime of the quasi-bound state. Equation 2.206 can be rewritten as,

$$S_l = e^{2i\pi\mu_l}e^{2i\pi\mu_l^0} \tag{2.208}$$

where the resonant quantum defect μ_l is given by,

$$\mu_l = (1/\pi)arctan(\frac{\Gamma}{2(E_{res} - E)}), \tag{2.209}$$

and the total scattering phase-shift is obtained from Eqs.2.208 and 2.209 as,

$$\eta_l = \pi\mu_l^0 + arctan(\frac{\Gamma}{2(E_{res} - E)}), \tag{2.210}$$

Equation 2.210 is the Breit-Wigner form for the resonant phase shift [104] . The inverse tangent function in Eq. 2.210 is evaluated by convention in the $[0, \pi]$ branch. Therefore, the scattering phase shift η_l rises rapidly by π over an energy width of magnitude 2Γ, as E crosses the value E_{res}, becoming $\pi/2$ when $E = E_{res}$. The typical resonant behavior of the scattering phase shifts for fixed $E_{res} = 0.1au$ and various choices of Γ are shown in Fig. 2-13. Wigner uses a wavepacket argument in reference [136] to demonstrate that the energy derivative of the phase shift corresponds to the total time spent by the scattered electron in the ion-core before reemerging in an outgoing radial wave. This collision time-delay is given by,

$$\tau = 2\frac{d\eta_l}{dE}. \tag{2.211}$$

If the background phase shift is nearly energy independent, the collision time-delay can be calculated from Eq. 2.210 as,

$$\tau = \frac{\Gamma}{(E_{res} - E)^2 + \frac{\Gamma^2}{4}}. \tag{2.212}$$

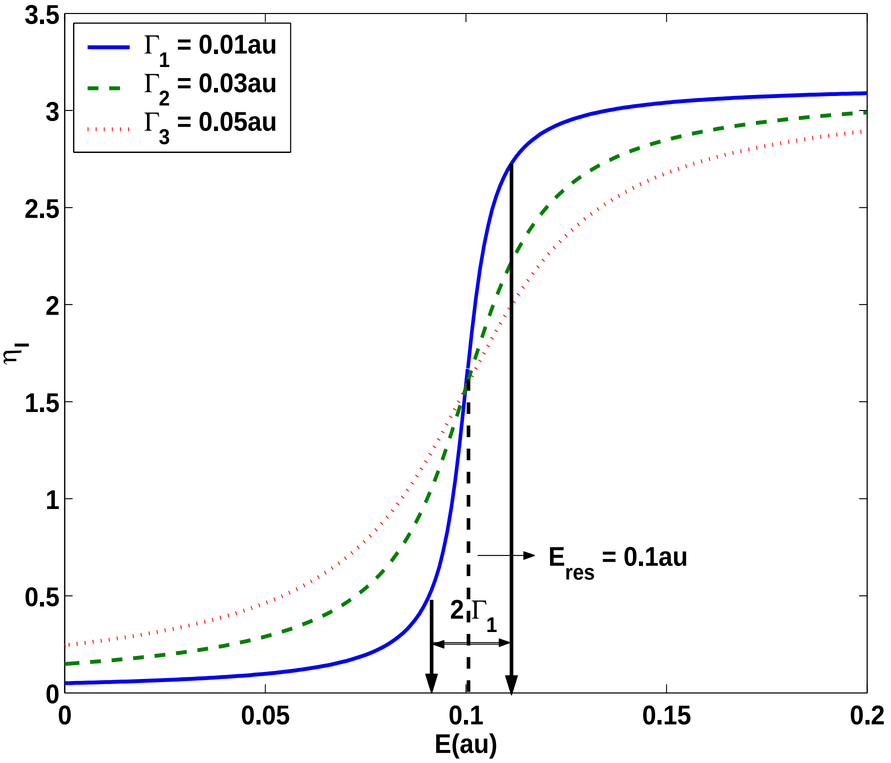

Figure 2-13: The behavior of the scattering phase shift on resonance. The scattering phase shifts are shown for three values of the resonance width, Γ, and a common resonance center , $E = E_{res} = 0.1au$. The background phase is assumed to be zero. The curves increase by π across their energy width becoming $\pi/2$ at $E = E_{res}$. A smaller resonance width corresponds to a sharper rise in the scattering phase shift. Such narrow, isolated resonances can easily be fitted to the Breit-Wigner form to obtain the resonance parameters. However, difficulties arise in fitting a broad resonance to the Breit-Wigner form, especially if the background phase is energy dependent. An additional difficulty might originate from the presence of multiple broad resonances that may overlap. We discuss how to analyze these types of resonances in **Chapter 5**.

Thus, the time delay is a Lorentzian in energy with a maximum at $E = E_{res}$ and a full width at half maximum (FWHM) of Γ. The indicated maximum corresponds to a resonance capture process of the electron by the ion-core. We interpret E_{res} as the resonance energy and Γ as the resonance width. The portion of the scattering amplitude due to short-range ion-core/electron interactions is obtained from Eq. 2.89 as,

$$f(\theta) = \frac{1}{2ik}\sum_l (2l+1)e^{2i\sigma_l}(e^{2i\eta_l}-1)P_l(cos\theta), \tag{2.213}$$

where σ_l is the Coulomb phase-shift. Equation 2.213 yields the short-range portion of the total scattering cross section as,

$$\sigma_{TOT} = 2\pi \textstyle\int d\theta |f(\theta)|^2 sin\theta \tag{2.214}$$

$$= \textstyle\sum_l \sigma_l^{par}, \tag{2.215}$$

where the partial cross section, σ_l^{par}, is obtained from Eq. 2.213 as,

$$\sigma_l^{par} = \frac{4\pi}{k^2}(2l+1)sin^2\eta_l. \tag{2.216}$$

In Eq. 2.216, $k^2 = 2(E - E_0)$, where E_0 is the energy of the channel internal state, as before. Substituting Eq. 2.210 in Eq. 2.216, one obtains,

$$\sigma_l^{par} = \frac{4\pi}{k^2}(2l+1)\left(sin^2\pi\mu_l^0 + \frac{\Gamma^2 cos2\pi\mu_l^0 - 2\Gamma(E-E_{res})sin2\pi\mu_l^0}{4(E_r-E)^2+\Gamma^2}\right). \tag{2.217}$$

When the background quantum defect is an integer, the cross section simplifies to the special symmetric form,

$$\sigma_l^{par} = \frac{4\pi}{k^2}(2l+1)\left(\frac{\Gamma^2}{4(E_r-E)^2+\Gamma^2}\right), \tag{2.218}$$

which is a Lorentzian with FWHM of Γ when rescaled with a factor of $\frac{k^2}{4\pi(2l+1)}$. The cross section has an asymmetric line shape when the background quantum defect differs from an integer. Resonance line shapes (σ_l^{par} rescaled with a factor of $\frac{k^2}{4\pi(2l+1)}$) for various constant values of the background quantum defect are displayed in Fig. 2-14. Additional distortions in the line shape arise when the background quantum defect has an energy dependence.

This energy dependence complicates the parametric fitting of an experimental resonance to the Breit-Wigner form, especially if the resonance has a broad width.

2.5.1 Shape Resonances

A resonance is called a shape resonance if the internal state of the system remains unchanged upon disintegration of the quasi-bound level. Thus, all single channel resonances are of the shape resonance type. Shape resonances may also arise in multichannel elastic scattering processes. Shape resonances are caused by the trapping of the scattered electron within an attractive well in the core potential $V_0(r)$ defined in Eq. 2.102. This type of feature in the core potential is shown diagrammatically in Fig. 2-15. The electron can escape this well by quantum tunneling through a repulsive barrier. The tunneling results in an increased time delay and the time delay reaches a maximum at the resonance energy, E_{res}. In the limit of an infinitely high barrier, the state with the energy E_{res} would be a bound state with an infinite life-time. Thus, the resonance width and the resonance center energy depend on the height and width of the repulsive barrier as well as the width of the attractive well. Simple formulas relating the resonance parameters to the shape of the potential function cannot be derived using exact quantum mechanics. However, Child [16] uses the WKB approximation to derive such shape resonance formulas. These formulas can be used to obtain the shape of the potential function in the barrier region from experimentally determined resonance parameters. In **Chapter 5**, the profound effects of a multichannel shape resonance on the Rydberg spectrum of the molecule CaF are discussed.

2.5.2 Feshbach Resonances

A resonance is called a Feshbach resonance if the internal state of the system is changed upon disintegration of the quasi-bound level. Therefore, Feshbach resonances always arise in multichannel inelastic scattering processes. The autoionizing resonances mentioned in Section 2.4.3 are of Feshbach type. Other examples of Feshbach resonances are predissociative states that disintegrate into two separated atoms. Here, we present the formal theory of the Feshbach resonance and derive some important properties of the autoionizing resonances.

We return to the case of a mixture of open and closed channels in multichannel scat-

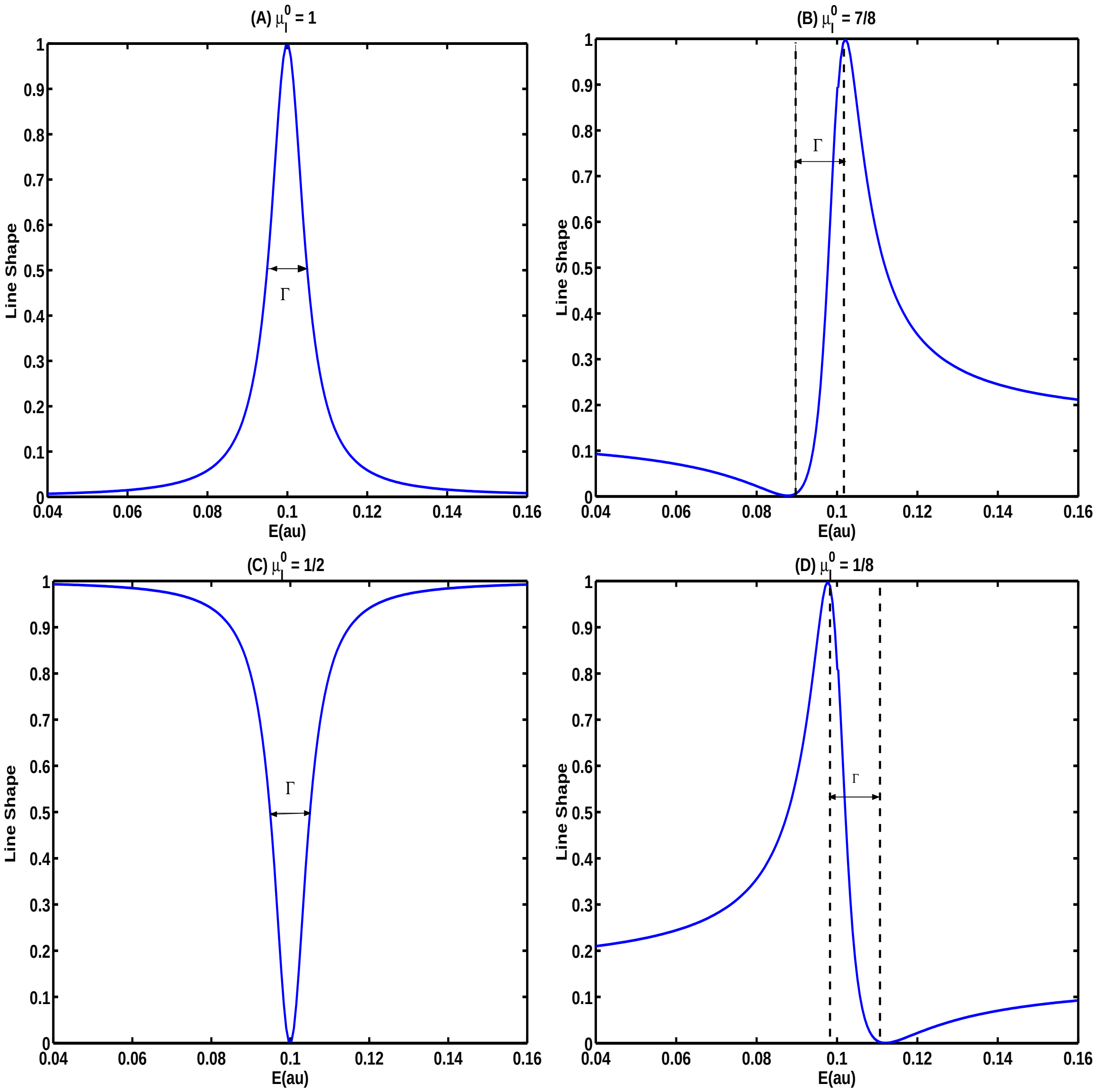

Figure 2-14: Resonance line shapes for various values of the background quantum defect, μ_l^0. The resonance parameters are $E_{res} = 0.1au$ and $\Gamma = 0.01au$.(A) The resonance line shape for $\mu_l = 1$. The line shape is a Lorentzian with a FWHM of Γ. For this integer value, the outgoing and incoming waves are in phase at $E = E_{res}$. (B) The resonance line shape for $\mu_l = 7/8$. For this fractional value, the outgoing spherical wave that corresponds to the disintegrating quasi-bound level interferes constructively with the incoming spherical wave, resulting in a sharp rise in the cross section slightly below E_{res}. Complete destructive interference occurs at an energy slightly above E_{res}. Asymmetric line shapes are typical indicators of such interference effects. (C) The resonance line shape for $\mu_l = 1/2$. The physical situation is opposite to that of the case depicted in (A). At this value of the quantum defect, the incoming and outgoing waves are out of phase, resulting in the abrupt vanishing of the cross section near $E = E_{res}$. The resonance energy in this case corresponds to the center of the dip. (D) The resonance line shape for $\mu_l = 1/8$. The physical situation is opposite to that of the case depicted in (B).

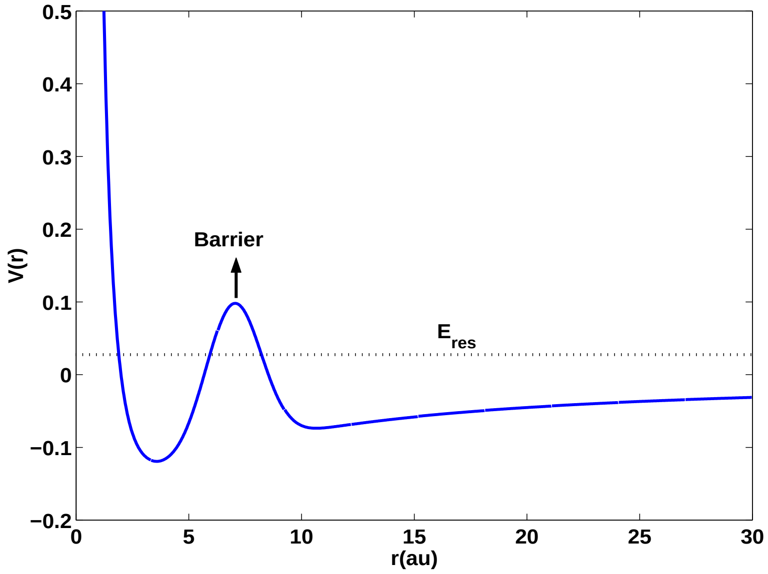

Figure 2-15: Illustration of a shape resonance. A shape resonance arises from the trapping of an electron within a well in the effective core potential. The quasi-bound level with energy E_{res} would be an authentic bound level in the limit of an infinitely high barrier. The energy of the quasi-bound level can be determined using the WKB quantization condition [18]. The electronic wavefunction (wavepacket) for the quasi-bound level is initially localized inside the well. As the wavepacket time-evolves, it leaks out by quantum mechanical tunneling across the barrier [18]. The resonance lifetime and energy depend on the shape of the potential. Analytical formulas can be derived using the WKB approximation [16].

tering. We assume that there are $N_o < N_c$ open channels. Therefore, we let $\epsilon_i = k_i^2$ for $i = 1 \cdots N_o$ and $\epsilon_i = -\frac{1}{\nu_i^2}$ for $i = N_o + 1 \cdots N_c$. We partition the matrix solutions $\mathbf{F^S}$ of Eq. 2.180 into open-open, open-closed, closed-open and open-open blocks as,

$$\mathbf{F^S} = \begin{pmatrix} \mathbf{F}^{\mathbf{S}}_{oo} & \mathbf{F}^{\mathbf{S}}_{oc} \\ \mathbf{F}^{\mathbf{S}}_{co} & \mathbf{F}^{\mathbf{S}}_{cc} \end{pmatrix}. \tag{2.219}$$

We must transform these solutions to ensure that physical boundary conditions are satisfied. These physical boundary conditions are that (i) the solutions must satisfy incoming/outgoing wave boundary conditions in the open channels and (ii) all exponentially increasing terms in the closed channels must vanish. We define the transformed solutions as,

$$\mathbf{H} = \begin{pmatrix} \mathbf{H}_o \\ \mathbf{H}_c \end{pmatrix} = \begin{pmatrix} \mathbf{F}^{\mathbf{S}}_{oo} & \mathbf{F}^{\mathbf{S}}_{oc} \\ \mathbf{F}^{\mathbf{S}}_{co} & \mathbf{F}^{\mathbf{S}}_{cc} \end{pmatrix} \begin{pmatrix} \mathbf{T}_o \\ \mathbf{T}_c \end{pmatrix} \tag{2.220}$$

$$= \begin{pmatrix} \mathbf{F}^{\mathbf{S}}_{oo}\mathbf{T}_o + \mathbf{F}^{\mathbf{S}}_{oc}\mathbf{T}_c \\ \mathbf{F}^{\mathbf{S}}_{co}\mathbf{T}_o + \mathbf{F}^{\mathbf{S}}_{cc}\mathbf{T}_c \end{pmatrix}. \tag{2.221}$$

From the boundary condition (i) we must have,

$$\mathbf{H}_o = \underline{\psi}^- - \underline{\psi}^+\mathbf{S}_o. \tag{2.222}$$

Using Eq. 2.180 and comparing Eqs. 2.221 and 2.222 we obtain,

$$\mathbf{T}_o = \mathbf{I} \tag{2.223}$$

$$\mathbf{S}_o = \mathbf{S}_{oo}\mathbf{T}_o + \mathbf{S}_{oc}\mathbf{T}_c. \tag{2.224}$$

From the boundary condition (ii) we must have,

$$\mathbf{H}_c(r \to \infty) = 0. \tag{2.225}$$

Using the phase-amplitude form of the Coulomb functions in the definitions of $\underline{\psi}^-$ and $\underline{\psi}^+$, we can rewrite the asymptotic limit of $\mathbf{H}_c$ as,

$$\mathbf{H}_c = \frac{1}{\sqrt{\pi}}\underline{\alpha}\left(-e^{i\pi(\nu-l)}\mathbf{S}_{co}\mathbf{T}_o + (e^{-i\pi(\nu-l)} - e^{i\pi(\nu-l)}\mathbf{S}_{cc})\mathbf{T}_c\right), \tag{2.226}$$

where $\underline{\alpha}$ and $e^{\pm i\pi(\nu-l)}$ are diagonal matrices with diagonal matrix elements $\alpha_{l_i}(\epsilon_i, r)$ and $e^{\pm i\pi(\nu_i-l_i)}$. Since α_i are exponentially divergent for $\epsilon_i < 0$ and $\mathbf{T}_0 = 1$, the quantity in the parentheses of Eq. 2.226 must be equal to zero for the vanishing boundary conditions in Eq. 2.225. Thus, we must have

$$-e^{i\pi(\nu-l)}\mathbf{S}_{co} + (e^{-i\pi(\nu-l)} - e^{i\pi(\nu-l)}\mathbf{S}_{cc})\mathbf{T}_c = 0 \tag{2.227}$$

$$(-e^{-2i\pi\nu} + \mathbf{S}_{cc})\mathbf{T}_c = -\mathbf{S}_{co} \tag{2.228}$$

$$\mathbf{T}_c = -(\mathbf{S}_{cc} - e^{-2i\pi\nu})^{-1}\mathbf{S}_{co}. \tag{2.229}$$

Substituting Eq. 2.229 in Eq. 2.224 yields the open-continuum scattering matrix as,

$$\mathbf{S}_o = \mathbf{S}_{oo} - \mathbf{S}_{oc}\left(\mathbf{S}_{cc} - e^{-2i\pi\nu}\right)^{-1}\mathbf{S}_{co}. \tag{2.230}$$

Next, we investigate the analytical properties of the open-continuum scattering matrix. The symmetry of the reaction matrix, $\mathbf{K}$, and the definition of $\mathbf{S}$ in Eq. 2.181 implies that $\mathbf{S}$ is symmetric and complex valued. Therefore, the block $\mathbf{S}_{cc}$ is also symmetric and complex valued. We can diagonalize $\mathbf{S}_{cc}$ as in Eq. 2.125,

$$\mathbf{S}_{cc} = \mathbf{U}_{cc}e^{2i\mu_a}\mathbf{U}_{cc}^T \tag{2.231}$$

where U is orthogonal. From Eq. 2.185 we also have that,

$$\mathbf{S}^*\mathbf{S} = \mathbf{S}\mathbf{S}^* = \mathbf{I}. \tag{2.232}$$

Equation 2.232 implies that,

$$\mathbf{S}_{oc}^*\mathbf{S}_{co} + \mathbf{S}_{cc}^*\mathbf{S}_{cc} = 1. \tag{2.233}$$

It follows from Eq. 2.233 that $\mathbf{S}_{cc}^*\mathbf{S}_{cc} < 1$. Based on the definition in Eq. 2.231, this inequality can be satisfied only if the eigenquantum defects μ_a have positive imaginary components. We write the complex eigenquantum defects as,

$$\mu_a = \mu_\alpha + i\beta. \tag{2.234}$$

We can substitute the Eq. 2.231 eigenvalue factorization in Eq. 2.230 to obtain,

$$\mathbf{S}_o = \mathbf{S}_{oo} - \mathbf{S}_{oc}\mathbf{U}_{cc}\left(e^{2i\mu_a} - e^{-2i\pi\nu}\right)^{-1}\mathbf{U}_{cc}^T\mathbf{S}_{co}. \tag{2.235}$$

In component form, Eq. 2.235 becomes,

$$(\mathbf{S}_o)_{ij} = (\mathbf{S}_{oo})_{ij} - \sum_a \frac{y_{ia}y_{aj}}{e^{2i\pi\mu_a} - e^{-2i\pi\nu_a}}, \tag{2.236}$$

where $y_{ia} = (\mathbf{S}_{oc}\mathbf{U}_{cc})_{ia}$. Equation 2.236 shows that the open-continuum scattering matrix has poles at values of ν_a such that,

$$e^{2i\pi\mu_a} - e^{-2i\pi\nu_a} = 0 \Rightarrow \tag{2.237}$$

$$\nu_a = n - \mu_a \qquad n = 1, 2 \cdots \infty. \tag{2.238}$$

From Eq. 2.238, we deduce that the scattering matrix has poles at energies such that,

$$E_n = E_a - \frac{1}{2(n-\mu_a)^2}. \tag{2.239}$$

where E_a is the ionization threshold for the closed channel labeled by index a. However, μ_a is complex valued. Substituting Eq. 2.234 in Eq. 2.239 we obtain,

$$E_n = E_a - \frac{1}{2(n-\mu_\alpha-i\beta)^2}. \tag{2.240}$$

Defining $x = i\beta/(n-\mu_\alpha)$ and assuming $n - \mu_\alpha >> \beta$, we can simplify Eq. 2.240 as,

$$E_n = E_a - \tfrac{1}{2(n-\mu_\alpha)^2}(1-2x) \tag{2.241}$$

$$= E_a - \tfrac{1}{2(n-\mu_\alpha)^2} - \tfrac{i\beta}{(n-\mu_\alpha)^3}. \tag{2.242}$$

From Eq. 2.242, we deduce that a series of autoionizing Feshbach resonances forms, the energies of which coincide with the energies of the members of a Rydberg series converging to the $a'th$ ionization threshold. The widths of the Feshbach resonances are given by $\Gamma = \frac{i\beta}{(n-\mu_\alpha)^3}$ and they scale as the inverse of the principal quantum number cubed. The Feshbach resonances disintegrate by decaying into an adjacent continuum above an ionization threshold of energy E_i such that $E_i < E_a$.

An autoionizing Feshbach resonance in a molecule is a manifestation of nuclear-electronic energy exchange. A Rydberg electron decays into an adjacent continuum by colliding with the ion-core and de-exciting it to a lower ro-vibrational state. The energy released by the nuclei when they make the transition to a lower energy level gets picked up as kinetic energy by the electron, which is then able to escape to the continuum.

We illustrate the resonance properties of the multichannel scattering matrix with an example. In this example, we use a three channel model to describe the autoionizing Rydberg states of a molecule. These channels correspond to the lowest three ionization thresholds with energies $E_0 < E_1 < E_2$. We focus on the autoionization region above the second ionization threshold but below the third ionization threshold ($E_1 < E < E_2$). Therefore, we have two open channels and one closed channel. The dimensionality of the open-continuum scattering matrix is 2×2. We represent the resonance parameters in terms of the quantum defect matrix elements defined in Eq. 2.147. Two physical cases are considered. For the first case, we turn off all direct coupling between the two continua and include only the indirect couplings between the continua via the Rydberg state. For the second case, we include both the direct and the indirect couplings between the two continua. A rich variety of interference effects arise in the latter case. Choices of quantum defect parameters that correspond to each physical case are tabulated in Table 2.1.

In multichannel problems, we define the resonance line shape as,

$$\sigma = |\mathbf{S}_o|^2_{01}. \tag{2.243}$$

The calculated resonance line shapes in the autoionizing region are shown in Figs. 2-16A and B. Fig. 2-16A displays the resonance line shapes for the case of no direct coupling between the continua. Autoionizing resonances are visible at the positions of the Rydberg states converging to the $E = 0.8$ au ionization threshold. The line shapes are symmetric Lorentzians centered on the energy of the Rydberg state. The resonances get sharper closer to the ionization threshold in accord with the Rydberg scaling law.

Table 2.1: Resonance Parameters Describing the Channel Interactions

Parameter	Direct Coupling of Continua Off	Direct Coupling of Continua On
μ_{00} (Eq. 2.147)	0.13	0.13
μ_{01} (Eq. 2.147)	0.0	0.07
μ_{02} (Eq. 2.147)	0.17	0.17
μ_{11} (Eq. 2.147	0.17	0.17
μ_{12} (Eq. 2.147)	0.02	0.02
μ_{22} (Eq. 2.147)	0.2	0.2
E_0 (au)	0.0	0.0
E_1 (au)	0.3	0.3
E_2 (au)	0.8	0.8
$\mu_{\alpha=2}$ (Eq. 2.234)	0.18	0.18
β (Eq. 2.234)	0.07	0.06

Fig. 2-16B displays the resonance line shapes for the case of direct coupling between the continua. In this situation, the interaction pathway that couples continuum-bound-continuum interferes with the pathway that couples continuum-continuum. This interference is manifested as asymmetric line shapes for each of the Rydberg resonances. These asymmetric line shapes are sometimes called Fano profiles after the person who first studied them. A parameterization of the Fano line shape is given in reference [29].

There are many instances of interference between multiple interaction pathways. Other examples can be interference between bound-bound and bound-continuum or bound-bound and bound-continuum-bound pathways. The possibilities increase as the number of channels that describe the system increases. All such multiple pathway interferences would be manifest by Rydberg spectra in the form of asymmetric line shapes as in Fig. 2-16B.

There is a simple multichannel generalization of the Breit-Wigner formula in Eq. 2.210. Huzi shows in reference [60] that the *eigenphase sum*, δ^{sum}, satisfies the single channel Breit-Wigner formula,

$$\delta^{sum} = \sum_{\alpha} \pi\mu_{\alpha} = \pi\mu^{0} + \sum_{E_{res}} arctan\left(\frac{\Gamma}{2(E_{res} - E)}\right), \tag{2.244}$$

where μ_{α} are the eigenquantum defects of the open-continuum scattering matrix, Γ is the resonance width, and E_{res} is the resonance energy. The calculated eigenphase sum for the three channel example problem is shown in Fig. 2-17. The eigenphase sum goes through transitions at each of the resonances, increasing by π in the vicinity of each Rydberg energy.

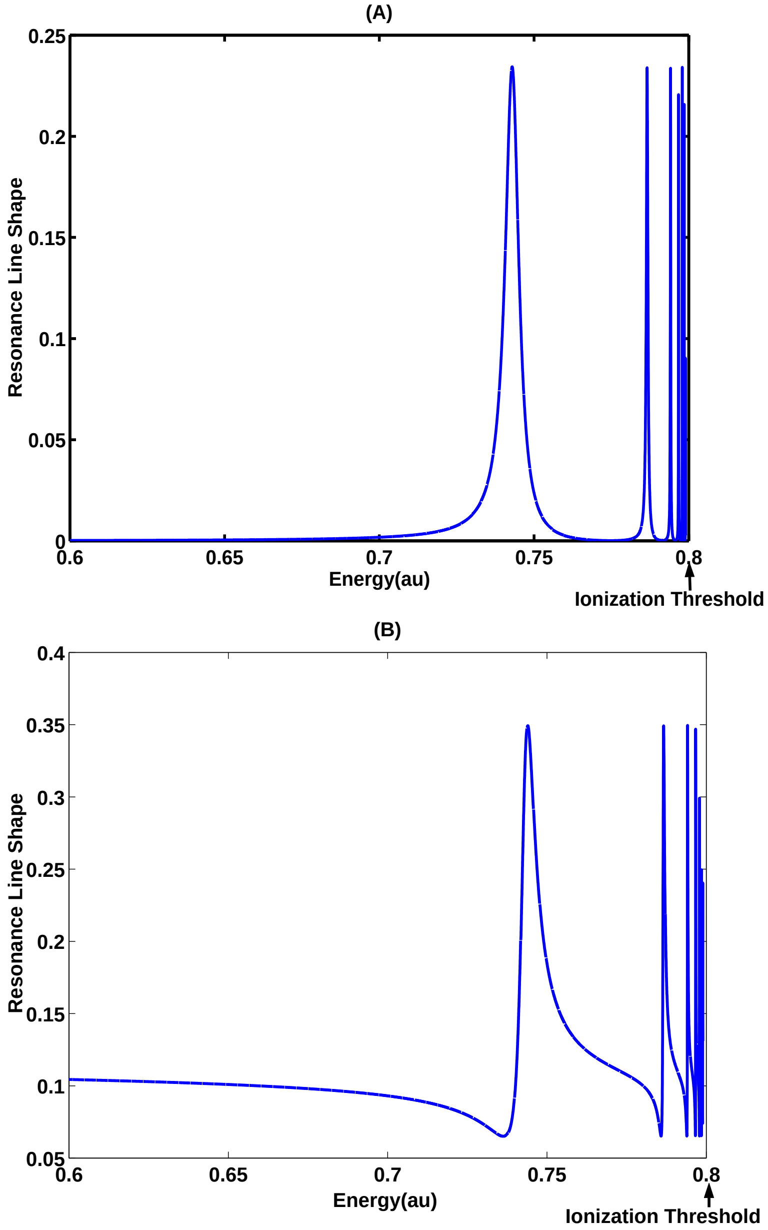

Figure 2-16: (A) Resonance line shapes for the case in which the direct coupling between the two continua is turned off. The two continua interact only indirectly via their coupling to the Rydberg state. The line shapes are symmetric Lorentzians, the widths of which scale as the inverse of the principal quantum number cubed. Symmetric line shapes occur in rare instances when there is a single pathway to ionization. (B) Resonance line shapes for the case in which the direct coupling between the two continua is turned on. The continuum-bound-continuum interaction pathway interferes with the continuum-continuum pathway resulting in asymmetric line shapes. The widths of the asymmetric lines scale as the inverse principal quantum number cubed. Such asymmetric line shapes are common in Rydberg spectroscopy and they are called Fano profiles.

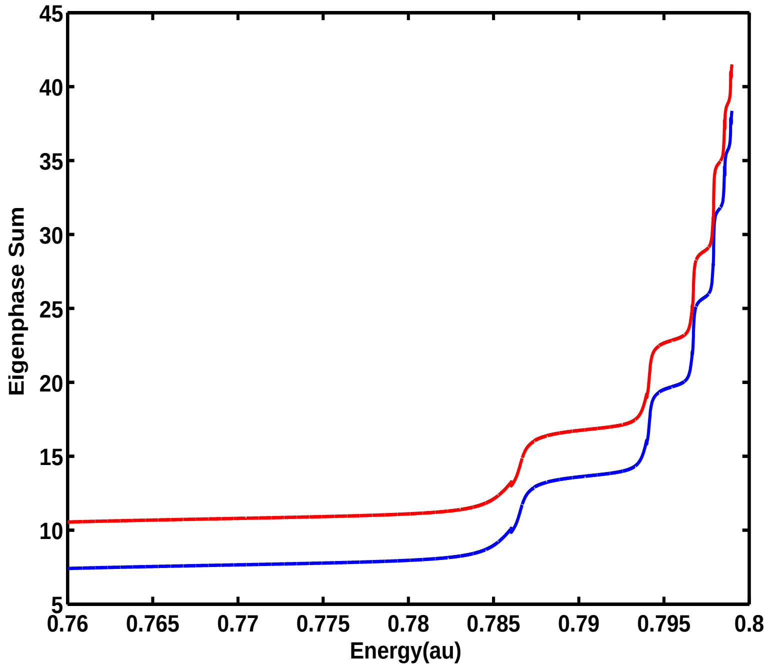

Figure 2-17: The behavior of the eigenphase sum at the autoionizing resonances. The top curve is obtained by shifting the lower curve upward by π. The eigenphase sum increases rapidly by π near the energy of each Rydberg state. The resonances are sharper closer to the ionization threshold. The magnitudes of the gaps at the avoided crossings measure the strength of the interactions between the neighboring resonances, as in the Lu-Fano plot described in Section 2.4.1. The gaps scale inversely with the principal quantum number cubed, all interactions vanish at the ionization threshold and the eigenphase sum diverges to infinity. The divergence is caused by the infinite number of Rydberg levels supported in the Coulomb potential. I thank Dr. Stephen Coy for writing and providing the computer programs, which were used for resonance analysis and the generation of this figure.

The increases become sharper as the ionization threshold is approached. The top curve in Fig. 2-17 is obtained by shifting the lower curve upward by π. Since the eigenphase sum is defined modulo π, the two curves are physically identical. However, as in the Lu-Fano plot, the gaps at the avoided crossings provide visual estimates of the strength of the interactions between neighboring resonances. The size of the gaps scales inversely with principal quantum number cubed and the curves cross at the ionization threshold, while the eigenphase sum diverges to infinity. The cause of this divergence is the infinite number of Rydberg levels that lie close to the ionization threshold, as discussed in Section 2.2.9.

The resonance formulas provided in this section in terms of the scattering matrix provide all the tools necessary for resonance analysis of Rydberg spectra. However, Rydberg spectra are typically analyzed and fitted using the reaction matrix rather than the scattering matrix. This should pose no serious problems, since the **S** and **K** matrices are related by the simple expression in Eq. 2.181. There are alternate resonance formulas provided in the literature that are expressed in terms of the reaction matrix. A particularly helpful formula, which is a multichannel generalization of the Breit-Wigner form in Eq. 2.210, is derived by Mies [87]. This formula states that,

$$\mu_{ij} = arctan\left(\sum_{p}\frac{\Gamma_{ip}\Gamma_{pj}}{E - E_p}\right), \tag{2.245}$$

where μ_{ij} is the quantum defect matrix and Γ_{ip} is the partial width for the resonance with energy E_p. However, Eq. 2.245 is valid when resonances are isolated in energy regions far from the ionization thresholds. Eq. 2.245 also assumes that the background quantum defect is small and has negligible energy dependence.

2.6 Conclusions

Multichannel quantum defect theory is an extension of continuum scattering theory below ionization thresholds. It is mathematically founded on the theory of Coulomb scattering and the analytical properties of the Coulomb radial wavefunctions. Interactions of all orders between members of a Rydberg series, interlopers or perturbations from adjacent Rydberg series are described in terms of a single entity called the reaction matrix. The reaction matrix is also capable of revealing any resonance behavior in the Rydberg spectrum, whether it is spread over an entire Rydberg series in the form of a shape resonance or it is localized in the energy region around a Rydberg state in the form of a Feshbach resonance. In molecular applications, the method of the frame transformation makes a connection between the quantum defect method and quantum chemistry. It allows for the representation of the entire molecular Rydberg spectrum in terms of a short-range reaction matrix that can be computed using the Born-Oppenheimer approximation and the standard techniques of quantum chemistry. In **Chapter 3**, we develop an electronic structure method for the *ab initio* determination of the short-range reaction matrix. It is shown that the calculation of the reaction matrix presents new and rather complex challenges, which are not encountered in a Hartree-Fock type variational calculation.

Until now, MQDT remains the most complete and elegant theory of electronic spectroscopy. There are several intriguing theoretical questions that remain and they might provide new venues for research. Most notably, the relationships between the reaction matrix and an effective Hamiltonian representation are not well understood. In the molecular case, it is clear that the two matrices belong to the same irreducible representation of the point symmetry group. In addition to this, it is likely that there are energy scaling laws obeyed by each of the matrices even if there are no simple formulas that relate them to one another. Establishing these scaling laws can allow for a better qualitative understanding of the reaction matrix and the information it provides. Another outstanding question is whether MQDT can be derived as a rigorous theory when electron exchange is included. This question is addressed in **Chapter 6**, where the reaction matrix is derived using a variational method that stems from orbital functional theory [95].

Chapter 3

Calculation of the Short-Range Reaction Matrix from First Principles

3.1 Introduction

Since the realization that the long range forces between a Rydberg electron and an ionic core are predominantly Coulombic [54, 112], reaction matrix methods (quantum defect theory) [112] have been widely used to model atomic and molecular electronic spectra. The subsequently developed eigenchannel approach to quantum defect theory [41] provides a minimal set of parameters, namely the eigenvalues and the corresponding eigenvectors of the reaction matrix, which can accurately represent spectroscopic data. Eigenchannel methods paved the way for empirical analyses (fits) of experimental results [41, 79, 138] as well as interpolation/extrapolation procedures to calculate quantities of interest, such as photoionization cross-sections and scattering amplitudes [26].

There have been relatively fewer calculations of MQDT reaction matrices from first principles. A commonly used method, developed by Greene [44], is based on Kohn's variational expression for the logarithmic derivative of the scattering wave function on a surface that bounds a finite intra-core volume at a given energy (the **R**-matrix method) [69]. The variational **R**-matrix scheme has been applied to determine the photoionization cross section of the hydrogen atom in a strong magnetic field [44] and spin-orbit effects in heavy alkaline-earth atom systems [45]. All-electron **R** matrix calculations for molecular systems have been carried out by Tennyson and Noble [132] by and Rabadan and Tennyson[100]. More recent **R** matrix work by Hyama and Child [59], and Telmini and Jungen [130] include calculation of the MQDT reaction matrix. Arif, Jungen, and Roche [5] used the variational **R**-matrix method to calculate the short range quantum defect matrix [64] of CaF and obtained good agreement with experimental results [7] . Their approach is based on the multiple scattering method [22] and makes use of the generalized form of quantum defect theory [50]. One limitation of this method is that it cannot easily be extended to include the effects of electronic configuration interaction at large internuclear distances [5], which are important in most molecular systems. For example, the X $^2\Sigma^+$ ground electronic state of the molecule calcium monofluoride adiabatically evolves toward the ^1S Ca($4s^2$)-^2P F separated atom limit. The repulsive state in the Ca($4s^2$)+F$2p\sigma^{-1}$ hole $^2\Sigma^+$ configuration, which also evolves toward to the same separated atom limit, goes through numerous avoided crossings with the Rydberg states of the type $n^{*2}\Sigma^+$ (Ca^{+2}F$^-$) at various internuclear distances. It would thus be desirable to include these effects in an *ab initio* calculation of the reaction matrix. In the following analysis, it is demonstrated that the specialized, closed-shell calculations presented here can be expediently extended to account for configuration interaction.

Computationally, the most expensive aspect of the variational scheme is the evaluation of the required matrix elements over the intra-core volume that is surrounded by the bounding surface. The dimension of the basis set used in the calculation must be scaled in proportion to this volume in order to achieve convergence [45]. For large volumes, the calculation of the reaction matrix at a single collision energy becomes time consuming.

These difficulties in applying *ab initio* reaction matrices to molecular spectra limit their implementation, for example by making it difficult to develop an efficiently converging MQDT fit [65] to the energy levels; an *ab initio* determined body-fixed reaction matrix would provide reliable estimates of key parameters for a global MQDT fit to the ro-vibrational energy levels. The new procedure described below, which can include configuration interaction, converges rapidly and can be conveniently used by both experimentalists and theorists in the analysis of molecular spectra and to describe molecular dynamics.

Our method is outlined here: First, we consider the interaction between an ionic molecular aggregate described by wavefunction $\boldsymbol{\psi_i}$ and an electron with energy $E - E_i > 0$ (E_i is the energy of the target state labeled by index i and E is the total energy [112]). If the static charge density approximation [128] is used, the core is a closed-shell configuration frozen in its ground state, $\boldsymbol{\psi_0}$. The state, $\boldsymbol{\psi_0}$, yields an effective electron-core interaction potential, $V_o(\mathbf{r})$.

It is also possible to include the mixing of several electronically excited core states, $\boldsymbol{\psi_i}$, by adding polarizability interactions to the effective one-electron potential, $V_{\text{eff}}(\mathbf{r})$. Core polarizability effects are included in the application presented in **Chapter 4**, where the Rydberg states of CaF are studied, using the effective potential given by Arif, Jungen, and Roche [5].

In molecules, whether modeled by a frozen core or a polarizable core, the potential is necessarily non-spherical and results in a set of one-dimensional coupled Schrödinger equations in a partial-l expansion scheme. We construct solutions to these equations that are regular at the origin and that satisfy the standing-wave boundary condition at a large radius (effectively infinite) in integro-matrix form using the principal value Coulomb Green's function [96].

Functional analysis shows that the formal Born series for the collision channels will not converge over any spatial region that contains the origin. We solve this problem by separately analyzing a small spherical region of space about the origin.

The effect of the electronic wave function *inside* this region is represented by the value of its logarithmic derivative *on the boundary* (**R**-matrix eigenvalue). The wave function in the outer region can then be determined in a convergent Born series by using a modified form of the principal value Green's function.

Green's function methods have been used previously to explain the connection between quantum defect theory and the configuration interaction approach [31], in generalizations of quantum defect theory [24], and in other closely related fields [39, 80, 97, 81]. However, iterative Green's function methods are not commonly used in the current *ab initio* **R**-matrix/MQDT calculations tailored toward molecular applications. Our work demonstrates the practical utility of the iterative Green's function methods in calculating reaction matrices and presents a viable alternative to the standard variational approaches. In the analysis presented below, special care is taken to provide rigorous mathematical answers to some important theoretical questions that arise in the derivations but that are often neglected in practical applications.

A diatomic molecular ion-core with a large electric dipole moment has a long-range interaction with its Rydberg electron. For such molecules, the assumption that all non-Coulombic potentials can be neglected beyond some finite range is violated and the equations of ordinary quantum defect theory cannot be used. Generalized quantum defect theory [50, 42] is needed, with the proviso that the effective single-electron potential must allow for a separation of the radial and angular variables of the Schrödinger equation at all points on the surface that surrounds the reaction volume [5]. If this requirement is met, then it is possible to define an alternative pair of quantum defect basis functions (the QDT base pair), which are often defined numerically [66] as replacements of the analytic Coulomb wavefunctions given by Seaton [112]. However, the separability requirement makes it difficult to embed within the generalized **R**-matrix treatment a quantum chemical multi-configuration *ab initio* calculation. In an MCSCF calculation, the spatial potentials for the Rydberg electron are expressed in numerical form on a grid of the radial variable. Numerical techniques might be used to approximate the required separation of variables; however, for nonlinear nuclear configurations in polyatomic molecules, such a separation is not possible due to the lack of cylindrical symmetry. Our equations do not require assumption of any restricted form for the interaction potential and should be valid for a wide range of molecular systems. This paves the way for facile incorporation of rigorous quantum chemical treatments of multi-electron interactions into **R**-matrix methods.

The treatment presented here considers the behavior of the solutions of the coupled equations at infinite electron-core separation, where the interaction potential reduces to the Coulomb field. For the electronic energies in the continuum, Seaton's analytical Coulomb functions remain linearly independent in the asymptotic limit, so that a **K**-matrix can be defined. However, since this reaction matrix is defined at long range, it necessarily displays a strong energy dependence. Such energy dependent behavior in the **K**-matrix renders extrapolation of its eigenvalues to the region of negative energy (i.e. below the ionization limit) difficult. Furthermore, numerical determination of the **K** matrix at energies below the ionization limit is not computationally feasible due to the poor linear independence of the Coulomb functions at negative energies. We show in Section 3.2 that much of this strong energy dependence can be removed by performing a transformation of the reaction matrix, **K**, to obtain a dipole-reduced matrix, $\bar{\mathbf{K}}$, which is defined at short range. The bound states of the combined electron-ion-core system can then be determined by using the transformed reaction matrix, which is shown here to have a smooth energy dependence [112, 25]. Accordingly, the method presented in the current work treats both polar and non-polar ion-cores in a unified fashion and yields a reaction matrix with a smooth energy dependence, which can be used in ro-vibrational MQDT calculations [130]. The theory discussed in this chapter has been published in the Journal of Chemical Physics [117].

3.2 Theory

We begin by considering the collision of an electron with an N-electron molecular ion-core. In our analysis, the nuclei are fixed in a spatial configuration near the equilibrium geometry of a particular electronic state of the molecular-ion.

Let ψ_i denote a collision channel, which is a vector coupled product of an electronic state of the ion with the spin coordinates of the colliding electron. Then,

$$(\psi_{i'}|\psi_i) = \delta_{i'i} \quad \big(\psi_{i'}|\mathbf{H}^{+}|\psi_i\big) = E_i\delta_{i'i}. \tag{3.1}$$

Here $\mathbf{H}^{+}$ is the electronic Hamiltonian for the ion and E$_i$ is the energy for the i'th electronic state. The collision wave function for the electron-core system is represented as

$$\Psi(E) = \sum_{i=0}\sum_{l=0}^{l_{\max}}\sum_{\lambda}\psi_i(\tau)\frac{M_{il\lambda}(r)}{r}Y_l^{\lambda}(\theta,\phi), \tag{3.2}$$

where $Y_l^{\lambda}(\theta,\phi)$ is a spherical harmonic, and the sums are over electronic states (ψ_i) of the core and over the l,λ quantum numbers associated with the Rydberg electron. The coupled equations of collision theory can be obtained from the matrix element

$$\Big(Y_l^{\lambda}\psi_i|\mathbf{H}^{tot} - E|\Psi(E)\Big) = 0. \tag{3.3}$$

The integration in Eq. 3.3 is over all of the core internal coordinates, τ, the Rydberg electron angular coordinates (θ,ϕ), and $\mathbf{H}^{\mathbf{tot}}$ is the Hamiltonian for the combined system.

Equation 3.3, in atomic units, becomes

$$\left\{-\frac{1}{2}\left(\frac{d^2}{dr^2}-\frac{l(l+1)}{r^2}\right)-\frac{\epsilon_i}{2}\right\}M_{il\lambda}(r)+\sum_{i'=0}^{l}\sum_{l'=0}^{l_{\max}}\sum_{\lambda'}V_{il\lambda;i'l'\lambda'}M_{i'l'\lambda'}(r)=0 \tag{3.4}$$

where $\epsilon_i = 2(E - E_i) > 0$, and the radial interaction potential matrix elements for N electrons around κ nuclei are

$$V_{il\lambda;i'l'\lambda'}(r)=\left(Y_l^{\lambda}\psi_i\left|\sum_{n=1}^{N}\frac{1}{|\vec{r}-\vec{r}_n|}-\sum_{a=1}^{\kappa}\frac{Z_a}{|\vec{r}-\vec{r}_a|}\right|\psi_{i'}Y_{l'}^{\lambda'}\right). \tag{3.5}$$

Here, Z_a is the positive charge on nucleus a, $\vec{r}_a$ is the position of that nucleus, κ is the number of nuclei, and the vectors $\vec{r}_n$ are the positions of the core electrons. Making use of the Legendre polynomial expansion,

$$\frac{1}{|\vec{r}-\vec{r}_j|}=\sum_{s=0}^{\infty}P_s(\hat{r}\cdot\hat{r}_j)\frac{r_<^s}{r_>^{s+1}}, \tag{3.6}$$

it can be shown that

$$V_{il\lambda;i'l'\lambda'}(r\to\infty)=-\frac{Z}{r}\delta_{ii'}\delta_{ll'}\delta_{\lambda\lambda'} \tag{3.7}$$

where the net charge $Z=\sum_a Z_a - N$.

At this stage, we specialize to the case of a diatomic molecule, where we place two nuclei on the z-axis separated by a distance $R = R_e^+$. Because of cylindrical symmetry, the radial interaction potential matrix elements are diagonal in λ, and Eqs. 3.4 may be solved as separate systems for each value of λ. Furthermore, we assume that the ion is a singly charged ($Z = 1$) diatomic, and that the collision between the electron and the core does not cause electronic excitation of the ion ($i = i' = 0$). We will relax this assumption when we address the Rydberg states of the CaF molecule in **Chapter 4**. It should be noted that more general cases will depart only in minor details from our analysis, and they can be dealt with by returning to Eq. 3.4. Based on our special conditions, we get

$$V_{il\lambda;i'l'\lambda'}(r)\to V_{ll'}^{(0,\lambda)}(r,R)\delta_{i0}\delta_{\lambda\lambda'}. \tag{3.8}$$

Subscripts i and λ can be suppressed, so we rewrite the coupled equations of Eq. 3.4 in the form

$$\left(\frac{d^2}{dr^2}-\frac{l(l+1)}{r^2}+\epsilon+\frac{2}{r}\right)M_l(r)-\sum_{l'=0}^{l_{\max}}2\widetilde{V}_{ll'}^{(0,\lambda)}(r,R)M_{l'}(r)=0 \qquad l=0\ldots l_{\max} \tag{3.9}$$

where we have separated the long range Coulombic part from the potential, $V^{(0,\lambda)}(\vec{r},R)$, by defining

$$\widetilde{V}^{(0,\lambda)}(\vec{r},R)=V^{(0,\lambda)}(\vec{r},R)+\frac{1}{r}. \tag{3.10}$$

Next we require that Eq. 3.9 is regular at $r=0$ but leave the boundary condition at $r=\infty$ unspecified:

$$M_l(0)=0 \qquad l=0\ldots l_{\max}. \tag{3.11}$$

These coupled equations with the specified boundary conditions have $l_{\max}+1$ linearly independent solutions, $\vec{M}_\alpha$, which we write as row vectors:

$$\vec{M}_\alpha(r)=(M_{\alpha 0}(r)\ldots M_{\alpha l_{\max}}(r)) \qquad \alpha=0\ldots l_{\max}. \tag{3.12}$$

Each value of α defines a collisional wavefunction via Eq. 3.2.

3.2.1 Solutions of the Zero-Order Equations

Following Seaton [112], we now obtain the two linearly independent solutions to the zero-order Coulombic radial equation:

$$\left(\frac{d^2}{dr^2}-\frac{l(l+1)}{r^2}+\epsilon+\frac{2}{r}\right)\zeta(r)=0. \tag{3.13}$$

Write $\kappa^2=-\frac{1}{\epsilon}=-\frac{1}{k^2}$ and define

$$z=\frac{2r}{\kappa} \qquad \eta=l+\frac{1}{2}. \tag{3.14}$$

Substitution of Eq. 3.14 in Eq. 3.13 brings Eq. 3.13 into the form of the Whittaker equation

$$\left(\frac{d^2}{dz^2}-\frac{\eta^2-\frac{1}{4}}{z^2}+\frac{\kappa}{z}-\frac{1}{4}\right)\zeta(z)=0. \tag{3.15}$$

A solution of Eq. 3.15 that is regular at the origin is [112],[2]

$$\zeta_1(\kappa,\eta,z) = \frac{(\kappa z)^{\eta+\frac{1}{2}}}{\Gamma(2\eta+1)} e^{-\frac{z}{2}} {}_1F_1(\frac{1}{2}+\eta-\kappa, 1+2\eta, z), \tag{3.16}$$

where ${}_1F_1(a,b,c)$ is the confluent hypergeometric function and $\Gamma(z)$ is the Gamma function. Since η enters Eq. 3.15 through η^2, a second solution can immediately be defined as

$$\zeta_2(\kappa,\eta,z) = \zeta_1(\kappa,-\eta,z). \tag{3.17}$$

The functions (ζ_1,ζ_2) are linearly dependent when η is equal to a half integer [112]. In order to obtain a linearly independent pair of solutions, the theory should be developed for arbitrary η and then the limit as $\eta \rightarrow l+\frac{1}{2}$ should be considered. For $\epsilon << 4\pi^2$, we define the pair of solutions

$$\begin{aligned} f(\epsilon,\eta,r) &= (\frac{A(\kappa,\eta)}{2})^{\frac{1}{2}}\zeta_1(\kappa,\eta,z) \\ g(\epsilon,\eta,r) &= (2A(\kappa,\eta))^{-\frac{1}{2}}\frac{A(\kappa,\eta)cos(2\pi\eta)\zeta_1(\kappa,\eta,z)-\zeta_2(\kappa,\eta,z)}{sin(2\pi\eta)} \\ A(\kappa,l+\frac{1}{2}) &= \frac{\Gamma(l+1+\kappa)}{\kappa^{2l+1}\Gamma(-l+\kappa)}. \end{aligned} \tag{3.18}$$

The function g remains finite in the limit $\eta \rightarrow l+\frac{1}{2}$ and is linearly independent of f for all η except when η is an integer. The functions (f,g) have the asymptotic forms

$$f(\epsilon,l+\frac{1}{2},r\rightarrow\infty) = \sqrt{\frac{1}{\pi}}k^{-\frac{1}{2}}sin(\phi_l) \tag{3.19}$$

$$g(\epsilon,l+\frac{1}{2},r\rightarrow\infty) = -\sqrt{\frac{1}{\pi}}k^{-\frac{1}{2}}cos(\phi_l), \tag{3.20}$$

where ϕ_l is the Coulomb phase defined by,

$$\phi_l(r) = kr - \frac{l\pi}{2} + \frac{1}{k}log(2rk) - arg(\Gamma(l+1+\frac{i}{k})). \tag{3.21}$$

Equations 3.19, 3.20, and 3.21 show that the functions (f_l,g_l) satisfy the Wronskian relation

$$W(f_l,g_l) = f_l g_l' - g_l f_l' = \frac{1}{\pi}\ . \tag{3.22}$$

The behavior of the Coulomb functions near the origin is given by:

$$\begin{aligned} f_l(r,\epsilon) &\xrightarrow[r\to 0]{} r^{l+1} \\ g_l(r,\epsilon) &\xrightarrow[r\to 0]{} r^{-l}. \end{aligned} \tag{3.23}$$

Thus, the solutions to Eq. 3.13 that are regular at the origin can be written in the form:

$$M_{\alpha l}(r) = f_l(r)\delta_{\alpha l}. \tag{3.24}$$

3.2.2 Coupled Equations

We now seek solutions to the complete set of coupled radial equations, Eq. 3.9. These solutions have an asymptotic behavior that is expressed through the reaction matrix, **K**, as a sum of regular and irregular Coulomb functions:

$$M_{\alpha l}(r \to \infty) = f_l(r)\delta_{\alpha l} - K^{\lambda}_{\alpha l} g_l(r). \tag{3.25}$$

Since the potential is Coulombic at long range, (Eq. 3.7), the existence of solutions in this form is guaranteed by the linear independence of the Coulomb functions in the asymptotic limit for $\epsilon > 0$.

A formal solution can be written in the form

$$M_{\alpha l}(r) = f_l(r)\delta_{\alpha l} + 2\sum_{l'=0}^{l_{\max}} \int_0^{\infty} dr' G_l(r,r') M_{\alpha l'}(r') \widetilde{V}^{(0,\lambda)}_{l'l}(r',R), \tag{3.26}$$

where $G_l(r,r')$ is a principal-value Green's function for the zero-order equations. Due to the boundary conditions given in Eq. 3.11 and Eq. 3.25, it is necessary that

$$G_l(r,r') = \pi f_l(r_<) g_l(r_>), \tag{3.27}$$

and the **K** matrix becomes

$$K^{\lambda}_{\alpha l} = -2\pi \sum_{l'=0}^{l_{\max}} \int_0^{\infty} dr' f_l(r') M_{\alpha l'}(r') \widetilde{V}^{(0,\lambda)}_{l'l}(r',R). \tag{3.28}$$

It is natural, at this stage, to attempt an iterative procedure to obtain the solutions $\vec{M}_{\alpha}$.

Mathematical appendix A at the end of this chapter shows that a Born series expansion for $M_{\alpha l}(r)$, which uses the Green's function given in Eq. 3.27, does not converge. The difficulty arises from the inverse-r type singularity in the perturbing potential at the origin. However, use of the variational [33, 44] method of calculating **R**-matrix eigenvalues in combination with an alternate Born series expansion can yield a convergent Green's function iteration scheme, because it excludes the region near $r = 0$.

3.2.3 Iterative Procedure to Calculate the K-Matrix

Following Greene [44], we consider the expression

$$\epsilon = \frac{\int_0^{r_0} \int_0^{\pi} \int_0^{2\pi} \psi^*(\vec{r})(-\nabla^2 + 2V^{(0)}(\vec{r}))\psi(\vec{r}) d^3r}{\int_0^{r_0} \int_0^{\pi} \int_0^{2\pi} \psi^*(\vec{r})\psi(\vec{r}) d^3r}, \tag{3.29}$$

where $\psi(\vec{r})$ is the one-electron wave function expanded in spherical harmonics, as in Eq. 3.2, and $r_o < \infty$. The equation is an identity when ψ is a solution to the Schrödinger equation within a sphere of radius r_o, and has stationary properties for ψ near a solution [44]. We impose the condition

$$\left. \frac{\partial \psi(\vec{r})}{\partial r} \right|_{r=r_o} = -b\psi(\vec{r})|_{r=r_o} . \tag{3.30}$$

Note that there is no loss of generality here: we are looking at a specific class of solutions, namely those solutions with a constant logarithmic derivative on the spherical surface and we prove the existence of these solutions by explicit construction. The undetermined quantity we are trying to calculate is b. Stated more precisely, we are trying to find the allowed values of b for which the Schrödinger equation is soluble at a pre-selected value of ϵ. Let us consider a basis set expansion of the solution, ψ, in terms of basis set elements that all have a fixed logarithmic derivative at the boundary, $r = r_o$. A natural choice for a basis set [1] is the set of orthonormal solutions of the free particle radial equation

$$\left(\frac{d^2}{dr^2} - \frac{l(l+1)}{r^2} + k^2 \right) u_l(r) = 0 \tag{3.31}$$

---

[1] We use a specific basis set here for the sake of clarity. In practice other basis sets, such as the Fourier basis [5] may be more convenient to use.

with the boundary conditions

$$u_l(0) = 0 \qquad\qquad u_l'(r_o) = (\frac{1}{ro} - \tilde{b})u_l(r_o). \tag{3.32}$$

The differential equation and the first of these conditions identifies the $u_l(r)$ as Riccati-Bessel functions and the derivative condition at r_o defines the scale factors of the Riccati-Bessel function arguments at each l. Letting $j_l(r) = \frac{u_l(r)}{r}$, the basis set expansion for ψ becomes

$$\psi(\vec{r}) = \sum_{j=1}^{j_{\max}} \sum_{l=1}^{l_{\max}} a_{jl}\tilde{j}_l(k_{lj}, r)Y_l^{\lambda}(\theta, \phi), \tag{3.33}$$

where $k_{lj}r_o$ is the j'th solution of the second equation in Eq. 3.32 for the l'th order spherical Bessel function, j_l, and $\tilde{j}_l(k_{lj}, r)$ are the original $j_l(k_{lj}, r)$ functions renormalized by the square integral with r^2 over the interval $[0, r_o]$. The basis set $\vartheta_{jl}(\vec{r}) = \tilde{j}_l(k_{lj}r)Y_l^{\lambda}(\theta, \phi)$ is complete in the interval $0 \leq r \leq r_o$. The solution ψ will be stationary with respect to variations in the $\{a_{jl}\}$,

$$\frac{\partial \epsilon}{\partial a_{jl}} = 0. \tag{3.34}$$

The variational condition in Eq. 3.34 yields, through Eq. 3.29, a generalized eigenvalue equation of the form [44]

$$(\epsilon \mathbf{I} - 2\mathbf{H})\vec{a} = (b - \tilde{b})\mathbf{\Lambda}\vec{a}. \tag{3.35}$$

The definitions are

$$H^{\lambda}_{j'l'jl} = \int_0^{r_0} \int_0^{\pi} \int_0^{2\pi} d^3r \; (-1)^{\lambda}\tilde{j}_{l'}(k_{l'j'}r)Y_{l'}^{-\lambda}(\theta, \phi)\left(-\frac{\nabla^2}{2} + V^{(0)}(\vec{r})\right)\tilde{j}_l(k_{lj}r)Y_l^{\lambda}(\theta, \phi)$$

$$\Lambda_{j'l'jl} = \tilde{j}_{l'}(k_{l'j'}r_o)\tilde{j}_l(k_{lj}r_o)\delta_{l'l}. \tag{3.36}$$

In Equation 3.35, $\mathbf{I}$ denotes the identity matrix and $\vec{a}$ is a column vector whose components consist of the coefficients $\{a_{jl}\}$. Thus the allowed values of b can be found by solving the generalized eigenvalue equation shown in Eq. 3.35. This generalized problem can be converted to a simple eigenvalue problem for values of $\frac{1}{b - \tilde{b}}$ by exploiting the properties of the matrix $\mathbf{\Lambda}$. The method employed to solve the generalized eigenvalue problem in the current work is presented in Appendix B. Solution of Eq. 3.35 yields $l_{max} + 1$ eigenvalues,

b_β, and $l_{max} + 1$ eigensolutions, $\Psi_\beta(\vec{r})$, which can be expanded as

$$\Psi_\beta(\vec{r})\,|_{r<r_o} = \sum_{l=0}^{l_{\max}} \frac{\Sigma_{\beta l}(r)}{r} Y_l^\lambda(\theta,\phi), \tag{3.37}$$

where,

$$\begin{aligned}
\Sigma_{\beta l}(r \le r_o) &= \sum_{j=0}^{j_{\max}} a_{\beta j l}\, r \tilde{j}_l(k_{lj} r) \\
\sum_{j=1}^{j_{\max}} \sum_{l=0}^{l_{\max}} |a_{\beta j l}|^2 &= 1 \\
\frac{d}{dr}\Sigma_{\beta l}(r)\Big|_{r=r_o^+} &= \frac{\Sigma_{\beta l}(r_o)}{r_o} - b_\beta \Sigma_{\beta l}(r_o).
\end{aligned} \tag{3.38}$$

We note that for some problems it may be necessary to include non-orthogonal basis functions with different values of $\tilde{b}$ in the Eq. 3.33 expansion to facilitate the convergence of the computed b values. The extension of the theory to permit the use of such a non-orthogonal basis is straightforward and is given in reference [44].

Solutions of the Zero-Order Equations

For $r \ge r_o$, the solutions of the uncoupled zero-order equations can be written as

$$M_{\beta l}^{(0)}(r \ge r_o) = a_{\beta l} f_l(r) - b_{\beta l} g_l(r), \tag{3.39}$$

where, imposing continuity, we have

$$\begin{aligned}
a_{\beta l} &= \pi \left(\Sigma_{\beta l}(r_o) g_l'(r_o) - \Sigma_{\beta l}'(r_o^+) g_l(r_o)\right) \\
b_{\beta l} &= \pi \left(\Sigma_{\beta l}(r_o) f_l'(r_o) - \Sigma_{\beta l}'(r_o^+) f_l(r_o)\right).
\end{aligned} \tag{3.40}$$

Solutions of the Coupled Equations

We write the solutions to the full set of coupled equations in the form

$$M_{\beta l}(r \geq r_o) = M^{(0)}_{\beta l}(r) + \sum_{l'=0}^{l_{\max}} 2 \int_{r_o}^{r} dr' G_l(r,r') M_{\beta l'}(r') \widetilde{V}^{(0,\lambda)}_{l'l}(r',R), \tag{3.41}$$

where the principal-value Green's function generalizes as

$$G_l(r,r') = \begin{cases} 0 \quad for \quad r' > r \\ \pi\left(f_l(r')g_l(r) - g_l(r')f_l(r)\right) \quad for \quad r' < r. \end{cases} \tag{3.42}$$

From Eqs. 3.42 and 3.41, it is evident that the functions $M_{\beta l}$ automatically satisfy the continuity requirements at $r = r_o$. We can calculate the exact solutions iteratively as,

$$M^{(n)}_{\beta l}(r \geq r_o) = M^{(0)}_{\beta l}(r \geq r_o) + 2 \sum_{l'=0}^{l_{\max}} \int_{r_o}^{r} dr' G_l(r,r') M^{(n-1)}_{\beta l'}(r') \widetilde{V}^{(0,\lambda)}_{l'l}(r',R). \tag{3.43}$$

The exact solutions are found when the input set, $\{M^{(n-1)}_{\beta l}(r)\}$ is identical to the output set, $\{M^{(n)}_{\beta l}(r)\}$. This is decided based upon the convergence criterion that is specified in Eq. 3.4.83 in the Appendix. The iterative procedure in Eq. 3.43 has much stronger convergence properties than the formal Born series expansion (Appendix Eq. 3.4.81), because a spherical region of radius r_0 is excluded from the integration, removing the divergent contribution at the origin. Furthermore, for every finite value of r, the integrations are carried out on a finite length interval and the values of the function for large r are obtained using already converged values of the function at smaller r.

It is known [140] that the use of integral operators in numerical propagation is superior to the use of differential operators. For example, if a finite difference method is used to propagate the solutions known at $r = r_o$, the numerical error will almost always grow significantly as r approaches ∞. Such accumulated errors do not arise in Eq. 3.43, mainly due to its restricted region of radial integration. This iterative method is a numerically stable and efficient procedure to obtain the exact solutions of the full set of coupled equations. Technical algorithms that facilitate the fast convergence of Eq. 3.43 are presented in reference [3]. It should be noted that the calculated solutions, $\vec{M}_\beta(r)$, are linearly independent when all the eigenvalues b_β are distinct. A proof is given in Appendix C.

The Reaction Matrix

The linearly independent solutions, $\vec{M}_\beta$, of Eq. 3.43 are related to the alternate set of linearly independent solutions, $\vec{M}_\alpha$, of Eq. 3.12 through a linear transformation $\mathbf{T}$

$$\mathbf{M}_\beta = \mathbf{T}\mathbf{M}_\alpha, \tag{3.44}$$

where $\mathbf{T}$ is of dimensions $((l_{\max}+1)\times(l_{\max}+1))$ and $\mathbf{M}$ is a fundamental matrix for the system of coupled equations, the rows of which consist of linearly independent solutions. In particular, in the asymptotic limit we get

$$\begin{aligned} M_{\beta l}(r\to\infty) &= \sum_{\alpha=1}^{l_{\max}+1} T_{\beta\alpha}(f_l\delta_{\alpha l} - K_{\alpha l}g_l) \\ &= T_{\beta l}f_l - T^{(2)}_{\beta l}g_l, \end{aligned} \tag{3.45}$$

where we have defined the composite transformation

$$\mathbf{T}^{(2)} = \mathbf{T}\mathbf{K}. \tag{3.46}$$

Imposing continuity on Eq. 3.45 we get

$$\begin{aligned} T_{\beta l} &= \pi(M_{\beta l}g_l' - M_{\beta l}'g_l) \\ T^{(2)}_{\beta l} &= \pi(M_{\beta l}f_l' - M_{\beta l}'f_l). \end{aligned} \tag{3.47}$$

The function values and derivatives must be evaluated at sufficiently large values of r. The reaction matrix is finally obtained from Eq. 3.46

$$\mathbf{K} = \mathbf{T}^{-1}\mathbf{T}^{(2)}. \tag{3.48}$$

This completes the procedure for calculating the reaction matrix.

3.2.4 The Energy Dependence of the Reaction Matrix

In our previous discussion we have assumed that $\epsilon \geq 0$ and restricted our attention to collision energies in the ionization continuum. In order to locate the bound states, we must consider $\epsilon < 0$. From the analyticity of the Coulomb functions, it follows that the matrices

$\mathbf{T}$ and $\mathbf{T}^{(2)}$ are analytic in ϵ except possibly at a few isolated points and therefore the matrices can be expanded in a power series:

$$\mathbf{T} = \sum_j \mathbf{T}_j \frac{\epsilon^j}{j!} \qquad\qquad \mathbf{T}^{(2)} = \sum_j \mathbf{T}_j^{(2)} \frac{\epsilon^j}{j!} \tag{3.49}$$

Properties of this expansion, which have been determined empirically through numerical computations [111], are as follows:

(1) When the perturbing potential $\widetilde{V}^{(0\lambda)}(\vec{r}, R)$ effectively vanishes at short range, the matrices $\mathbf{T}$ and $\mathbf{T}^{(2)}$ can be fitted to the polynomial series in Eq. 3.49, retaining only a few terms. The calculated reaction matrix usually varies slowly with energy.

(2) The fitted polynomial series can be extrapolated to the regions below the ionization threshold and the reaction matrix can be obtained for negative energies. This reaction matrix can then be used [112] to determine the bound state energy levels.

An important exception occurs when the leading term in the asymptotic expansion of $\widetilde{V}^{(0\lambda)}(\vec{r}, R)$ is a dipole term that falls off as $\frac{1}{r^2}$. The long range nature of such a potential forces the value of r where the reaction matrix is determined to become large ($r \geq 100a_o$). In most cases, this leads to a strong energy dependence in the reaction matrix, rendering extrapolation of the reaction matrix to negative energies difficult. We show next how this energy dependence can be removed by a diagonalization procedure developed by Dubau [25]. A related approach is also presented in reference [46]. Define the dipole moment of the electrostatic interaction as:

$$\mu(R) = \lim_{r \to \infty} -\frac{3r^2}{2} \int_0^{\pi} \widetilde{V}^{(0,\lambda)}(r, \theta, R) P_1(cos\theta) sin\theta d\theta. \tag{3.50}$$

The value of $\mu(R)$ will be coordinate-system dependent in the presence of a monopole contribution. It is in general possible to define an $r_c < \infty$ such that for $r \geq r_c$ the coupled equations reduce to:

$$\left(\frac{d^2}{dr^2} + \epsilon + \frac{2}{r} \right) M_l(r) = \sum_{l'=0}^{l_{\max}} \frac{C_{ll'}^{\lambda}}{r^2} M_{l'}(r), \tag{3.51}$$

where the dipole matrix $C_{ll'}^{\lambda}$, expressed in terms of Wigner 3-j coefficients, is given by:

$$C^{\lambda}_{ll'} = l(l+1)\delta_{l'l} + 2\mu(R)(-1)^{(\lambda+1)}\sqrt{(2l+1)(2l'+1)}\begin{pmatrix}1 & l & l' \\ 0 & 0 & 0\end{pmatrix}\begin{pmatrix}1 & l & l' \\ 0 & \lambda & -\lambda\end{pmatrix}. \quad (3.52)$$

Let $\mathbf{F}$ be the similarity transformation that diagonalizes $\mathbf{C}^{\lambda}$. Applying $\mathbf{F}^{T}$ to both sides of Eq. 3.51, we get

$$\sum_{l}\left(\frac{d^2}{dr^2} + \epsilon + \frac{2}{r}\right)F^{T}_{kl}M_l(r) = \sum_{l}\sum_{i}\sum_{j}\sum_{l'=0}^{l_{\max}}\frac{F^{T}_{kl}C^{\lambda}_{li}F_{ij}}{r^2}F^{T}_{jl'}M_{l'}(r). \quad (3.53)$$

The diagonal matrix of eigenvalues of $\mathbf{C}^{\lambda}$ is given by

$$\bar{\mathbf{C}}^{\lambda} = \mathbf{F}^{T}\mathbf{C}^{\lambda}\mathbf{F}. \quad (3.54)$$

We define the functions $\bar{\mathbf{M}}$ as

$$\bar{\mathbf{M}} = \mathbf{M}\mathbf{F}. \quad (3.55)$$

and the uncoupled equations for the $\bar{\mathbf{M}}(r \geq r_c)$ follow from Eq. 3.53,

$$\left(\frac{d^2}{dr^2} + \epsilon + \frac{2}{r} - \frac{\bar{C}^{\lambda}_{nn}}{r^2}\right)\bar{M}_n(r) = 0. \quad (3.56)$$

Here $\bar{C}^{\lambda}_{nn}$ is the n'th eigenvalue of the matrix $\mathbf{C}^{\lambda}$.

Alternate Pair of Basis Functions

Equation 3.56 has the form of the Coulomb equation and therefore the functions, $\bar{M}_n$, are linear combinations of Coulomb functions for $r > r_c$. By analogy with the centrifugal barrier term in the Coulomb equation, the appropriate solutions are Coulomb functions for non-integer or complex angular momenta that satisfy $\bar{l}(n)(\bar{l}(n)+1) - \bar{C}^{\lambda}_{nn} = 0$. These solutions are defined as [25],

$$\bar{f}(\epsilon,\bar{l},r) = \frac{A(\kappa,\eta)^{-\frac{1}{2}}}{2\sqrt{2}} \left(\frac{A\zeta^{(1)} - \zeta^{(2)}}{sin\pi\eta} \right) \tag{3.57}$$

$$\bar{g}(\epsilon,\bar{l},r) = -\frac{A(\kappa,\eta)^{-\frac{1}{2}}}{2\sqrt{2}} \left(\frac{A\zeta^{(1)} + \zeta^{(2)}}{cos\pi\eta} \right) \tag{3.58}$$

$$W(f_{\bar{l}}, g_{\bar{l}}) = f_{\bar{l}} g'_{\bar{l}} - f'_{\bar{l}} g_{\bar{l}} = \frac{1}{\pi} \tag{3.59}$$

$$\eta = \bar{l} + \frac{1}{2}. \tag{3.60}$$

The expression $A(\kappa,\eta)$ and the functions $(\zeta^{(1)},\zeta^{(2)})$ are given in Section 3.2.1. The parameters η and κ can be either real or imaginary. The pair of Coulomb functions $(\bar{f},\bar{g})$ are linearly independent for all η, but when η is neither an integer nor a half integer they both show a divergence at $r = 0$ due to the contribution from the $\zeta^{(2)}$ term in Eq. 3.57. This is an important difference between this new pair of basis functions and the pair defined in Eq. 3.18. The functions $(\bar{f},\bar{g})$ have the asymptotic forms

$$\bar{f}(\epsilon,\bar{l}(n),r\to\infty) \sim \sqrt{\frac{1}{\pi}} k^{-1/2} sin(\bar{\phi}_n) \tag{3.61}$$

$$\bar{g}(\epsilon,\bar{l}(n),r\to\infty) \sim -\sqrt{\frac{1}{\pi}} k^{-1/2} cos(\bar{\phi}_n), \tag{3.62}$$

where $\bar{\phi}_n$ is the Coulomb-Dipole phase defined by,

$$\bar{\phi}_n(r) = kr + \frac{\bar{l}(n)\pi}{2} + \frac{1}{k} log(2rk) - arg(\Gamma(\bar{l}(n) + 1 + \frac{i}{k})) \qquad for\ \bar{l}(n)\ real \tag{3.63}$$

$$\bar{\phi}_n(r) = kr + \frac{1}{k} log(2rk) - \frac{\pi}{4} + \frac{1}{2}\left(arg(\Gamma(-\bar{l}(n) - \frac{i}{k})) + arg(\Gamma(\bar{l}(n) + 1 - \frac{i}{k})) \right) \quad for\ \bar{l}(n)\ complex. \tag{3.64}$$

In practice, it is more convenient to use the function $Im(log\Gamma(z))$ for evaluating the expressions of the form $arg(\Gamma(z))$ in the definitions of the Coulomb and Coulomb-Dipole phases. The function $log\Gamma(z)$ is an entire function with a single branch cut along the negative real axis. Using $Im(log\Gamma(z))$ makes the phases a continuous function of the collision energy, without the π ambiguity that occurs in evaluating Eq. 3.64.

The $l_{max} + 1$ linearly independent solutions in Eq. 3.12 for all $\widetilde{V}^{(0,\lambda)}(r,\theta,R)$ generalize as:

$$\bar{M}_{\alpha n}(r \geq r_c) = \bar{f}_{\bar{l}(n)}\delta_{\alpha n} - \bar{K}_{\alpha n}\bar{g}_{\bar{l}(n)}, \tag{3.65}$$

where $\bar{l}(n) = \sqrt{\bar{C}^{\lambda}_{nn} + \frac{1}{4}} - \frac{1}{2}$ as before. The *dipole reduced reaction matrix* $\bar{\mathbf{K}}$ accounts for the contributions from the terms in the perturbing potential that fall off faster than $\frac{1}{r^2}$. The effects of both the monopole and dipole terms are absorbed in the $(\bar{f}, \bar{g})$ pair in this form. Therefore the $\bar{\mathbf{K}}$ matrix is defined at *short range* and thus varies slowly with energy. Since the $\bar{\mathbf{K}}$ matrix is defined at short range, it can be directly calculated at negative energies or can be extrapolated from positive energies by exploiting its smooth energy dependence. The construction of the $\bar{\mathbf{K}}$ matrix enables the current formalism to treat polar and non-polar ion-cores in a unified fashion.

3.2.5 The Transformation between $\mathbf{K}(\epsilon)$ and $\bar{\mathbf{K}}$

Due to its smooth dependence on energy, the matrix $\bar{\mathbf{K}}$ can be reliably extrapolated to negative energy, and is thus the proper reaction matrix to use for the study of the bound states of systems with long-range non-Coulomb potentials. In addition to the mathematical reasons discussed previously, we provide a full discussion in **Chapter 4** of the physical reasons that justify the use of the $\bar{\mathbf{K}}$ matrix. Comparing Eqs. 3.63 and 3.64 to Eq. 3.21, it is possible to express the dipole reduced reaction matrix in terms of the asymptotic reaction matrix $\mathbf{K}$ of Eq. 3.25. Since this expression is algebraically complicated, we instead present a simpler relationship between the corresponding scattering matrices [1]. We define the functions,

$$\Phi^{\pm}_{l}(r) = -g_l(r) \pm i\, f_l(r). \tag{3.66}$$

Therefore the functions $\Phi^{\pm}_{l}$ behave asymptotically as outgoing and incoming waves. Notice that

$$\mathbf{M}_{\alpha}(r \to \infty) = \underline{f} - \mathbf{K}\underline{g} \tag{3.67}$$

$$= \frac{1}{2i}\left((\mathbf{I} + i\mathbf{K})\underline{\Phi}^{+} - (\mathbf{I} - i\mathbf{K})\underline{\Phi}^{-}\right), \tag{3.68}$$

where $\mathbf{I}$ is the identity matrix and $\underline{f}$ and $\underline{g}$ denote diagonal matrices with the $l + 1$'th diagonal element being equal to $f_l(r)$ and $g_l(r)$ respectively. The scattering solutions are obtained by transforming $\mathbf{M}_\alpha(r)$:

$$\mathfrak{M} = -2i(\mathbf{I} - i\mathbf{K})^{-1}\mathbf{M}_\alpha \tag{3.69}$$

$$\xrightarrow[r\to\infty]{} \underline{\Phi}^- - \mathbf{S}\underline{\Phi}^+, \tag{3.70}$$

where,

$$\mathbf{S} = (\mathbf{I} - i\mathbf{K})^{-1}(\mathbf{I} + i\mathbf{K}). \tag{3.71}$$

Scattering solutions for Eq. 3.51 are obtained by applying $\mathbf{F}$ to the solutions ,$\mathfrak{M}$:

$$\mathfrak{M}(r \to \infty)\mathbf{F} = \underline{e}^{-ip}\mathbf{F}\underline{e}^{i\bar{p}}\underline{\bar{\Phi}}^- - \mathbf{S}\underline{e}^{ip}\mathbf{F}\underline{e}^{-i\bar{p}}\underline{\bar{\Phi}}^+, \tag{3.72}$$

where we have set

$$\bar{p}_n = \bar{\phi}_n(r) - kr - \frac{1}{k}log(2kr) \tag{3.73}$$

$$p_l = \phi_l(r) - kr - \frac{1}{k}log(2kr) \tag{3.74}$$

$$\bar{\Phi}_n^{\pm}(r) = -\bar{g}_{\bar{l}(n)}(r) \pm i\, f_{\bar{l}(n)}(r). \tag{3.75}$$

Using Eq. 3.72, one gets

$$\bar{\mathfrak{M}} = \underline{e}^{-i\bar{p}}\mathbf{F}^T\underline{e}^{ip}\mathfrak{M}\mathbf{F} \tag{3.76}$$

$$\xrightarrow[r\to\infty]{}\underline{\bar{\Phi}}^- - \bar{\mathbf{S}}\underline{\bar{\Phi}}^+. \tag{3.77}$$

In Eq. 3.77 we have,

$$\bar{\mathbf{S}} = \underline{e}^{-i\bar{p}}\mathbf{F}^T\underline{e}^{ip}\mathbf{S}\underline{e}^{ip}\mathbf{F}\underline{e}^{-i\bar{p}} \tag{3.78}$$

$$= (\mathbf{I} - i\bar{\mathbf{K}})^{-1}(\mathbf{I} + i\bar{\mathbf{K}}). \tag{3.79}$$

The $\bar{\mathbf{K}}$ matrix can be obtained from the $\mathbf{K}$ matrix using Eqs. 3.71, 3.78 and 3.79. The physical meaning of the dipole reduced reaction matrix is apparent in the transformation given in Eq. 3.78. The various mixings of the partial l's due to the core dipole are accounted for in the $\bar{\mathbf{K}}$ matrix by folding some information from the off-diagonal parts of the $\mathbf{K}$ matrix onto the diagonal parts of the $\bar{\mathbf{K}}$ matrix. The transformation, viewed in this sense,

Table 3.1: Summary of the Terms Used in the Reaction Matrix Calculations

Expression	**K** Matrix Calculation	$\bar{\mathbf{K}}$ Matrix Calculation
Coulomb Functions	$(f_l(\epsilon, r), g_l(\epsilon, r))$	$(f_{\bar{l}}(\epsilon, r), \bar{g}_{\bar{l}}(\epsilon, r))$
Green's Function	$G_l(\epsilon, r, r')$	$G_{\bar{l}}(\epsilon, r, r')$
The Solutions	$\mathbf{M}(r)$	$\bar{\mathbf{M}}(r) = \mathbf{M}(r)\mathbf{F}$
The Perturbing Potential	$\widetilde{V}^{(0,\lambda)}(\vec{r}, R) = V^{(0,\lambda)}(\vec{r}, R) + \frac{1}{r}$	$\widetilde{V}^{(0,\lambda)}(\vec{r}, R) = V^{(0,\lambda)}(\vec{r}, R) + \frac{1}{r} + \frac{\mu(R)cos(\theta)}{r^2}$
Input in Eq. 3.43	$\tilde{\mathbf{V}}^{(0,\lambda)}(r)$	$\tilde{\mathbf{U}}^{(0,\lambda)}(r) = \mathbf{F}^T\tilde{\mathbf{V}}^{(0,\lambda)}\mathbf{F}$

resembles the *Van Vleck* transformation encountered in quasi-degenerate perturbation theory [74]. A Van Vleck transformation is used to account for the effect of the interactions between members of a quasi-degenerate block of the Hamiltonian matrix and all out-of-block states while keeping the dimensionality of the calculation constant. The analogous effect of the transformation that we have described here is to reduce the undesired strong energy dependence in the reaction matrix, allowing for a stable and reliable extrapolation to the region of negative energies.

Alternatively, one can directly calculate the $\bar{\mathbf{K}}$ matrix rather than initially calculating the **K** matrix. For some problems, this might speed up the computations since the length of the radial interval in which the solutions are propagated using Eq. 3.43 is smaller for the $\bar{\mathbf{K}}$ matrix than for the **K** matrix. By making the correspondences listed in Table 3.1, the equations derived in the previous sections can be used, without any modification, to calculate the $\bar{\mathbf{K}}$ matrix.

3.3 Conclusions

We have presented a new method for the calculation of reaction matrices based on a Green's function numerical propagation scheme. This method is a viable alternative to the standard variational approaches and removes some of the previous theoretical difficulties with *ab initio* calculations of reaction matrices. First, because we do not assume that the interaction potential reduces to the Coulomb field at any finite distance of the electron from the ion-core, our calculations are equally valid for both short and long-range potentials. Therefore, the analytical Coulomb functions derived by Seaton [112] can be used even in the presence of long-range potentials within the present framework. The calculation can be tailored toward either the determination of the **K** or the $\bar{\mathbf{K}}$ matrix. The $\bar{\mathbf{K}}$ matrix has the analytical properties that are required for practical computation and its eigenvalues and eigenvectors vary slowly with energy, as shown in Fig. 3-1 below. On the other hand, ordinary angular momentum algebra is inapplicable to the $\bar{\mathbf{K}}$ representation; the $\mathbf{K}$ matrix is needed as input to the frame transformation to describe electronic coupling to the nuclear rotation. The $\mathbf{K}$ matrix can be obtained by performing a simple transformation of the $\bar{\mathbf{K}}$ matrix. Figure 3-2 shows that the eigenvalues of the $\mathbf{K}$ matrix possess a prominent energy dependence, in contrast to the behavior of the $\bar{\mathbf{K}}$ eigenvalues displayed in Fig. 3-1. The eigenquantum defects obtained from the $\mathbf{K}$ matrix cannot be easily extrapolated to the region of negative energies. Although the $\mathbf{K}$ matrix might possess a strong energy dependence, it reveals physical insights into the mechanism of $e^- \leftrightarrow$ ion-core interactions more straightforwardly than the $\bar{\mathbf{K}}$ matrix [117].

Another significant improvement is the time required to calculate the matrices needed to obtain the values of the logarithmic derivatives. In the present context, the bounded volume used in the variational calculation need not extend into the asymptotic region. The effects of all medium to long range interactions enter into the solutions through the numerical propagation in Eq. 3.43.

In practice, the radius of the bounded volume, r_o, should be made as small as possible, contingent upon convergence of Eq. 3.43. The maximum value of r_o used in the calculations reported in **Chapter 4** is 6 a_o as opposed to a typical $\mathbf{R}$-matrix box length of 25 a_o [45]. The use of a smaller bounded volume allows for a reduction of the size of the variational basis set and further speeds up the numerical integrations.

An efficient iterative method to solve the integral equations, such as one of the methods described in reference [3], combined with the reduced volume variational calculation, makes implementation of the entire computation fast; we refer the reader to **Chapter 4** for a detailed discussion of the application of the current technique to an example system, the Rydberg electronic structure of CaF.

The output of the computation for $^2\Sigma$ and $^2\Pi$ Rydberg states of CaF is represented by the eigenquantum defect data shown in Fig. 3-1. Each data point shown on the graph requires less than 3 minutes of computation time on a 1GHz PC; the method presented here achieves both rapid convergence and acceptable agreement with the experiment. The filled circles in Figure 3-1 are the experimentally determined eigenquantum defects [5, 7], whereas the points on the solid curves are the theoretical data points computed on an energy grid. The plus signs above each curve are the eigenquantum defects of the reaction matrices determined by a global MQDT fit to 617 previously assigned energy levels of CaF in the $7 < n^* < 18$ region [37]. The reaction matrix was assumed to be energy independent in that global fit, and the result of the calculation is shown only for the $n^* \approx 10$ region in Fig. 3-1. It is seen that the current eigenquantum defects are, on average, within ± 0.02 of the experimental and global fit results. This value would correspond to a discrepancy of 15.56 cm^{-1} in the $n^* = 6$ region. However, there are larger deviations from the theoretical curves in the $n^* \approx 10$ region. The expanded views of the eigenquantum defects shown in the right panels of Fig. 3-1A and B illustrate that the deviations are systematic. This suggests that the error is due to an effect that is not explicitly included in the calculations, namely the configuration interaction of the Rydberg levels with the Ca($4s^2$)+F2pσ hole $^2\Sigma^+$ and Ca($4s^2$)+F2pπ hole $^2\Pi$ repulsive states, which dissociate to separated neutral atoms (it should be noted, however, that the effects of these repulsive states are included in the energetics of the scattering electron in a perturbative sense due to the various polarizability interactions included in the calculation. The reader is referred to **Chapter 4** for an expanded discussion). The largest discrepancies between the calculated and the experimental eigenquantum defect values occur for the $0.88^2\Sigma^+$ series in the $n^* \approx 10$ region ($E \approx -0.005\,au$) and for the $0.36^2\Pi$ series in the $n^* \approx 7$ region. The magnitude of the discrepancies in electronic energies amount to 11.66 cm^{-1} for the $10.88^2\Sigma^+$ state and 44.23 cm^{-1} for the $7.36^2\Pi$ state. The mean discrepancy between experiment and theory (i.e average deviations apart from the systematic deviations due to repulsive states) is likely due to incomplete deperturbation of the experimental data, particularly for rotating molecule effects, which are excluded here.

The procedure is capable of generalization to configuration interaction treatments often used in conventional quantum chemical calculations; the flexibility in the theory developed here makes it straightforward to remove a limitation [5] in previous treatments of the CaF Rydberg states. The mixing of configurations of type $\mathrm{Ca}^{++}\mathrm{F}^{-}e^{-}$ and $\mathrm{Ca}^{+}\mathrm{F}e^{-}$ can be approximated by an effective one-electron potential at short internuclear distances in the perturbative limit by including various core polarizability terms. However, the systemic discrepancies between the calculated and experimental eigenquantum defects at the equilibrium internuclear distance, shown in Fig. 3-1, highlights the fact this approximation is not entirely satisfactory. There is yet a stronger interaction between the two ion-core elec-

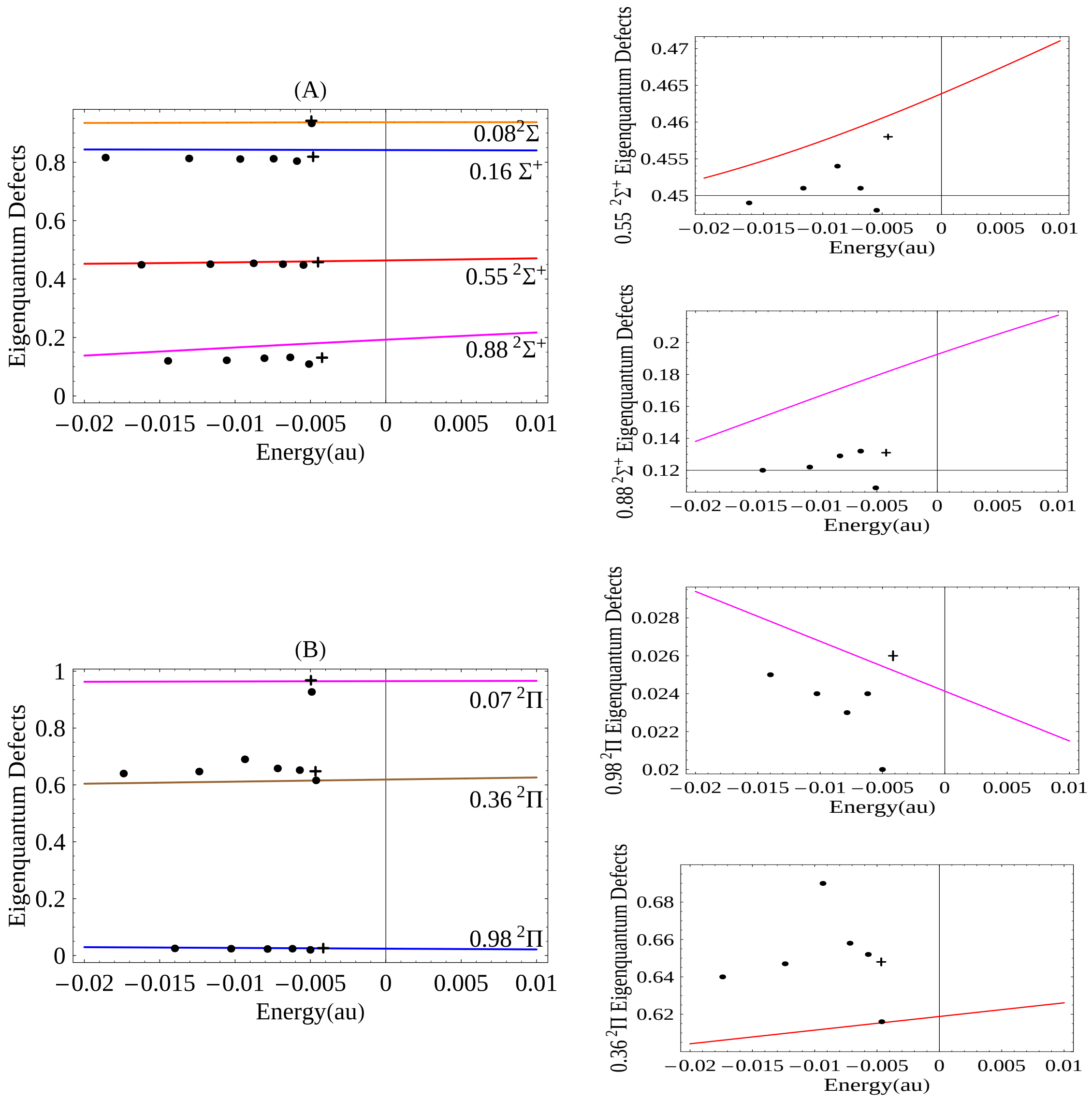

Figure 3-1: (A) The Calculated Eigenquantum Defects of CaF in the $^2\Sigma^+$ Electronic Symmetry, obtained from the $\bar{\mathbf{K}}$ matrix . The eigenquantum defect curves characterize the four penetrating $^2\Sigma^+$ Rydberg series of CaF, which have been observed in the electronic spectrum [7]. The Rydberg series are labeled by the value $mod(\nu, 1)$ where ν is the effective principal quantum number [7, 91]. The filled circles are the experimentally determined eigenquantum defects, whereas the plus signs are the eigenquantum defects determined from a global fit by Field et. al. [37]. (B) The Calculated Eigenquantum Defects of CaF in the $^2\Pi$ Electronic Symmetry. The eigenquantum defect curves characterize the three penetrating $^2\Pi$ Rydberg series of CaF, which have been observed in the electronic spectrum [7]. The Rydberg series are labeled by the value $mod(\nu, 1)$ where ν is the effective principal quantum number [7, 91]. Experimental eigenquantum defects are marked by the filled circles and the plus signs are the eigenquantum defects determined from a global fit by Field et. al. [37].

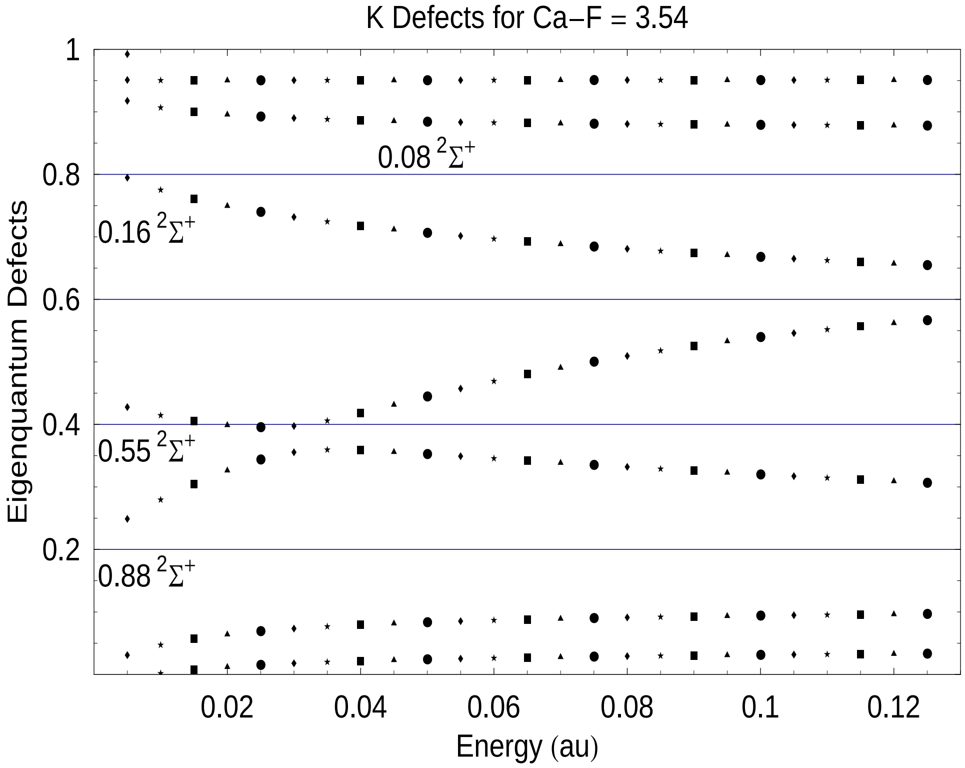

Figure 3-2: The Calculated Eigenquantum Defects of CaF in the $^2\Sigma^+$ Electronic Symmetry, obtained from the integer-l $\mathbf{K}$ matrix. The calculation of the $\mathbf{K}$ matrix was carried out for the ionization continuum only and the eigenchannels are labeled using the scheme of Fig. 3-1. The eigenquantum defects show a prominent energy variation, due to the effects of the long range dipole field; this strong energy dependence is not present in the behavior of the eigenquantum defects of the $\bar{\mathbf{K}}$ matrix shown in Fig. 3-1. The strong energy dependence of the $\mathbf{K}$ matrix eigenquantum defects makes it difficult to extrapolate their values to the region of negative energies. The eigenquantum defects for the eigenchannels labeled as $0.55^2\Sigma^+$ and $0.88^2\Sigma^+$ experience an avoided crossing at $E \approx 0.03\,au$. The $0.55^2\Sigma^+$ eigenquantum defect continues to resonantly rise on the high energy side of the avoided crossing, intersecting 0.5 at $E \approx 0.07\,au$. This conspicuous behavior is due to a molecular shape resonance, whose properties are explored in more detail in **Chapter 4**.

tronic states at larger internuclear distances, which cannot be treated in the perturbative limit. This configuration mixing, that becomes important as the internuclear separation increases, is responsible for the predissociation of various Rydberg states. Predissociation has been observed in experimental spectra and it remains a theoretical challenge to explain these strongly series, n^*, and rotation-dependent measurements. Treatment of predissociation is feasible within the present framework. The dynamical effects of small amplitude vibrations of the nuclei about the equilibrium bond length can also be accounted for by calculating the derivatives of the reaction matrix components with respect to internuclear distance. This will help establish quantitative relationships between measured perturbation and autoionization matrix elements and various parameters that define the ion-core potential.

An important extension of the theory would be to polyatomic molecules with non-linear geometries. These systems do not possess cylindrical symmetry, which allows for a separation of variables in the Schrödinger equation at short range. Since separability is not a requirement in the theory presented here, the bound or free electron properties for these molecules can be treated with the same technique without a significant increase in computational burden. This is a decisive step toward generalizing the application of reaction matrix theories to systems more complicated than diatomics and will provide valuable tools to molecular spectroscopists.

The use of the analytical Coulomb functions given in this work is best restricted to values of the effective principal quantum number that are greater than the maximum value of the orbital angular momentum quantum number that enters the calculation. This leads to difficulties in the study of very tightly bound Rydberg levels with low values of the effective principal quantum number because unphysical solutions in this energy range will be obtained if Seaton's analytical Coulomb functions are used [112]. It is necessary to define the pair of basis solutions numerically in the context of generalized quantum defect theory to study these very low lying bound states. Such a numerical approach is described in reference [66].

It is shown in **Chapter 4** that the formalism developed in this work permits accurate predictions of experimental results and can guide in formulating qualitative interpretations of physical interactions. We believe the unified theory presented here, along with its fundamental simplifications, should make *ab initio* reaction matrix methods accessible to experimentalists in their analyses of molecular spectra, and to theorists in their quantitative computation and qualitative explanation of molecular electronic structure, and molecular dynamics.

3.4 Mathematical Appendix A

In the Born-series expansion, we define:

$$M_{\alpha l}^{(0)}(r) = f_l(r)\delta_{\alpha l} \tag{3.4.80}$$

and compute by iteration

$$M_{\alpha l}^{(n)}(r) = f_l(r)\delta_{\alpha l} + 2\sum_{l'=0}^{l_{\max}} \int_0^\infty dr' G_l(r,r') M_{\alpha l'}^{(n-1)}(r') \widetilde{V}_{l'l}^{(0,\lambda)}(r',R) \tag{3.4.81}$$

until the input becomes identical to the output (in Eq. 3.4.81, $G_l(r,r')$ is the standard radial Green's function, given in Eq. 3.27). However, the infeasibility of this approach can be understood by testing the convergence properties of Eq. 3.4.81. Define the norm of a function by [140]

$$\|f(x)\| = max\,(|f(x)|) \qquad 0 \leq x \leq \infty \tag{3.4.82}$$

and ask that at convergence

$$\left\| M_{\alpha l}^{(n)}(r) - M_{\alpha l}^{(n-1)}(r) \right\| \to 0. \tag{3.4.83}$$

The Banach Fixed-Point theorem [140] is used to establish convergence for a large class of iteration methods. The theorem requires k-contractivity for convergence (the iteration operator must reduce the distance between any two members of a closed non-empty set in a given Banach space by a multiplicative factor $k < 1$). For our integral operator in Eq. 3.4.81, k-contractivity results in a set of statements [140], including the following two:

For convergence,

(1) There must be a number Δ_l such that

$\left|G_l(r,r')\widetilde{V}_{ll}^{(0,\lambda)}(r,R)\right| < \Delta_l(L) \quad \text{for all } r,r' \in [0,L]$

(2) $L\Delta_l(L) < 1$ as $L \to \infty$. (3.4.84)

The second statement can be seen to be violated for electrostatic potentials. The r dependent part of the potential near the ion-core varies as $-\frac{Z_o}{r}$ where Z_o is a positive integer or zero. We exclude the case of a pure Coulomb field $Z_o = 1$. Thus, the reduced perturbing potential, $\widetilde{V}_{ll}^{(0,\lambda)}$, has a divergence at $r = 0$ that varies as $\frac{|Z_0-1|}{r}$. As r decreases along the line $r = r'$, Eq. 3.23 shows that $G_l(r,r) \sim r$ as $r \to 0$, bounding $\Delta_l(L)$ from below by $|Z_o - 1|$, and violating statement (2) above.

This result indicates the need for a different iteration scheme.

3.5 Mathematical Appendix B

From the properties of the spherical Bessel functions, all elements of $\mathbf{\Lambda}$ are zero except those of the form $\Lambda_{jl,j'l}$, and those are non-zero by the properties of the scale factors, k, for finite $\tilde{b}$. In addition, the matrix is highly degenerate, because $\Lambda_{jl,j"l} = \Lambda_{jl,j'l}\,\frac{\tilde{j}_l(k_{j"l}r_o)}{\tilde{j}_l(k_{j'l}r_o)}$. This reduces the rank of $\mathbf{\Lambda}$ to $l_{\max}+1$ even though it is a square matrix with each dimension $j_{\max}(l_{\max}+1)$. The *singular value decomposition (SVD)* of $\mathbf{\Lambda}$ [126] is

$$\mathbf{\Lambda} = \mathbf{U}^T\mathbf{D}\mathbf{V}, \tag{3.5.85}$$

where $\mathbf{U}$ and $\mathbf{V}$ are orthogonal matrices and $\mathbf{D}$ is a diagonal matrix of the same rank as $\mathbf{\Lambda}$. Since the rank of $\mathbf{\Lambda}$ is $l_{\max}+1$, $\mathbf{D}$ has $l_{\max}+1$ non-zero elements. In the next step, we will need the following corollary:

Corollary: The matrix $(\epsilon\mathbf{I} - 2\mathbf{H})$ is singular if and only if ϵ is an eigenvalue of $2\mathbf{H}$.

Proof: If ϵ is an eigenvalue of $2\mathbf{H}$ then the determinant of $(\epsilon\mathbf{I}-2\mathbf{H})$ is zero and therefore singular. Eigenvector $\vec{\nu}_k$ of $2\mathbf{H}$ with eigenvalue ϵ_k satisfies

$$(\epsilon\mathbf{I}-2\mathbf{H})\vec{\nu}_k = (\epsilon-\epsilon_k)\vec{\nu}_k.$$

The set of eigenvalues of $(\epsilon\mathbf{I}-2\mathbf{H})$ is $\{\epsilon-\epsilon_k\}$ where ϵ_k are the eigenvalues of $2\mathbf{H}$. If the matrix $(\epsilon\mathbf{I}-2\mathbf{H})$ is singular, at least one of its eigenvalues must be equal to zero, so ϵ must be equal to an eigenvalue of $2\mathbf{H}$. QED.

Clearly, the eigenvalues ϵ_k in the proof correspond to the simple poles of the $\mathbf{R}$-matrix, defined in this context by,

$$R_{ll'} = \sum_{k=1}^{\infty} \frac{X_{k,l}(r_o)X_{k,l'}(r_o)}{E_k-\frac{\epsilon}{2}}, \tag{3.5.86}$$

where $X_k(\vec{r})$ is the k'th eigenstate of the Hamiltonian $\mathbf{H}$ and E_k is the corresponding eigenenergy. If we choose a value for ϵ that does not coincide with any of the eigenvalues of $2\mathbf{H}$, then $(\epsilon\mathbf{I}-2\mathbf{H})$ is non-singular, and the eigenvalue equation for the logarithmic derivatives, b, can be written in standard form as an eigenvalue problem for $\frac{1}{b-\tilde{b}}$ with eigenvectors $\mathbf{V}\vec{a}$ as follows ,

$$\begin{gathered}(\epsilon\mathbf{I}-2\mathbf{H})\vec{a} = (b-\tilde{b})\mathbf{\Lambda}\vec{a}\\ \mathbf{\Lambda} = \mathbf{U}^T\mathbf{D}\mathbf{V} \quad \text{so}\\ [\mathbf{U}(\epsilon\mathbf{I}-2\mathbf{H})\mathbf{V}^T]^{-1}\mathbf{D}(\mathbf{V}\vec{a}) = \left(\frac{1}{b-\tilde{b}}\right)(\mathbf{V}\vec{a}).\end{gathered}$$

$\mathbf{D}$ has $l_{\max}+1$ non-zero diagonal components, so we find exactly $l_{\max}+1$ logarithmic derivatives, b_β.

3.6 Mathematical Appendix C

Corollary: The solutions $\vec{M}_\beta(r)$ are linearly independent if all the elements of the set $\{b_\beta\}$ are distinct.

Proof: Suppose the eigenvalues b_β are distinct. Since the functions $M_{\beta,l}(r)$ solve the coupled equations, we have

$$\sum_{l'=0}^{l_{max}} D_{ll'} M_{\beta,l'}(r) = 0, \tag{3.6.87}$$

$$D_{ll'} = \left(\frac{d^2}{dr^2} - \frac{l(l+1)}{r^2} + \epsilon + \frac{2}{r}\right)\delta_{ll'} - 2\tilde{V}_{ll'}^{0,\lambda}(r,R). \tag{3.6.88}$$

From Eq.3.6.88 we get,

$$\sum_{l=0}^{l_{max}}\sum_{l'=0}^{l_{max}}\left(\int_0^{r_o} dr' M_{\beta',l}(r') D_{ll'} M_{\beta,l'}(r') - \int_0^{r_o} dr' M_{\beta,l}(r') D_{ll'} M_{\beta',l'}(r')\right) = 0. \tag{3.6.89}$$

Equation 3.6.89 simplifies upon integrating by parts to give:

$$(b_{\beta'} - b_\beta)\sum_{l=0}^{l_{max}} M_{\beta',l}(r_o) M_{\beta,l}(r_o) = 0. \tag{3.6.90}$$

Since $b_{\beta'} \neq b_\beta$, it follows from Equation 3.6.90 that $\sum_{l=0}^{l_{max}} M_{\beta',l}(r_o)M_{\beta,l}(r_o) = 0$. Consider the matrix $\mathbf{X}$ whose rows are the solutions $\vec{M}_\beta(r)$,

$$\mathbf{X} = \begin{pmatrix} M_{10}(r) & M_{11}(r) & \cdots & M_{1l_{\max}-1}(r) & M_{1l_{\max}}(r) \\ \vdots & \vdots & \cdots & \vdots & \vdots \\ M_{(l_{\max}+1)0}(r) & M_{(l_{\max}+1)1}(r) & \cdots & M_{(l_{\max}+1)l_{\max}-1}(r) & M_{(l_{\max}+1)l_{\max}}(r) \end{pmatrix}. \tag{3.6.91}$$

At $r = r_o$, Eq. 3.6.90 shows that the rows of the matrix $\mathbf{X}$ are mutually orthogonal. Therefore the Wronskian of the solutions $W(r) = \det(\mathbf{X})$ is not zero at $r = r_o$. Then by the uniqueness theorem, the Wronskian never vanishes in the interval $r_o \leq r < \infty$. Hence the solutions $\vec{M}_\beta(r)$ are linearly independent.

Chapter 4

Electronic Spectrum of CaF

4.1 Introduction

Multichannel quantum defect theory(MQDT) uses a scattering formalism to explain the properties of bound and continuum states of an electron interacting with an atomic or molecular ion-core [112, 34]. The equations of MQDT are derived from a few key observations. Far from the ion core, the radius of which extends on the order of 2-3 $\dot{A}$ngstroms, a Coulomb field prevails and the motion of the external electron is separable. Inside the ion-core, complicated many-body interactions dominate and there is no simple description of the electron's motion. However since the ion-core is confined within a small region of space, the electron in a highly excited bound or continuum state samples mostly the region exterior to the ion-core. Therefore the net effect of the ion-core can be incorporated into a few QDT parameters that depend weakly on the total energy of the combined system [30, 43, 78]. These parameters provide a compact representation of all spectroscopic and dynamical observables and can be determined by fitting to experimental data [41, 79].

Although the use of MQDT had been restricted primarily to empirical analyses of data, recent work has focused on the calculation of the quantum defect parameters from first principles. The *ab initio* calculation of these parameters has presented theorists with practical challenges, especially in the determination of body-fixed quantum defect matrices in molecular problems [130]. Most of the *ab initio* techniques use Kohn's variational scheme (**R**-matrix method) [69] to solve for the electronic wavefunction inside the ion-core and the solutions over all space are determined by matching the wavefunctions inside the core to the wavefunctions in the exterior region by the appropriate continuity relations. As a consequence of this boundary matching procedure, the calculated quantities are sensitive to the size of the ion-core. In particular, a large ion-core may result in strong energy dependences of the QDT parameters [5, 52]. In order to use the body-fixed quantum defect matrix in the context of ro-vibrational quantum defect theory [64, 47], it is necessary to remove (or minimize) the energy dependences from the quantum defect matrix [130].

The problem associated with the energy dependence of the body-fixed quantum defect matrix becomes more severe when the system under consideration is a dipolar molecule. CaF^+ has a permanent dipole moment of 8.82 Debye (coordinate origin at the center of mass), and this large value of the dipole moment leads to a long range dipole interaction in the exterior region, in addition to the Coulomb field. In order to use ordinary quantum defect theory, it would be necessary to extend the core out to the asymptotic region, where the potential reduces to a Coulomb field. However, this results in undesired strong energy dependences in the quantum defect matrix. Arif, Jungen, and Roche [5] treated the CaF problem using elliptical coordinates [55] and defining a quantum defect matrix at short range. That treatment, which was successful in describing the entire electronic spectrum of CaF, required the use of the generalized form of quantum defect theory [46, 50] and separability in the radial and angular coordinates of the effective one-electron potential in the exterior region.

In **Chapter 3**, we describe an alternative method for calculating the scattering theory reaction matrix [96]. The method utilizes a Green's function numerical propagation scheme and allows for a reduction of the bounded core volume that enters into Kohn's variational calculation. This results in significant improvements of convergence rate, accuracy, and calculation speed over current methods. It is also shown in **Chapter 3** that information in the calculated reaction matrix, $\mathbf{K}$, can be re-expressed in a form in which the energy dependence is minimized. This is accomplished by defining a new matrix, $\bar{\mathbf{K}}$ [117, 25], by performing a transformation on the $\mathbf{K}$ matrix to remove the effects of the non-spherical long-range dipole field. The effects of the dipole field are in turn absorbed into a new pair of quantum defect basis functions.

The computational procedure developed in **Chapter 3** is applied to the Rydberg electronic structure of CaF in the present chapter. Two purposes are addressed here: first, to validate and demonstrate the practical use of the method developed in **Chapter 3** and, second, to reproduce current experimental results and make predictions about other observables from first principles. These predictions can be used to guide future experiments. One of the goals of this work is to develop physical pictures that can provide causal explanations of specific interactions and the mechanisms responsible for resonance features in the experimental data. The majority of the results presented in this chapter have been published in the Journal of Chemical Physics [118].

We analyze the $^2\Sigma^+$, $^2\Pi$, $^2\Delta$, and $^2\Phi$ Rydberg states of the CaF molecule by determining the body-fixed reaction matrix. Particular emphasis is placed on the high Rydberg states close to ionization and in the continuum. The analysis of the continuum focuses on the structure of the scattering matrix and the resultant features in the integrated ionization cross section, photoelectron angular distribution, and the anisotropy parameter. We show that the energy dependences of these parameters indicate the presence of a molecular shape resonance close to the ionization threshold. The existence of this resonance is a basis for l-specific probes of the dynamics and spectra of CaF.

4.2 Application and Results

In order to reproduce the experimentally observed Rydberg energy levels of CaF accurately [40] it is necessary to include the effect of Rydberg electron penetration into the core region. The most rigorous way to do this is to include a superposition of ion-core states in Eq. 3.4. However, such effects can be incorporated in an effective one-electron potential treatment that includes polarizability terms (a polarizable core) [86]. We take the explicit form of this potential from Arif, Jungen, and Roche [5], using coordinates illustrated in Fig. 4-1.

$$\begin{aligned} V^{(0)}(\vec{r}) \rightarrow V_{eff}(\vec{r}) = & -\left[\frac{Z_1}{r} + \frac{Z_2}{r_2}\right] \\ & + \left[-\alpha_1 f_1^2 \frac{1}{2r^4} + \alpha_1 f_1 \frac{Z_2 \cos\theta}{r^2 R^2} - \alpha_2 f_2^2 \frac{1}{r_2^2} + \alpha_2 f_2 \frac{Z_1 \cos\theta_2}{r_2^2 R^2}\right] \\ & - \frac{2\alpha_1 f_1 \alpha_2 f_2}{R^5}\left[\frac{Z_1 \cos\theta}{r^2} + \frac{Z_2 \cos\theta_2}{r_2^2}\right] \\ & + \frac{\alpha_1 f_1 \alpha_2 f_2}{R^3 r^2 r_2^2}\left[2\cos\theta\cos\theta_2 + \sin\theta\sin\theta_2\right] + V_l^{(Ca^{++}core)}(r). \end{aligned} \tag{4.2.1}$$

The expression in Eq. 4.2.1 contains the following interactions:

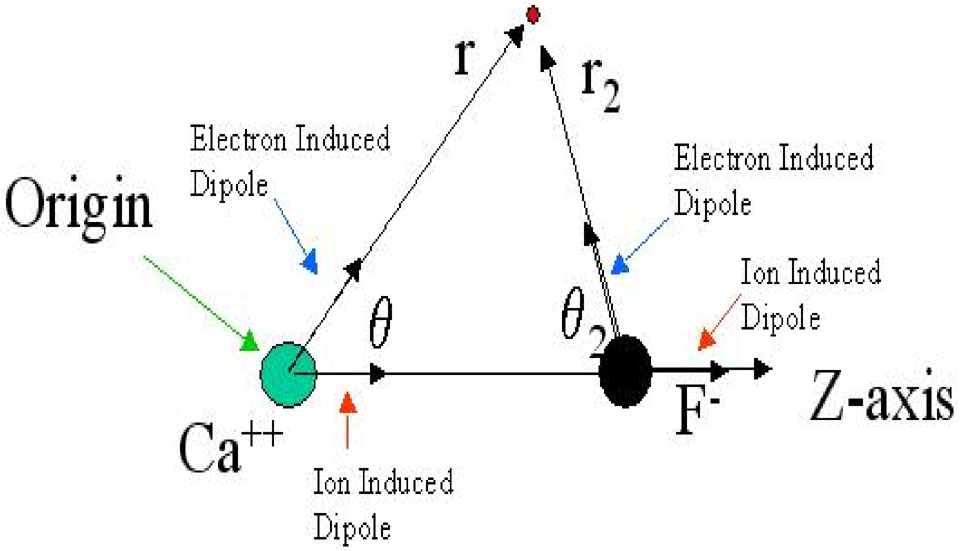

Figure 4-1: Coordinates used in the CaF calculation. The origin is fixed at the Ca nucleus.

(A) The Coulomb interaction between the integer charges Z_1 and Z_2 on the calcium and the fluorine atoms and the Rydberg electron.

(B) The monopole-dipole interaction of the Rydberg-electron-induced dipole on one ion with the integer charge on the other ion (See Figure 4-1).

(C) The dipole-dipole interaction of the electron-induced and ion-induced dipoles on opposite centers.

(D) The dipole-dipole interaction of the two electron-induced dipoles on opposite centers.

(E) A Ca^{++} core correction that includes core-penetration(deshielding) effects.

(F) All terms independent of the electronic coordinate, r, are part of the energy of the ion-core and are not considered explicitly in the potential. Accordingly, the zero of energy is set at the minimum of the potential curve of the ion-core when $R = R_e^+$, the equilibrium bond length, and the Rydberg electron is removed to $r \to \infty$.

Table 4.1 explains the symbols in Eq. 4.2.1 and lists their numerical values. The last term in Eq. 4.2.1, $V_l^{(\mathrm{Ca}^{++}\ \mathrm{Core})}(r)$, is a pseudopotential that approximates the many-body interactions of the Rydberg electron inside the Ca^{++} electron distribution. This potential depends on the orbital angular momentum quantum number, l, and its terms have been

Table 4.1: Terms that define the Electron ↔ Core Interaction from Arif *et al.*[5]

Term	Symbol	Value (au)
Ca^{++} Charge	Z_1	2
F^{-} Charge	Z_2	-1
Ca^{++} Polarizability	α_1	3.5
F^{-} Polarizability	α_2	4.7
Polarizability Cutoff Function for Ca^{++}	$f_1(r)$	$\left[1 - e^{-(r/r_{1c})^6}\right]^{(1/2)}$
Polarizability Cutoff Function for F^{-}	$f_2(r_2)$	$\left[1 - e^{-(r_2/r_{2c})^6}\right]^{(1/2)}$
The Radius of the Ca^{2+} Atomic Core	r_{1c}	1.6
F^{-} Ionic Radius	r_{2c}	2.3
Equilibrium Bond Length of CaF^{+}	R_e^{+}	3.54

Table 4.2: Pseudo-potential parameters for Ca^{++} from Aymar et al.[6]

	l = 0	1	2	$l \geq 3$
a_1^l	4.0099	4.2056	3.5058	3.7741
b_1^l	13.023	12.658	12.399	13.232
c_1^l	2.1315	2.0186	2.2648	3.1848
r_{1c}^l	1.6352	1.5177	1.6187	0.7150

optimized to reproduce the experimentally observed quantum defects of the atomic Ca^{+} ion [6]. The form of this potential is

$$V_l^{(\mathrm{Ca}^{++}\ \mathrm{Core})}(r) = -\frac{1}{r}\left[(Z_n - Z_1)e^{-a_1^l r} + b_1^l r e^{-c_1^l r}\right] + \frac{\alpha_1}{2r^4}\left\{e^{-\left(\frac{r}{r_{1c}^l}\right)^6} - e^{-\left(\frac{r}{r_{1c}}\right)^6}\right\} \tag{4.2.2}$$

where $Z_n = 20$ is the total charge on the Ca nucleus and r_{1c}^l is the l dependent size of the Ca^{++} core. The pseudopotential parameters that we use in this calculation are listed in Table 4.2. It should be noted that the physical picture we are using in this model resembles ligand-field theory [102]. The Rydberg energy levels we calculate can be understood to correspond to the Rydberg levels of the Ca^{+} atom perturbed by an external ligand, F^{-}. Our choice of the coordinate origin to coincide with the center of the Ca nucleus, although motivated by convenience, coincides with that picture (the molecular center of mass must be used in a theory that includes rotating molecule effects. The calculation presented here is tailored toward the calculation of the body-fixed reaction matrix and the following results are compared with deperturbed spectroscopic data for the non-rotating molecule).

Details of the Calculation

(1) The choice of $\mathbf{r}_o$, the radius of the spherical dividing surface

Several considerations go into the determination of the value of r_o that appears in the variational expression in Eq. 3.29. From a practical point of view, we would like r_o to be on the order of several Bohr so that the numerical computations of the expressions in Eq. 3.36 are fast. However, if r_o is made too small, then some of the high-l members of the basis set functions in Eq. 3.33 will have very small amplitude in the integration region, resulting in numerical instabilities. This trade-off can be summarized by the following statements.

(A) r_o must be small enough so that the magnitude of $V^{(eff)}(\vec{r})$ differs from its asymptotic value at least by 10%.

(B) r_o needs to be large enough so that the truncated l expansion that accounts for all l-mixing in Eq. 3.33 converges for $r < r_o$.

Tests show that r_o in the range from 4 to 6 au works well for $l \leq 7$. We use $r_o = 6\,au$. A physical lower bound for r_o is the CaF$^+$ equilibrium bond length, $R_e^+ = 3.54\ au$.

(2) The choice of ε.

Since there are no exact results for this problem, it is not possible to know *a priori* the nature of the energy dependence of the asymptotic reaction matrix. Therefore we calculate the $\bar{\mathbf{K}}$ matrix instead of the $\mathbf{K}$ matrix. As we have demonstrated, the weakly energy dependent $\bar{\mathbf{K}}$ matrix can be used to recover the analytical properties of the strongly energy dependent $\mathbf{K}$ matrix. We determine the $\bar{\mathbf{K}}$ matrix on a coarse energy grid over an interval that extends from negative to positive values of $\epsilon = 2E$ and obtain its energy dependence by interpolation.

(3) The Basis Set

To facilitate the convergence of the calculation, we use a non-orthogonal basis. This allows us to employ a basis set of smaller dimensionality, with 30 radial functions for each l-component and a total of 7 l-components. We design 28 of the 30 radial functions for each l to have a node at $r_o(\tilde{b} = 10)$ and the remaining two radial functions are chosen to have an anti-node at $r_o(\tilde{b} = 0)$. In addition, we exclude a small spherical region of space about the Ca nucleus from the calculations, following Arif, Jungen, and Roche [5]. The excluded region of space, which we refer to as the atomic zone, is defined by electron radial distances $r < r_a \approx 0.8au$. Although this exclusion is not strictly necessary, it facilitates the rapid convergence of the calculation since it excludes the singularity at the origin (the center of

Table 4.3: The Angular Momenta, $\bar{l}$ for CaF

Term	$\bar{s}$	$\bar{p}$	d	f	$\bar{g}$
$\bar{l}$	$-\frac{1}{2}+1.38i$	1.2	2.11	3.04	4.02

the Ca nucleus) from the numerical integrations. Another slight change from the analysis in **Chapter 3** is our choice of the basis for the variational calculation. Spherical Bessel functions can be used, but it is computationally more convenient to use a Fourier basis of the form [5],

$$u_l(r) = a_l sin(k_{lj}r) + b_l cos(k_{lj}r), \tag{4.2.3}$$

where the parameters a_l, b_l, and k_{lj} are determined by the boundary condition $\tilde{b}$ at r_o and normalization [5].

(4) The Angular Momenta $\bar{l}$

The real or complex generalized angular momentum, $\bar{l}$, that are defined in Eq. 3.60 depend on the permanent dipole moment of the CaF$^+$ core. The value of the dipole moment, as measured from the origin located at the Ca nucleus used to define the long-range wave functions, can be calculated using Eq. 3.50. This value is $\mu = -2.33$ *au* at $R = R_e^+$. The values of $\bar{l}$ for $\lambda = 0\,(^2\Sigma^+)$ Rydberg states are given in Table 4.3.

(5) Iteration Procedure

Using the following convergence criterion with the norm of Eq. 3.4.82

$$\left\| M_{\beta\bar{l}}^{(n)}(r) - M_{\beta\bar{l}}^{(n-1)}(r) \right\| \leq 10^{-3} \tag{4.2.4}$$

we achieve convergence in 3 iterations of Eq. 3.43. r is restricted to a finite interval, $r_o \leq r \leq 30$. Each iteration requires less than 10 seconds of computation on a PC. The converged solutions, $M_{\beta\bar{l}}(r)$, used in Eqs. 3.45-3.48, give the $\bar{\mathbf{K}}$ matrix. The inner 5×5 block of the $\bar{\mathbf{K}}$ matrix for the $\lambda = 0$ symmetry, calculated at a reference energy of $\epsilon = -0.02$ and $R = R_e$, is shown in Table 4.4.

Table 4.4: The Reaction Matrix, $\bar{\mathbf{K}}$, for the $^2\Sigma^+$ Rydberg States of CaF. Columns denote the $\bar{l}$ channels and rows denote a particular set of solutions.

$$\begin{pmatrix} 7.1445 & 1.2433 & -1.8086 & 0.0884 & -0.0271 \\ 1.2433 & 0.4920 & 0.2148 & 0.0287 & 0.0008 \\ -1.8087 & 0.2149 & 0.2116 & 0.0578 & 0.0025 \\ 0.0884 & 0.0287 & 0.0577 & -0.2078 & 0.0108 \\ -0.0271 & 0.0008 & 0.0025 & 0.0108 & -0.0925 \end{pmatrix}$$

Large matrix elements of $\bar{\mathbf{K}}$ in Table 4.4 correspond to strong scattering and large contributions from the irregular Coulomb functions. We see that the off-diagonal elements in the upper 3×3 block are large and comparable in size to the diagonal elements, signaling significant l-mixing in this class of angular momentum states. Clearly this upper-block belongs to the penetrating states whereas the 2×2 lower block is nearly uncoupled from the penetrating states and belongs to the non-penetrating states . The reaction matrix elements progressively get smaller as l increases for non-penetrating states and they can be more simply treated with an approximate theory, such as the point dipole model of Watson [134].

Bound States

For electronic energies below the ionization threshold, one can set $\varepsilon = -\frac{1}{\nu^2}$, where ν is the effective principal quantum number that must be regarded as a running number at this stage. The quantization condition [111, 25] for bound states is

$$\det(\tan \pi v \delta_{\alpha\bar{l}} + \bar{K}_{\alpha\bar{l}}) = 0. \tag{4.2.5}$$

The eigenquantum defects are defined as,

$$\tilde{\delta}_i = -\frac{1}{\pi} arctan(\bar{K}_i), \tag{4.2.6}$$

where $\bar{K}_i$ is the i'th eigenvalue of the reaction matrix, $\bar{\mathbf{K}}$. According to the eigenvalue equation (Eq. 4.2.5), the bound state quantum defects must lie on the energy-dependent eigenquantum defect curves of the $\bar{\mathbf{K}}$ matrix. The eigenquantum defect curves of CaF that characterize the $^2\Sigma^+$,$^2\Pi$,$^2\Delta$, and $^2\Phi$ Rydberg series are plotted in Fig.4-2. As expected, they show a very smooth and slow energy dependence. The experimentally observed quantum defects from Berg *et al.* [7] are marked as filled circles on the figure. Most of the experimental values of the eigenquantum defects fall very near our theoretical series curves, verifying the trend along the curves as well as the numerical accuracy of the points on them. Our quantum defects lie within ±0.02 of the experimental results, with the exception of isolated deviations visible in the $0.88^2\Sigma^+$ and $0.36^2\Pi$ curves. Possible sources of deviation include interactions with the repulsive $^2\Sigma^+$ and $^2\Pi$ states, which have the $\mathrm{Ca^+4s{+}F2p}\sigma^{-1}$ and $\mathrm{Ca^+4s{+}F2p}\pi^{-1}$ hole electronic configurations respectively. The plus signs shown in each figure denote the eigenquantum defects obtained from a global ro-vibrational MQDT fit to 617 previously assigned energy levels of CaF in the $7 < n^* < 18$ region [37]. The global fit results for the eigenquantum defects in the high n^* region are less sensitive to the local perturbations due to the repulsive states and therefore agree more closely with the theoretical values.

The 3-dimensional plots of the calculated $^2\Sigma^+$ bound state wavefunctions, $r\Psi_{n^*}(\vec{r})$, in the $n^* = 10$ region, for the $\phi = 0$, $x - z$ azimuthal plane, are shown in Fig. 4-3. The spectral decomposition [5] of these states are reported in Table 4.5 through the eigenfunction expansion coefficients. While it would be an almost impossible task to calculate an excited electronic wavefunction with such a high value of the principal quantum number using a traditional *ab initio* method of computation, the current formalism achieves accurate wavefunctions with minimal effort once the iterative equations are solved. Figure 4-3A shows a plot of the X $^2\Sigma^+$ ground electronic state calculated using the ligand-field model of Rice, Martin and Field [102]. All the amplitude in this low-lying state is confined within $5\,Bohr$ of the origin. The angular structure seen in the X state resembles the angular structure of the $10.55^2\Sigma^+$ wavefunction shown in Fig. 4-3B. Both states are approximate mixtures of s and p partial-l waves. This is in agreement with Mulliken's rule [90], which states that every Rydberg orbital is built upon an innermost lobe which does not change in shape or nodal position as a function of n^*("ontogeny recapitulates phylogeny"). The X $^2\Sigma^+$ state is the series terminus for the 10.55 state. Figure 4-3C shows a plot of the $10.88^2\Sigma^+$ state, whose series terminus orbital is the B $^2\Sigma^+$ state [7]. The wavefunction for this state is polarized behind the F^- ion and it is approximately a $p + s$ partial-l wave mixture. This has important consequences for the relative intensities of transitions that may be observed out of this state. Figure 4-3D displays the wavefunction for the $10.16^2\Sigma^+$ state, whose series

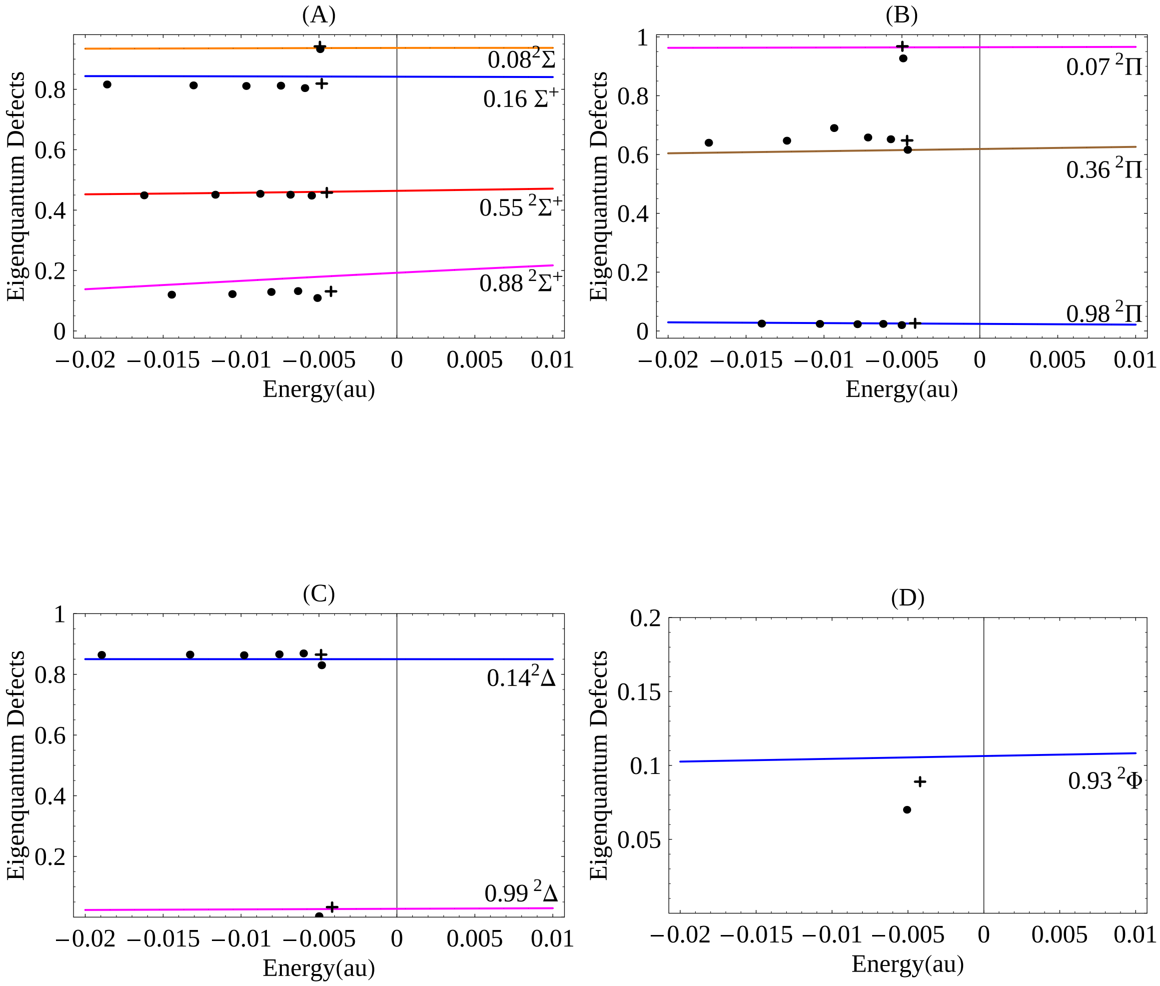

Figure 4-2: (A) $^2\Sigma^+$ State eigenquantum defects of CaF from the $\bar{\mathbf{K}}$ matrix. The filled circles are the experimentally observed $^2\Sigma^+$ Rydberg series and the plus signs denote the eigenquantum defects obtained from a global MQDT fit by Field et. al. [37]. The scatter in the experimental eigenquantum defects seen in the $0.88^2\Sigma^+$ series in the $E = -0.006\,au$ region is likely due to a perturbation interaction with the Ca^+4s+F2pσ^{-1} hole $^2\Sigma^+$ repulsive state. (B) $^2\Pi$ State eigenquantum defects of CaF. The experimental and fit data points are marked as in panel A. The scatter in the experimental eigenquantum defects seen in the $0.36^2\Pi$ series in the $E = -0.009\,au$ region is likely due to a perturbation interaction with the Ca^+4s+F2pπ^{-1} hole $^2\Pi$ repulsive state. (C) $^2\Delta$ State eigenquantum defects of CaF. The experimental, and fit data points are marked as in panel A. (D) $^2\Phi$ State eigenquantum defects of CaF. The experimental, and fit data points are marked as in panel A.

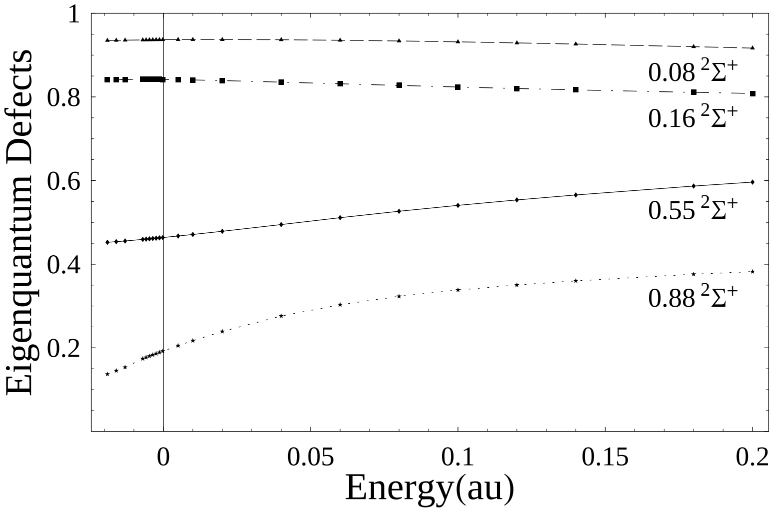

Figure 4-4: The $\bar{\mathbf{K}}$ eigenquantum defects over a larger domain of collision energy. The 0.55 and 0.88 $^2\Sigma^+$ eigenquantum defect curves smoothly rise with increasing collision energy. The 0.16 and 0.08 $^2\Sigma^+$ eigenquantum defects are approximately constant on the energy interval.

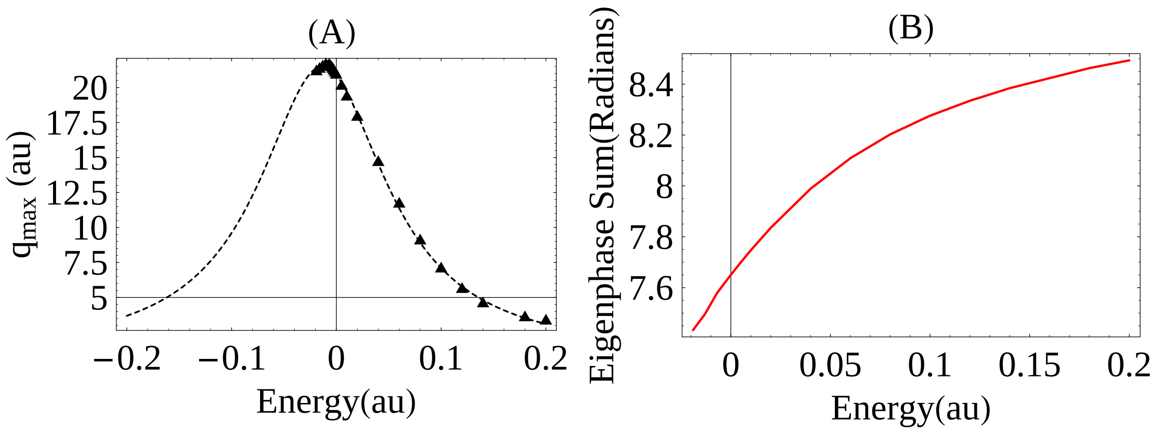

Figure 4-5: (A) The largest eigenvalue of the lifetime matrix, q_{max}, as a function of energy. The theoretical data points are marked with triangles and the dashed curve is a Lorentzian fit to the data points. The Lorentzian fit gives the resonance center energy as $E_{res} = -0.013\,au$ and resonance width as $\Gamma = 0.15\,au$. (B) The eigenphase sum as calculated from the $\bar{\mathbf{K}}$ matrix. The overall rise in the eigenphase sum may indicate a shape resonance. However, the eigenphase sum rises on very a wide interval and it cannot be satisfactorily fit to the standard Breit-Wigner form.

peaks in the plot of q_{max} as a function of energy can be identified with resonances [27]. The resonance lineshape in q_{max} can be fitted to a Lorentzian form to determine the resonance energy and width [27, 125]. The calculated q_{max} from the $\bar{\mathbf{S}}$ matrix is shown in Fig. 4-5A. The peak near $E \approx -0.01\,au$ decisively establishes the existence of the shape resonance. The Lorentzian fit (dashed curve in the figure) to the theoretical data points yields the resonance center energy and width as $-0.013\,au$ and $0.15\,au$ respectively.

It shall be shown in **Chapter 5** that the molecular shape resonance is due to the trapping of the continuum electron behind a barrier on the F^- ion, which arises in the *adiabatic* molecular effective potential. The theory of the *adiabatic* molecular effective potential for the continuum electron is explained by Dourneuf et al. [23]. The lifetime determined here can be interpreted as the time it takes for the electron to tunnel across the barrier on the F^- ion to the classically allowed region in the adiabatic potential. Since the resonance is very broad, it affects the properties of the electronic spectrum over the whole energy domain studied here. The effects of the shape resonance on the electronic spectrum is best understood in terms of the probability of decay, or branching ratios, into the collision eigenchannels. The branching ratio, B, into a particular eigenchannel j is given by,

$$\bar{B} = |\tilde{\mathbf{V}}.\tilde{\mathbf{U}}_j|^2, \tag{4.2.8}$$

where $\tilde{\mathbf{V}}$ the eigenvector of $\bar{\mathbf{Q}}$ corresponding to q_{max} and $\tilde{\mathbf{U}}_j$ is the eigenvector of $\bar{\mathbf{K}}$ associated with the eigenchannel. The branching ratios to four of the eigenchannels for $E = E_{res}$ and $E = 0.2\,au$ are given in Table 4.4. The values indicate that the $0.88^2\Sigma^+$ eigenchannel contains a prominent resonance character near the resonance center. This is consistent with the behavior of the corresponding eigenquantum defect, which shows the largest rise in Fig. 4-4. The structure of the $10.88\,^2\Sigma^+$ wavefunction shown in Fig. 4-3 further illuminates the point. The wavefunction in this eigenchannel is polarized *behind* the F^- and the electron has to tunnel across the repulsive barrier on the ligand to reach the asymptotic region. The values of branching ratios at high collision energies show that there is no preference for decay into either the 0.55 or the 0.88 eigenchannels. This is a consequence of the vanishing influence of the shape resonance when the collision energy exceeds far above the energy of the resonance center. Table 4.5 also reports the branching ratios to the integer-l Rydberg channels. These branching ratios correspond to the squared components of the transformed

Table 4.6: The Branching Ratios

	$0.55\,^2\Sigma^+$	$0.88\,^2\Sigma^+$	$0.16\,^2\Sigma^+$	$0.08\,^2\Sigma^+$	s	p	d	f
$B\,(E = E_{res})$	0.16	0.80	0.04	0.004	0.20	0.77	0.03	0.003
$B\,(E = 0.2\,au)$	0.47	0.47	0.05	0.01	0.19	0.74	0.02	0.001

lifetime matrix eigenvector $\tilde{\mathbf{V}}' = \mathbf{F}.\tilde{\mathbf{V}}$, where $\mathbf{F}$ is the dipole matrix defined in Eq. 3.54. It is seen that the largest probability of decay is to the p-type Rydberg channels.

The Integer-l Reaction Matrix Eigenquantum Defects

The eigenquantum defects obtained from the integer-l reaction matrix, $\mathbf{K}$, for the $\lambda = 0$ symmetry, defined in Eq. 3.48 are shown in Fig. 4-6. The eigenquantum defects possess a conspicuous energy dependence in contrast to the smooth energy dependence displayed by the $\bar{\mathbf{K}}$ matrix, shown in Fig. 4-4. The strong energy dependence in the $\mathbf{K}$ matrix is due to the long-range dipole field; the effects of the dipole field are removed from the $\bar{\mathbf{K}}$ matrix and included instead in the $(\bar{f}, \bar{g})$ base-pair in the $\bar{K}$ theory (see **Chapter 3**). This highlights the success of the $\bar{K}$ theory in minimizing the energy dependence of the reaction matrix.

Figure 4-7 shows the energy dependence of the squared magnitude partial-l decomposition of the $0.55^2\Sigma^+$ and $0.88^2\Sigma^+$ collision eigenchannels. The results indicate that these states are primarily s and p mixed and that their partial-l decomposition changes rapidly across the avoided crossing. These rapid changes in the partial-l character of the eigenchannels cause important interference effects, which are explored further below in the context of the photoionization properties of CaF. The mechanics of the energy of evolution of the partial-l decompositions can be understood in relation to the influence of the shape resonance. The p-dominated 0.88 eigenchannel has a prominent resonance character near the ionization threshold. The p-dominant increasing eigenphase would pass through the 0.55 curve, but undergoes an avoided crossing (Fig. 4-6), so the p-dominant curve is labeled 0.88 near threshold and 0.55 beyond the energy range affected by the resonance of Fig. 4-5. At higher energy, the shape resonance effect decreases, leaving the 0.55 and 0.88 states in a different, more pure, s and p mixture than the mixture seen at lower energy.

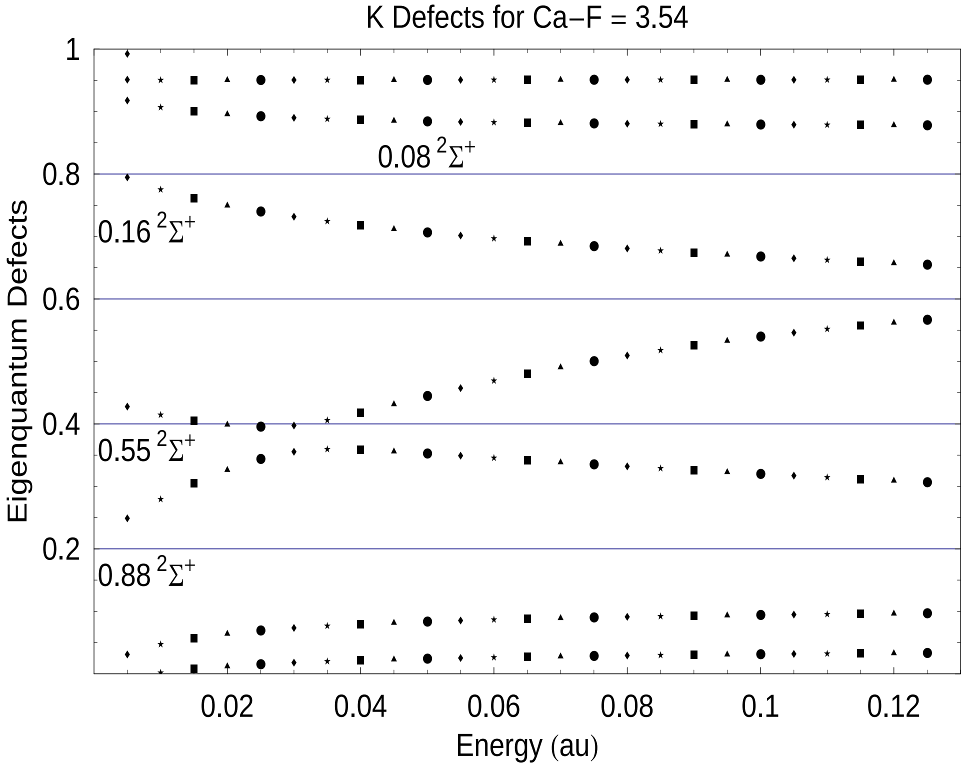

Figure 4-6: The eigenquantum defects obtained from the integer-l **K** matrix. These curves correlate with the 0.55, 0.16, 0.88, 0.08, and $0.06^2\Sigma^+$ Rydberg series at $E < 0$. The eigenquantum defects for the 0.55 and 0.88 eigenchannels display an avoided crossing at $E \approx 0.03\,au$. The partial-l decomposition of these eigenchannels vary rapidly across the avoided crossing (see Fig. 4-7).

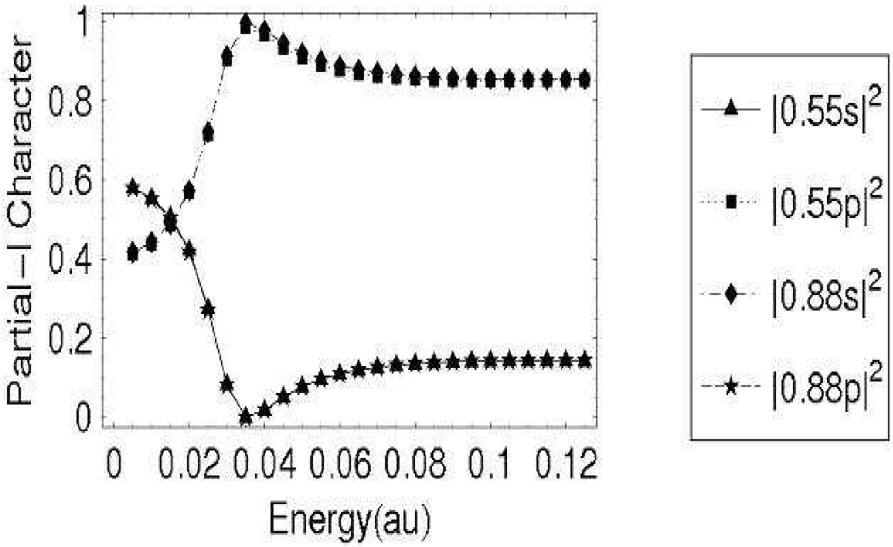

Figure 4-7: The energy dependence of the squared magnitude of the partial-l decomposition of the 0.55 and 0.88 eigenchannels. The plotted coefficients are the squares of the components of the corresponding eigenvectors of the integer-l $\mathbf{K}$ matrix . Four curves are plotted, but only two curves are visible. This is because the $|0.55s|^2$ curve overlaps with the $|0.88p|^2$ curve and the $|0.55p|^2$ curve overlaps with the $|0.88s|^2$ curve. The 0.55 eigenchannel, which is a dominant s wave near the ionization threshold becomes a dominant p wave above the avoided crossing. Conversely, the 0.88 eigenchannel, which is a dominant p wave near the ionization threshold becomes a dominant s wave above the avoided crossing.

4.2.1 Analytical Continuation of the Integer K Matrix to Negative Energy

The calculation of the **K** matrix at negative energy requires careful analysis, because the transformation from the $\bar{\mathbf{K}}$ to **K** given in Eq. 3.79 is only valid at positive energy. The analytical continuation of this transformation does not simply follow from the replacement $k = \frac{1}{\nu}$, because the phase matrices in Eq. 3.79 are not analytic at the ionization threshold. In this section, we derive this transformation to the integer-l representation at negative energy and investigate the energy behavior of the **K** matrix elements. The results in this subsection have not been published previously in [118]. We let $E < 0$ denote the collision energy in atomic units. We define the quantities,

$$\epsilon = 2E \qquad \nu = \sqrt{-\frac{1}{\epsilon}} \tag{4.2.9}$$

For $\epsilon < 0$, the Dipole-Coulomb functions, $\bar{\mathbf{f}}$ and $\bar{\mathbf{g}}$, defined in **Chapter 3** have the following forms,

$$\bar{\mathbf{f}}(r) = \tfrac{sin\pi\nu}{(2\nu)^{1/2}}\xi(r)\bar{\varpi} - cos\pi\nu\left(\tfrac{\nu^3}{2}\right)^{1/2}\Theta(r)\bar{\varpi}^{-1} \tag{4.2.10}$$

$$\bar{\mathbf{g}}(r) = -\tfrac{cos\pi\nu}{(2\nu)^{1/2}}\xi(r)\bar{\varpi} - sin\pi\nu\left(\tfrac{\nu^3}{2}\right)^{1/2}\Theta(r)\bar{\varpi}^{-1}, \tag{4.2.11}$$

where,

$$\bar{\varpi}_{\bar{l}\bar{l}'} = \nu\left(\Gamma(\nu+\bar{l}+1)\Gamma(\nu-\bar{l})\right)^{1/2}\delta_{\bar{l}\bar{l}'} \qquad for\, Im(\bar{l}) = 0 \tag{4.2.12}$$

$$\bar{\varpi}_{\bar{l}\bar{l}'} = \nu\left|\Gamma(\nu - i\bar{l} + \tfrac{1}{2}(1-i))\right|\delta_{\bar{l}\bar{l}'} \qquad for\, Im(\bar{l}) \neq 0, \tag{4.2.13}$$

and the definition of $\bar{l}$ is given in **Chapter 3**. The asymptotic limits of $\xi(r)$ and $\Theta(r)$ are given as,

$$\xi(r\to\infty) = \left(\frac{2r}{\nu}\right)^{-\nu} e^{r/\nu} \tag{4.2.14}$$

$$\Theta(r\to\infty) = \left(\frac{2r}{\nu}\right)^{\nu} e^{-r/\nu} \tag{4.2.15}$$

For the $\bar{\mathbf{K}}$ normalized solutions, we have the asymptotic limit

$$\bar{\mathbf{M}}(r) = \bar{\mathbf{f}}(r) - \bar{\mathbf{g}}(r)\bar{\mathbf{K}}. \tag{4.2.16}$$

We would like to relate these to the alternate set of solutions,

$$\mathbf{M}(r) = \mathbf{f}(r) - \mathbf{g}(r)\mathbf{K}, \tag{4.2.17}$$

where $\mathbf{K}$ is the reaction matrix in the integer l representation. The ordinary Coulomb functions can be expressed as [112],

$$\mathbf{f}(r) = \tfrac{sin\pi\nu}{(2\nu)^{1/2}}\xi(r)\mathbf{P}\varpi - cos\pi\nu\left(\tfrac{\nu^3}{2}\right)^{1/2}\Theta(r)\mathbf{P}\varpi^{-1} \tag{4.2.18}$$

$$\mathbf{g}(r) = -\tfrac{cos\pi\nu}{(2\nu)^{1/2}}\xi(r)\mathbf{P}\varpi - sin\pi\nu\left(\tfrac{\nu^3}{2}\right)^{1/2}\Theta(r)\mathbf{P}\varpi^{-1}, \tag{4.2.19}$$

where

$$\varpi_{ll'} = \nu\left(\Gamma(\nu+l+1)\Gamma(\nu-l)\right)^{1/2}\delta_{ll'} \tag{4.2.20}$$

$$\mathbf{P}_{ll'} = (-1)^l\delta_{ll'}. \tag{4.2.21}$$

Using Eqs. 4.2.10 and 4.2.11, Eq. 4.2.19 can be rewritten as,

$$\bar{\mathbf{M}} = \frac{\xi}{(2\nu)^{1/2}\pi}\left(sin\pi\nu\bar{\varpi} + cos\pi\nu\bar{\varpi}\bar{\mathbf{K}}\right) + \Theta\left(\frac{\nu^3}{2}\right)^{1/2}\left(sin\pi\nu\bar{\varpi}^{-1}\bar{\mathbf{K}} - cos\pi\nu\bar{\varpi}^{-1}\right). \tag{4.2.22}$$

Similarly,

$$\mathbf{M} = \frac{\xi}{(2\nu)^{1/2}\pi}\left(sin\pi\nu\mathbf{P}\varpi + cos\pi\nu\mathbf{P}\varpi\mathbf{K}\right) + \Theta\left(\frac{\nu^3}{2}\right)^{1/2}\left(sin\pi\nu\mathbf{P}\varpi^{-1}\mathbf{K} - cos\pi\nu\mathbf{P}\varpi^{-1}\right) \tag{4.2.23}$$

In order to relate Eqs. 4.2.22 and 4.2.23, we first linearly transform the solutions $\bar{\mathbf{M}}$ and then rotate the channel space onto the integer l representation using the orthogonal transformation $\mathbf{F}$ defined in **Chapter 3**. The intermediate matrix solutions are defined as,

$$\tilde{\mathbf{M}} = \mathbf{F}\bar{\mathbf{M}}\left(sin\pi\nu\bar{\varpi} + cos\pi\nu\bar{\varpi}\bar{\mathbf{K}}\right)^{-1}, \tag{4.2.24}$$

which yields,

$$\tilde{\mathbf{M}} = \frac{\xi}{(2\nu)^{1/2}\pi}\mathbf{F} + \Theta\left(\frac{\nu^3}{2}\right)^{1/2}\mathbf{F}\left(sin\pi\nu\bar{\varpi}^{-1}\bar{\mathbf{K}} - cos\pi\nu\bar{\varpi}^{-1}\right)\left(sin\pi\nu\bar{\varpi} + cos\pi\nu\bar{\varpi}\bar{\mathbf{K}}\right)^{-1}. \tag{4.2.25}$$

A further linear transformation,

$$\tilde{\mathbf{M}}' = \tilde{\mathbf{M}}\mathbf{F}^T, \tag{4.2.26}$$

yields,

$$\tilde{\mathbf{M}}' = \frac{\xi}{(2\nu)^{1/2}\pi} + \Theta\left(\frac{\nu^3}{2}\right)^{1/2}\mathbf{A}, \tag{4.2.27}$$

where

$$\mathbf{A} = \mathbf{F}\left(sin\pi\nu\bar{\varpi}^{-1}\bar{\mathbf{K}} - cos\pi\nu\bar{\varpi}^{-1}\right)\left(sin\pi\nu\bar{\varpi} + cos\pi\nu\bar{\varpi}\bar{\mathbf{K}}\right)^{-1}\mathbf{F}^T. \tag{4.2.28}$$

Comparison of Eqs. 4.2.27 and 4.2.23 allows us to deduce the identity,

$$\mathbf{A}\left(sin\pi\nu\mathbf{P}\varpi + cos\pi\nu\mathbf{P}\varpi\mathbf{K}\right) = sin\pi\nu\mathbf{P}\varpi^{-1}\mathbf{K} - cos\pi\nu\mathbf{P}\varpi^{-1} \tag{4.2.29}$$

Eq. 4.2.29 can be inverted for the symmetric **K** matrix to yield

$$\mathbf{K} = -\left(\mathbf{A}cos\pi\nu\mathbf{P}\varpi - sin\pi\nu\mathbf{P}\varpi^{-1}\right)^{-1}\left(\mathbf{A}sin\pi\nu\mathbf{P}\varpi + cos\pi\nu\varpi\right) \tag{4.2.30}$$

Equation 4.2.30 defines the **K** matrix in terms of the $\bar{\mathbf{K}}$ matrix at negative energy. The behavior of the diagonal and off-diagonal matrix elements of the calculated quantum defect matrix in the integer l representation ($\mu = arctan(\mathbf{K})$) are shown in Figs. 4-8 and 4-9 for $\lambda = 0$, Σ symmetry. The matrix elements are rapidly oscillatory as a function of energy below the ionization threshold. The integer **K** is defined strictly in the limit $r \to \infty$, because of the existence of the dipole field. The Coulomb functions are exponentially divergent at long range, which causes the **K** matrix to have a very strong and sensitive energy dependence. The strong energy dependence of the **K** matrix makes it unsuitable to be used in the rovibrational frame transformation, because the validity of the frame transformation necessitates that the body-fixed reaction matrix depends weakly on energy [48].

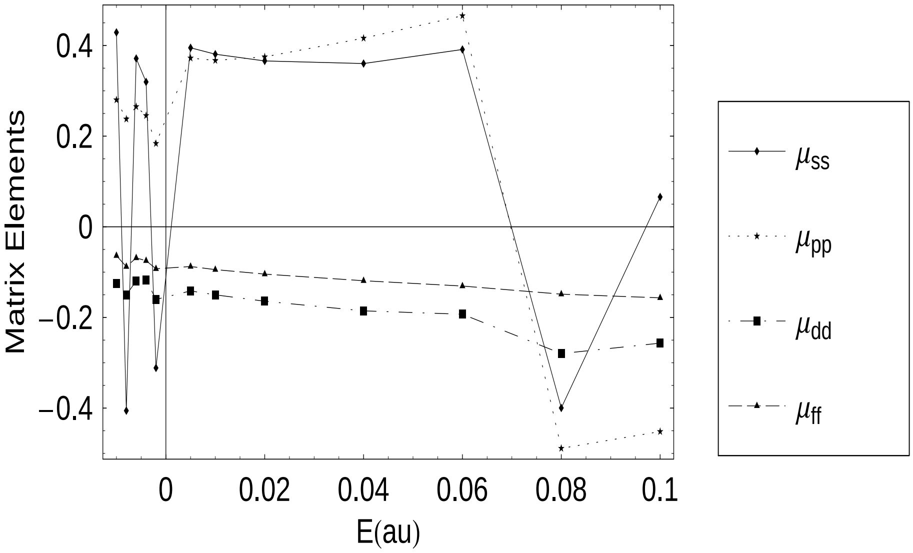

Figure 4-8: The diagonal matrix elements of the quantum defect matrix shown for $-0.01 < E < 0.1$ and $\lambda = 0$, Σ symmetry. Rapid oscillations of the matrix elements are visible for $E < 0$. The strong energy dependence of the of the reaction matrix elements is a consequence of the exponential divergences in the Coulomb functions at negative energy. Such a strong energy dependence in the integer l reaction matrix renders it unsuitable as input to the rovibrational frame transformation. The diagonal matrix elements oscillate about the values determined from a fit to extensive experimental data [65, 37].

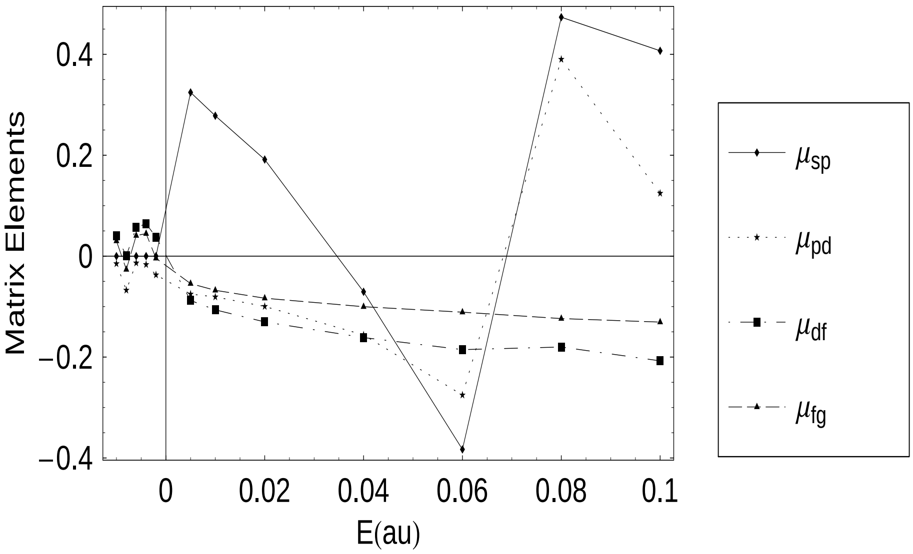

Figure 4-9: The off-diagonal matrix elements of the quantum defect matrix shown for $-0.01 < E < 0.1$ and $\lambda = 0$, Σ symmetry . Rapid oscillations of the matrix elements are visible for $E < 0$ as in the diagonal elements displayed in Fig. 4-8

4.3 Photoionization of CaF

Consider the reaction

$$h\nu + \mathrm{CaF}(^2\Sigma^+ n^*) \rightarrow \mathrm{CaF}^+(^1\Sigma^+) + e^-, \tag{4.3.31}$$

where $^2\Sigma^+ n^*$ specifies an electronic state of the molecule. We define the quantum numbers $\mathbf{j_r} = 1$, $\mathbf{N}$, $\mathbf{N}^+$ and $\mathbf{l}$ to denote the angular momenta for the incoming photon, the neutral CaF molecule (exclusive of electron spin), the CaF$^+$ ion, and the ejected electron. The angular momentum

$$\mathbf{j_t} = \mathbf{N}^+ - \mathbf{N} = \mathbf{j_r} - \mathbf{l}, \tag{4.3.32}$$

is the total angular momentum transferred in the photoionization. The advantage of the use of the transferred angular momentum, $\mathbf{j_t}$, lies in the fact that the differential cross section for ionization, when averaged over all molecular orientations in space-fixed axes, can be expressed in terms of the body-frame projections of the angular momenta, $\mathbf{l}$ and $\mathbf{j_r}$, without explicit reference to the angular momenta, $\mathbf{N}$ and $\mathbf{N}^+$ [22, 32]. After the average

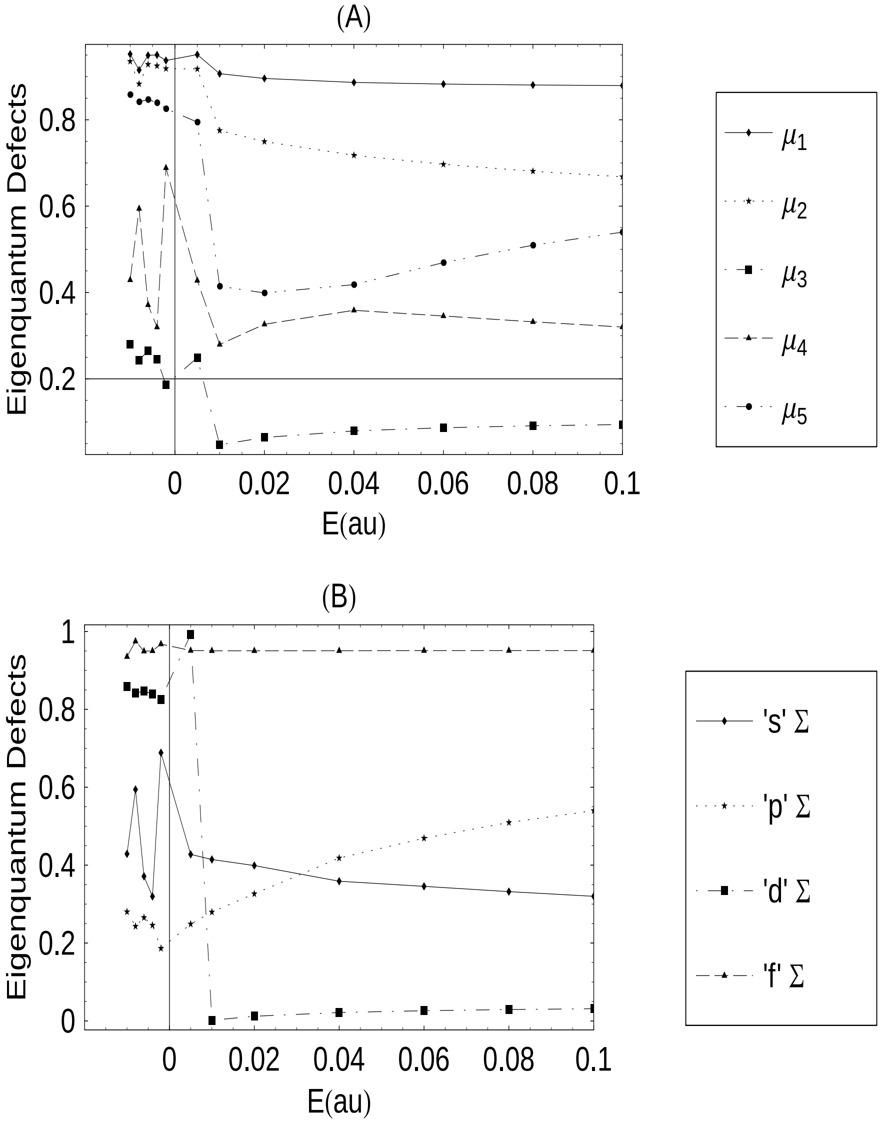

Figure 4-10: (A) The eigenquantum defects obtained from the $\mathbf{K}(E)$ matrix for the $\lambda = 0$, Σ symmetry ordered by rank. (B) The same eigenquantum defects as in (A), ordered by assignment based on the dominant l character in the corresponding eigenchannel. The eigenquantum defects at negative energy oscillate rapidly about their equilibrium values determined from a fit to extensive experimental data [65, 37]. It may be possible to average out these oscillations to define a stationary reaction matrix in the integer-l representation. However, it is more logical to use the $\bar{\mathbf{K}}$ matrix directly in the frame transformation and the fit routines, since the physical meaning of the dipole-reduction is clear.

is performed, the differential cross section for ionization becomes, in atomic units [22],

$$\frac{d\sigma}{d\Omega(\theta',\phi')} = 8\pi^2\alpha\omega \sum_{j_t,l,\lambda,l',\lambda'} (2j_t+1)^{-1} i^{l-l'} e^{i(arg(\Gamma(l'+1+i/k)-arg(\Gamma(l+1+i/k))} D_{l,\lambda,j_t} D^*_{l',\lambda',j_t} \Theta(j_t;10,ll',\theta'), \tag{4.3.33}$$

where [1]

$$\Theta(j_t;10,ll',\theta') = \frac{1}{4\pi}(2j_t+1)[(2l+1)(2l'+1)]^{\frac{1}{2}}(-1)^{j_t} \sum_K \begin{Bmatrix} 1 & 1 & K \\ l & l' & j_t \end{Bmatrix} (l0,l'0|K0) P_K(cos\theta')(K0|10,10), \tag{4.3.34}$$

ω is the energy of the ionizing radiation and D_{l,λ,j_t} are the reduced dipole matrix elements defined below. It should be noted that the cross section given here, obtained by taking an equally weighted average over molecular orientations, can be measured in an experiment that does not resolve the various rotational states of the ion-core. The primed angles, (θ',ϕ'), are the electronic coordinates in the space-fixed axes and the unprimed angles are electronic coordinates in the body-fixed axes. Equations 4.3.33 and 4.3.34 completely determine the angular distribution of the ejected electrons. The four triangle relations satisfied by the $6j$ coefficient that appears in Eq. 4.3.34 restrict the photoelectron angular distribution to the form,

$$\frac{d\sigma}{d\Omega(\theta',\phi')} = a + bP_2(cos\theta'). \tag{4.3.35}$$

From Eq. 4.3.35 one gets $a = \frac{\sigma}{4\pi}$, where σ is the integrated cross section. The dimensionless ratio $\beta = \frac{b}{a}$ defines the anisotropy parameter, which is frequently measured in photoionization experiments. For light polarized in the $\hat{z}'$ direction in the space-fixed coordinate system, the reduced dipole matrix element is [22],

$$D_{l,\lambda,j_t} = (\frac{4\pi}{3})^{\frac{1}{2}} \sum_m (-1)^m (j_t\lambda - m|1 - m, l\lambda) \left(\Psi^{(-)}_{l,\lambda}(\vec{r}) | rY_{1m}(\hat{r})(1-g(\vec{r})) | \Psi_0(\vec{r}) \right). \tag{4.3.36}$$

The state $\Psi_0(\vec{r})$ is the $^2\Sigma^+ n^*$ electronic state of CaF and $\Psi^{(-)}_{l,\lambda}$ is an energy normalized continuum state (see Appendix for a proof) that satisfies the *incoming wave boundary*

---

[1] An extra factor of 2 arises in the definition of the cross section in Eq. 4.3.33 because the continuum wavefunction we use here is normalized per unit ϵ where $\epsilon = 2E$ and E is the excess of the excitation energy over the ionization threshold. See Appendix for a discussion of the energy normalization.

condition [43]. The function $g(\vec{r})$ is a correction to the independent electron approximation [8], and has the form [101],

$$g(\vec{r}) = \frac{\alpha_1 f_1(r)}{r^3} + \frac{\alpha_2 f_2(r_2)}{r_2^3}. \tag{4.3.37}$$

Definitions and values for the terms used in Eq. 4.3.37 are given in Table 4.1. This correction in some cases accounts for approximately 10% of the calculated dipole matrix element [101]. The continuum wavefunction is expanded in spherical harmonics,

$$\Psi_{l,\lambda}^{(-)}(\vec{r}) = \sum_{l'} \psi_{ll'}^{(-)}(r) Y_{l',\lambda}(\hat{r}) \tag{4.3.38}$$

where, by virtue of the incoming wave boundary condition, we have:

$$\psi_{ll'}^{(-)}(r \to \infty) = \frac{1}{2i\sqrt{\pi k}} \left(e^{iu(r)} \delta_{ll'} - e^{-iu(r)} \tilde{S}_{l,l'} \right). \tag{4.3.39}$$

In the $\bar{K}$ formalism [117], we may similarly write

$$\bar{\psi}_{nn'}^{(-)}(r \to \infty) = \frac{1}{2i\sqrt{\pi k}} \left(e^{iu(r)} \delta_{nn'} - e^{-iu(r)} \bar{\tilde{S}}_{n,n'} \right), \tag{4.3.40}$$

where we let,

$$\bar{\tilde{S}}_{n,n'} = e^{-i(\bar{p}_n + \bar{p}_{n'})} \sum_j e^{-2\pi i \mu_j} U_{nj} U_{n'j}, \tag{4.3.41}$$

$$\bar{p}_n = \bar{\phi}_n(r) - u(r), \tag{4.3.42}$$

$$\mu_j = \frac{1}{\pi} arctan \left(\mathbf{U^T \bar{K} U} \right)_{jj}. \tag{4.3.43}$$

Therefore, $\bar{p}_n, \mu_j$, and $\mathbf{U}_j$ are the Coulomb-Dipole phase shift, the eigenquantum defect, and the corresponding eigenvector of the reaction matrix ($\mathbf{\bar{K}}$), respectively. According to Eqs. 4.3.40 and 4.3.39, the unitary matrix $\mathbf{\tilde{S}}$ is given by,

$$\mathbf{\tilde{S}} = \mathbf{F}_\lambda \bar{\tilde{\mathbf{S}}} \mathbf{F}_\lambda^{\mathbf{T}}. \tag{4.3.44}$$

Thus, the continuum state that satisfies the incoming wave boundary condition can be expressed as,

$$\Psi_{l,\lambda}^{(-)}(\vec{r}) = \sum_n F_{l\lambda n} \bar{\Psi}_{n,\lambda}^{(-)}(\vec{r}). \tag{4.3.45}$$

The reduced dipole matrix element then becomes,

$$D_{l,\lambda,j_t} = (\frac{4\pi}{3})^{\frac{1}{2}} \sum_n F_{l\lambda n} \sum_m (-1)^m (j_t\lambda - m|1-m, l\lambda) \left(\bar{\Psi}^{(-)}_{n,\lambda}(\vec{r})|rY_{1m}(\hat{r})(1-g(\vec{r}))|\Psi_0(\vec{r})\right). \tag{4.3.46}$$

In order to further simplify Eq. 4.3.46, a third set of linearly independent solutions can be introduced by transforming the solutions $\mathbf{M}_\alpha$ of Part I into a representation in which the reaction matrix is diagonal [43],

$$\mathbf{M}_j = cos(\pi\mu_{\mathbf{j}})\mathbf{U}^T\mathbf{M}_\alpha. \tag{4.3.47}$$

The eigenquantum defects μ_j and the vectors $\mathbf{U}_j$ were previously defined in Eq. 4.3.43. In Eq. 4.3.47, $cos(\pi\mu_{\mathbf{j}})$ denotes a diagonal matrix with the j-th diagonal element being equal to $cos(\pi\mu_j)$. Asymptotically, the eigenchannel radial functions $M_{jn}(r)$ behave as

$$M_{jn}(r \to \infty) = cos(\pi\mu_j)U_{nj}\bar{f}_{\bar{l}(n)}(r) - sin(\pi\mu_j)U_{nj}\bar{g}_{\bar{l}(n)}(r). \tag{4.3.48}$$

It may be verified that the functions $\bar{\psi}_{nn'}(r)$ are obtained from the $M_{jn}(r)$ via the transformation,

$$\bar{\psi}_{nn'}(r) = \sum_j M_{jn'}(r)e^{-i(\bar{p}_n+\pi\mu_j)}U_{nj}. \tag{4.3.49}$$

Using Eq. 4.3.49 in Eq. 4.3.46 we get,

$$D_{l,\lambda,j_t} = \sum_n F^{\lambda}_{ln} \sum_j e^{i(\eta_n+\pi\mu_j)}U_{nj} \sum_m (-1)^m (j_t\lambda - m|1-m, l\lambda) d^{\lambda}_{jm}, \tag{4.3.50}$$

where,

$$d^{\lambda}_{jm} = \left(\frac{4\pi}{3}\right)^{\frac{1}{2}} \left(M^{\lambda}_j(\vec{r})|rY_{1m}(\hat{r})(1-g(\vec{r}))|\Psi_0(\vec{r})\right). \tag{4.3.51}$$

The total cross section for ionization is determined by integrating the differential cross section in Eq. 4.3.33. The result is:

$$\sigma = \frac{8\pi^2\alpha\omega}{3} \sum_{l,\lambda,j_t} |D_{l,\lambda,j_t}|^2 . \tag{4.3.52}$$

Inserting Eq. 4.3.50 into Eq. 4.3.52 and using the orthonormality of **U** and $\mathbf{F}^{\lambda}$ as well as the normalization of the Clebsch-Gordan coefficients, one obtains

$$\sigma = \frac{8\pi^2\alpha\omega}{3}\left(\sum_j (d^0_{j0})^2 + \sum_j (d^1_{j1})^2\right). \tag{4.3.53}$$

The functions $M^{\lambda}_{j}(\vec{r})$ can be obtained from the numerically calculated $M^{\lambda}_{\beta}(\vec{r})$, by the method of Part I, using the relation,

$$M^{\lambda}_{j}(\vec{r}) = \sum_{n\beta} (\bar{T}^{-1})_{n\beta} M^{\lambda}_{\beta}(\vec{r}) U_{nj} cos(\pi\mu_j). \tag{4.3.54}$$

Equations 4.3.53 and 4.3.54 together demonstrate that the "open-continuum" cross section for the ionization of CaF is completely determined by the eigenvalues and eigenvectors of the reaction matrix and the **R**-matrix eigenstates, $M^{\lambda}_{\beta}(\vec{r})$. The parameters that characterize the photoionization from the bound states in the $n^* = 10$ region, shown in Fig. 4-2, can be determined *ab initio* by employing the relevant equations derived above. The calculation involves numerical computation of the continuum channels, $M_{\beta}(\vec{r})$, as well as the bound state wavefunctions. The solutions $M_{\beta}(\vec{r})$ are given by Eq. 3.41 of **Chapter 3** for $r > r_o$. For $r_a < r < r_o$, Eq. 3.37 is used to represent $M_{\beta}(\vec{r})$. Inside the atomic zone, where $r < r_a$, the interactions are spherically symmetric and the solutions can be numerically determined by integration of the radial Schrödinger equation. The solutions for $r < r_a$ are then connected to the solutions in the region $r_a < r < r_o$ by imposing the relevant continuity relations. This procedure numerically determines the $M_{\beta}(\vec{r})$ over all space. The collision eigenchannels, $M^{\lambda}_{j}(\vec{r})$, are then determined from $M^{\lambda}_{\beta}(\vec{r})$ using Eq. 4.3.54. An example plot of a collision eigenchannel wavefunction for $\lambda = 1$ symmetry in the $\phi = 0$, $x - z$ plane is shown in Fig. 4-11.

Figure 4-12 shows the calculated photoelectron distributions for ionization from the $10.55^2\Sigma^+$ Rydberg state. The coordinates used to describe the photoionization process are explained in Fig.4-12A. The $\hat{x}', \hat{z}'$ unit vectors define the plane of the electromagnetic wave. $\hat{z}'$ is the direction of the electric field and $\hat{x}'$ is the propagation direction of the laser pulse. The unprimed coordinate, $\hat{z}$, which is directed along the internuclear axis, defines the orientation of the body frame together with the rotation axis, $\hat{x}$. The parameter θ is the polar angle that the ejected electron makes with the $\hat{z}$ axis. The photoelectron distri-

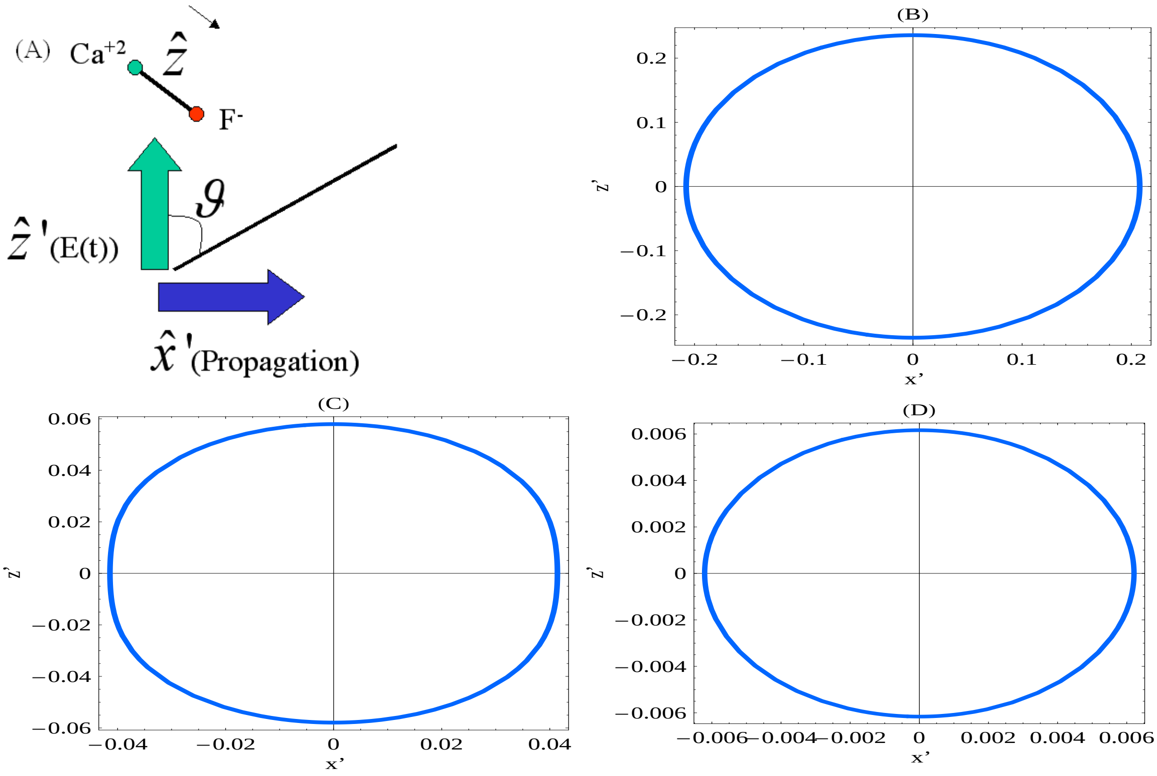

Figure 4-13: The polar plots of the photoelectron distributions for ionization from the $10.08^2\Sigma^+$ Rydberg state. (A) Coordinates used to represent the photoionization process. (B) The photoelectron distribution at $E = 0.01\,au$. The radial distance from the origin to the displayed curve measures the photoelectron distribution in megabarns. (C) The photoelectron distribution in the avoided crossing region, $E = 0.03\,au$. (D) The photoelectron distribution in the high energy limit, $E = 0.15\,au$.

with expectation for non-penetrating states. Photoionization of the predominantly f-type electron in the $10.08\Sigma^+$ state, produces primarily g-type partial-waves in the continuum. These high-l partial waves interact with the ion-core only at long-range through the ion-core dipole-field. Consequently, they are insensitive to the short-range interactions that cause much of the structure seen in the distributions shown in Fig. 4-12.

The distinct structures seen in Figures 4-12 and 4-13 can be used to distinguish the photoelectrons detected by ionizing a non-stationary electronic state of the molecule. Based on Mulliken's rule, the photoionization transitions from the members of a given Rydberg series produce the same partial-l waves in the continuum. Thus, the structure seen in the photoelectron distributions is common to all members of a Rydberg series. Therefore, if the non-stationary state consists of a superposition of several members from the $0.08^2\Sigma^+$ series (for example $n^* \approx 9, 10,$ and 11) and several members from the $0.55^2\Sigma^+$ states,

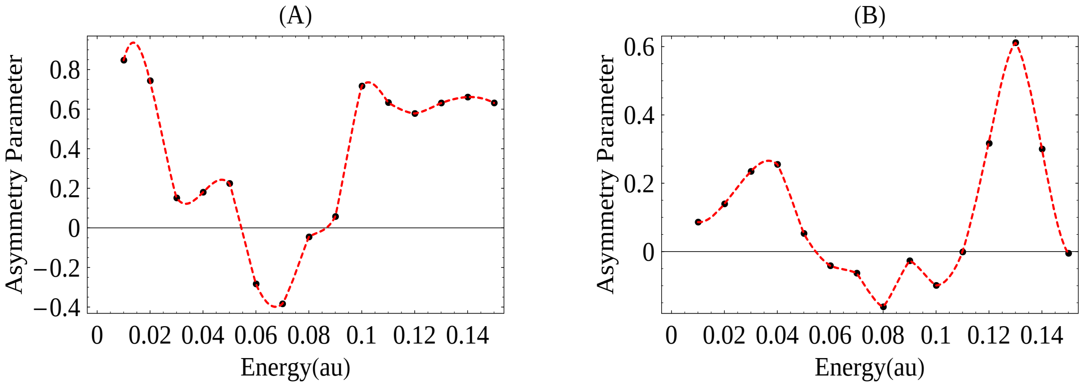

Figure 4-14: The anisotropy parameter, β, as a function of energy, calculated *ab initio* for ionization from the $10.55^2\Sigma^+$ and $10.08^2\Sigma^+$ Rydberg states. (A) β parameter for ionization from the $10.55^2\Sigma^+$ Rydberg state. (B) β parameter for ionization from the $10.08^2\Sigma^+$ Rydberg state.

comparison of Figs. 4-12B and 4-13B reveals that the photoelectrons at low continuum energy, detected along the propagation direction would predominantly originate from the $0.08^2\Sigma^+$, non-penetrating states. The resultant time-dependent signal [116], would display Kepler beats characteristic of the $0.08^2\Sigma^+$ series alone, and the beat contribution from the $0.55^2\Sigma^+$ series would be filtered out. Alternatively, the photoelectron signal along the propagation direction in the region of the avoided crossing, would depend predominantly on the time-dependent amplitudes of the $0.55^2\Sigma^+$ states and a time-dependent trace of the signal would display Kepler beats characteristic of the $0.55^2\Sigma^+$ series alone.

Figure 4-14 shows a plot of the calculated anisotropy parameter, β, as a function of continuum energy for ionization from the $10.55^2\Sigma^+$ and $10.08^2\Sigma^+$ Rydberg states, respectively. The anisotropy parameter shows a very strong energy dependence in both cases, a behavior which is characteristic of long-range fields [34]. The anisotropy parameter for the $10.55^2\Sigma^+$ state, shown in Fig. 4-14A, goes through rapid variations in the intermediate energy region. It attains its maximal values at low continuum energy and becomes approximately constant at high continuum energy. Figure 4-14B shows the anisotropy parameter for ionization from the $10.08^2\Sigma^+$ state. The value for β in this case is on average smaller than the value for β shown in Fig. 4-14A. The anisotropy parameter goes through small amplitude oscillations (with the exception of a large peak around $E = 0.13\,au$) throughout the range of energy, reflecting the energy dependence in the Coulomb phase-shift.

An alternative to the l-selective ionization technique is to detect the electrons ejected in all directions. The plots of the integrated cross sections for ionization, shown in Fig. 4-15, illustrate the principle. Figure 4-15A displays the total cross section for ionization from the $10.55^2\Sigma^+$ Rydberg state. The shape resonance is manifest in this plot by a depressed value of the cross section followed by a broad peak, which extends across the resonance width. The effects of the shape resonance on the cross section are diminished as the non-penetrating limit is approached, as demonstrated by Figs. 4-15B, 4-15C and 4-15D. In particular, there is hardly any structure in the cross section for ionization from the $10.08^2\Sigma^+$ state, shown in Fig. 4-15D. By tuning the frequency of the ionizing radiation to the maximum of the broad peak in Fig. 4-15A, the contributions to the signal from the $n.55^2\Sigma^+$ photoelectrons can be amplified in the time-domain experiment described previously. In turn, ionizing to slightly above threshold produces predominantly non-penetrating photoelectrons from the $n.08^2\Sigma^+$ states, which yield a simple experimental signal that may be used to infer the properties of the ion-core, such as the ion-core dipole and quadrupole moments.

4.4 Conclusions

The reaction matrix calculations performed for the study of the Rydberg states of CaF have produced results in quantitative agreement with the experimental data. These calculations also serve to demonstrate the utility of the $\bar{\mathbf{K}}$-matrix method. The study of the $\mathbf{K}$ matrix provides physical explanations for the coupling mechanisms that govern the interactions between the scattering electron and the CaF$^+$ ion-core. We have found that there is strong coupling between the s, p, and d channels below the ionization threshold and that this l-mixing can be explained by using Mulliken's Rydberg terminus orbital concept and ligand-field theory [102]. Much of the structure in the continuum is affected by a broad shape resonance centered slightly below the ionization threshold. The partial-l decomposition of the penetrating type 0.55 and 0.88 eigenchannels rapidly vary with increasing energy, as the scattered electron escapes the shape resonance.

The variation of the spectral decomposition of the eigenchannels causes the transition intensities into each of the eigenchannels to interfere. The effects of the shape resonance are manifest in the integrated photoionization cross sections from the penetrating states as depressed values of the cross-section near the ionization threshold, followed by broad peaks at higher energy. The non-penetrating states are insensitive to both the short-range

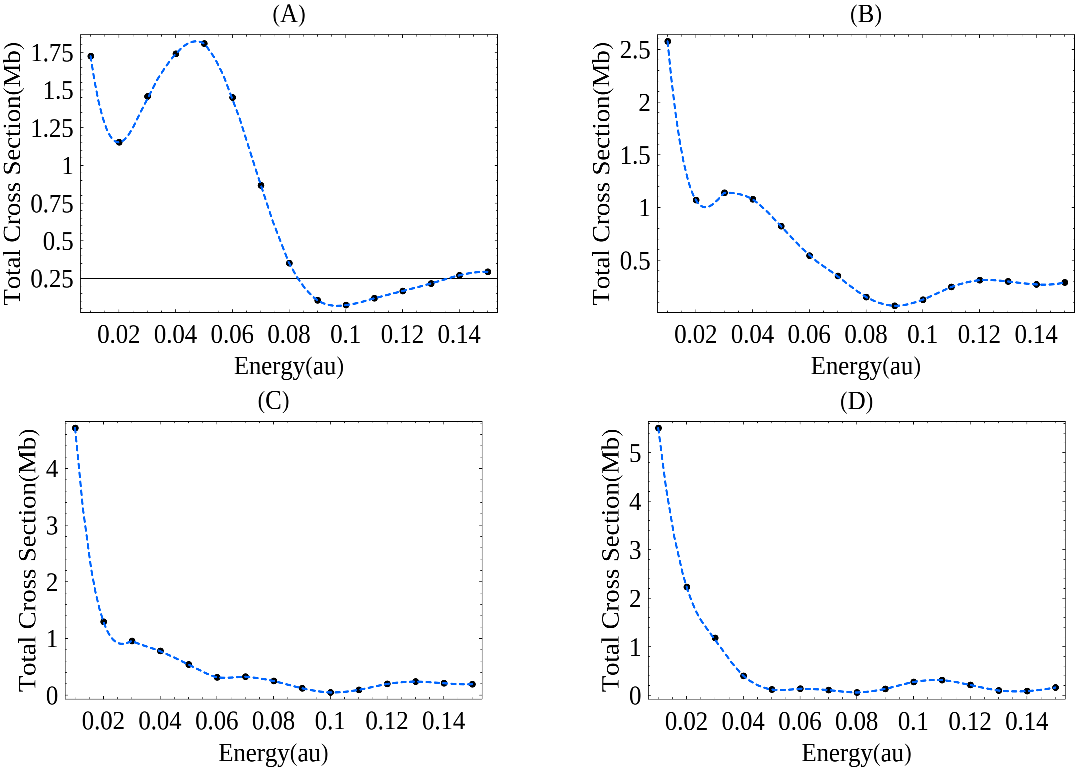

Figure 4-15: The integrated cross section for ionization, σ, as a function of continuum energy. The theoretical data points are displayed on the interpolated dashed curves. (A) Integrated cross section for ionization from the $10.55^2\Sigma^+$ Rydberg state. (B) Integrated cross section for ionization from the $10.88^2\Sigma^+$ Rydberg state. (C) Integrated cross section for ionization from the $10.16^2\Sigma^+$ Rydberg state. (D) Integrated cross section for ionization from the $10.08^2\Sigma^+$ Rydberg state.

forces and the dipole field. Accordingly, the cross sections for ionization from these states vary smoothly with energy and do not exhibit resonance-related interference patterns. The photoionization transitions from the members of a given Rydberg series terminate in the same partial-l waves in the continuum. Therefore the structure identified here is a property of an entire series and implies that the energy dependent cross section is a direct probe of the l-character of the bound state. Experimental techniques, as described previously, can be developed that allow for selective detection of states with the specified l characters. These techniques offer unique, l-selective ways to observe the dynamics and spectroscopy of CaF.

The photoelectron distributions for ionization from penetrating states differ remarkably from the distributions obtained by ionizing non-penetrating states. The distribution recovered by ionizing a penetrating state possesses a prominent anisotropy, which is absent in a distribution that originates from a non-penetrating state. The anisotropy identifies the angular nature of the ionizing bound state and can be used as a benchmark to assign quantum numbers to the Rydberg levels. The unique structures in the photoelectron distributions can be further exploited in time-domain experiments. By detecting the photoelectrons in carefully pre-selected directions, the complicated signals arising from the ionization of a non-stationary electronic state (which contains penetrating and non-penetrating components) can be pre-sorted and thereby simplified. This would reveal information about the ion-core dipole and quadrupole moments in a very straightforward fashion.

We conclude by making a distinction between the Mulliken picture of molecular Rydberg dynamics, and the dipole-influenced long-range Rydberg dynamics that was studied in this work. Molecules with highly polar ion-cores conform to the Mulliken picture in the electronic energy regimes that are close to the Rydberg terminus state energies of the molecule. In these energy regimes, all members of an eigenchannel have an innermost lobe with a common shape and the partial-l characters of each eigenchannel do not vary significantly with energy. However, for sufficiently high electronic energies in the continuum, the long-range fields alone determine the electronic structure. This transition to long-range dominated Rydberg dynamics that are qualitatively different from the Mulliken picture of Rydberg dynamics, has a unique signature in observables such as the photoionization cross section. We expect much of the new physical behavior that we have identified here, which should not commonly occur in atoms and homonuclear molecules, to reappear in the study of the Rydberg structure and dynamics for molecules with a strongly dipolar ion-core, especially when there is a closed shell ligand significantly displaced from the center of mass.

4.5 Mathematical Appendix

Consider the integral,

$$\int_{0<r<r_c} d^3r\ \Psi^{(-)*}_{l,\lambda}(\epsilon,\vec{r})\Psi^{(-)}_{l,\lambda}(\epsilon',\vec{r}). \tag{4.5.55}$$

Using the expansion,

$$\Psi^{(-)}_{l,\lambda}(\epsilon,\vec{r}) = \sum_{l'} \psi^{(-)}_{ll'}(\epsilon,r) Y_{l',\lambda}(\hat{r}). \tag{4.5.56}$$

The integral in Eq. 4.5.55 can be re-written as,

$$\int_0^{r_c} dr\ \mathbf{\Psi}^\dagger_l(\epsilon,r)\mathbf{\Psi}_l(\epsilon',r), \tag{4.5.57}$$

where $\mathbf{\Psi}_l(\epsilon,r)$ is a column vector with the l' component being equal to $\psi_{ll'}(\epsilon,r)$. Observe that,

$$(\epsilon-\epsilon')\int_0^{r_c} dr\ \mathbf{\Psi}^\dagger_l(\epsilon',r)\mathbf{\Psi}_l(\epsilon,r) = \int_0^{r_c} dr\mathbf{\Psi}^\dagger_l(\epsilon',r)\left(\frac{d^2}{dr^2} - \frac{l(l+1)}{r^2} + \mathbf{V}\right)\mathbf{\Psi}_l(\epsilon,r) \tag{4.5.58}$$

$$-\int_0^{r_c} dr\mathbf{\Psi}^\dagger_l(\epsilon,r)\left(\frac{d^2}{dr^2} - \frac{l(l+1)}{r^2} + \mathbf{V}\right)\mathbf{\Psi}_l(\epsilon',r) \tag{4.5.59}$$

which gives, through integration by parts,

$$\int_0^{r_c} dr\ \mathbf{\Psi}^\dagger_l(\epsilon,r)\mathbf{\Psi}_l(\epsilon',r) = \frac{1}{\epsilon-\epsilon'}\left(\mathbf{\Psi}^\dagger_l(\epsilon',r)\frac{d\mathbf{\Psi}_l(\epsilon,r)}{dr} - \mathbf{\Psi}^\dagger_l(\epsilon,r)\frac{d\mathbf{\Psi}_l(\epsilon',r)}{dr}\right)|_{r=r_c}. \tag{4.5.60}$$

In the limit $r_c \to \infty$ Eq. 4.5.60 reduces to,

$$\int_0^{r_c} dr\ \mathbf{\Psi}^\dagger_l(\epsilon,r)\mathbf{\Psi}_l(\epsilon',r) = \tag{4.5.61}$$

$$\frac{1}{\epsilon-\epsilon'}\frac{1}{4\pi\sqrt{kk'}}\left(iu(r_c,\epsilon)(e^{i(u(r_c,\epsilon)-u(r_c,\epsilon'))} - e^{i(u(r_c,\epsilon')-u(r_c,\epsilon))}\sum_i |\tilde{S}_{iL}|^2 - (\epsilon'\to\epsilon))\right), \tag{4.5.62}$$

where the symbol $(\epsilon'\to\epsilon)$ means that the expression to the immediate left is repeated with the replacement of the primed terms with the unprimed terms. For $k' \approx k$, Eq. 4.5.62 can be simplified to

$$\int_0^{r_c} dr\ \mathbf{\Psi}_l^\dagger(\epsilon, r)\mathbf{\Psi}_l(\epsilon', r) = \frac{1}{2k}\frac{sin(\frac{(k'-k)}{g(r_c,k)})}{\pi(k-k')}, \tag{4.5.63}$$

where $g(r_c, k) = \frac{1}{r_c - log(2r_c k)/k^2}$. Thus in the limit $r_c \to \infty$, Eq. 4.5.63 becomes,

$$\int_0^{r_c} dr\ \mathbf{\Psi}_l^\dagger(\epsilon, r)\mathbf{\Psi}_l(\epsilon', r) = \frac{1}{2k}\delta(k'-k) = \delta(\epsilon' - \epsilon). \tag{4.5.64}$$

The last equality in Eq. 4.5.64 follows from $\epsilon = k^2$. Therefore the state $\Psi_{l,\lambda}^{(-)}(\vec{r})$ is normalized per unit energy.

Chapter 5

Broad Shape Resonance Effects in CaF Rydberg States

5.1 Introduction

Rydberg molecules are a class of molecules in which all bound electronic states are members of Rydberg series [5]. Optical-optical double resonance studies of CaF [91] show that CaF is a "Rydberg molecule". The interactions of the electron with the ion-core are non-central and the motion of the Rydberg electron is separately influenced by the attractive forces from the positive center (Ca^{+2}) and the repulsive forces from the ligand center (F^{-}). Rice, Martin, and Field (RMF) used a ligand-field model to account for the measured energies and the mixed-l characters of the low-lying electronic states [102]. Each of these states is the low-energy terminus of a Rydberg series. The RMF model is based on the observation that the energies and wavefunctions of the lowest states of the bound Rydberg electron correspond to the energies and wavefunctions of a Ca^{+} ion perturbed by an external F^{-} ligand. The ligand-field spoils the electron orbital angular momentum quantum number, l, causing l-mixing among the atomic Ca^{+} eigenstates.

Arif, Jungen, and Roche [5] developed an accurate **R**-matrix procedure to treat the global electronic spectrum of CaF. This procedure was based on the non-iterative, variational **R**-matrix scheme, formulated by Greene [44]. Their calculation used a single electron effective potential to model the CaF^{+}-electron interactions and retained the atom-in-molecule concept of ligand-field theory [55]. Recently, Altunata, Coy, and Field introduced an alternative **R**-matrix procedure, which utilized a combination of the variational method and a Green function propagation scheme to obtain the **R**-matrix eigenstates [117]. That calculation used the single electron effective potential given by Arif et al. and extended the Arif et al. results to the region of the ionization continuum. Analysis of the numerically determined short-range scattering matrix [118] indicated the presence of a broad shape resonance with E_{res} near the ionization threshold for $^2\Sigma^+$ electronic symmetry. The effects of this resonance on the spectrum and dynamics of CaF are of surprising extent in view of the nominal simplicity of the doubly closed-shell $(\mathrm{Ca}^{+2}\mathrm{F}^-)\mathrm{e}^-$ electronic structure and the apparent regularity of the spectrum.

In experimental spectra, the anomalous quantum defects or irregularities due to special effects in Rydberg spectra are identified based on the underlying "zero-order" Mulliken's rule description. Mulliken's rule for the structure of Rydberg states, "ontology (sic) recapitulates phylogeny" [90], specifies that all wavefunctions in a Rydberg series and the associated ionization continuum are built upon innermost lobes that remain approximately invariant in shape and nodal position with electronic energy; the amplitudes in these innermost lobes scale as $(n^*)^{-3/2}$, where n^* is the effective principal quantum number for the Rydberg state. These statements are rooted in the observation that the kinetic energy of the electron at short-range is fractionally much less dependent on excitation energy than the kinetic energy at long-range. Accordingly, the shape of the wavefunction at short-range is determined by the molecular potential and it is largely insensitive to total energy.

Mulliken's rule predicts slow, secular energy dependences of the quantum defects for each of the Rydberg series, because of small and quantifiable (perturbative) changes in the turning point location and electronic kinetic energies at short-range (inside the ion-core) as a function of the electronic principal quantum number. These energy dependences are described by the Rydberg-Ritz formula [62],

$$\delta(E) = \alpha + \beta E, \tag{5.1.1}$$

where δ is the quantum defect. A quantum mechanical derivation of the Rydberg-Ritz formula for the atomic problem [62], shows that β is proportional to the difference between the radial period of an electron moving in the full atomic field and the period of a hydrogenic orbit with the same energy. For non-penetrating electrons, characterized by large values of the orbital angular momentum quantum number, β is positive and it is proportional to the dipole-polarizability of the ion core [68]. For penetrating states with low angular momenta, β is negative and the quantum defects decrease with increasing n^*. For the penetrating case, the magnitude of β is proportional to the charge on the bare atomic nucleus [62]. Jungen has demonstrated that the Rydberg-Ritz formula is also widely applicable to unperturbed molecular Rydberg series [68]. The magnitude of β for a penetrating-type molecular Rydberg series can be estimated by comparison with that for an atom of similar size.

Uniquely among all of the Rydberg series in the CaF spectrum, eigenquantum defects for the $s \sim p \sim d$ mixed penetrating $0.88^2\Sigma^+$ series are predicted and observed [118] to be energy dependent over the *entire* $n^* = 5 \rightarrow \infty$ bound region. In Section 5.3, we show that this energy dependence induced by the shape resonance is smooth and continuous but it corresponds to a slow, monotonic, and increasingly pronounced violation of Mulliken's rule and the implied Rydberg-Ritz formula, as a function of the effective electronic principal quantum number, n^*. Therefore, the effect of the shape resonance is manifest as a global "scarring" of the Rydberg spectrum, which is distinct from the familiar types of localized irregularities due to much weaker level interactions. Localized irregularities are typically apparent as rapid rises of one unit in the quantum defects or discontinuous behavior as a function of n^*. Examples of localized irregularities include the anomalous (discontinuous) behavior of the quantum defects in the energy region between $n^* = 3$ and 4 for the $ns\sigma$ Rydberg series of NO [68] and the Feshbach type resonance in the Rydberg spectrum of the Ca atom due to the 3d4p$^3P^o$ perturbing configuration [49]. In contrast, the Σ symmetry shape resonance in CaF amounts to a strong perturbation that affects all the levels in the resonant Rydberg series in a systematic way and the cost of this global, methodical perturbation is the appearance of a misguidingly regular spectrum. The physical reasons for the strong nature of the shape resonance are discussed in Section 5.3 . The key point is that the inherent anomaly can only be uncovered if the spectrum is viewed globally and Mulliken's rule is used as a diagnostic tool in experimental analyses.

Section 5.2 begins with a discussion of the properties of the shape resonance that exclusively affects the $^2\Sigma^+$ states of CaF. We use the potential-adapted, adiabatic, partial-wave expansion of the scattered electron. This adiabatic approach was introduced by Le Dourneuf, Kay, and Launay [23]. We show that the broad shape resonance, which influences an infinity of $^2\Sigma^+$ Rydberg states (primarily belonging to the 0.88 $^2\Sigma^+$ series [118]) and the associated ionization continuum of CaF, is due to the trapping of a Σ symmetry Rydberg electron between a centrifugal barrier on the Ca^{+2} ion and the excluded volume around the F^- ion. A shape resonance that is of remarkably similar nature has been been reported for BF_3 [127]. The single quasi-bound level in the well at short-range decays either because of electron tunneling through the F^- barrier or by non-adiabatic coupling between the potential-adapted partial waves. The non-adiabatic interactions occur because of strong radial dependences of the potential-adapted partial waves. These interactions originate almost exclusively within the volume occupied by the F^- ion.

By taking into account the non-adiabatic interactions, we derive an integral formula for the short-range reaction matrix in the dipole representation ($\bar{\mathbf{K}}$ matrix) [117]. In connection with the limited radial range of the non-adiabatic interactions, the formula shows that the $\bar{\mathbf{K}}$ matrix (i) depends primarily on the values of the potential function near the F^- ion and (ii) is free of all influences of long-range fields. For this reason, the $\bar{\mathbf{K}}$ matrix theory enables removal of the strong energy dependence of the scattering due to the extremely polar ion-core. Since the $\bar{\mathbf{K}}$ matrix is expected to be devoid of significant energy dependence, it transparently reveals an energy dependence that arises from a physically distinct origin: a shape resonance that is generated by features in the short-range molecular potential.

In Section 5.3, we show that the short-range portions of the CaF electronic wavefunctions in the resonant eigenchannel are conspicuously different at energies below and above the energy of the shape resonance. Below the energy of the shape resonance, the wavefunction is polarized at short range toward the excluded volume of the F^- ion. At energies far above the energy of the resonance, the short-range polarization of the electronic wavefunction toward the excluded volume diminishes. Consequently, the Rydberg spectrum slowly but systematically deviates from a Mulliken's rule description across the broad energy width of the shape resonance. We conclude with a discussion on the implications of this global and strong perturbation of the Rydberg spectrum for the analyses of experimental data. The results presented in this chapter have been published in the Journal of Chemical Physics [119].

5.2 Results and Discussion

In atoms, the analysis of shape resonances starts from an investigation of the interaction potential for each partial-l wave, which is given by

$$V_l(r) = V(r) + \frac{l(l+1)}{2r^2}. \tag{5.2.2}$$

Since molecular fields are in general anisotropic, effective potentials for electrons in molecules cannot be defined as simply as in Eq. 5.2.2. In CaF, the potential is anisotropic even at long-range, because the CaF ion-core has a relatively large electric dipole moment, μ, which generates a strong, non-spherical dipole field in the asymptotic region ($\mu = 3.46\,au$, as measured from the molecular center of mass [101]). However, Le Dourneuf et al. realized that one can invoke an adiabatic approximation in the electronic coordinate, r, in the spirit of the Born-Oppenheimer approximation used for the nuclear coordinate, R, to define effective potentials for the electronic motion in the corresponding adiabatic channels. The fixed-r adiabatic partial waves, $\Phi_{l\lambda}(r,\Omega)$, are obtained by diagonalizing the fixed-r Hamiltonian, which has the form:

$$\left(V(\vec{r}) + \frac{\hat{l}^2}{2r^2}\right)\Phi_{l\lambda}(r,\Omega) = V_{l\lambda}(r)\Phi_{l\lambda}(r,\Omega), \tag{5.2.3}$$

where λ denotes an irreducible representation of the molecular symmetry group ($\lambda = \sigma, \pi, \delta, ...$ for ${}^2\Sigma, {}^2\Pi, {}^2\Delta, ...$ electronic symmetries of CaF) and the angular coordinates $\Omega = \theta, \phi$ describe the orientation of the electron in the body-fixed frame with origin at the Ca nucleus. The index l is a label to order the eigenvalues $V_{l\lambda}(r)$ by energy rank and is not meant as an angular momentum quantum number. The choice of the origin to coincide with the Ca nucleus follows the ligand-field model, which has shown that the molecular wavefunctions for the calcium monohalides correspond to metal centered wavefunctions perturbed by the influence of the electric field from the ligand center [102]. Each adiabatic mode, $\Phi_{l\lambda}(r,\Omega)$, in Eq. 5.2.3 may be expanded in spherical harmonics as,

$$\Phi_{l\lambda}(r,\Omega) = \sum_{l'} a^{\lambda}_{ll'}(r) Y_{l'\lambda}(\Omega)\,. \tag{5.2.4}$$

When the exact molecular electronic wavefunction is expanded in the adiabatic modes, as

$$\Psi^{\lambda}(\vec{r}) = \sum_{l} \frac{F_l^{\lambda}(r)}{r} \Phi_{l\lambda}(r,\Omega), \tag{5.2.5}$$

the Schrӧdinger equation becomes,

$$\sum_{l} \left\{ -\frac{1}{2}\frac{d^2}{dr^2} - \frac{1}{r}\frac{d}{dr} + \frac{\hat{l}^2}{2r^2} + V(\vec{r}) - E \right\} \frac{F_l^{\lambda}(r)}{r} \Phi_{l\lambda}(r,\Omega) = 0. \tag{5.2.6}$$

Using the orthogonality of the $\Phi_{l\lambda}(r,\Omega)$, Eq. 5.2.6 can be reduced to,

$$\frac{d^2F_l(r)}{dr^2} + 2(E - V_l(r))F_l(r) + \sum_{l'} \left(2A_{ll'}(r)\frac{dF_{l'}^{\lambda}(r)}{dr} + B_{ll'}(r)F_{l'}^{\lambda}(r) \right) = 0, \tag{5.2.7}$$

where

$$\begin{aligned} A_{ll'}^{\lambda}(r) &= \int d\Omega \, \Phi_{l\lambda}(r,\Omega) \, \frac{d\Phi_{l'\lambda}(r,\Omega)}{dr} \\ B_{ll'}^{\lambda}(r) &= \int d\Omega \, \Phi_{l\lambda}(r,\Omega) \, \frac{d^2\Phi_{l'\lambda}(r,\Omega)}{dr^2}. \end{aligned} \tag{5.2.8}$$

The matrix element $A_{ll'}^{\lambda}(r)$ is antisymmetric with respect to exchange of its indices. According to Eqs. 5.2.7 and 5.2.8, the adiabatic channels couple due to the r-dependence of the $\Phi_{l\lambda}(r,\Omega)$. If we impose the adiabatic approximation, in which the r-dependence of $\Phi_{l\lambda}(r,\Omega)$ is neglected, the equations decouple,

$$\frac{d^2F_l^{\lambda}(r)}{dr^2} + 2(E - V_{l\lambda}(r))F_l^{\lambda}(r) = 0. \tag{5.2.9}$$

Equation 5.2.9 can be solved using WKB methods.

Figure 5-1 displays the calculated one-electron adiabatic potential energy curves, $V_{l\lambda}(r)$, of CaF at the equilibrium internuclear separation, $R = 3.54\,au$, and for $\lambda = 0$ (σ orbitals) symmetry. The origin, $r = 0$, is at the position of the Ca nucleus and the nucleus of the F$^-$ ion is at $r = 3.54\,au$. The physical circumstances that prevail in different regions of space control the evolution of the partial-l characters of the adiabatic partial waves as a function of r. For small-r, the atomic field dominates the molecular field. Thus the adiabatic modes must be pure-l partial waves at short range. For large-r, the dipole tail of the molecular field is dominant. Thus the adiabatic partial waves *must* reduce to the

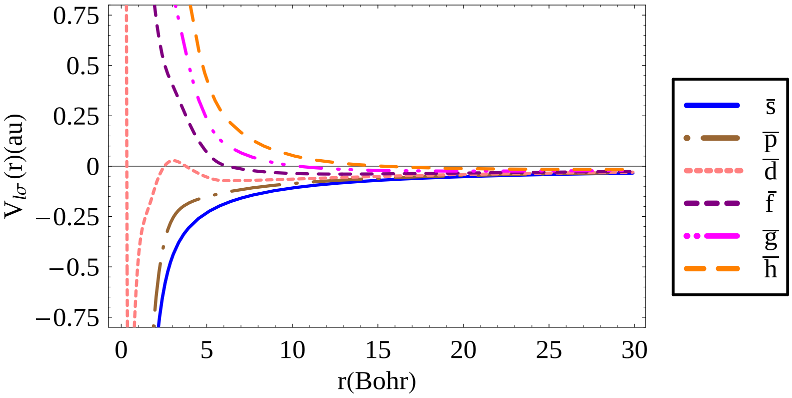

Figure 5-1: The calculated adiabatic potential energy curves, $V_{l\sigma}(r)$, for CaF. The potential curves are labeled, from bottom to top, by complex or fractional angular momenta, $\bar{l}$, to emphasize the convergence of the corresponding adiabatic mode, $\Phi_{l\lambda}(r,\Omega)$, to a dipolar mode characterized by a value of $\bar{l}$. The adiabatic partial waves evolve along these curves, from pure-l modes at small r toward a single dipolar mode at large-r. Only the $V_{\bar{d}\sigma}$ potential has a barrier in the vicinity of the F$^-$ nucleus. WKB methods can be used to decide whether a quasi-bound level is localized inside this barrier.

various r-independent dipolar modes at long range. The mechanism of this evolution will be examined more closely below. However, since the dipolar modes differ significantly from pure-l modes for low values of l, one expects a rapid variation of $\Phi_{l\lambda}(r,\Omega)$ with r in the neighborhood of $r = 3.54\,au$ and a breakdown of the adiabatic approximation for CaF. We label each dipolar mode by non-integer or complex angular momenta $\bar{l}$, where the values $\bar{l}(\bar{l}+1)$ correspond to the eigenvalues of the operator $\hat{l}^2 - 2\mu.\hat{\mathbf{r}}$ (μ is the dipole moment of the ion-core with respect to an origin at the Ca nucleus). We use a lettering scheme to indicate the values for $\bar{l}$, wherein $\bar{s}$, $\bar{p}$, $\bar{d}$, ... correspond to dipolar modes with dominant s, p, d, ... characters, respectively. In Fig. 5-1, the energy rank ordering index l is replaced by the more physical label $\bar{l}$ to emphasize the convergence of the adiabatic modes along each curve to dipolar modes associated with the specified value of $\bar{l}$, at $r = \infty$. The third curve from the bottom, which is labeled as $\bar{d}$, shows a barrier in the vicinity of the F$^-$ nucleus. The WKB quantization condition can be used to decide whether one (or more) quasi-bound level is localized inside this barrier [17]. Such a localized state is a shape resonance in the corresponding adiabatic channel. The WKB quantization condition is,

$$\int_{r_{in}}^{r_{out}} p_{\bar{d}\sigma}(r')dr' = \left(n - \frac{1}{2}\right)\pi, \tag{5.2.10}$$

where r_{in} and r_{out} are the inner and outer turning points, respectively, and $p_{\bar{d}\sigma}(r')$ is the classical momentum in the adiabatic $\bar{d}\sigma$ channel, given by,

$$p_{\bar{d}\sigma}(r') = \sqrt{2(E - V_{\bar{d}\sigma}(r'))}, \quad E < V_{max}. \tag{5.2.11}$$

Here V_{max} denotes the maximum value of the potential, $V_{\bar{d}\sigma}(r)$, on the barrier. In Eq. 5.2.11, the classical momentum is calculated using a Langer correction in the molecular potential [50] and r_{out} is a turning point on the small-r side of the barrier. A root of Eq. 5.2.10 would correspond to an authentic bound state in the limit of an infinitely broad barrier. In Fig. 5-2, we compare the qualitative predictions from the adiabatic approximation and the WKB analysis to the *ab initio* results obtained previously [118].

We use the collision lifetime matrix for resonance analysis of the *ab initio* results. The lifetime matrix is defined as [114],

$$\bar{\mathbf{Q}} = -i\bar{\mathbf{S}}^{\dagger}\frac{d\bar{\mathbf{S}}}{dE}, \tag{5.2.12}$$

where $\bar{\mathbf{S}}$ is the short range scattering matrix in the dipole representation [117, 25]. The largest eigenvalue of the lifetime matrix, q_{max}, is associated with the channel that experiences the largest time-delay during the collision. Each maximum in a plot of q_{max} as a function of energy can be identified with a resonance [27]. The resonance lineshape in q_{max} vs. E near the maximum value of q_{max} can be fitted to a Lorentzian form to determine the resonance energy, E_{res}, and width, Γ [27, 125]. The lifetime matrix analysis is especially useful for the identification of broad shape resonances, because it bypasses the difficulties that would result from a rapidly varying background phase in a fit of the eigenphase sum to the standard Breit-Wigner expression [125].

Figure 5-2c shows the variation of the WKB phase $\int_{r_{in}}^{r_{out}} p_{d\sigma}(r')dr'$ with energy, at the equilibrium internuclear separation, $R = 3.54\,au$. The WKB phase becomes $\pi/2$ at $E = -0.035\,au$. This value of the energy corresponds to a root of Eq. 5.2.10 and implies the presence of a quasi-bound level localized inside the barrier. The largest eigenvalue of the

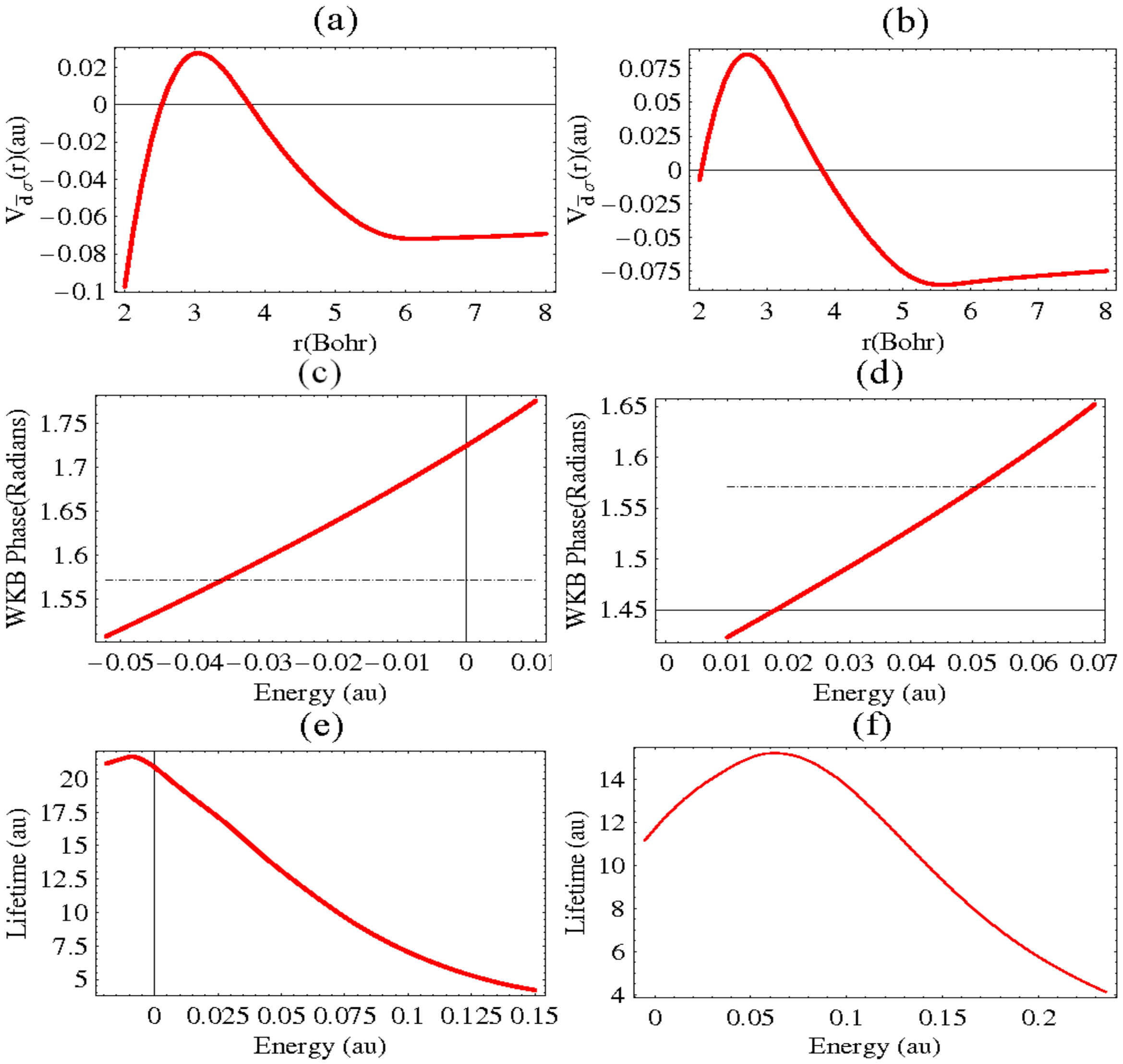

Figure 5-2: (a) The barrier at short range on the $\bar{d}\sigma$ potential. The nuclei are at the equilibrium internuclear separation, $R = 3.54\,au$. (b) The barrier at short range on the $\bar{d}\sigma$ potential for $R = 3.1\,au$. The barrier is higher than the barrier shown in Fig. 1-4a. (c) The WKB phase, $\int_{r_{in}}^{r_{out}} p_{d\sigma}(r')dr'$ as a function of energy, for $R = 3.54\,au$. The intersection of the WKB phase with the dashed $\pi/2$ line indicates the presence of a quasi bound level inside the barrier with energy $E = -0.035\,au$ (abscissa of the intersection).(d) The WKB phase as a function of energy, for $R = 3.1\,au$. The energy of the quasi bound level has increased from its value at the equilibrium internuclear separation, to an energy in the ionization continuum. (e) The largest eigenvalue of the lifetime matrix determined from the *ab initio* scattering matrix for $R = 3.54\,au$. The maximum value of the lifetime located at an energy slightly below the ionization threshold implies the existence of a shape resonance at energy $E = -0.013\,au$. (f) The largest eigenvalue of the lifetime matrix determined from the *ab initio* scattering matrix for $R = 3.1\,au$. The resonance peak shifts into the ionization continuum at this internuclear distance, in qualitative agreement with the WKB result.

Table 5.1: Comparison of the resonance parameters obtained from the WKB approximation and the *ab initio* results. All quantities are reported in atomic units.

Int. Distance	E_{res}(WKB) [1]	E_{res}(Exact) [2]	Collision Frequency [3]	Γ [4]
$R = 3.54$	-0.035	-0.013	0.2	0.15
$R = 3.1$	0.051	0.062	0.21	0.25

ab initio lifetime matrix is shown as a function of energy in Fig. 5-2e. The lifetime curve displays a resonance peak at $E_{res} = -0.013\,au$. Thus, although the adiabatic approximation and the WKB analysis predict the presence of a shape resonance correctly, the WKB result significantly underestimates the energy of the resonance (for reasons discussed below). Figure 5-2d displays the WKB result for $R = 3.1\,au$. At this shorter internuclear distance, the barrier height centered on the F$^-$ ion increases (Figs. 5-2a and 5-2b) and the energy of the quasi-bound level, as predicted by the WKB approximation, rises to $E = 0.051\,au$. This behavior is also reflected in the *ab initio* result for $R = 3.1\,au$ shown in Fig. 5-2e, which displays a maximum in the lifetime curve at value of E_{res} that has increased from $-0.013\,au$ to $E_{res} = 0.062\,au$.

Figures 5-2a and 5-2b show that at the resonance center, the electronic energy on the $R = 3.1\,au$ curve is just below the barrier maximum and the electron must tunnel through a relatively narrow barrier width to reach the classically allowed region. This results in an increased probability for transmission at the shorter internuclear distance. The entries in Table 5.1 indicate that the frequencies of collisions with the barrier are approximately the same for both values of R. Thus, the increased value of the transmission probability should immediately lead to a decreased lifetime and a broader resonance on the $R = 3.1\,au$ curve (The lifetime is, by definition, the inverse of the product of the collision frequency and the transmission probability.) The resonance widths at the two internuclear distances, which are obtained from a Lorentzian fit to the maximum eigenvalue of the lifetime matrix, are reported in Table 5.1. The relative values of the two widths are consistent with expectations based on the qualitative discussion of the WKB results.

---

[1] The energy of the quasi-bound level determined by the WKB approximation.

[2] The energy of the quasi-bound level determined from the short-range scattering matrix.

[3] The collision frequency is defined as $< v > /[2(r_{out}(E_{res}) - r_{in}(E_{res}))]$, where $< v >$ is the average velocity inside the well and $r_{in}\,, r_{out}$ are the classical turning points defined in Eq. 1.9. It can be interpreted as the inverse of the time it takes for a classical particle in the well to return to the outer turning point after bouncing back from the inner wall near the Ca nucleus. The collision frequency simplifies to $\frac{\pi}{4(r_{out}-r_{in})^2}\frac{\hbar}{m_e}$ at the energy of the quasi-bound level.

[4] The resonance width calculated from a Lorentzian fit to the maximum eigenvalue of the lifetime

Table 5.2: Branching Ratios

Int. Distance	$\bar{s}$	$\bar{p}$	$\bar{d}$	$\bar{f}$
$R = 3.54\,au$	0.17	0.44	0.39	0.01
$R = 3.1\,au$	0.08	0.39	0.50	0.02

The preceding analysis demonstrates that the combination of the adiabatic approximation of Le Dourneuf et al. [23] and WKB theory describes the qualitative aspects of the shape resonance. In particular, the use of the approximate theory allows for prediction of the variation of both the resonance center and width with internuclear distance. However, the *ab initio* results and the results of the adiabatic approximation are not in quantitative agreement. There is also a disagreement in the respective partial-l descriptions of the shape resonance obtained from the two methods. The amplitude squared components of the eigenvector of the lifetime matrix associated with the eigenvalue q_{max}, or the *branching ratios*, characterize the probability of decay into the collision channels, labeled by $\bar{l}$. The branching ratios shown in Table 5.2 indicate that the shape resonance decays to $\bar{p}$ and $\bar{d}$ channels with nearly equal probability at both internuclear distances. The adiabatic approximation, on the other hand, suggests that the resonance must occur in the $\bar{d}$ channel alone. Clearly, the discrepancy is due to the neglected coupling terms in Eq. 5.2.8, which describe the non-adiabatic coupling between the modes that belong to the potential curves of Fig. 5-1. The adiabatic approximation breaks down within the compact region of the CaF ion-core, because the adiabatic modes of Eq. 5.2.4 change from pure-l type angular modes at short r to highly l-mixed dipolar modes at larger r, $r \geq R$. Figure 5-3 displays the amplitude squared partial-l decomposition ($(|a_{\bar{d}l'}(r)|^2$ from Eq. 5.2.4) of the adiabatic $\bar{d}$ mode as a function of r, for $R = 3.1\,au$. An important observation can be made from this figure: the pure-d type angular mode at small-r evolves quickly at short range, toward a single dipolar mode at long range. The rapid change in character of the adiabatic mode occurs within a small interval of r confined near the position of the fluorine nucleus ($r = R$). This statement is valid for all of the adiabatic modes at both (R= 3.54 and 3.10 au) internuclear distances. The underlying physical cause of this behavior is, in fact, quite general. Abrupt, r-dependent distortions occur in the adiabatic channel wavefunctions near

---

matrix.

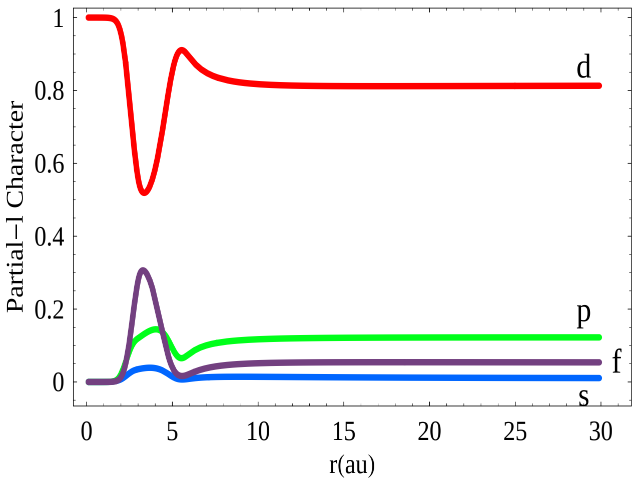

Figure 5-3: The amplitude squared partial-l components of the $\bar{d}$ adiabatic mode as a function of r, for $R = 3.1\,au$. The adiabatic mode starts out as a pure-d state at small r and evolves toward a d-dominant dipolar mode at large r. The change in character occurs rapidly within a small interval of r near the fluorine nucleus.

the fluorine center. These distortions arise as the electron tries to avoid the excluded volume associated with the F$^-$ ionic core. The Fluoride ion-core has a radius of $2.5\,au$ and marks the boundary between short-range and long-range behavior in the channel wavefunctions. As a consequence, the coupling between the adiabatic channels is significant only over this limited range of r. Starting from this observation, we explain below the generic energy dependence of the short-range reaction matrix.

Our analysis of the energy dependence of the dipole-reduced reaction matrix, $\bar{\mathbf{K}}$ [117] begins from the terms neglected in the adiabatic approximation. Based on the observation stated above, to an excellent approximation,

$$A^{\sigma}_{ll'}(r), B^{\sigma}_{ll'}(r) = 0 \qquad for\ r \notin (r_{min}, r_{max}) \tag{5.2.13}$$

for all l and l' and where (r_{min}, r_{max}) is a small interval centered about the fluorine nucleus. The matrices **A** and **B** are defined in Eq. 5.2.8. In the following, the label σ $(\lambda = 0)$ will be suppressed. We let the functions $(f_l(r,E), g_l(r,E))$ denote the energy-normalized regular and irregular solutions for each adiabatic curve $V_l(r)$. Since the adiabatic modes converge to the various dipole modes as $r \to \infty$, the dipole-reduced reaction matrix normalized solutions are given by [117],

$$F_{ll'}(r \to \infty) = f_l(r)\delta_{ll'} - g_l(r)\bar{K}_{ll'}. \tag{5.2.14}$$

For these $\bar{\mathbf{K}}$-matrix normalized solutions, we define the radial Green function as,

$$G_l(r, r') = \frac{\pi}{2} f_l(r_<) g_l(r_>). \tag{5.2.15}$$

The formal solution to the coupled equations can be expressed in terms of the Green function as,

$$\begin{aligned} F_{ll'}(r) &= \delta_{ll'} f_{l'}(r) \\ &\quad - \sum_{l''} \int_0^\infty dr' G_l(r, r') \left(2A_{ll''}(r') \frac{dF_{l''l'}(r')}{dr} + B_{ll''}(r') F_{l''l'}(r') \right). \end{aligned} \tag{5.2.16}$$

Using Eqs. 5.2.16 and 5.2.15, we can write a first order expression for the $\bar{\mathbf{K}}$-matrix:

$$\bar{K}^{(1)}_{l,l'} = -\tfrac{\pi}{2} \int_0^\infty dr' f_l(r') \left(2A_{ll'}(r') \tfrac{df_{l'}(r')}{dr'} + B_{ll'}(r') f_{l'}(r') \right), \tag{5.2.17}$$

$$= -\tfrac{\pi}{2} \int_{r_{min}}^{r_{max}} dr' f_l(r') \left(2A_{ll'}(r') \tfrac{df_{l'}(r')}{dr'} + B_{ll'}(r') f_{l'}(r') \right). \tag{5.2.18}$$

Equation 5.2.18 shows that the reaction matrix elements in the dipole representation are obtained from non-adiabatic interactions confined to a limited range of r; the $\bar{\mathbf{K}}$ matrix depends only on the short-range features of the molecular potential in the vicinity of the F^- nucleus and is free of influence from the long-range field. This shows that the $\bar{\mathbf{K}}$ matrix treatment removes all strong energy dependences that are due to the extremely polar ion-core. In addition, it allows for the transparent identification of any significant energy dependence that arises from a physical origin distinct from long-range field effects.

The energy normalized regular solutions, $f_l(r)$, for the barrier-free adiabatic potential curves vary slowly with energy, and the sole effect of increasing the energy for these solutions is to cause them to oscillate at higher spatial frequency. Therefore, the corresponding elements of the reaction matrix decrease monotonically with increasing energy. However, the regular solution for the $\bar{d}$ curve varies significantly as the energy is increased above the barrier height. When the energy is below the barrier maximum, a second turning point appears on the small-r side of the barrier. This leads to confinement in the well between the Ca^{+2} and F^- ions and an accumulation of amplitude near the outer turning point, which is within the (r_{min}, r_{max}) interval. Consequently, large off-diagonal contributions to the $\bar{\mathbf{K}}$ matrix arise in components that couple to the adiabatic $\bar{d}$ channel (components $\bar{K}_{ll'}$ with l or $l' = 2$). This causes mixing between the adiabatic $\bar{d}$ channel and the other channels of penetrating character (the lower two curves in Fig. 5-1). Accordingly, $\bar{d}$ character is mixed into the interacting channels in the shape-resonance/confinement region, as is evident in the branching ratios displayed in Table 5.2. When the collision energy is above the barrier maximum, the regular solution for the $\bar{d}$ curve again oscillates at higher spatial frequency with increasing E. This implies that all the elements of the $\bar{\mathbf{K}}$ matrix eventually decrease with energy and the eigenquantum defects approach 0. A formal derivation of this result can be developed . The behavior is analogous to the energy dependence of the phase shifts for electron scattering by atomic fields studied by Manson [82].

5.3 Violation of Mulliken's Rule Caused by the Shape Resonance

The values for the resonance width and center at $R = R_{eq}$, shown in Table 5.1, indicate that the *entire* Rydberg spectrum of CaF for the 0.88 $^2\Sigma^+$ series is affected by the shape resonance . This is also demonstrated by the increase of the eigenquantum defect for the resonant 0.88 $^2\Sigma^+$ channel as a function of energy below the ionization threshold [112]. Mulliken's rule [90] stipulates that the shapes (partial-l characters) and nodal positions of the electronic wavefunctions within a Rydberg series should be nearly energy-independent at short-range. However, Mulliken's rule cannot be obeyed in the vicinity of a shape resonance, precisely because of the underlying physical circumstances that give rise to such a resonance. As an illustration, Figures 5-4a-d display the plots of the resonance-free $0.55^2\Sigma^+$ series wavefunctions at three different energies in the $\phi = 0$, x-z plane. In these figures, the Ca nucleus is placed at $z = 0$ and the F nucleus is at $z = R_e = 3.54\,au$. The $n^* = 10.55^2\Sigma^+$ bound Rydberg state, shown in Fig.5-4a, is polarized behind the Ca nucleus at long-range. The innermost lobes of the 10.55 wavefunction and two continuum 0.55-series $^2\Sigma^+$ wavefunctions ($E = 0.01\,au$ and $E = 0.15\,au$) are displayed in Figs.5-4b , 5-4c and 5-4d. The shapes and the nodal positions of the innermost lobes are approximately preserved throughout this energy interval, which is in agreement with Mulliken's rule. Comparison

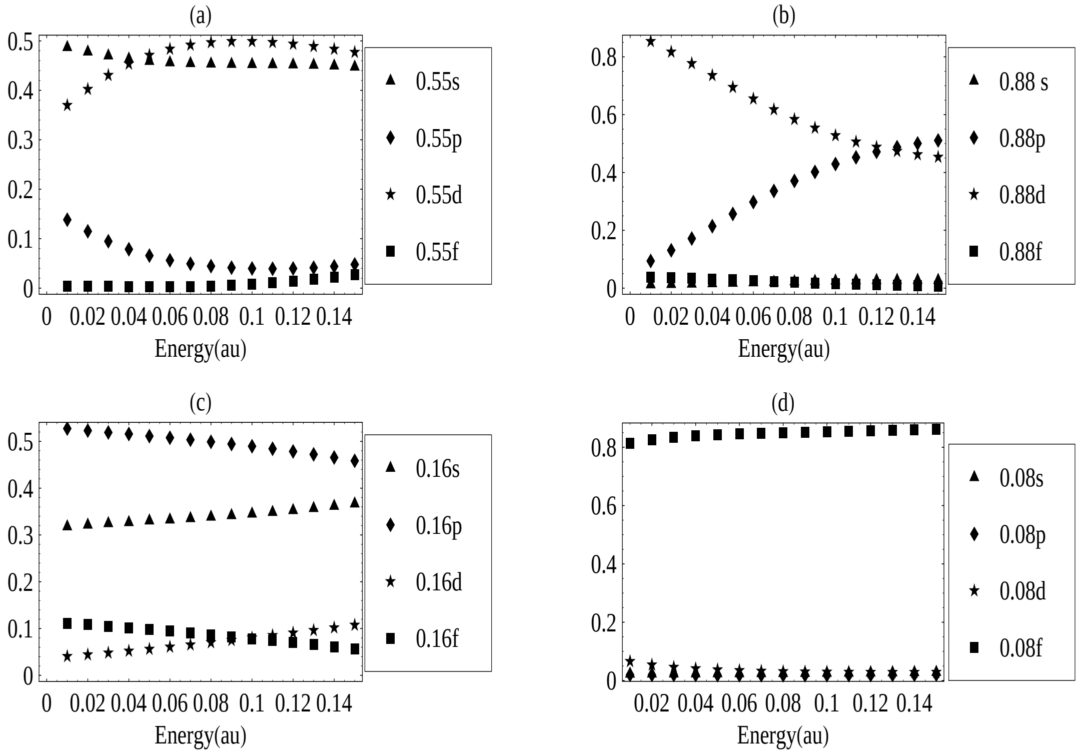

Figure 5-5: The energy dependence of the calculated parameters c_l for the four $^2\Sigma^+$ symmetry eigenchannels. (a) The parameters c_l for the $0.55^2\Sigma^+$ channel. (b) The parameters c_l for the $0.88^2\Sigma^+$ channel. The figure illustrates that the 0.88 wavefunction has almost pure d character at low-energy. It rapidly evolves to become an equal d-p mixture at higher energy. This strong energy dependence at short-range is in violation of Mulliken's rule. (c) The parameters c_l for the $0.16^2\Sigma^+$ channel.(d) The parameters c_l for the $0.08^2\Sigma^+$ channel.

Table 5.3: Branching Ratios to the Eigenchannels

	$0.55\,^2\Sigma^+$	$0.88\,^2\Sigma^+$	$0.16\,^2\Sigma^+$	$0.08\,^2\Sigma^+$
$B\,(E = E_{res})$	0.16	0.80	0.04	0.004

eigenchannels. These quantities are defined as,

$$\bar{B} = |\tilde{\mathbf{V}}.\tilde{\mathbf{U}}_j|^2, \tag{5.3.21}$$

where $\tilde{\mathbf{V}}$ is the eigenvector of $\bar{\mathbf{Q}}$ (Eq. 4.2.7) that corresponds to q_{max} and $\tilde{\mathbf{U}}_j$ is the eigenvector of $\bar{\mathbf{K}}$ associated with the eigenchannel. The calculated branching ratios to the four eigenchannels are shown in Table 5.3 near the resonance energy, E_{res}, and the equilibrium internuclear separation $R = 3.54\,au$ of CaF$^+$. According to these results, the $0.88^2\Sigma^+$ eigenchannel is most strongly affected by the shape resonance. This is fully consistent with the predictions of the one-dimensional adiabatic approximation discussed above. The $0.88^2\Sigma^+$ wavefunctions, which are dominantly d-type orbitals at short-range, are affected strongly by the barrier on the F$^-$ ion seen on the $\bar{d}$-labeled adiabatic curve in Fig. 5-1. The wavefunctions in the non-resonant eigenchannels are largely unaffected by the barrier, because they have less d character at short-range. At collision energies far above the resonance energy, E_{res}, the electron escapes the influence of the shape resonance; the innermost lobe of the resonant eigenchannel wavefunction changes its shape from a dominant d-type orbital (polarized toward the F$^-$) near the resonance to a $p-d$ mixture (polarized away from the F$^-$) above the resonance. However, the innermost lobes of the eigenchannel wavefunctions that are unaffected by the shape resonance remain largely invariant. For the uniquely resonant eigenchannel, a breakdown of Mulliken's rule occurs centered at the energy of the shape resonance.

Clearly, a violation of Mulliken's rule is generic to any molecular system the electronic structure of which is perturbed by a resonance. A strong broad resonance perturbs the electronic structure globally, but its effect on the electronic spectrum is subtle and easily missed. A weak, narrow resonance perturbs the electronic structure locally but profoundly, and its effect on the electronic spectrum is obvious. Both kinds of resonances are recognizable and fittable since one knows the nature of the underlying Mulliken's rule zero-order picture, with its explicitly expected energy and wavefunction scalings. Namely, the expected Mulliken's rule energy dependence of the quantum defect is given by the Rydberg-Ritz formula in Eq. 5.1.1 and leads typically to monotonic changes of a few percent in the eigenquantum defects over the entire energy range of the Rydberg states.

In analyses of experimental data, Mulliken's rule can be used as a diagnostic tool to identify a global "scarring" of the spectrum, represented by the broad shape resonance found in CaF. For example, the $0.88^2\Sigma^+$ series can be designated as a $np\sigma$ penetrating type-Rydberg series in the spirit of Mulliken's rule [65]. According to the Rydberg-Ritz formula given in Eq. 5.1.1, the coefficient β should be negative and an estimate on its magnitude is found to be $0.32/au$ by comparison to the slope of the plot of the p-wave scattering phase-shift for Cu as a function of energy near the ionization threshold (this plot is given in reference [82]). However, the β coefficient for the 0.88 eigenquantum defect is everywhere *positive* [118] and its magnitude is calculated to be $2.73/au$ near the ionization threshold, which is much *larger* than the estimate for the unperturbed case. Thus, the violation of Mulliken's rule in the CaF spectrum gives clear experimental evidence for the presence of a strong and global perturbation, which is otherwise concealed by the apparent regularities of the Rydberg energies, spectral intensities and the smooth, perturbation-free behavior of the eigenquantum defect as a function of energy.

The global "scarring" of the spectrum is best uncovered by an extended, global analysis based on a multi-channel quantum defect theory (MQDT) fit [37] in which selected elements of the quantum defect matrix are allowed to be energy dependent. In practice, if the quantum defect matrix elements are permitted to have an arbitrary energy dependence, then a large number of adjustable parameters are required and the fit results are likely to be non-physical and non-unique owing to the inevitably incomplete and undemocratic experimental sampling of the energy levels. However, guided by the present results, a restricted fit procedure can be developed to yield a quantum defect matrix that incorporates (i) the physically significant energy dependences in the quantum defects determined a-priori by using the Mulliken's rule test (ii) the expected generic analytical energy dependences given by the Rydberg-Ritz formula for those quantum defects that are well described by Mulliken's rule.

It should be mentioned that there are numerous reported cases, where a violation of Mulliken's rule is diagnostic of a perturbation that distorts a large portion of a Rydberg series. An illustrative example that is similar to the present shape resonance is the perturbation found in the $3s^2nd$ $^2D^e$ Rydberg series of aluminum [76, 98]. This Rydberg series interacts with a $3s3p^2$ $^2D^e$ configuration, and the effect of this interaction is spread over the entire series and the adjoining continuum. Since the oscillator strength to the $3s3p^2$ $^2D^e$ configuration is distributed throughout the series, the perturbation is globally pervasive, but it is not easily recognizable locally. Another example is the 4snd $^1D_2$ Rydberg series of atomic calcium [6]. This series strongly interacts with two doubly excited configurations of the type $3d^2$ and $4p^2$ $^1D_2$. The perturbation spans the high Rydberg members of the 4snd series and the quantum defects vary with energy over many principal quantum numbers. In both the aluminum and the calcium examples, the global distortion of the Rydberg spectra indicated by the violation of Mulliken's rule reveals the presence of these strong perturbations.

5.4 Conclusions

We have demonstrated that the combination of the adiabatic theory of Le Dourneuf et al. and the WKB approximation describes the qualitative aspects of a $^2\Sigma^+$ shape resonance in CaF^+-electron scattering. In particular, we have shown that the shape resonance is due to the trapping of the electron inside a well that is localized between the Ca^{+2} and F^- atomic ions. This well consists of an inner wall generated by the centrifugal barrier near the Ca^{+2} ion and an outer wall due to the excluded volume around the F^- ion. The WKB analysis correctly predicts the qualitative dependence of the energy of the resonance center and the resonance width on internuclear distance.

Rapid changes in the adiabatic channel wavefunctions occur in the vicinity of the excluded volume around the F^- ion. This leads to a non-adiabatic coupling of the collision channels and a breakdown of the WKB-based one-dimensional adiabatic approximation. The rapid variations in the wavefunctions are confined to the small radial interval occupied by the excluded volume. Within this radial interval, the adiabatic modes change character from single-l angular momentum modes near the Ca nucleus to mixed-l dipolar modes at larger radial distances. The quasi-bound level in the well, localized between the centrifugal barrier on Ca^{+2} and the excluded volume around F^-, decays into the classically allowed region either because of electron tunneling through the barrier shown in Fig. 5-2a or by non-adiabatic coupling to the collision channels that are associated with one of the barrier-free potential curves shown in Fig. 5-1. Exploiting the confinement of the rapid variations of the adiabatic modes to a limited radial interval, an integral formula (Eq. 5.2.18) is derived for the elements of the dipole-reduced reaction matrix for CaF. The formula indicates that the dipole-reduced reaction matrix depends on the molecular potential in a limited radial range near the F^- nucleus. The dipole-reduced $\bar{\mathbf{K}}$ matrix is free of the effects of all long-range fields, in particular the energy dependences due to polar cores. Therefore, the $\bar{\mathbf{K}}$ matrix formalism provides information on purely the short-range dynamical effects, such as the shape resonance in CaF.

Finally, we have demonstrated that Mulliken's rule for the structure of Rydberg states is diagnostically violated in the presence of a class of resonance that globally scars the spectrum. The presence of this resonance is displayed in the spectrum at all energies as slow and subtle violations of Mulliken's rule as a function of the principal electronic quantum number. In this sense the spectrum below the resonance is *not regular*, although no anomalies in terms of local level perturbations are visible. The irregularity is best uncovered from the collective behavior of the electronic energy levels, which requires a theoretical model that is not local but global. Such a global analysis is a restricted MQDT fit of the energy dependent quantum defect matrix [37] to the energy levels for a significant range of principal electronic quantum numbers (e.g. $n^* = 6 - 30$). The extraction of these global, systematic and often unnoticed effects from Rydberg spectra requires a different view from the usual perspective, which is primarily focused on irregularities manifest as local perturbations.

Chapter 6

Many Electron Generalization of the *ab initio* Reaction Matrix Calculation

6.1 Introduction

In this chapter, we present a many electron generalization of the *ab initio* reaction matrix calculation discussed in **Chapter 3**. We take into account the ion-core electrons explicitly and develop a unified treatment of Rydberg states built upon open and closed shell ion-cores. A variational formalism is used for facile incorporation of electron exchange effects and molecular symmetry. This variational formalism is constructed in the spirit of orbital-functional theory of which Hartree-Fock theory is a special case [95]. Feshbach's projection operator theory is used to partition the orbital-Hilbert space into subspaces spanned separately by bound and continuum type configurations [35, 36]. The bound-type configurations are square integrable and they are formed as antisymmetrized products of one-electron spin-orbitals optimized on the molecular ion-core in a Hartree-Fock calculation. An **R**-matrix radius, r_o, is chosen sufficiently large such that the non-zero spatial parts of the one-electron spin-orbitals are contained within the radial extent of the **R**-matrix box. In contrast, the continuum orbitals are diffuse and they have non-zero amplitudes on the spherical **R**-matrix boundary. The continuum configurations are formed as antisymmetrized products of continuum orbitals with the orthonormal eigenvectors of the ion-core Hamiltonian expressed in a common set of N-electron basis functions, where N is the number of active electrons on the ion-core.

The advantage of using Feshbach's projection operator theory is that all many-electron Hamiltonian matrix elements between bound-bound and bound-continuum configurations can be evaluated using the methods of standard quantum chemistry. For this reason, it is practical to express all one-electron orbitals in terms of Cartesian or spherical Gaussian functions [137, 103, 84] and obtain the molecular integrals from a quantum chemistry computer program such as *Gaussian 03.* The reaction matrix calculation departs from the quantum chemistry approach in the evaluation of Hamiltonian matrix elements involving the continuum orbitals. The continuum orbitals are not orthonormal to the bound-type orbital basis functions by construction. The combined set of continuum and bound type basis functions must be Schmidt orthonormalized, so that the Slater rules for evaluating matrix elements between Slater determinants can be applied [128]. Furthermore, the analytical results for molecular integrals over standard Gaussian basis functions are valid when the integrations are over all space. Since the molecular integrals involving the continuum orbitals are calculated within the **R** matrix box, the analytical expressions for these integrals must be corrected by subtracting out the tail contributions outside the **R**-matrix box. Wong, Altunata, and Field have demonstrated that these non-standard tail integrals over Gaussian basis functions can be evaluated analytically [137]. The results presented in that work allow for the determination of all the molecular integrals required for the reaction matrix calculation from the output of *Gaussian 03.*

The many-electron theory adapted to total electronic spin and molecular symmetry is discussed in Section 5.2. The reaction matrix is derived from a variational constraint on the Hamiltonian matrix, which is stationarized when a trial wavefunction coincides with the stationary state of the collision. As a validating test of the theory, in Section 5.3, we calculate the single-channel reaction matrix for the 1sσ npσ $^1\Sigma_u^+$ Rydberg states of H_2. Satisfactory agreement with previous *ab initio* calculations employing different methods is obtained [1]. The computer program that performed these calculations was written by Bryan

---

[1] Low lying Rydberg states can also be calculated using excited-state quantum chemistry methods. Most noted among these are the coupled cluster excited state methods (EOM-CCSD) developed by Stanton and co-workers [122] and the symmetry adapted cluster/configuration interaction (SAC-CI) method of Nakatsuji and coworkers [92, 93, 94].

M. Wong and Serhan Altunata. The theory developed here constitutes the final step for embedding the generalized quantum defect methods presented in this thesis into quantum chemistry. An approximate theory that is similar to the current approach has already been developed by our group [4].

6.2 The Variational K-Matrix Theory

The reaction matrix calculation uses a set of orbital basis functions that are variationally optimized on the molecular ion-core Hamiltonian. We first review the construction of these orbital basis functions and derive the Slater-rule expressions for the matrix elements between electronic configurations. These rules will also apply in the computation of the reaction matrix.

6.2.1 The N-electron Ion-Core Hamiltonian

The variational equation for the N-electron molecular ion-core is,

$$(H-E)\Psi = 0, \tag{6.2.1}$$

where $H = T + U + V$ and

$$T = -\tfrac{1}{2}\textstyle\sum_i \nabla_i^2 \tag{6.2.2}$$

$$U = \tfrac{1}{2}\textstyle\sum_{ij} \frac{1}{r_{ij}} = \tfrac{1}{2}\sum_{ij} u(r_{ij}) \tag{6.2.3}$$

$$V = \textstyle\sum_i v(\vec{r}_i). \tag{6.2.4}$$

In Eq. 6.2.4, T is the total electronic kinetic energy, V is the total potential energy of nuclear-electron attraction and U is the total energy of electron-electron repulsion. We define a reference state as a single Slater determinant, which is a normalized antisymmetrized product of N orthonormal spin-orbital wavefunctions of the one-electron coordinates (spatial and spin),

$$\Phi = (N!)^{-1/2} det[\phi_1(1)\cdots\phi_N(N)]. \tag{6.2.5}$$

A complete set of determinants is defined by virtual excitations from the reference state. The virtual excitations are obtained by replacing one (or more) of the N occupied orbital functions of Φ by functions from the residual unoccupied orbital basis set, which is complete and infinite. The present theory is restricted to particle-hole and double particle-hole excitations, which are defined as,

$$\begin{aligned} \phi_i^a &= det[1, \cdots, i \to a, \cdots, N] \\ \phi_{ij}^{ab} &= det[1, \cdots, i \to a, \cdots, j \to b, \cdots, N]. \end{aligned} \tag{6.2.6}$$

Following Fermi-Dirac statistics, we define the occupation numbers for the zero-temperature reference state wavefunction as,

$$n_i = 1 \quad n_a = 0 \qquad i \leq N < a. \tag{6.2.7}$$

We also define an exchange adapted electron/electron repulsion operator as,

$$\bar{u} = \frac{1}{r_{12}}(1 - P_{12}), \tag{6.2.8}$$

where P_{12} permutes the labels of the two electrons. The one-electron orbital basis set $\{\phi_i\}$ is optimized by requiring that the energy functional $E_o = (\Phi|H|\Phi)$ is stationarized with respect to variations in the one-electron orbitals. The total energy functional can be expressed as the sum of explicit functionals using the Slater rules as [128],

$$T(\{\phi_i\}) = (\Phi|\hat{T}|\Phi) = -\tfrac{1}{2}\textstyle\sum_i n_i(i|\nabla^2|i) \tag{6.2.9}$$

$$U(\{\phi_i\}) = (\Phi|\hat{U}|\Phi) = \tfrac{1}{2}\textstyle\sum_{ij}(ij|\bar{u}|ij) \tag{6.2.10}$$

$$V(\{\phi_i\}) = (\Phi|\hat{V}|\Phi) = \textstyle\sum_i n_i(i|v(\mathbf{r})|i), \tag{6.2.11}$$

where the $\hat{U}$ operator defines Coulomb and exchange functionals of the form,

$$E_{Coulomb} = \tfrac{1}{2}\textstyle\sum_{ij} n_i n_j (ij|u|ij) \tag{6.2.12}$$

$$E_{Exchange} = -\tfrac{1}{2}\textstyle\sum_{ij} n_i n_j (ij|u|ji). \tag{6.2.13}$$

In Eqs. 6.2.12 and 6.2.13, the two electron matrix elements are defined as,

$$(ij|u|ij) = \int d^4x_1 d^4x_2 \phi_i^*(\mathbf{r}_1, \sigma_1)\phi_j^*(\mathbf{r}_2, \sigma_2)\bar{u}\phi_i(\mathbf{r}_1, \sigma_1)\phi_j(\mathbf{r}_2, \sigma_2), \tag{6.2.14}$$

where the integrations are over spatial ($\mathbf{r}$) and spin (σ) coordinates. From Eqs. 6.2.9, 6.2.10 and 6.2.11, we determine the functional derivatives with respect to the basis orbitals as,

$$\begin{aligned} \tfrac{\delta T}{n_i \delta \phi_i^*} &= -\tfrac{1}{2}\nabla^2 \phi_i && (6.2.15)\\ \tfrac{\delta V}{n_i \delta \phi_i^*} &= v(\mathbf{r})\phi_i && (6.2.16)\\ \tfrac{\delta E_{Coulomb}}{n_i \delta \phi_i^*} &= v_{Coulomb}(\mathbf{r})\phi_i = \textstyle\sum_j n_j (j|\tfrac{1}{r_{12}}|j)\phi_i && (6.2.17)\\ \tfrac{\delta E_{Exchange}}{n_i \delta \phi_i^*} &= \hat{v}_{Exchange}\phi_i = -\textstyle\sum_j n_j (j|\tfrac{1}{r_{12}}|i)\phi_j. && (6.2.18) \end{aligned}$$

The total energy functional becomes,

$$\frac{\delta E}{n_i \delta \phi_i^*} = \frac{\delta(T + V + E_{Coulomb} + E_{Exchange})}{n_i \delta \phi_i^*}. \qquad (6.2.19)$$

We seek to make $E = E_o$ stationary subject to the constraint $(i|j) = \delta_{ij}$. This constraint is introduced through a matrix of Lagrange multipliers λ_{ij}. Thus,

$$\begin{aligned} &\delta\left(E - \left(\textstyle\sum_{ij} n_i n_j \int d^3r \phi_i^* \phi_j - \delta_{ij}\right)\lambda_{ij}\right) = \\ &\textstyle\sum_i n_i \left[\int \delta\phi_i^* \left(\tfrac{\delta E}{n_i \delta\phi_i^*} - \sum_j n_j \phi_j \lambda_{ji}\right) d^3r + cc\right] \\ &\qquad + \textstyle\sum_i \delta n_i \int \phi_i^* \tfrac{\delta E}{n_i \delta \phi_i^*} = 0, \qquad (6.2.20) \end{aligned}$$

where *cc* denotes the complex conjugate of the preceding term. The arbitrary variation $\delta\phi_i^*$ implies that,

$$\frac{\delta E}{n_i \delta \phi_i^*} = h\phi_i = \sum_j n_j \phi_j \lambda_{ji}, \qquad (6.2.21)$$

wherein, through Eqs.6.2.15-6.2.18, the effective one-electron Hamiltonian is given by,

$$h = -\frac{1}{2}\nabla^2 + v(\mathbf{r}) + v_{Coulomb}(\mathbf{r}) + \hat{v}_{Exchange}(\mathbf{r}). \qquad (6.2.22)$$

The Canonical Form

Let **T** be the orthonormal matrix that diagonalizes λ. Define a transformed basis,

$$\tilde{\phi}_i = \sum_k \phi_k T_{ki}. \tag{6.2.23}$$

Then

$$h\tilde{\phi}_i = h\sum_k \phi_k T_{ki} = \sum_{jlk} n_j \tilde{\phi}_l (T_{lj})^{-1} \lambda_{jk} T_{ki} \tag{6.2.24}$$

Imposing the boundary condition $n_j = 1$ gives,

$$h\tilde{\phi}_i = \sum_l \tilde{\phi}_l \delta_{li} \epsilon_i = \epsilon_i \tilde{\phi}_i, \tag{6.2.25}$$

where ϵ_i are the eigenvalues of the Lagrange matrix λ. Equation 6.2.25 is the canonical form of the orbital Euler-Lagrange equations. The set of solutions to this equation, $\tilde{\phi}_i$, are the optimized one-electron orbitals that will be used in the reaction matrix calculation. They automatically define a basis for an irreducible representation of the molecular point group [128]. The total electronic energy of the ion-core is found from the matrix element

$$E = (\Phi(\{\tilde{\phi}\})|H|\Phi(\{\tilde{\phi}\})). \tag{6.2.26}$$

6.2.2 Reaction Matrix Calculation for an N+1 Electron Molecule

We write the multi-configuration $N + 1$ electron wavefunction for scattering of an electron from an N-electron diatomic molecule as,

$$\Psi_s(S, M_s, X \in \{C_{\infty v}, D_{\infty h}\}, \{\vec{r}_i\}) = \sum_P A\Theta_p \phi_{ps}(\vec{r}) + \sum_\mu \Phi_\mu c_{\mu s}, \tag{6.2.27}$$

where, Θ_p denotes a vector coupled product of an N-electron wavefunction of the isolated ion-core (derived in the previous subsection) and the spin of the scattered electron. The definition of Θ_p is

$$\Theta_p = \sum_{m_s=-\frac{1}{2}}^{\frac{1}{2}} (s_p, M_s - m_s, \tfrac{1}{2}, m_S|S, M_s) W_p u_{m_s}(\sigma), \tag{6.2.28}$$

$$u_{\frac{1}{2}}(\sigma) = \alpha(\sigma), \tag{6.2.29}$$

$$u_{-\frac{1}{2}}(\sigma) = \beta(\sigma). \tag{6.2.30}$$

In Eqs. 6.2.29 and 6.2.30 the standard quantum chemistry notation for the spin coordinates are used. Equation 6.2.28 defines the internal state of the collision channel indexed by p. The expression W_p denotes the N-electron wavefunction for the ion-core, which is defined for total ion-core spin s_p and ion-core symmetry X'. The ion-core symmetry is characterized by the set of one-electron spin-orbitals that transform under coordinate rotations according to an irreducible representation in the molecular point group $C_{\infty v}$ for heteronuclear diatomics or the point group $D_{\infty h}$ for homonuclear molecules. We define E_p to be the energy eigenvalue of the ion-core eigenstate, W_p, and E is the total energy of the $N+1$ electron molecule.

The function $\phi_{ps}(\vec{r})$ is the diffuse "continuum" orbital for the Rydberg or scattered electron defined as [2],

$$\phi_{ps}(\vec{r}) = \frac{f_{ps}(r)}{r} Y_{l_p, m_{l_p}}(\theta, \phi). \tag{6.2.31}$$

At $r > r_o$, the functions $\phi_{ps}(\vec{r})$ are given by linear combinations of the Coulomb functions as,

$$f_{ps}(r > r_o) = f_{l_p}(\epsilon_p, r)\alpha_{0ps} - g_{l_p}(\epsilon_p, r)\alpha_{1ps}, \tag{6.2.32}$$

The quantity $\epsilon_p = E - E_p$ is the electronic binding energy in the $p'th$ collision channel. If there are additional long-range fields present, the expression in Eq. 6.2.32 must be modified according to the $\bar{\mathbf{K}}$ representation described in **Chapter 3**.

In Eq. 6.2.27, A is an operator that antisymmetrizes the spatial-spin coordinates of the $N+1$'st electron, $(r, \theta, \phi, \sigma)$, to the spatial-spin coordinates of all the remaining electrons, $(x_i, y_i, z_i, \sigma_i)$, on the ion-core. The effect of the antisymmetrization operation is that all the

---

[2] We note that if the ion-core symmetry differs from Σ, the use of the complex-valued spherical harmonic to describe the angular portion of the continuum orbital implies that correct linear combinations of the *Gaussian 03* output for the ion-core wavefunction must be taken so that the direct product $X' \otimes x(m_{l_p})$ yields the irreducible representation X of $C_{\infty v}$ or $D_{\infty h}$. Otherwise the calculated reaction matrix will be reducible. This is acceptable if one is interested only in the eigenquantum defects of the short-range reaction matrix. However, irreducible representations must be constructed for the rovibrational frame transformation.

Slater determinants describing multi-electron configurations of the ion-core in Eq. 6.2.27 get augmented by an extra column that corresponds to the continuum orbital of the Rydberg electron.

The expression $\{\Phi_\mu\}$ in Eq. 6.2.27 is an antisymmetrized $N+1$ electron CI basis function defined as

$$\Psi_\mu \equiv \Psi_\mu(S, M_s, X \in C_{\infty v}, \{\vec{r_i}\}). \tag{6.2.33}$$

The bound-type configurations in Eq. 6.2.33 are built from one-electron orbitals optimized on the ion-core Hamiltonian following the procedure in Section 6.2.1. They are obtained by single and double excitations from the reference configuration with an additional electron placed in one of the hole orbitals to form an $N+1$ electron eigenstate of total spin. An important property of Φ_μ is that the spatial extent of the molecular orbitals in Φ_μ must be within the R-matrix radius, r_o. In the spirit of the Feshbach projector formalism [35, 36], the expression for the wavefunction shown in Eq. 6.2.27 consists of the superposition of an orbital Hilbert space component,

$$\Psi_Q = Q\Psi_s = \sum_\mu \Phi_\mu(\Phi_\mu|\Psi_s) \tag{6.2.34}$$

with an orthogonal non-Hilbert space complement,

$$\Psi_P = P\Psi_s = \sum_P A\Theta_p\phi_{ps}(\vec{r}). \tag{6.2.35}$$

Q is a projection operator that projects into the orbital Hilbert space and P is an orthogonal complement of Q. The subspace Q is a function space with an L-2 (square integrable) norm, whereas only continuum normalization can be imposed on the complement space P. We seek to find the best variational solution to Ψ_Q in the designated subspace S spanned by the configurations Φ_μ in Eq. 6.2.27.

By definition, the reaction matrix is,

$$\mathbf{K} = \alpha_\mathbf{1}{\alpha_\mathbf{o}}^{-1}. \tag{6.2.36}$$

Since the reaction matrix is by assumption defined at short range ($r = r_o$), the expression shown in Eq. 6.2.36 does not distinguish between closed and open channels. Thus, the same reaction matrix yields positions of bound states in the region of the spectrum where all channels are closed, as well as doubly excited resonances, which autoionize into the continuum above the ground electronic state of the ion-core. We consider variations of the channel radial wavefunctions $f_{ps}(r)$ about the canonical form,

$$\alpha_o = \mathbf{I} \quad \alpha_1 = \mathbf{K}. \tag{6.2.37}$$

We begin by constructing continuum basis. This basis consists of functions, which are regular at the origin and connect with the regular and irregular functions beyond r_o. The basis functions of "0" type are defined as,

$$F_{0p}(r > r_o) = f_{l_p}(\epsilon_p, r). \tag{6.2.38}$$

The basis functions of "1" type are defined as,

$$F_{1p}(r > r_o) = g_{l_p}(\epsilon_p, r). \tag{6.2.39}$$

The forms of the basis functions F_{op} and F_{1p} for $r < r_o$ can be selected subject to the wavefunction continuity requirement at $r = r_o$. Here, we make the choice,

$$F_{0p}(r) = f_{l_p}(\epsilon_p, r), \tag{6.2.40}$$

$$F_{1p}(r) = (1 - e^{-\lambda_p r^{l_p+1}}) g_{l_p}(\epsilon_p, r). \tag{6.2.41}$$

In Eq. 6.2.41, the term $e^{-\lambda_p r^{l_p+1}}$ serves to remove the divergence at the origin in the irregular Coulomb function. In the next step, the diffuse basis, $\phi_{0p}(r) = F_{0p}(r) Y_{l_p, m_{l_p}}(\theta, \phi)$ and $\phi_{1p}(r) = F_{1p}(r) Y_{l_p, m_{l_p}}(\theta, \phi)$ must be orthonormalized to the square integrable molecular basis ϕ_i (index i for occupied orbital) and ϕ_a (index a for virtual orbital), which generate W_p and Φ_μ respectively. This involves calculation of the overlap matrices,

$$S_{\nu,0p} = \int_{r<r_o} d^3 r \phi_\nu^* \phi_{0p}, \tag{6.2.42}$$

$$S_{\nu,1p} = \int_{r<r_o} d^3 r \phi_\nu^* \phi_{1p}, \tag{6.2.43}$$

with $\phi_\nu \in \{\phi_i, \phi_a\}$. We further require the normalization constants

$$\begin{aligned} N_{0p} &= \sqrt{(\phi_{0p}|\phi_{0p}) - \sum_\nu |S_{\nu,0p}|^2} \\ N_{1p} &= \sqrt{(\phi_{1p}|\phi_{1p}) - \sum_\nu |S_{\nu,1p}|^2}. \end{aligned} \tag{6.2.44}$$

The transformed basis,

$$\begin{aligned} \tilde{\phi}_{0p} &= \frac{1}{N_{0p}} \left(\phi_{0p} - \sum_\nu \phi_\nu S_{\nu,0p} \right) \\ \tilde{\phi}_{1p} &= \frac{1}{N_{1p}} \left(\phi_{1p} - \sum_\nu \phi_\nu S_{\nu,1p} \right) \end{aligned} \tag{6.2.45}$$

is orthonormal to the ion-core molecular basis and the transformation rescales the asymptotic forms in Eqs. 6.2.38 and 6.2.39. Following this logic, the variational coefficients $c_{\mu s}$ in Eq. 6.2.27 can be factored out as,

$$c_{\mu s} = \sum_{ip} c_\mu^{ip} \alpha_{ip} \quad i \in \{0, 1\}. \tag{6.2.46}$$

The variational approximation to Ψ_s in Eq. 6.2.27 becomes,

$$\Psi_s = \sum_{ip} \left(A\Theta_p \tilde{\phi}_{ip} + \sum_\mu \Phi_\mu c_m^{ip} \right) \alpha_{ips}. \tag{6.2.47}$$

Next, we construct the functional,

$$\aleph_{st} = (\Psi_s|H - E|\Psi_t), \tag{6.2.48}$$

bearing in mind that the integrations are always confined within the **R**-matrix volume. $\aleph$ is an $n \times n$ matrix where n is the sum of the number of open and closed channels used in the calculation. Thus,

$$\aleph_{st} = \sum_{ip,jq} \alpha_{ips}\alpha_{jqt} \left(A\Theta_p \tilde{\phi}_{ip} + \sum_\mu \Phi_\mu c_\mu^{ip} | H - E | A\Theta_q \tilde{\phi}_{jq} + \sum_\nu \Phi_\nu c_\nu^{jq} \right). \tag{6.2.49}$$

For arbitrary values of α_{jqt}, setting the functional derivative

$$\frac{\delta \aleph_{st}}{\delta c_{\mu}^{ip*}} = 0, \tag{6.2.50}$$

yields

$$\left(\Phi_{\mu} | H - E | A\Theta_q \tilde{\phi}_{jq} + \sum_{\nu} \phi_{\nu} C_v^{jq} \right) = 0, \tag{6.2.51}$$

for all j, q. We can use Eq. 6.2.51 to rewrite $\aleph st$. The first term in this expression is,

$$M_{ij}^{pq} = \left(A\Theta_p \tilde{\phi}_{ip} | H - E | A\Theta_q \tilde{\phi}_{jq} \right). \tag{6.2.52}$$

The remaining term is $\left(A\Theta_p \tilde{\phi}_{ip} | H - E | \sum_{\nu} \phi_{\nu} c_v^{jq} \right)$. This reduces to,

$$\left(A\Theta_p \tilde{\phi}_{ip} | (H-E)(H-E)^{-1}(H-E) | \sum_{\nu} \phi_{\nu} c_v^{jq} \right) \tag{6.2.53}$$

$$= \sum_{\mu'\nu'} (A\Theta_p \tilde{\phi}_{ip} | (H-E) | \Phi_{\mu'})(\Phi_{\mu'} | (H-E)^{-1} | \Phi_{\nu'})(\Phi_{\nu'} | H - E | \sum_{\nu} \Phi_{\nu} c_v^{jq}) \tag{6.2.54}$$

$$= -\sum_{\mu'\nu'} (A\Theta_p \tilde{\phi}_{ip} | (H-E) | \Phi_{\mu'})(\Phi_{\mu'} | (H-E)^{-1} | \Phi_{\nu'})(\Phi_{\nu'} | H - E | A\Theta_q \tilde{\phi}_{jq}). \tag{6.2.55}$$

Equation 6.2.55 is obtained from the completeness condition in Eq. 6.2.51. Using Eqs. 6.2.52 and 6.2.55 we can re-write $\aleph_{st}$ as,

$$\aleph_{st} = \sum_{ip} \sum_{jq} \alpha_{ips} m_{ij}^{pq} \alpha_{jqt}, \tag{6.2.56}$$

where

$$m_{ij}^{pq} = M_{ij}^{pq} - \sum_{\mu,\nu} M_{ip,\mu} (M^{-1})_{\mu,\nu} M_{v,jq}, \tag{6.2.57}$$

and

$$M_{\mu,\nu} = (\Phi_{\mu} | H - E | \Phi_{\nu}) \tag{6.2.58}$$

$$M_{\mu,ip} = (\Phi_{\mu} | H - E | A\Theta_p \phi_{ip}) \tag{6.2.59}$$

$$M_{ij}^{pq} = \left(A\Theta_p \tilde{\phi}_{ip} | H - E | A\Theta_q \tilde{\phi}_{jq} \right). \tag{6.2.60}$$

In Eqs. 6.2.58, 6.2.59 and 6.2.60

- $M_{\mu,\nu}$ is a Hermitian bound-bound matrix, which can be determined from *Gaussian 03* output.

- $M_{\mu,ip}$ is a rectangular bound-continuum matrix. The calculation of $M_{\mu,ip}$ does not require the use of tail integrals derived by Wong et al. [137] and this matrix can also be obtained from *Gaussian 03* output.

- M_{ij}^{pq} is a non-Hermitian continuum-continuum matrix. The calculation of this matrix requires the use of tail integrals derived by Wong et al. [137].

The condition $\aleph_{st} = 0$ for an exact solution yields by Eq. 6.2.56,

$$\sum_{jq} m_{ij}^{pq} \alpha_{jqt} = 0. \tag{6.2.61}$$

From the general theory of partial differential equations we know that we must have n linearly independent solutions to the Schrödinger equation for t ranging from 1 to n. This implies that the $2n \times 2n$ matrix m_{ij}^{pq} must be a matrix of rank n for an exact solution. This condition is not going to be true for subspace-restricted expansions of the wavefunction Ψ_s. Thus a variational condition must be set up to approximate the coefficients α_{jqt}. The variational functional $\aleph$ in matrix form is given by,

$$\aleph = \alpha^\dagger \mathbf{m} \alpha = \alpha_0^\dagger (\mathbf{m}_{00}\alpha_0 + \mathbf{m}_{01}\alpha_1) + \alpha_1^\dagger (\mathbf{m}_{10}\alpha_0 + \mathbf{m}_{11}\alpha_1). \tag{6.2.62}$$

The variation of $\aleph$ becomes,

$$\delta\aleph = \delta\alpha^\dagger \mathbf{m}\alpha + (\mathbf{m}\alpha)^\dagger \delta\alpha + \alpha^\dagger(\mathbf{m} - \mathbf{m}^\dagger)\delta\alpha. \tag{6.2.63}$$

Equation 6.2.63 demonstrates that $\aleph$ is non-stationary for exact solutions since $\mathbf{m} - \mathbf{m}^\dagger \neq 0$ due to the non-Hermitian continuum-continuum matrix in Eq. 6.2.60.

The channel radial wavefunctions, f, g are normalized per Rydberg unit of energy. This implies,

$$m_{ij}^{pq} - m_{ji}^{qp} = M_{ij}^{pq} - M_{ji}^{qp} = \frac{\delta_{pq}}{2\pi N_{jq} N_{ip}} \left(\delta_{i1}\delta_{j0} - \delta_{i0}\delta_{j1}\right). \tag{6.2.64}$$

In matrix notation Eq. 6.2.64 becomes,

$$\mathbf{m}_{10} - \mathbf{m}_{01}^\dagger = \frac{1}{2\pi}\mathbf{B}, \quad B_{pq} = \delta_{pq}\frac{1}{N_{1p}N_{0q}}. \tag{6.2.65}$$

Equation 6.2.65 is the generalized Wronskian condition. We write, $\mathbf{B} = \mathbf{B}_0\mathbf{B}_1$ where,

$$\mathbf{B}_0 = \delta_{pq}\frac{1}{N_{0p}} \quad \mathbf{B}_1 = \delta_{pq}\frac{1}{N_{1p}}. \tag{6.2.66}$$

Equation 6.2.64 also shows that the matrices $\mathbf{m}_{00}$ and $\mathbf{m}_{11}$ are real and symmetric. The variation of $\aleph$ becomes,

$$\delta\aleph = \delta\alpha^\dagger \mathbf{m}\alpha + (\mathbf{m}\alpha)^\dagger\delta\alpha + \frac{1}{2\pi}\left(\alpha_1^\dagger \mathbf{B}\delta\alpha_0 - \alpha_0^\dagger\mathbf{B}\delta\alpha_1\right). \tag{6.2.67}$$

The variations of $\aleph$ are restricted to the modified canonical form,

$$\alpha_0 = \mathbf{B}_0^{-1}, \quad \alpha_1 = \mathbf{B}_1^{-1}\mathbf{K}. \tag{6.2.68}$$

At the exact solution, $\delta\aleph$ becomes,

$$\delta\aleph = -\frac{1}{2\pi}\delta\mathbf{K}. \tag{6.2.69}$$

Therefore the functional,

$$\mathbf{L} = \mathbf{K} + 2\pi\aleph, \tag{6.2.70}$$

is stationary for all variations. For a trial reaction matrix $\mathbf{K}_{trial}$, we have

$$\begin{aligned}\delta\aleph = {} & \delta\mathbf{K}_{trial}^\dagger(\mathbf{B}_1^{-1}\mathbf{m}_{10}\mathbf{B}_0^{-1} + \mathbf{B}_1^{-1}\mathbf{m}_{11}\mathbf{B}_1^{-1}\mathbf{K}_{trial}) \\ & + (\mathbf{B}_1^{-1}\mathbf{m}_{10}\mathbf{B}_0^{-1} + \mathbf{B}_1^{-1}\mathbf{m}_{11}\mathbf{B}_1^{-1}\mathbf{K}_{trial})^\dagger\delta\mathbf{K}_{trial} - \frac{1}{2\pi}\delta\mathbf{K}_{trial}.\end{aligned}$$

Therefore, $\mathbf{K}_{trial} = -\mathbf{B}_1\mathbf{m}_{11}^{-1}\mathbf{m}_{10}\mathbf{B}_0^{-1}$ stationarizes $\mathbf{L}$ consistent with Eq. 6.2.70. This defines,

$$\mathbf{L}_{min} = -\mathbf{B}_1\mathbf{m}_{11}^{-1}\mathbf{m}_{10}\mathbf{B}_0^{-1} + 2\pi\left(\mathbf{B}_0^{-1}\mathbf{m}_{00}\mathbf{B}_0^{-1} - \mathbf{B}_0^{-1}\mathbf{m}_{01}\mathbf{m}_{11}^{-1}\mathbf{m}_{10}\mathbf{B}_0^{-1}\right), \tag{6.2.71}$$

$$= \mathbf{B}_0^{-1}\left(2\pi(\mathbf{m}_{00} - \mathbf{m}_{10}^\dagger\mathbf{m}_{11}^{-1}\mathbf{m}_{10})\right)\mathbf{B}_0^{-1}. \tag{6.2.72}$$

Equation 6.2.72 allows us to recognize the best variational solution to the reaction matrix as,

$$\mathbf{K}_{var} = 2\pi\mathbf{B}_0^{-1}\left(\mathbf{m}_{00} - \mathbf{m}_{10}^\dagger\mathbf{m}_{11}^{-1}\mathbf{m}_{10}\right)\mathbf{B}_0^{-1}. \tag{6.2.73}$$

Equation 6.2.73 demonstrates that the reaction matrix is real and symmetric. In practice, Eq. 6.2.73 cannot be used to calculate the reaction matrix, because with increased basis set size the matrix $\mathbf{m}_{11}$ will start to have null eigenvalues. Instead we consider the eigenvalue decomposition of $\mathbf{m}_{11}$ to obtain the reaction matrix. The factorization of $\mathbf{m}_{11}$ is given by,

$$\mathbf{m}_{11} = \mathbf{U}\mathbf{D}\mathbf{U}^{T}, \tag{6.2.74}$$

where $\mathbf{U}$ is the orthogonal matrix of eigenvectors and $\mathbf{D}$ is a diagonal matrix of eigenvalues of $\mathbf{m}_{11}$. We factor, $\mathbf{K}_{trial} = \mathbf{B}_1\mathbf{U}\mathbf{S}\mathbf{U}^{T}\mathbf{B}_0^{-1}$. The condition $\mathbf{m}_{10}\mathbf{B}_0^{-1} + \mathbf{m}_{11}\mathbf{B}_1^{-1}\mathbf{K}_{trial} = 0$ yields,

$$\mathbf{D}\mathbf{S} = -\mathbf{U}^{T}\mathbf{m}_{10}\mathbf{U}, \tag{6.2.75}$$

defining a subspace of trial matrices. The trial matrix condition gives an expression for $\mathbf{L}_{min}$ as,

$$\begin{aligned}\mathbf{L}_{min} &= \mathbf{K}_{trial} + 2\pi\left(\mathbf{B}_0^{-1}\mathbf{m}_{00}\mathbf{B}_0^{-1} + \mathbf{B}_0^{-1}\mathbf{m}_{01}\mathbf{B}_1^{-1}\mathbf{K}_{trial}\right) &(6.2.76)\\ &= 2\pi\mathbf{B}_0^{-1}\mathbf{m}_{00}\mathbf{B}_0^{-1} + 2\pi\mathbf{B}_0^{-1}\mathbf{U}\mathbf{S}^{\dagger}\mathbf{D}\mathbf{S}\mathbf{U}^{T}\mathbf{B}_0^{-1}. &(6.2.77)\end{aligned}$$

Equation 6.2.77 allows us to deduce the best variational solution to the $\mathbf{K}$ matrix as,

$$\mathbf{K}_{var} = 2\pi\mathbf{B}_0^{-1}\left(\mathbf{m}_{00} - \mathbf{U}\mathbf{S}^{\dagger}\mathbf{D}\mathbf{S}\mathbf{U}^{T}\right)\mathbf{B}_0^{-1}, \tag{6.2.78}$$

where the matrix $\mathbf{S}^{\dagger}\mathbf{D}\mathbf{S}$ is given from Eq. 6.2.75 as,

$$(\mathbf{S}^{\dagger}\mathbf{D}\mathbf{S})_{st} = \sum_{k, D_k \neq 0} \frac{(\mathbf{U}^{T}\mathbf{m}_{10}\mathbf{U})^{*}_{ks}}{D_k}(\mathbf{U}^{T}\mathbf{m}_{10}\mathbf{U})_{kt}. \tag{6.2.79}$$

Combination of Equations 6.2.78 and 6.2.79 determine the real and symmetric reaction matrix. The calculation of the reaction matrix is now reduced to the numerical determination of the matrix elements $M_{\mu,\nu}$, $M_{ip,\mu}$ and $M_{ij,pq}$. These matrix elements can be calculated by expanding the one-electron orbital functions in Cartesian or spherical Gaussian functions and making use of the analytical results for all one- and two- electron molecular integrals.

6.3 Test Calculation on the $^1\Sigma_u^+$ States of the H_2 Molecule

Test calculations were performed on the $1s\sigma_g np\sigma_u$ Rydberg series of the two-electron H_2 molecule. At the lowest level of calculation, a single channel was included and the ion-core internal state was modeled as a single determinant reference state. This reference state was calculated using a restricted Hartree-Fock method for open shells and the 6-31G [128] atomic Gaussian basis.

The bound-type configurations were obtained by placing an additional electron in the lowest three virtual orbitals determined in the restricted Hartree-Fock calculation. The symmetry of these orbitals was selected as σ_u so that an overall state in the $^1\Sigma_u^+$ symmetry could be constructed. The two-electron reaction matrix was determined as a function of energy using Eqs. 6.2.78 and 6.2.79. The calculated quantum defects were found to depend very weakly on energy. The quantum defects as a function of energy were used in Eq. 2.205 to determine the potential energy curve for the $1s\sigma_g 4p\sigma_u$ electronic state of H_2. The results are compared with a very high level calculation reported by Wolniewicz et al. [124] in Fig. 6-1. There is a close agreement between the results of the present low-level calculation and the previous high-level calculation in the vicinity of the equilibrium internuclear distance. Deviations are seen at larger and smaller internuclear distances. These deviations are expected, since it is known that the restricted Hartree-Fock calculation is inaccurate at small and large electronic distances [128]; the method fails to capture the correct separated atom limit and the rapid change in the electronic structure as a function of increasing R. A CI-expansion of the ion-core internal state is required in order to correctly reproduce the small- and large- R behavior in the potential energy curve. However, as a validation test, the current results seem satisfactory.

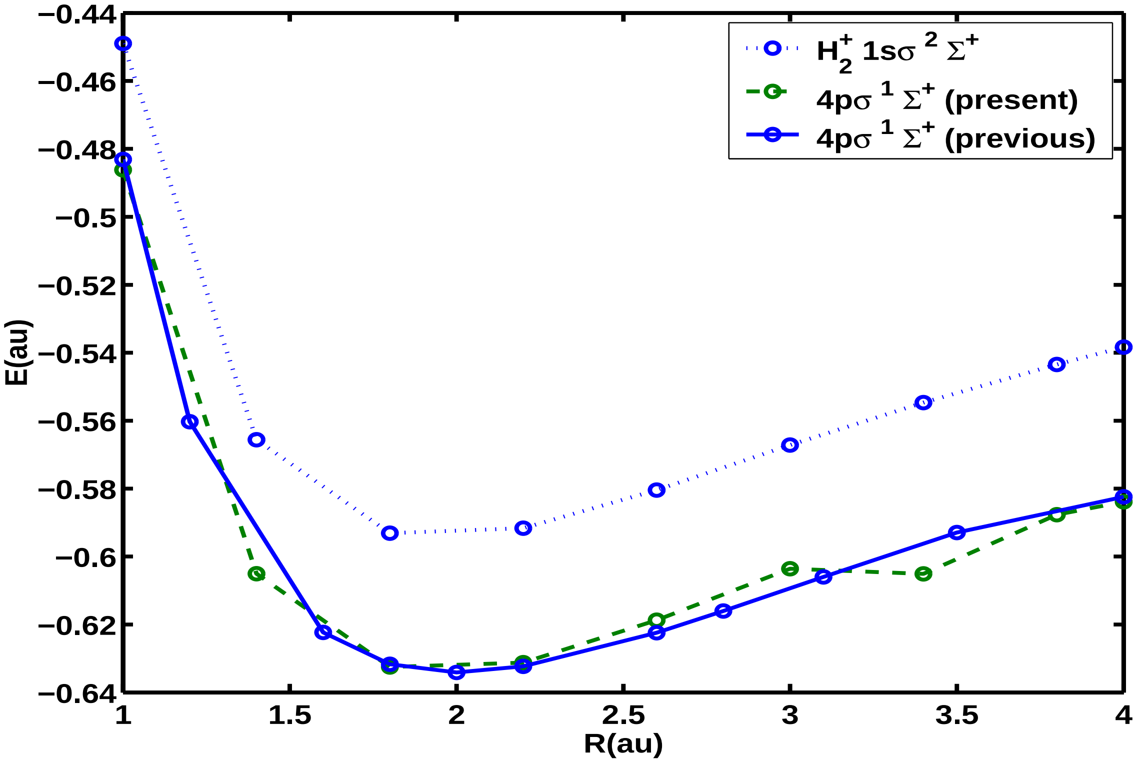

Figure 6-1: The potential curve for the $1s\sigma_g 4p\sigma_u$ electronic state of H_2. The zero of energy is measured with respect to vacuum. The top curve is the potential energy curve for the ground electronic state of the ion. The solid curve is the result of a high-level calculation performed by Wolniewicz et al. [124]. The dashed curve is the result obtained from the present two-electron reaction matrix calculation. There is a close agreement between the present and the previous results in the vicinity of the equilibrium internuclear distance. Deviations are seen at larger and smaller values of R. The error is likely due to the use of a single determinant to model the ion-core internal state (restricted Hartree-Fock). I thank Bryan Wong for preparing this figure.

Chapter 7

Conclusion

7.1 Summary

The main goal of this thesis was to discover the quantum chemical foundation of the quantum defect method, which is the most successful theory of electronic spectroscopy. The question that we have set out to answer was whether the central construct of multichannel quantum defect theory, the reaction matrix, could be determined accurately and efficiently from a first principles electronic structure calculation. The primary challenge was the development of a high-level calculation akin to quantum chemical computations that determine bound state molecular properties such as transition energies, force constants, and transition dipole moments to spectroscopic accuracy.

Such a calculation was built on the variational **R**-matrix theory of Kohn [69]. The variational theory was complemented by a Green's function propagation scheme that allowed for a significant decrease in the size of the **R**-matrix box. This made the calculation efficient, because it expedited the calculation of continuum type molecular integrals that would otherwise be prohibitively time consuming. A new representation of the reaction matrix was developed to ameliorate the energy dependence problem in the quantum defect matrix, which is most severe for molecules with highly polar ion-cores. The dipole-reduced $\bar{\mathbf{K}}$-matrix was derived from an algebraic transformation of the **K**-matrix in the orbital angular momentum representation. This transformation was made possible, because of the introduction of an analytically stronger pair Coulomb functions that absorbed some of the energy dependence in the **K**-matrix. The formalism of the $\bar{\mathbf{K}}$ matrix was a decisive step in the *ab initio* calculation of reaction matrices that could be input to the rovibrational frame transformation, the validity of which requires that the short-range reaction matrix depends only weakly on energy.

The $\bar{\mathbf{K}}$ matrix method was used to compute the Rydberg spectrum of the molecule CaF. The entire Rydberg spectrum for all principal quantum numbers and symmetries (Σ through Φ) was calculated in close agreement with the observed experimental data. The method was also used to characterize the electronic states in terms of their shapes, polarizations, and orbital angular momentum decompositions. Assignments based on dominant orbital angular momentum characters were made that can be used as benchmarks for further spectroscopic analyses. The calculation was then extended above the ionization threshold and photoionization cross sections were calculated to aid in the design of l-selective time domain experiments. The energy dependence of the photoionization cross sections as well as that of the eigenquantum defects indicated that the $^2\Sigma^+$ Rydberg states of CaF were collectively under the influence of a unique physical effect. This effect was that of a broad shape resonance, which was spread over the entire $^2\Sigma^+$ Rydberg series.

The adiabatic, potential-adapted partial wave method of Le Dourneuf et al. [23] was used for the analysis of the shape resonance. The analysis revealed that the broad shape resonance was due to the trapping of the Rydberg electron between a centrifugal barrier on the Ca^{+2} ion and the excluded volume of space around the F^- ion. The resonance was short-lived and, therefore, its effect was not localized about the resonance center energy; it was instead spread over the entire $^2\Sigma^+$ Rydberg series. This resulted in subtle but significant violations of Mulliken's rule [90], which establishes some of the fundamental properties of Rydberg states. Such an effect had been unnoticed in the spectrum previously.

Finally the variational reaction matrix calculation was generalized to a many-electron formalism. In this formalism, spin and electron exchange was explicitly taken into account and the reaction matrix was obtained directly from a stationary condition imposed on the collision wavefunction. This theory necessitated the development of methods for evaluating non-standard molecular integrals over continuum-type basis functions. Once such methods were incorporated into the Gaussian-based quantum chemistry program, we were able seamlessly merge the reaction matrix calculation with quantum chemistry. The computer programs for the many-electron calculation were written by Bryan M. Wong and Serhan Altunata. Test calculations on the $1s\sigma np\sigma$ $^1\Sigma_u^+$ Rydberg states of the H_2 molecule were carried out. Close agreement was obtained between the results of the present theory and previous *ab initio* calculations. The generalization of the reaction matrix theory was the final step for embedding the generalized quantum defect methods presented in this thesis into quantum chemistry.

Thus, the quantum chemical foundation of the quantum defect method has been comprehensively determined. High-level calculations comparable in accuracy to standard quantum chemistry were developed using the reaction matrix method. It is possible that these results can pave the way for a novel type of quantum chemistry that aims to calculate the electronic structure over the entire bound-state region, as opposed to the current methods that focus on state-by-state calculations.

7.2 Future Directions

The computer programs that were used to implement the reaction matrix calculation can be employed with minor changes to calculate the Rydberg spectra of other alkaline-earth monohalides such as BaF and CaCl. The nature of the shape resonance in CaF suggests that similar shape resonances might be present in these molecules as well. The existence of a shape resonance in BaF has already been verified by another research group [67]. In order to understand how the shape resonance behaves in different molecular environments, the possible shape resonances in BaF and CaCl can be investigated in a future project.

The polyatomic analogues of the shape resonance in CaF are of physical interest. One can expect a double well-double barrier generalization of the CaF shape resonance in a linear triatomic molecule. The only difference would be that the Lorentzian profile of the shape resonance would be split, as in Fig. 7-1, due to interference of partial waves reflecting off of the barriers at the opposite ends of the molecule. The splitting in the shape resonance profile would depend on the vibrational state of the molecule and this dependence can provide rich probes of the effect of molecular geometry on electron dynamics.

The existence of the shape resonance in CaF has implications about how MQDT fits to experimental data can be implemented. The short-range reaction matrix for CaF $^2\Sigma^+$ states cannot be assumed to be energy independent. The explicit energy dependence in the short-range matrix should be built into to the fit program using the expressions derived in **Chapter 2**. This is likely to result in a better fit to data over a broader region of the

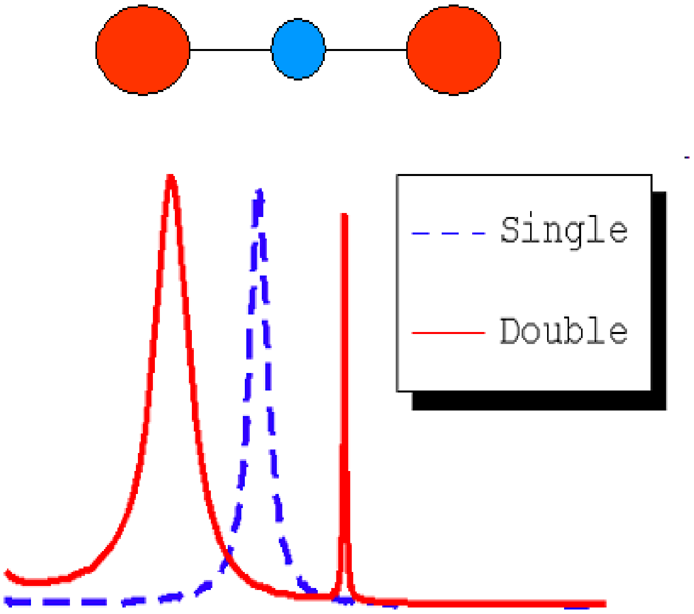

Figure 7-1: Illustration of a shape resonance in a linear triatomic molecule. The single shape resonance in the diatomic molecule has the profile shown by the dashed curve. In an ABA triatomic molecule, there are two degenerate shape resonances due to the double well-double barrier structure on the left and the right hand sides of the molecule. The degenerate resonances interfere because of the reflection of the scattering partial waves off of the barriers at the two atoms on opposite sides. The resonance profile splits, giving rise to a broader resonance at lower energy and a much sharper resonance at higher energy. The sharper resonance is an example of a quantum proximity resonance discussed by Heller [56, 75].

spectrum.

The fit programs should also account for the strong energy dependence of the reaction matrix, $\mathbf{K}$, in the orbital angular momentum representation. In previous studies, the experimental data was fitted directly to the $\mathbf{K}$ matrix, because the frame transformation assumes such an integer-l representation. Comparison of the fit results [37] and the plots of the energy dependence of the $\mathbf{K}$ matrix presented in **Chapter 4** suggest that the experimental data samples the average values of the highly oscillatory reaction matrix elements. A more satisfactory fit can be obtained if the $\bar{\mathbf{K}}$ matrix is used in the frame transformation instead of the $\mathbf{K}$ matrix. The $\bar{\mathbf{K}}$ matrix has a mild dependence on energy, which is appropriate for the validity of the frame transformation. However, angular momentum algebra is inapplicable to such a representation. In a future project, a theory can be developed that adapts the frame transformation to non-integer or complex values of orbital angular momentum.

The many-electron generalization of the reaction matrix can be applied to resolve a long-standing question about the Rydberg states of CaF. This question concerns the location of the repulsive potential energy curve of CaF that belongs to the Ca(4s) + F(σ)-hole valence electronic state cannot be answered with an effective single electron treatment. The coupling to the repulsive curve is a charge transfer process, which involves the transfer of the electron on the F^- to the $4s$ shell on the Ca atom in the repulsive state. The repulsive state is responsible for predissociation of ${}^2\Sigma^+$ Rydberg states converging to the $v^+ = 0$ ionization threshold. It has been suggested that the onset of predissociation is at $n^* \approx 10$ [38]. A future project can begin the search for the repulsive state in this region of the principal quantum number. It is expected that the repulsive state will appear as a Feshbach resonance in the Rydberg-Rydberg block of the many electron reaction matrix, causing the eigenquantum defects to increase sharply at the energy of the curve crossings. It has also been suggested that there is an indirect coupling of the vibrational states of the ion-core that violates the $\Delta v^+ = \pm 1$ rule [38] for low quanta of vibration. Interlopers have been observed from $v^+ = 4$ and $v^+ = 5$ levels in Rydberg spectra converging to the $v^+ = 1$ vibrational state of the ion-core. This indirect coupling has been attributed to a pathway via in an intermediate step through the nuclear continuum associated with the repulsive state [38]. This type of indirect coupling can also be investigated with an R-dependent resonance analysis of the many electron reaction matrix.

Bibliography

[1] The S matrix used here is the same as the matrix χ defined by Seaton in [111].

[2] M. Abramowitz and I.A. Stegun. *Handbook of Mathematical Functions.* U.S. Department of Commerce, National Bureau of Standard, 1970.

[3] A.B.Samokhin. *Integral Equations and Iteration Methods in Electromagnetic Scattering.* VSP Publications, The Netherlands, 2001.

[4] S. N. Altunata and R. W. Field. *Phys. Rev. A*, 67:022507, 2003.

[5] M. Arif, Ch. Jungen, and A. L. Roche. *J. Chem. Phys.*, 106:4102, 1997.

[6] M. Aymar and M.Telmini. *J. Phys. B*, 24:4935, 1991.

[7] J. M. Berg, J. E. Murphy, N. A. Harris, and R. W. Field. *Phys. Rev. A*, 48:3012, 1993.

[8] H. A. Bethe and E. E. Salpeter. *Quantum Mechanics of One and Two-Electron Atoms.* Springer-Verlag, Berlin, 1957.

[9] J.M. Brown and B.J. Howard. *Mol. Phys.*, 31:1517, 1976.

[10] P. G. Burke. *Phys. Rev. A*, 160:719, 1968.

[11] P. G. Burke, I Mackey, and I Shimamura. *J. Phys. B*, 10:2497, 1977.

[12] P. G. Burke and M. J. Seaton. *J. Phys. B*, 17:L683, 1984.

[13] P.G. Burke. *The Physics of Electronic and Atomic Collisions*, Pub: Boulder Colorado, JILA:128, 1968.

[14] P.G. Burke, A. Hibbert, and W.D. Robb. *J. Phys. B*, 4:153, 1971.

[15] P. J. A. Buttle. *Phys. Rev.*, 160:719, 1967.

[16] M. S. Child. *Molecular Collision Theory.* Dover Publications INC., Mineola, New York, 1996.

[17] Michael Chrysos. *J. Phys. B.*, 31:1391, 1998.

[18] Claude Cohen-Tannoudji, Bernard Diu, and Franck Laloë. *Quantum Mechanics.* Wiley and Sons, New York, 1977.

[19] J. W. Cooley. *Math. Comput.*, 615:363, 1961.

[20] Michael Courtney and Daniel Kleppner. *Phys. Rev. A*, 53:178, 1996.

[21] Philippe Denery and Andre Krzywicki. *Mathematics for Physicists.* Dover Publications,INC., New York, 1995.

[22] Dan Dill and J.L.Dehmer. *J. Chem. Phys.*, 61:692, 1974.

[23] M Le Dourneuf, Vo Ky Lan, and J M Launay. *J. Phys. B*, 15:L685, 1982.

[24] Ning Yi Du and C. H. Greene. *Phys. Rev. A*, 36:971, 1987.

[25] J. Dubau. *J. Phys. B*, 11:4095, 1978.

[26] J. Dubau and J. Wells. *J. Phys. B*, 6:1452, 1973.

[27] K. M. Dunseath, M. Terao-Dunseath, and J. M. Launay. *J. Phys. B.*, 33:3037, 2000.

[28] W Eissner and M J Seaton. *J. Phys. B*, 5:2187, 1972.

[29] U. Fano. *Phys. Rev.*, 124:1866, 1961.

[30] U. Fano. *Phys. Rev. A*, 7:353, 1970.

[31] U. Fano. *Phys. Rev. A*, 17:93, 1978.

[32] U. Fano and Dan Dill. *Phys. Rev. A*, 6:185, 1972.

[33] U. Fano and C.M. Lee. *Phys. Rev. Lett.*, 31:1573, 1973.

[34] U. Fano and A. R. P. Rau. *Atomic Collisions and Spectra.* Academic Press, New York, 1986.

[35] H. Feshbach. *Ann. Phys.*, 5:357, 1958.

[36] H. Feshbach. *Ann. Phys.*, 19:287, 1962.

[37] R. W. Field, C. M. Gittins, N. A. Harris, and Ch. Jungen. *J. Chem. Phys.*, 122:184314, 2005.

[38] Robert W. Field. Private Communication.

[39] Arne W. Flifet and Vincent McKoy. *Phys. Rev. A*, 18:1048, 1978.

[40] C. M. Gittins, N. A. Harris, Ma Hui, and R. W. Field. *Can. J. Phys.*, 79:247, 2001.

[41] A Giusti-Suzor and U. Fano. *J. Phys. B*, 17:215, 1984.

[42] C. H. Greene. *Phys. Rev. A*, 22:149, 1980.

[43] C. H. Greene. *Phys. Rev. A*, 22:149, 1980.

[44] C. H. Greene. *Phys. Rev. A*, 28:2209, 1983.

[45] C. H. Greene and M. Aymar. *Phys. Rev. A*, 44:1773, 1991.

[46] C. H. Greene, U. Fano, and G. Strinati. *Phys. Rev. A*, 19:1485, 1979.

[47] C. H. Greene and Ch. Jungen. *Adv. At. Mol. Phys.*, 21:51, 1985.

[48] C. H. Greene and Ch. Jungen. *Phys. Rev. Lett.*, 55:1066, 1985.

[49] C. H. Greene and Longhuan Kim. *Phys. Rev. A*, 36:2706, 1987.

[50] C. H. Greene, A. R. P. Rau, and U. Fano. *Phys. Rev. A*, 26:2441, 1982. For errata see [51]. This is Paper II. Paper I is [46].

[51] C. H. Greene, A. R. P. Rau, and U. Fano. *Phys. Rev. A*, 30:3321, 1984.

[52] C. H. Greene and B. Yoo. *J. Phys. Chem.*, 99:1711, 1995.

[53] David J. Griffiths. *Introduction to Quantum Mechanics.* Prentice Hall, New Jersey, 1994.

[54] Frank S. Ham. *Solid State Phys.*, 1:127, 1955.

[55] N. A. Harris and Ch. Jungen. *Phys. Rev. Lett.*, 70:2549, 1993.

[56] E. J. Heller. *Phys. Rev. Lett.*, 77:4122, 1996.

[57] G. Herzberg. *Phys. Rev. Lett.*, 23:1081, 1969.

[58] Gerhard Herzberg. *atomic spectra and atomic structure.* Dover Publications, New York, 1944.

[59] Miyabi Hiyama and Mark S. Child. *J. Phys. B*, 36:4547, 2003.

[60] A. U. Huzi. *Phys. Rev. A*, 19:920, 1979.

[61] E. L. Ince. *Ordinary Differential Equations.* Dover Publications,INC., New York, 1956.

[62] R. Jastrow. *Phys. Rev.*, 73:60, 1948.

[63] C. Jungen and G. Raseev. *Phys. Rev. A*, 57:2407, 1998.

[64] Ch. Jungen and O. Atabek. *J. Chem. Phys.*, 66:5584, 1977.

[65] Ch. Jungen and A.L. Roche. *Can. J. Phys.*, 79:287, 2001.

[66] Ch. Jungen and F. Texier. *J. Phys. B*, 33:2495, 2000.

[67] Christian Jungen. Private Communication.

[68] Christian Jungen. *J. Chem. Phys.*, 53:4168, 1970.

[69] W. Kohn. *Phys. Rev.*, 74:1763, 1948.

[70] V. Kokoouline, C. H. Greene, and B. D. Esry. *Nature(London)*, 412:891, 2001.

[71] L. D. Landau and E. M. Lifshitz. *Quantum Mechanics.* Butterworth and Heinemann, Oxford, 1997.

[72] A. M. Lane and R. G. Thomas. *Rev. Mod. Phys.*, 30:257, 1958.

[73] M. N. Lebedev. *Special Functions And Their Applications.* Dover Publications INC., Mineola,New York, 1965.

[74] Helene Lefebvre-Brion and Robert W. Field. *The Spectra and Dynamics of Diatomic Molecules.* Academic Press, New York, 2004.

[75] Sheng Li and E. J. Heller. *Phys. Rev. A*, 67:032712, 2003.

[76] C. D. Lin. *Astrophys. J.*, 187:385, 1974.

[77] K. T. Lu. *Phys. Rev. A*, 4:579, 1971.

[78] K. T. Lu. *Phys. Rev. A*, 4:579, 1971.

[79] K.T. Lu and U. Fano. *Phys. Rev. A*, 2:81, 1970.

[80] Robert R. Lucchese and Vincent McKoy. *Phys. Rev. A*, 21:112, 1980.

[81] Nasser Maleki. *Phys. Rev. A*, 29:2470, 1984.

[82] Steven Trent Manson. *Phys. Rev.*, 182:97, 1969.

[83] Jerrold E. Marsden and Michael J. Hoffman. *Basic Complex Analysis.* W. H. Freeman, New York, 1999.

[84] R. J. Mathar. *Int. J. Quant. Chem.*, 90:227, 2002.

[85] Albert Messiah. *Quantum Mechanics.* Dover Publications INC., New York, 1999.

[86] Gregory Miecznik and C. H. Greene. *Chem. Phys. Lett*, 258:607, 1996.

[87] F. H. Mies. *Phys. Rev. A*, 20:1773, 1979.

[88] C. E. Moore. *Atomic Energy Levels.* Natl. Bur. Std. Circular No. 467 Vol.III, US GPO, Washington DC, 1958.

[89] L. A. Morgan, C. J. Gillan, J. Tennyson, and Xiushan Chen. *J. Phys. B*, 30:4087, 1997.

[90] R. S. Mulliken. *J. Am. Chem. Soc.*, 86:3183, 1964.

[91] J. E. Murphy, J. M. Berg, A. J. Merer, Nicole A. Harris, and R. W. Field. *Phys. Rev. Lett.*, 65:1861, 1990.

[92] H. Nakatsuji. *Chem. Phys. Lett.*, 59:362, 1978.

[93] H. Nakatsuji and K. Hirao. *J. Chem. Phys.*, 68:2053, 1978.

[94] H. Nakatsuji and K. Hirao. *Chem. Phys. Lett.*, 67:329, 1979.

[95] Robert K. Nesbet. *Variational Principles and Methods in Theoretical Physics and Chemistry.* Cambridge University Press, The Edinburgh Building, Cambridge CB2 2RU, UK, 2003.

[96] Roger G. Newton. *Scattering Theory of Particles and Waves.* Springer-Verlag, New York, 1982.

[97] J. V. Noble. *Phys. Rev.*, 161:945, 1967.

[98] Patrick F. O'Mahoney. *Phys. Rev. A*, 32:908, 1985.

[99] William H. Press, Saul A. Teukolsky, William T. Vetterling, and Brian P. Flannery. *Numerical Recipes in C++.* Cambridge University Press, Cambridge, UK, 2002.

[100] Ismanuel Rabadan and Jonathan Tennyson. *J. Phys. B*, 30:1975, 1997.

[101] S. Raouafi, Gh. Jeung, and Ch. Jungen. *J. Chem. Phys.*, 115:7450, 2001.

[102] S.F. Rice, H.Martin, and R. W. Field. *J. Chem. Phys.*, 82:5023, 1985.

[103] H Le Rouzo. *Int. J. Quant. Chem.*, 64:647, 1997.

[104] J.J. Sakurai. *Modern Quantum Mechanics.* Addison-Wesley, New York, 1994.

[105] B. I. Schneider. *Phys. Rev. A*, 11:1957, 1975.

[106] B. I. Schneider and P J Hay. *Phys. Rev. A*, 13:2049, 1976.

[107] M. J. Seaton. *Mon. Not. R. Astron. Soc.*, 118:504, 1958.

[108] M. J. Seaton. *Proc. Phys. Soc.*, 88:801, 1966a.

[109] M. J. Seaton. *Proc. Phys. Soc.*, 88:815, 1966b.

[110] M. J. Seaton. *J. Phys. B*, 2:5, 1969.

[111] M. J. Seaton. *J. Phys. B*, 11:4067, 1978.

[112] M. J. Seaton. *Rep. Prog. Phys.*, 46:167, 1983.

[113] Isao Shimamura. *J. Phys. B*, 10:2597, 1977.

[114] Felix T. Smith. *Phys. Rev.*, 118:349, 1960.

[115] K. Smith and L. Morgan. *Phys. Rev.*, 165:110, 1968.

[116] S.N.Altunata, J. Cao, and R.W.Field. *Phys. Rev. A*, 65:053415, 2002.

[117] S.N.Altunata, S.L.Coy, and R.W.Field. *J. Chem. Phys.*, 123:084318, 2005.

[118] S.N.Altunata, S.L.Coy, and R.W.Field. *J. Chem. Phys.*, 123:084319, 2005.

[119] S.N.Altunata, S.L.Coy, and R.W.Field. *J. Chem. Phys.*, 124:194302, 2006.

[120] Gregory L. Snitchler and Deborah K. Watson. *J. Phys. B*, 19:259, 1986.

[121] L. Spruch. *The Physics of Electronic and Atomic Collisions*, Pub: Boulder Colorado, JILA:89, 1968.

[122] J. F. Stanton and R.J. Bartlett. *J. Chem. Phys.*, 98:7029, 1993.

[123] A. F. Starace. *J. Phys. B*, 6:76, 1973.

[124] G. Staszewska and L. Wolniewicz. *J. Mol. Spec.*, 212:208, 2002.

[125] Darian T. Stibbe and Jonathan Tennyson. *J. Phys. B.*, 29:4267, 1996.

[126] Gilbert Strang. *Introduction to Applied Mathematics.* Wellesley-Cambridge Press, Wellesley MA USA, 1996.

[127] John R. Swanson, Dan Dill, and J.L. Dehmer. *J. Chem. Phys.*, 75:619, 1981.

[128] Attila Szabo and Neil S. Ostlund. *Modern Quantum Chemistry: Introduction to Electronic Structure Theory.* McGraw Hill, New York, 1982.

[129] S. Takezawa. *J. Chem. Phys.*, 52:5793, 1970.

[130] Mourad Telmini and Christian Jungen. *Phys. Rev. A*, 68:062704, 2003.

[131] J. Tennyson. *J. Phys. B*, 21:805, 1988.

[132] J. Tennyson and C. J. Noble. *J. Phys. B*, 18:155, 1985.

[133] J. Tennyson, C J Noble, and S Salvini. *J. Phys. B*, 17:905, 1984.

[134] J. K. G. Watson. *Mol. Phys.*, 81:277, 1994.

[135] E. P. Wigner and L. Eisenbud. *Phys. Rev.*, 72:29, 1947.

[136] Eugene Wigner. *Phys. Rev.*, 98:145, 1955.

[137] Bryan M. Wong, Serhan N. Altunata, and Robert W. Field. *J. Chem. Phys.*, 124:014106, 2006.

[138] J. J. Wynne and J. A. Armstrong. *IBM J. Res. Dev.*, 23:490, 1979.

[139] Richard N. Zare. *Angular Momentum.* John Wiley and Sons, US, 1987.

[140] Eberhard Zeidler. *Applied Functional Analysis.* Springer-Verlag, New York, 1991.